UNIVERSITAT
POLITÈCNICA
DE VALÈNCIA

COMPUTATIONAL FLUID DYNAMICS MULTISCALE MODELLING OF BUBBLY FLOW. A CRITICAL STUDY AND NEW DEVELOPMENTS ON VOLUME OF FLUID, DISCRETE ELEMENT AND TWO-FLUID METHODS

A dissertation submitted to the Universitat Politècnica de València in partial fulfilment of the requirements for the degree of Doctor of Philosophy.

by

Carlos Peña Monferrer

Supervised

by

Prof. Dr. Sergio Chiva Vicent
Prof. Dr. José Luis Muñoz-Cobo González

July 2017

Abstract

The study and modelling of two-phase flow remains a challenge that requires exploring the physical phenomena from different spatial and temporal resolution levels, even for the simplest regime such as bubbly flow. Computational Fluid Dynamics (CFD) is a widespread and promising tool for modelling, but nowadays, there is no single approach or method to predict the dynamics of these systems providing enough precision of the results. The inherent difficulties of the events occurring in this flow, mainly those related with the interface between phases, makes that low or intermediate resolution level approaches as system codes (RELAP, TRACE, etc.) or 3D TFM (Two-Fluid Model) have significant issues to reproduce acceptable results, unless well-known scenarios and global values are considered. Instead, methods based on high resolution level such as Interfacial Tracking Method (ITM) or Volume Of Fluid (VOF) require a high computational effort that makes unfeasible its use in complex systems.

In this thesis, an open-source simulation framework has been designed and developed using the OpenFOAM® library to analyse the cases from microescale to macroscale levels. The different approaches and the information that is required in each one of them is studied for bubbly flow. In the first part, the dynamics of single bubbles at a high resolution level are examined through VOF. This technique allowed obtaining accurate results related to the bubble formation, terminal velocity, path, wake and instabilities produced by the wake. However, this approach has been impractical for real scenarios with more than dozens of bubbles. Alternatively, this thesis proposes a CFD Discrete Element Method (CFD-DEM) technique, where each bubble is represented discretely. A novel solver for bubbly flow has been developed in this thesis. This includes numerous improvements necessary to reproduce the bubble-bubble and bubble-wall interactions, turbulence, velocity seen by the bubbles, momentum and mass exchange term over the cells or bubble expansion, among others. But also new implementations as an algorithm to seed the bubbles in the system have been incorporated. This new solver gives more accurate results as the provided up to date.

Following the decrease on resolution level, and therefore the required computational resources, a 3D TFM is developed with a population balance equation solved with an implementation of the Quadrature Method Of Moments (QMOM). The solver is implemented with the same closure models as the CFD-DEM to analyse the effect involved with the lost of information due to the averaging of the instantaneous Navier-Stokes equation. The analysis of the results with CFD-DEM reveals the discrepancies found by considering averaged values and homogeneous flow in the models of the classical TFM formulation. Finally, for the lowest resolution level approach, the system code RELAP5/MOD3 is used for modelling bubbly flow regime. The code is modified to reproduce properly the two-phase flow characteristics in vertical pipes, comparing the performance of the calculation of the drag term based on drift-velocity and drag coefficient approaches.

To perform this work it has been necessary not only the development of solvers and models for the different approaches, but it has also become essential to acquire an in-depth knowledge of the physical phenomena and interpretation of the real measurements in bubbly flow. Throughout the thesis, much effort has been put into performing a rigorous analysis. As a result, a virtual system has been incorporated in the numerical scheme to obtain variables from the signal generated by the bubbles and processed with the same program as the one used in the experiments. In this way, the results obtained by the measuring equipment and the simulations are fully equivalent and comparable. Experimental data from different authors has been taken to validate the solvers for the different approaches and all the available variables compared, analysing those that are not available or offered by the authors.

Resumen

El estudio y modelado de flujos bifásicos, incluso los más simples como *bubbly flow*, sigue siendo un reto que conlleva aproximarse a los fenómenos físicos que lo rigen desde diferentes niveles de resolución espacial y temporal. El uso de códigos CFD (*Computational Fluid Dynamics*) como herramienta de modelado está muy extendida y resulta prometedora, pero hoy por hoy, no existe una única aproximación o técnica de resolución que permita predecir la dinámica de estos sistemas, y que ofrezca suficiente precisión en sus resultados. La dificultad intrínseca de los fenómenos que allí ocurren, sobre todo los ligados a la interfase entre ambas fases, hace que los códigos de bajo o medio nivel de resolución, como pueden ser los códigos de sistema (RELAP, TRACE, etc.) o los basados en aproximaciones 3D TFM (*Two-Fluid Model*) tengan serios problemas para ofrecer resultados aceptables, a no ser que se trate de escenarios muy conocidos y se busquen resultados globales. En cambio, códigos basados en alto nivel de resolución, como los que utilizan VOF (*Volume Of Fluid*), requieren de un esfuerzo computacional tan elevado que no pueden ser aplicados a sistemas complejos.

En esta tesis, mediante el uso de la librería OpenFOAM® se ha creado un marco de simulación de código abierto para analizar los escenarios desde niveles de resolución de microescala a macroescala, analizando las diferentes aproximaciones, así como la información que es necesaria aportar en cada una de ellas, para el estudio del régimen de *bubbly flow*. En la primera parte se estudia la dinámica de burbujas individuales a un alto nivel de resolución mediante el uso del método VOF. Esta técnica ha permitido obtener resultados precisos como la formación de la burbuja, velocidad terminal, camino recorrido, estela producida por la burbuja e inestabilidades que produce en su camino. Pero esta aproximación resulta inviable para entornos reales con la participación de más de unas pocas decenas de burbujas. Como alternativa, se propone el uso de técnicas CFD-DEM (*Discrete Element Methods*) en la que se representa a las burbujas como partículas discretas. En esta tesis se ha desarrollado un nuevo solver para bubbly flow en el que se han añadido un gran número de nuevos modelos, como los necesarios para contemplar los choques entre burbujas o con las paredes, la turbulencia, la velocidad vista por las burbujas, la distribución del intercambio de momento y masas con el fluido en las diferentes celdas o la expansión de la fase gaseosa entre otros. Pero también se ha tenido que incluir nuevos algoritmos como el necesario para inyectar de forma adecuada la fase gaseosa en el sistema. Este nuevo solver ofrece resultados con un nivel de resolución superior a los desarrollados hasta la fecha.

Siguiendo con la reducción del nivel de resolución, y por tanto los recursos computacionales necesarios, se efectúa el desarrollo de un solver tridimensional de TFM en el que se ha implementado el método QMOM (Quadrature Method Of Moments) para resolver la ecuación de balance poblacional. El solver se desarrolla con los mismos modelos de cierre que el CFD-DEM para analizar los efectos relacionados con la pérdida de información debido al promediado de las ecuaciones

instantáneas de Navier-Stokes. El análisis de resultados de CFD-DEM permite determinar las discrepancias encontradas por considerar los valores promediados y el flujo homogéneo de los modelos clásicos de TFM. Por último, como aproximación de nivel de resolución más bajo, se investiga el uso de códigos de sistema, utilizando el código RELAP5/MOD3 para analizar el modelado del flujo en condiciones de *bubbly flow*. El código se ha modificado para reproducir correctamente el flujo bifásico en tuberías verticales, comparando el comportamiento de aproximaciones para el cálculo del término de drag basadas en velocidad de drift o del coeficiente de drag.

En esta tesis, sin embargo, no sólo ha sido necesario desarrollar solvers para las diferentes aproximaciones. Si no que ha sido imprescindible adquirir un conocimiento muy profundo de los fenómenos que ocurren y la comprensión e interpretación de los resultados experimentales que se obtienen desde los experimentos reales de *bubbly flow*. En la tesis se ha dedicado mucho esfuerzo a analizar con detalle los fenómenos físicos, y se ha tenido que desarrollar un sistema virtual de medida que coincide con el experimental, creando una señal equivalente a la que ofrece el equipo experimental del laboratorio, y que ha sido procesado con el mismo software que éste. Así, los resultados obtenidos por el equipo y la simulación son totalmente comparables. Se han tomado resultados experimentales de varios autores para validar de forma muy rigurosa los resultados obtenidos en las diferentes aproximaciones, comparando todos los parámetros disponibles en el experimento, y analizando aquellos que no ofrecían las publicaciones.

Resum

L'estudi i modelatge de fluxos bifàsics, fins i tot els més simples com *bubbly flow*, segueix sent un repte que comporta aproximar-se als fenòmens físics que ho regeixen des de diferents nivells de resolució espacial i temporal. L'ús de codis CFD (*Computational Fluid Dynamics*) com a eina de modelatge està molt estesa i resulta prometedora, però ara per ara, no existeix una única aproximació o tècnica de resolució que permeta predir la dinàmica de sistemes i que oferisca suficient precisió en els seus resultats. Les dificultats intrínseques dels fenòmens que hi tenen lloc, sobre tots els lligats a la interfase, fa que els codis de baix o mig nivell de resolució, com poden ser els codis de sistema (RELAP, TRACE, etc.) o els basats en aproximacions 3D TFM (*Two-Fluid Model*) tinguen seriosos problemes per a oferir resultats acceptables, llevat que es tracte d'escenaris molt coneguts i es persegueixen resultats globals. En canvi, codis basats en alt nivell de resolució, com els que utilitzen VOF (*Volume Of Fluid*), requereixen d'un esforç computacional tan elevat que no poden ser aplicats a sistemes complexos.

En aquesta tesi, mitjançant l'ús de la llibreria OpenFOAM® s'ha creat un marc de simulació de codi obert per a analitzar els escenaris des de nivells de resolució de microescala a macroescala, analitzant les diferents aproximacions, així com la informació que és necessària aportar en cadascuna d'elles, per a l'estudi del règim de *bubbly flow*. En la primera part s'estudia la dinàmica de bambolles individuals a un alt nivell de resolució mitjanant l'ús del mètode VOF. Aquesta tècnica ha permès obtenir resultats precisos com la formació de la bambolla, velocitat terminal, camí recorregut, estel·la produït per la bambolla i inestabilitats que produeix en el seu camí. Però aquesta aproximació resulta inviable per a entorns reals amb la participació de més d'unes poques desenes de bambolles. Com a alternativa en aqueix cas es proposa l'ús de tècniques CFD-DEM (*Discrete Element Methods*) en la qual es representa a les bambolles com a partícules discretes. En aquesta tesi s'ha desenvolupat un nou solver per a *bubbly flow* per al qual s'han afegit un gran nombre de nous models, com els necessaris per a contemplar els xocs entre bambolles o amb les parets, la turbulència, la velocitat vista per les bambolles, la distribució de l'intercanvi de moment i masses amb el fluid en les diferents celles per cadascuna de les bambolles o els models dexpansió de la fase gasosa entre uns altres. Però també s'ha hagut d'incloure nous algoritmes com el necessari per a injectar de forma adequada la fase gasosa en el sistema. Aquest nou solver ofereix resultats amb un nivell de resolució superior als desenvolupat fins a la data.

Seguint amb la reducció del nivell de resolució, i per tant els recursos computacionals necessaris, s'efectua el desenvolupament d'un solver tridimensional de TFM en el qual s'ha implementat el mètode QMOM (*Quadrature Method Of Moments*) per a resoldre l'ecuació de balanç poblacional. El solver es desenvolupa amb els mateixos models de tancament que el CFD-DEM per a analitzar els efectes relacionats amb la pèrdua d'informació a causa del promitjat de les equacions instantànies de Navier-Stokes. L'anàlisi de resultats de CFD-DEM permet deter-

minar les discrepàncies ocasionades per considerar els valors promitjats i el flux homogeni dels models clàssics de TFM. Finalment, com a aproximació de nivell de resolució més baix, s'analitza l'ús de codis de sistema, utilitzant el codi RELAP5/MOD3 per a analitzar el modelatge del fluxos en règim de *bubbly flow*. El codi és modificat per a reproduir correctament les característiques del flux bifàsic en canonades verticals, comparant el comportament d'aproximacions per al càlcul del terme de drag basades en velocitat de drift flux model i de les basades en coeficient de drag.

Però en aquesta tesi no solament ha sigut necessari desenvolupar solvers per a les diferents aproximacions. Ha sigut imprescindible adquirir un coneixement molt profund dels fenòmens que ocorren i la comprensió i la interpretació dels resultats experimentals que s'obtenen des dels experiments reals de *bubbly flow*. En la tesi s'ha dedicat molt esforç a analitzar amb detall els fenòmens físics, i s'ha hagut de desenvolupar un sistema virtual de mesura que coincideix amb l'experimental, creant un senyal equivalent a la qual ofereix l'equip experimental del laboratori, i que ha sigut processat amb el mateix software que aquest. Així, els resultats obtinguts per l'equip i la simulació són totalment comparables. S'han considerat resultats experimentals de diversos autors per a validar de la forma mes rigorosa possible els resultats obtinguts en les diferents aproximacions, comparant tots els paràmetres disponibles en l'experiment, i analitzant aquells que no oferien les publicacions.

Preface and acknowledgements

My research adventure started some years ago, in 2009, while finishing the Bachelor's degree in Industrial Engineering at *Universitat Jaume I* (UJI). Under the guidance of Prof. Dr. Sergio Chiva, I was introduced to the world of the Computational Fluid Dynamics techniques. I am especially grateful to him for all the support and the vast knowledge given, not only to this thesis, but to all the research activities in which I was involved.

Later, a year abroad at *Teschnische Universität München* helped me to move forward in the knowledge of the physical modelling and developing, using ANSYS CFX and OpenFOAM software. I would like to thank Prof. Dr. Macián-Juan and Dr. Filippo Pellacani to guide me in my first steps.

The research which led to this thesis started at *Universitat Politècnica de València* (UPV) where I was granted a fellowship of the Spanish Personnel Research Training Programme (FPI) funded by the Ministry of Economy and Competitiveness of Spain. During this time, the thesis has been supervised by Prof. Dr. José Luis Muñoz-Cobo and Prof. Dr. Sergio Chiva.

Two internships contributed to this thesis. My stay at *Iowa State University* helped me to learn about the quadrature-based moment methods thanks to the Prof. Dr. Alberto Passalacqua. Therefore, the work related with this is fruit of his contribution. The second stay was at *Imperial College London* related with the MEMPHIS Multiphase project, being useful for learning about interfacial tracking methods, so I must thank to Prof. Dr. Omar K. Matar and Dr. Lyes Kahouadji for this.

The last part of this work was performed back at *Universitat Jaume I* combined with other projects and teaching. There, I was able to deepen into the measurement techniques to extract the data in two-phase flow, to investigate and develop a rigorous validation procedure in the simulations. This was thanks to my college Guillem Monrós-Andreu, with whom I have had very profitable exchanges that have proved really useful, in addition to share coffee breaks, pains and *joys* of the PhD. I have also to thank Dr. Raúl Martínez-Cuenca for the advice related with the modelling in two-fluid model.

Regarding the simulations with system codes as RELAP or TRACE, I am grateful to Prof. Dr. Rafael Miró and Consuelo Gómez-Zarzuela from the UPV for the help in the simulations and developments performed.

Many people have contributed either directly or indirectly to this study. Fortunately, the list is so long that I can't write it down all, but I am grateful to my colleges in the Department of Chemical and Nuclear Engineering at UPV, especially to Álvaro Bernal, Carles Mesado and Nicolás Olmo. And, of course, thanks to all my colleges in the Chiva's group at UJI. Furthermore, I have to give a special

thanks to my parents, brother, sister-in-law (also to the little Lucas) and to my girlfriend *Dr. Carmen Díaz* for her love. Finally, I hope that readers will find this work interesting and I should like to conclude begging that *the defects in a subject so difficult be not so much reprehended as kindly supplied, and investigated by new endeavours of my readers.*

Contents

Chapter 1

Introduction

This chapter contains the discussion that has motivated the research described in this work. It summarises the available methods to compute two-phase flow with their strength and weaknesses, the state of the art and the scientific royalty of the presented work.

1.1 Overview

Multiphase flow is present in natural and industrial processes of different nature. Examples of multiphase flow are groundwater, sand storm, volcanic eruptions or ocean waves. Focusing the attention to gas-liquid two-phase flow, multiple industrial applications can be described. In nuclear power plants, Boiling Water Reactors or Pressurized Water Reactors under accident conditions, contain a steam-water mixture produced by the heat given by the fuel elements. In the chemical industry, multiphase reactors as bubble columns are used to perform chemical reactions as polymerization, chlorination, hydrogenation, polymerization or alkylation. In wastewater treatment plants, air-water or oxygen-water are used at different stages combined with microorganisms to decrease the organic content of the sewage. The oil or petroleum industry is also an example of two-phase flow as it is present in transport pipelines, pumps and production wells. Finally, two-phase flow exists in multiple generic devices as heat exchangers, boilers or phase separators.

In these activities and processes, it is usually required to know the exact flow behaviour to improve productivity, efficiency or for ensuring the safety of plant design and production activity. However, the understanding of two-phase flow is far from the single-phase flow knowledge.

The study of this flow can be done experimentally, theoretically or computationally. The experiments in multiphase flow provide insight into the characteristics of the flow. However, its application is limited to the size of the laboratory model, the costs or the current limits of the measurement techniques. In contrast, theory and computational models can contribute to understand the physics of multiphase flow and to extrapolate the results of these models to larger scale than the experiments used for validation.

Because of its importance and challenges related to predict the two-phase flow structure using computational methods, two-phase flow has been investigated over the years being a research focus with significant strides accomplished to date. Computational simulations employing very different approaches were used to predict the two-phase flow behaviour at different levels (Ishii et al. 2006a; Prosperetti et al. 2007). It is worth stressing that with high resolution level, the microscopic phenomena can be solved. In contrast, the more simple approaches need to model this effects by means of correlations. However, their validity is in the range of conditions and configuration for which have been obtained.

The choice of a specific method depends on its suitability for the range of operating conditions, the scale and the complexity of the domain to investigate. The method employed, is influenced by the computational limits and resources availability, the time needed to obtain the computational results and the precision. The literature includes developments at microscopic, mesoscopic and macroscopic levels as Interfacial Models (IM) , Discrete Element Model (DEM) or Two-Fluid Model (TFM) respectively. In practice, the IM are unfeasible for large or intermediate systems of bubbly flow, but TFM may not predict different scenarios without tuning model coefficients. Intermediate approaches as CFD-DEM applied to bubbly flow are less explored up to date, but promising. Figure 1.1 schematise these approaches showing how the dispersed phase is represented.

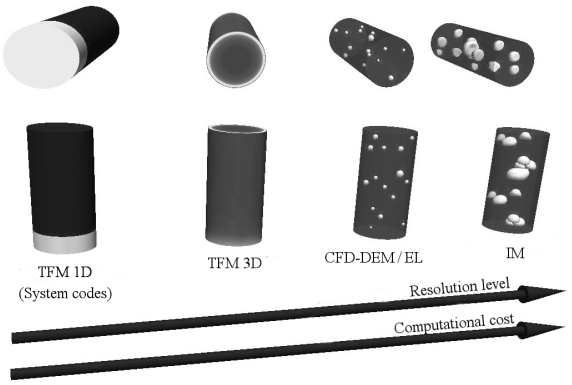

Figure 1.1: Schematic representation of the dispersed phase using different approaches.

In addition, there is added complexity to solve two-phase flow because the relation between the domain discretization (or mesh) and the bubbles. For a given mesh, the bubbles can be classified as particles in cell, resolved and under-resolved. Fig. 1.2 represents this classification for a complex real case and a given discretization. The coexistence of different bubble types difficults the use of a single method to solve a case as the shown in the figure. With IM all the bubbles must be resolved, then a sufficiently fine mesh would be needed in order to capture the interface of the small bubbles. CFD-DEM methods can be used with resolved or under-resolved formulations. The former implies similar restrictions as IM and the latter needs volume cells greater than the bubble one.

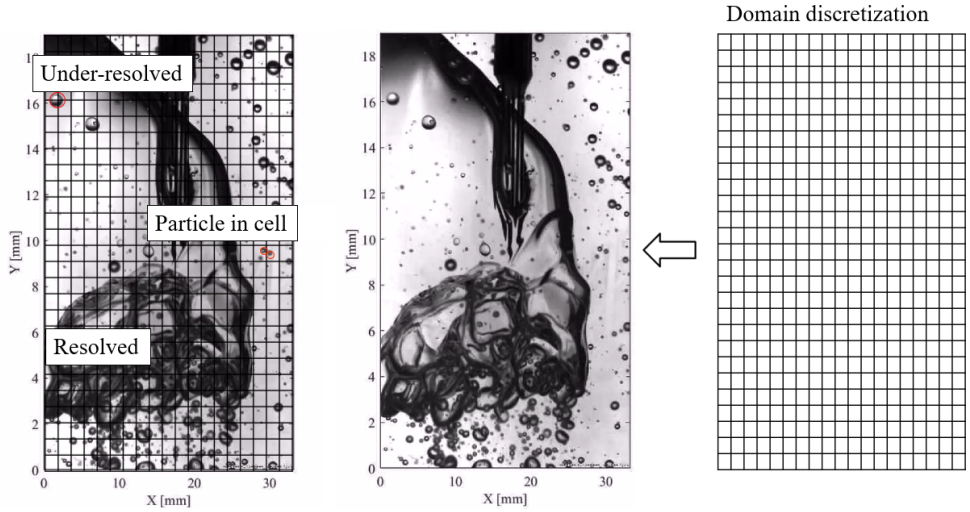

Figure 1.2: Slug flow with bubbles of different sizes and an example of its classification for a given domain discretization.

In general, much progress remains to be achieved to ensure the correctness of the modelling of two-phase flow. In this thesis this is tackled focusing the attention to the bubbly flow regime through and exhaustive study of the experiments and numerical methods at different scales.

1.2 State of the art

In order to better understand two-phase flow physical phenomena, authors from different research areas have focused their work on this field for decades, producing an extensive set of studies and models. Nonetheless, the lack of consensus surrounding the physical models used in computational methods to properly predict both the dispersed and continuous phase behavior can be noticed in the literature.

1.2.1 Experiments and techniques

Experimental work has been done during decades to analyse the two-phase flow behaviour and to assess the validity of existing and novel computational methods. The earlier experimental observations of bubbles are, in fact, attributed to Leonardo Da Vinci (Prosperetti 2004) who already reported in the Codex Leicester the instability of the path of a bubble rising.

By focusing on the objective of the experiments, the early researches were carried out to analyse the motion of single bubbles and its effect on the liquid. Allen (1900) investigated the terminal velocities of small bubbles and solid spheres in viscous fluids. This work concluded that for slow motion, if no eddies are set up in the fluid, the velocity of the bubble agrees with that deduced from theoretical considerations by Stokes. Davies et al. (1950) focused the attention to the terminal velocity including large bubbles. Different studies of drag and shape of bubbles rising in different liquids can be found in the literature (Haberman et al. 1953; Peebles et al. 1953; Aybers et al. 1969; Duineveld 1995). In the subsequent years, two-phase flow measurements were centred mainly in systems. Experiments where the air is generally injected in a stagnant liquid as channels (Wambsganss et al. 1991; Richardson et al. 1958; Troniewski et al. 1984; Ali et al. 1993; Zenit et al. 2001) and bubble columns (Kumar 1994; Kumar et al. 1997a; Kumar et al. 1997b; Degaleesan 1997; Chen et al. 1999a) represented the most popular research topic during decades. Bubbly flow mainly in *pipes* has been studied with an increasing number of investigations (Grossetête 1995; Wang et al. 1987; Prasser et al. 2002; Lucas et al. 2005). Two-phase *pipe flow* in horizontal or inclined angle has been investigated paying special attention to the regime transition (O'brien et al. 1935). Tee junctions has also been investigated to analyse the separation of the liquid and the gas as in Margaris (2007).

Isolated effects as bubble formation (Dietrich et al. 2013b; Dietrich et al. 2013b) collisions (Vries 2001; Zaruba et al. 2007; Zenit et al. 2009) breakup (Martínez-Bazán et al. 1999; Müller-Fischer et al. 2008; Solsvik et al. 2015) or coalescence (Marrucci et al. 1967; Prince et al. 1990) have also been investigated experimentally.

During these years the experimental techniques for measuring local properties of gas-liquid flows has undergone a great improvement with different methods for measuring continuous and dispersed phase (Monrós-Andreu et al. 2016). The most popular techniques to measure velocity and turbulence fields in continuous phases are based on optical techniques, such as LDA or PIV. Techniques based on heat transfer phenomenology such as Thermal Anemometry (TA) (Jensen 2004) are also being used. Optical techniques require seeding the flow with microscale tracers that reflect the impinging light, so the flow velocity is indirectly measured. Thermal techniques require positioning a sensor in the flow, thus altering its behaviour (sensor intrusiveness).

Laser Doppler Anemometry (LDA) is a local measurement technique that consists in the projection of a microscopic fringe pattern into the flow path. Whenever a seeding particle passes through the volume occupied by this pattern, it produces a characteristic set of gleams that is registered by a photodiode. The frequency of the gleams set, depends on the particle velocity across the direction of the pattern. In practice, a pair of mutually coherent laser beams must be used to produce a fringe pattern providing one velocity component (and 3 Reynolds stresses). The measurement of the three velocity components (and 6 Reynolds stresses) requires three pairs of such beams. Since its first proposal (Durst et al. 1976a), several researchers have used this technique for the measurement of flow velocity either in single-phase (Durst et al. 1995; Barnhart et al. 1994) and two-phase flows (Lance et al. 1991; Mudde et al. 1997b; Poorte et al. 2002). Leung et al. (1995), Hibiki et al. (1998), Hibiki et al. (2001a), and Fu (2001) developed experimental databases for two-phase pipe flow using LDA. Given its accuracy, this technique is the preferred amongst researchers for most purposes. But several problems limit its application. Measurements in high-void fraction conditions (over 20%) is unpractical (Mudde et al. 1997b). The measurement in non-regular containers can be cumbersome due to the optical aberrations affecting the fringe pattern (Zhang 2010). Also, as it is a local measurement technique, it needs for scanning to obtain flow fields. This can be actually complex in non-regular geometries, especially when three independent beam pairs are used (Zhang 2010).

Particle image velocimetry is a two-dimensional (2D) measurement technique that relies on the illumination of a flow section by using a light sheet (Raffel et al. 1998). Recently, three-dimensional vectors can be also measured by off-axis, double-pulsed holographic PIV (Barnhart et al. 1994) or tomographic principles (Scarano 2013). In standard 2D PIV, the seeding particles that pass across the illuminating sheet, reflect the light so that it is registered by a fast camera. The comparison between two consecutive acquisitions separated by a short delay (typically of the order of the millisecond) permits to obtain the velocity and Reynolds stresses fields over the whole image (Adrian et al. 2011). Although its accuracy remains under the LDA standards, this technique is the preferred to study complex flows where the flow structure is of primary importance. In addition, eddy structures can be

noticed and analysed from the images. As a counterpart, this technique is limited by its low dynamic range in velocity measurement. Also, the optimization of the seeding concentration to improve the PIV processing is quite complex. Finally, its accuracy strongly relies on the performance of pairing algorithms (Adrian 2005).

Thermal anemometry techniques are local measurement techniques that rely on the fact that the heat transfer coefficient of a sensing solid immersed in a fluid depends on the flow speed (Bauer 1965a; Bruun 1996). In practice, a wire is heated by an electrical current, and its electrical resistance is measured. As this property is temperature dependent, the measurement of the wire resistivity allows for the computation of the flow speed. TA based on hot-wires has been used to measure flow velocity and turbulence in single-phase flows (Siebert et al. 2007; Jørgensen 2001), and also in two-phase flows (Mendez-Díaz et al. 2013; Hibiki et al. 1998), where it also serves as a phase identifier. This technique provides measurements with high dynamic range at high-acquisition rates. However, the non-linearity of its signal requires for extensive calibrations that may change over time due to slight contamination of the working fluid. Also, the sensor is very fragile and easy to break, which makes them not suitable for industrial environments. With respect to the measurement of dispersed phase properties, the most widely used techniques are based in electrical tomographic systems (ETS), wire-mesh sensors (WMS), and needle-probe systems. Sensors based on nuclear tomographic systems have been also developed for the study of multiphase flows due to its non-invasive operation principle providing satisfactory results, but at an elevated cost.

Electrical tomographic systems aim at measuring the phase distribution over a cross-section. These systems rely on the fact that the electromagnetic properties of the two phases are different, either electric capacitance (ECT) or resistance (ERT). In this way, the signal between a pair of excitation-sensing electrodes is related to the phase distribution in the measurement volume enclosed by them. To obtain the whole phase distribution, an array of electrodes placed outside the test section generates excitation-sensing signals across different directions. They have been used for bubble columns (Schmitz 2000), pipe lines (Prasser et al. 1998), and three-phase fluidized beds (Maucci et al. 1999). Depending on the number of electrodes and the tomographic reconstruction algorithm used their characteristic response dynamics can be actually fast, and they can therefore describe rapid evolutions of phase distribution. These systems are easy to implement at relatively low cost and work really good for the detection of slugs in pipe flows and flow regime identification (Geraets et al. 1988; Ahmed 2006). However, the measured signals are difficult to handle. To start, they do not depend linearly with the phase fraction given that the phase distribution affects the electric field distribution. Thus, the reconstruction of the phase distribution relies on non-steady calibration (Jaworek et al. 2004). The spatial resolution is low and highly compromised unless a priori knowledge is included in the reconstruction procedure. Finally, they cannot measure the velocity of individual particles. Instead, the use of two electrode

planes axially separated is used to obtain the so-called structure velocity for pipe flows (Abdulkadir et al. 2014).

Another interesting tomographic system is the wire mesh sensor. By using two planes of electrodes (excitation plane and sensing electrodes plane) forming a grid settled within a pipe it is possible to measure the impedance at each crossing point, in a fast multiplexed way. Firstly, a conductivity based version was introduced by Johnson for oil-water systems (Johnson 1987). Later on Prasser et al. (1998) introduced improvements on the sensitivity and presented a WMS for air-water systems. Recently, Silva et al. (2007) expanded the applicability of WMS to non-conductive mixtures developing a WMS based on fluid permittivity measurements. Currently is the most widely used technique to obtain information from the dispersed phase including gas-liquid flows (Prasser et al. 1998) and three-phase flows (Silva 2008) because they provide cross-section phase distributions with high spatial resolution at moderate to high frequencies. Also, the use of two sensing planes permits the computation of the velocities of individual particles. As a counterpart, these systems are highly intrusive, especially when high spatial resolution is required (more wires are needed).

Needle probes detect the local physical properties of the fluid surrounding their sensing parts. A probe sensor consists of one or more thin electrodes settled to face the main flow direction. Two main types of needle probes can be distinguished according to its measuring principle: optical probes and resistive (or more generally, impedance) probes. Despite its intrusive principle and the fact that needs extra scanning systems to perform complete cross-sectional measurements, they allow a complete description of gas phase hydrodynamic characteristics (particle size and speed, local interfacial area concentration, etc.). Details about this technique will be extended throughout this thesis.

1.2.2 Analytical and numerical models

Analytical and numerical models have been used historically to predict the bubbles' behaviour. An analysis of the literature of the past few decades is performed to explore the trends followed by the scientific community. The number of relevant works are shown in Fig. 1.3 making a distinction between analytical models (AM), IM, EL or CFD-DEM and 3D TFM. The number of investigations related to AM have remained almost constant over the past years. However, the numerical methods analysed has gained popularity as the computational resources became faster and cheaper. This can clearly be seen for TFM, in the past decades it has been mainly used for general investigations or to focus on specific phenomena as breakup and coalescence. The IM need the use of massive parallel computing even for small domains. It has been increasingly selected as a tool to investigate bubble behaviour. The CFD-DEM methods are located between both techniques. The computational demanding is higher than for TFM but a modelling effort is still

needed in contrast to IM, in contrast the current technology makes feasible its use for industrial applications.

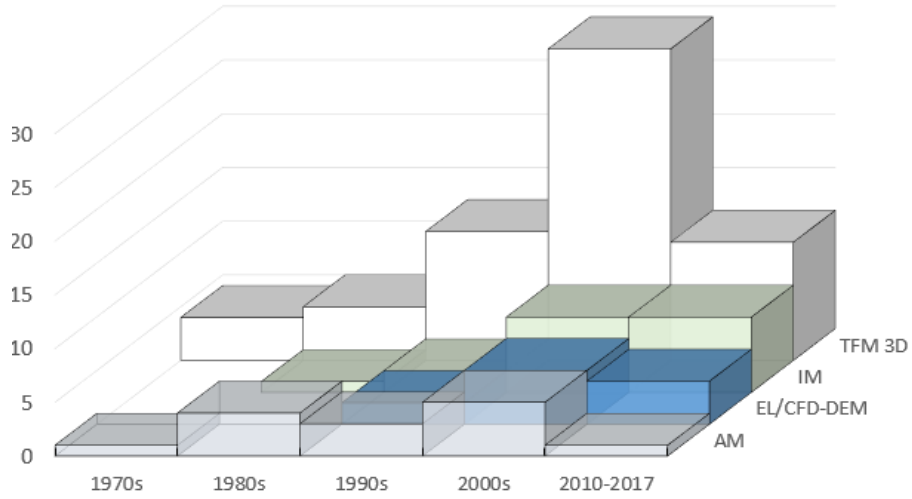

Figure 1.3: Number of relevant investigations over years for different approaches.

Many models and numerical predictions involving single bubbles have been performed trying to reproduce the experimental results. Theremin (1830) performed a theoretical analysis of the motion of a bubble in a liquid with constant liquid. Subsequently Hadamard (1911) and Witold (1911) developed an equation giving the terminal velocity of a spherical bubble moving slowly through an ambient fluid. Using analytical correlations Rosenberg (1950), Moore (1965), and Moore (1963) could determine the rise velocity of a bubble from a drag coefficient. Most of these findings were compiled in Clift et al. (1978). Toward the end of the 20th century, the basis of the nowadays available methods for two-phase flow were established. For instance, TFM (Drew et al. 1971a), VOF (Hirt et al. 1981), Level Set (Osher et al. 1988) or Front Tracking Method (Unverdi et al. 1992). Over the following decades, the investigations also focused on the use, improvement and development of hybrid methods.

Simulations involving air-water two-phase flow systems have been performed to validate different scenarios. However, only rarely, if at all, a single model has proved its correctness modelling experiments or industrial cases for different scenarios including various flow conditions and geometric configurations. Using analytical correlations (Rosenberg 1950; Moore 1965; Clift et al. 1978), the relative velocity of a single bubble can be predicted. Reproducing the flow in systems is

possible by means of an Eulerian-Eulerian (EE) approach as the TFM, where the local instantaneous equations of each phase are averaged to obtain an Euler-Euler two-phase flow description (Drew et al. (1971a)). Based on this approach several contributions showed its applications to bubble columns (Gupta et al. (2013), Pan et al. (1999), Pfleger et al. (1999), and Zhang et al. (2006)). Vertical pipes have taken particular attention as they are present in several industries. This flow involves wall-bounded turbulent flows and requires an exhaustive modelling of interfacial forces between phases and the turbulence interaction by bubbles and liquid. Some works were carried out in vertical pipes (Hosokawa et al. 2009; Krepper et al. 2005) and horizontal pipes (Ekambara et al. 2008). In addition, many researches using this approach have been done focusing on specific phenomena such as interfacial forces, breakup and coalescence or solving the bubble size field using a population balance equation approach (Cheung et al. (2013), Wang et al. (2005), and Buffo et al. (2013)).

Another strategy is to consider the dispersed phase discretely as ideal spheres using an Eulerian-Lagrangian (EL) approach. Using a method relying on a discrete model has the advantage of considering the following aspects inherently in the method:

- Inhomogeneity of the dispersed phase flow.
- Non-linearity of the bubble forces correlations.
- Bubble-bubble and bubble-wall interactions mechanistic computation.
- Turbulent dispersion effect for all the bubble forces.
- Interfacial force coefficients that were obtained experimentally for individual bubbles are applied directly in the simulation.

Note that the mentioned above could be considered, in principle, with TFM but the modelling becomes more complex or unfeasible as it is not clear nowadays that the required relationships can be found.

The EL approach started some decades ago for the mathematical simulation of sprays, O'Rourke (1981) and O'Rourke (1985) developed a new approach coupling the Lagrangian equation for droplet distribution function of Williams (1958) with an Eulerian description. In their calculations velocity and pressure were obtained by means of the Navier-Stokes equations while the motion of each particle was solved using the Newton's second law as well as the particle-particle, particle-wall, coalescence and breakup during the particle path. Lately Dukowicz (1980) developed a EL two-way coupling including momentum coupling and volume effects for computational particles, representing group of particles with the same characteristics.

Within the EL formulation holds the CFD-DEM method usually characterized to consider the elastic collisions of the particles based on a soft-sphere model. CFD-DEM model has been applied traditionally for dense flow systems (Matuttis et al. 2000; Alam et al. 2003) but could result especially useful to wall-bounded systems where the particle interactions play a crucial role as in the two-phase pipe flow investigated in this work.

For the most part, CFD-DEM has been applied to sprays or particle-laden flows. Further and in a lesser extent EL were applied to bubbly flow applications (Delnoij et al. 1997; E. Shams et al. 2010; Essa 2012). The reader is referred to Subramaniam (2013) for details about LE methods. The CFD-DEM approach has been extensively used to simulate two-phase flow systems as particle-laden flows, but new improvements to develop a new solver are needed to simulate bubbly flows accurately. In bubbly flow there are key differences comparing to particle-laden flows that need to be accounted. Magnaudet et al. (2000) noted three important differences that are listed below in words of the author:

- "When the liquid is pure enough, it has the possibility to slip along the surface of the bubbles, in contrast to the flow past rigid bodies where the non-slip conditions is imposed."
- "Owing to the very weak relative density of bubbles compared to that of the liquid, almost all the inertia is contained in the liquid, making inertia-induced hydrodynamic forces particularly important in the prediction of bubble motion."
- "The shape of the bubbles can change with the local hydrodynamics."

Additionally, we add to the list the following factors with relevance to bubbly flow systems as for example a pipe:

- The size and number of bubbles can change due to breakup or coalescence phenomena and can change the bubbles motion dramatically (e.g. negative lift force coefficient range).
- The bubble size and dispersed phase volume may vary with the pressure changes.
- The deformation of the bubble in a collision is not easily characterized with parameters that defines the resistance to being deformed elastically as elastic or shear modulus as in solid materials.

The mentioned above has several consequences in the requirements of the solver. First, in the computation of the interfacial forces, the modelling is more complicated in order to represent the real behaviour of the bubbles. Second the coupling between both phases including turbulence effects of the bubbles into the liquid and

vice versa will have a relevant influence into the flow characteristics. In addition, the particle sizes are usually smaller than the bubbles. Finally, the measurements of the bubble variables are in general more complicated.

As already mentioned in Allen (1900), when a bubble has a small size, the surface tension is large enough to keep the sphericity of the bubble. Then the EL method could be useful and more accurate. However, when the bubble has a large size its shape evolves forming other shapes. In order to consider these phenomena, interfacial techniques can reliably predict the dynamics of the bubble surface. These methods include the Volume of Fluid Method (VOF) (Hirt et al. 1981) and the front-tracking method (Muradoglu et al. 2008).

As regards turbulence modelling, the above strategies capturing two-phase flow can be applied to Direct Numerical Simulations (DNS), Large Eddy Simulations (LES) or Reynolds-averaged Navier-Stokes equations (RANS). The mechanism involving the influence of the dispersed phase on the continuous phase are unknown and the existing turbulence models contain, in greater or lesser degree, terms verified only for single-phase flow up to date. LES simulations has been also applied for bubbly flow simulations (Dhotre et al. 2013). Two-phase flow RANS models as κ-ε or κ-ω consider a pseudo-turbulence produced by the bubbles, however the set of constants of this model originally derived by Launder et al. (1974) for single-phase flow should be evaluated under different two-phase flow conditions.

In summary, up to date bubbly flows have been simulated mainly by the use of TFM and LE. Simulations at a microscopic level description of the dispersed phase are very enlightening though limited to small domains and number of bubbles. Works aiming at a microscopic description have not been included in the table as they have not been applied to the same kind of geometries and flow conditions. Particularly interesting are the works of Dijkhuizen et al. (2010b) who studied the bubble behaviour of isolated bubbles. Roghair et al. (2013) presented results of simulations for dense bubbly flow up to 31 bubbles. Tryggvason et al. (2009) simulated a vertical channel in a periodic domain with around 36 bubbles in the turbulent downflow case.

Table 1.1 and 1.2 summarizes main simulation works in the literature that have been validated with experimental datasets. The table points out the simulation method (TFM, EL), the geometry and flow conditions simulated, as well as the variables validated for each case.

In general, the TFM is the most established technique and has been therefore extensively validated. Datasets for validation typically comprise a wide number of variables as dispersed phase void fraction, α_{d}, axial velocity for dispersed phase, $U_{\mathrm{d,z}}$, and carrier phase, $U_{\mathrm{c,z}}$, interfacial area concentration, a_I, Sauter mean diameter obtained by probe sensors, d_{NP}, or by image processing, d_{IP}, bubble size distribution, BSD, carrier phase turbulence kinetic energy, κ_{c} or turbulence in-

Method	Simulation	Experiments	Type	D (mm)	L* (mm)
TFM	Yao et al. (2004a)	Grossetête (1995)	Pipe	38.1	6000
TFM	Krepper et al. (2005)	Same work	Pipe	51.2	3072
TFM	Cheung et al. (2007)	Liu et al. (1993b)	Pipe	38.0	2800
		Hibiki et al. (2001b)		50.8	3061
TFM	Hosokawa et al. (2009)	Same work	Pipe	25	2000
TFM	Buffo et al. (2013)	Pfleger et al. (1999) Cachaza Gianzo (2011)	2D column	200	1800
TFM	Rzehak et al. (2016)	Liu (1998)	Pipe	57.2	3430
		Mohd-Akbar et al. (2012)	Rect. Column	240	500
		Luo (2005)	Airlift column	65	677
LE	Delnoij et al. (1997)	Becker et al. (1994)	2D column	500	1500
LE	Laín et al. (2002)	Laín et al. (1999)	Circular column	140	650
LE	Hu et al. (2008)	Becker et al. (1994) Sokolichin et al. (1999)	2D column	40	3170
LE	Muñoz-Cobo et al. (2012)	Mendez Díaz (2008)	Pipe	52	2910

* Distance from the air flow injection to the water level in the column and to the top measurement port in the pipes

Table 1.1: Relevant simulations of air-water bubbly flow systems found in the literature.

Simulation	Experiments	z/D validated	j_l	j_g (m/s)	Variables validated (m/s)
Yao et al. (2004a)	Grossetête (1995)	55,155	0.877	0.058, 0.1851	α_d $U_{c,z}$ TI_c $U_{d,z}$ $d_{32,NP}$ a_I
Krepper et al. (2005)	Same work	60.0	1.0	0.037-0.342	α_d $U_{d,z}$ BSD
Cheung et al. (2007)	Liu et al. (1993b)	36.0	1.087	0.027-0.112	α_d $U_{c,z}$
	Hibiki et al. (2001b)	6,53.5	0.491-0.986	0.0275-0.242	α_d $U_{c,z}$ $U_{d,z}$ $d_{32,NP}$ a_I
Hosokawa et al. (2009)	Same work	68	0.018-0.036	0.5-1.0	α_d $U_{c,z}$ $U_{d,z}$ κ_c
Buffo et al. (2013)	Pfleger et al. (1999)	0.65, 1.25, 1.85	†	0.00133	$U_{c,z}$
	Cachaza Gianzo (2011)	-		0.0024-0.0213	Hold-up,POP‡,$d_{32,IP}$
Rzehak et al. (2016)	Liu (1998)	60	0.5-1.0	0.12-0.22	α_d $U_{c,z}$ κ_c
	Mohd-Akbar et al. (2012)	2.1	†	0.003-0.013	
	Luo (2005)	5.2	†	0.01	
Delnoij et al. (1997)	Becker et al. (1994)	-	†	0.00066, 0.0033	Bubble plume
Laín et al. (2002)	Laín et al. (1999)	0.71, 2.14, 3.40	†	0.0003, 0.0016	$U_{c,z}$ $U_{d,z}$ $u'_{c,z}$ $u'_{d,z}$ κ_c
Hu et al. (2008)	Becker et al. (1994)	-	†	0.00066	$U_{c,z}$ $u'_{c,z}$ $u'_{c,x}$ κ_c
	Sokolichin et al. (1999)	0.11-0.89			
Muñoz-Cobo et al. (2012)	Mendez Díaz (2008)	56	0.5-3.0	0.075-0.407	α_d

† Initially quiescent water
‡ Plume oscillation period

Table 1.2: Relevant simulations of air-water bubbly flow systems found in the literature.

tensity, TI_c. Let us note that these simulations are highly dependent on the set of correlations used for the interfacial force models and coefficients, break-up and coalescence and turbulence modelling. These sets vary widely amongs the different works and have not been included in the table for the sake of clarity. The main reasons are related to the difficulty of modelling two-phase flow phenomena with phase average equations as commented before. Indeed, a complex flow behavior difficult to model, is present even in simple geometries and low void fractions.

The LE works are usually limited to smaller domains and datasets for validation comprise general behaviour of bubble plumes and velocity fluctuations of the carrier phase (u') in addition to those used in TFM.

Finally, several works similar in nature to this thesis, have performed a multiscale study or multiscale modelling including several of the methods mentioned as in Gunsing (2004) and Deen et al. (2004).

1.3 Research objectives and thesis outline

The aim of this thesis is to study the modelling of two-phase flow with the use of experimental methods and through this, deepen on its physical behaviour. Numerical methods at different resolution levels as VOF, CFD-DEM, TFM and system codes (RELAP5/MOD3) were employed to compare the experimental results. In this way, more knowledge can be acquired for the modelling of lower resolution level approaches to apply it for industrial applications. The multiscale modelling with VOF, CFD-DEM, TFM and system codes involves the key aspects shown in Fig. 1.4.

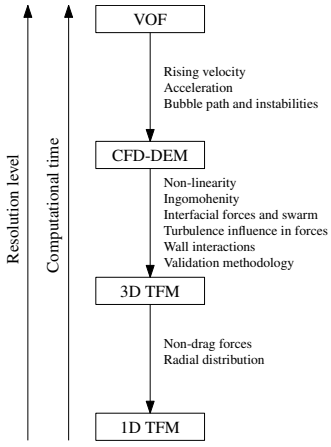

Figure 1.4: Overview of the approaches and information supplied.

To achieve these objectives, developments of models and solvers were performed, using the OpenFOAM® libraries to create an open-source multiscale framework of investigation. The choice of this software or library is justified by the fact that is free and open source, but also because its modular structure allows future contributions of different sub-models and methods. In this way, optimized methods from the wide variety of technical aspects related with CFD can be achieved and also sustained over time through the scientific community. Focused to two-phase flow, this encourages future contributions devoted to analyse complex phenomena as for example the presence of surfactants, chemical reactions, heat transfer or boiling and condensation. Furthermore, this is intended to serve as a basis for future hybrid codes or coupling between the solvers for solution of phenomena at different scales in the same simulations. A scheme of this framework is shown in Fig. 1.5.

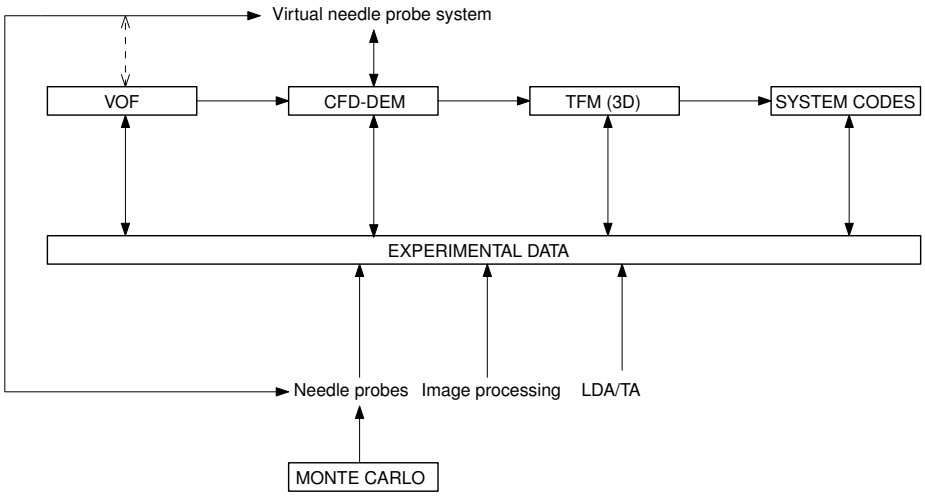

Figure 1.5: Scheme of the framework set for this thesis.

To fairly compare the simulation results with the experimental data, it should be required an adequate knowledge on how the experiments have been conducted and the processing procedure followed. For this reason, the study of two-phase flow phenomena in this thesis was performed jointly with the research of the experimental techniques. Consequently, this not only concerns the validation, but obtaining additional required data and integrating the experimental techniques in the simulations for a rigorous validation. Also, with this methodoogy one can investigate on the experimental techniques procedure itself. Simulations performed with approaches where the bubble is represented individually as CFD-DEM led to obtain the dispersed phase data similarly as in the experiments. This creates a potentially fruitful condition to compare the results in a rigorous way. The development of a Virtual Needle Probe System (VNPS) provides the same assumptions

as needle probes and can be used to extract the experimental data. In turn, Monte Carlo simulation can be used to verify the needle probe performance together with the VNPS. The experimental techniques and Monte Carlo simulations were investigated by Monrós-Andreu (2018) in a separate thesis in parallel with this work.

The remainder of this thesis comprises the following chapters. It starts with Chapter 2 dealing with the issues related with experimental data. This subject is dealt first as it is essential for trying to reproduce the data to know the scenarios and how the measurements are performed. A description of the datasets and the experimental facilities is performed. The techniques used to extract the information of the liquid field and the bubbles are studied together with the measurement methods. Finally, the validation methodology for the data measured with needle probes is reviewed making a classification of the variables and its relation with the information lost by the probes.

Next, Chapter 3 deepens into the choices for modelling the two-phase flow scenarios, focusing the attention in particular to bubbly flow. First, the different ways to represent the dispersed phase in the different existing approaches are analysed, defining what can be obtained or considered to each one of them. Through the chapter, an analysis is performed on the modelling, for the different methods, interfacial forces involved or bubbles collisions. The turbulence modelling plays an important role in this flow as the bubbles have an influence in the liquid fluctuations due to the wake produced. In the case of bubbly flow it produces an induced pseudo-turbulence. In addition, the effect of the liquid fluctuations on the interfacial forces is described. Most of the mentioned models have the bubble size as a determining factor. Not only the bubble size, if not the bubble size distribution must be taken into account to reproduce a polydispersed flow. Then, the methods for the modelling of the bubble size distribution in space and time, in particular the population balance equation are discussed. Finally, a brief analysis is focused on the effect that the existence of different bubble sizes can have on the other models, highlighting the non-linearity of the expressions used.

Chapter 4 is the first dedicated to numerical simulations. To start from the beginning, isolated bubbles are the focus of the chapter. Volume Of Fluid methods (interFoam) are employed to obtain detailed simulations of the bubble dynamics an even more important, its influence on the liquid and its interrelationship. Using parallel computing, the formation of the bubble from a nozzle is modelled and validated with experiments. A bubble generated from the detachment and the resulting equivalent diameter is compared with experimental correlations. This diameter is used to simulate other scenarios where the bubble is initially spherical and steady. Both cases, bubble from a nozzle and initially spherical bubble are used to analyse the bubble dynamics, path, velocities, wake and instabilities.

The simulation of bubbly flow for facilities at industrial scale or even laboratory scale with VOF is unfeasible nowadays. In bubbly flow, one would need a refine-

ment of the mesh sufficiently small to capture the smallest bubble. Then, a lower resolution level approach as CFD-DEM for unresolved particles is an option to consider. Chapter 5 proposes a novel CFD-DEM solver to simulate bubbly flow, developed using the OpenFOAM® tools and methods. As a starting point the Lagrangian libraries of OpenFOAM® (mainly the basic and intermediate) are considered to create a new *bubbly flow* library to create the new *bubbleCFDEM* solver. It started from the version 2.3.x and incorporates the structure from subsequent versions. In this chapter, a set of new models are developed and/or implemented: bubble-bubble and bubble-wall interaction, coupling between bubble and liquid, equivolumetric sub-element method of bubbles distribution in the grid, injection algorithm to represent the boundary conditions in a pipe, approximate model for the decompression of the air in the bubble, Continuous Random Walk stochastic model to consider the effect of the liquid fluctuations on the bubble and Virtual Needle Probe System for a critical validation with the experiments. Finally, bubble dynamics of isolated bubbles and three different experiments of bubbly flow in pipes from different authors are then validated and analysed in depth.

Although CFD-DEM requires less computational effort than VOF, it could result impractical for large-scale problems. Then, we can use a macroscopic formulation as TFM. Also, note that one goal of the computation is to solve a problem within the minimum time and computational resources. In Chapter 6, TFM is investigated using as a basis the twoPhaseEulerFoam of version 2.2.x (incompressible version of TFM) to incorporate the population balance equation solving it approximately with the quadrature method of moments. In addition, common interfacial forces and correlations, and induced pseudo-turbulence were added. A validation with classical models is performed with this solver. Later, with version 4.x (compressible version of TFM) and also implementing the quadrature method of moments, a modelling similar as for CFD-DEM in Chapter 5 is shown.

In some situations, spatial resolution may be less important and only global values are needed. In such a case, 1D TFM provides an useful tool. Chapter 7 provides simulations performed with a system code as RELAP5/MOD3. With this code, we analyse the drag force approaches that are traditionally applied proposing a version that takes into account the effects of the bubble size distributions in the results of 1D TFM simulations.

A preliminary study for bubbly flow in different industrial systems is performed in Chapter 8. Bubbly flow through a perforated plate is simulated with 3D TFM and CFD-DEM codes, to analyse the influence and highlight the limitations of each model on the results.

Chapter 9 presents the conclusions, recommendations and a description of the future work that is performed according to the investigations and results obtained along this thesis.

Finally, we briefly summarise the tasks that were required to achieve the aforementioned and are part of this thesis:

- Analysis of the measurement techniques in particular of the dispersed phase:
  - Critical study of the measurements with needle probes.
  - Measurement of the bubble size at different heights with image processing.
- In-depth review of numerical methods and models.
- Modelling of a detailed simulation with VOF (interFOAM) of bubbles injected from a nozzle and from an initially sphere at rest.
- Development of a new CFD-DEM solver using OpenFOAM® libraries for an accurate simulation of bubbly flow in pipes:
  - Implementation of a PISO algorithm to compute the CFD-DEM unresolved method.
  - New method to inject polydispersed flow in circular section.
  - New sub-element method for the assignment of void fraction and momentum exchange.
  - New simplified model for bubble volume and bubble size expansion.
  - Study of interfacial forces and appropriateness for this approach.
  - Development and implementation of a bubble-wall contact model with a soft-sphere model for bubbles.
  - Implementation of a Continuous Random Walk stochastic model to model the instantaneous liquid velocity seen by the bubbles.
  - Implementation of a two-phase flow RANS turbulence model for bubbly flow.
- Development and implementation of a novel validation procedure to validate the results from a critical point of view (VPNS).
- Implementation of particular interfacial force closures and turbulence models in twoPhaseEulerFoam for a proper comparison.
- Implementation of QMOM approach in the twoPhaseEulerFoam to consider the bubble size distribution evolution including a bubble growth term.

- Development and implementation of a bubble-wall contact force for ellastic bubbles for TFM.
- Implementation of the drag coefficient approach in RELAP5/MOD3 for bubbly flow with consideration of the bubble size distribution.
- Modelling and simulation with TFM and CFD-DEM of a more complex case as bubbly flow through a perforated plate scenario.

Chapter 2

Experimental data, measurement techniques and validation methodology

This chapter provides the description of the different experiments employed and the techniques used to obtain the data. These techniques are studied in depth as they will be later incorporated in the simulations to provide a new validation procedure. In particular, for needle probes, the signal processing and the variables obtained are studied comprehensively and thoroughly. A critical analysis between the experimental measures and the expected data is included. In addition, for one of the experimental facility, bubble size distribution at different heights is measured by image processing.

2.1 Introduction

The measurements performed in two-phase flow are still a challenge in the field. In the previous chapter, a state of the art about measurements and techniques was already provided. This chapter will focus on experimental facilities and measurement techniques related to bubbly flow in pipes as they are the core of the performed validation. However, other experiments can be found eventually in the document to support the investigation.

The uncertainties in the measurement from a conceptual point of view are still an unknown. The major complications are related to the fact that at the same time,

a wide range of bubble sizes and shapes are present in the system, evolving during the time.

In 2D systems, image processing techniques are able to extract the experimental data quite accurately. When referring to 3D systems, the occlusion of the different bubbles makes impossible to reconstruct hidden bubbles far from the wall even at rather low gas flow rates.

Alternatively, needle probes (NP) techniques can be used to measure the dispersed phase data. A probe hits the bubbles producing a different signal depending on the phase that is detecting. From the signal generated, a reconstruction can be made to obtain a great number of variables giving information about the kinematics, size and shape of the bubbles. The reconstruction of the signal to obtain the variables implies the consideration of several hypothesis as assuming a vertical rising, a shape or orientation. In addition, the measures with multi-needle probe depends on the probe design (e.g. tips distance) as demonstrated by Corre et al. 2002 for the measurement of interfacial area concentration. This can influence other measurements as will be explained later. The uncertainties in the measurements are given from the signal processing, the phase identification (e.g. threshold criteria) and the suitability of the assumptions adopted.

Multiple experimental datasets can be found in the literature (Grossetête 1995; Liu et al. 1993a; Liu et al. 1993b; Hibiki et al. 2001b; Mendez Díaz 2008) contributing to expand the knowledge of the two-phase flow structure. In fact, many numerical models and simulations rely on these experiments to calibrate its performance.

Often, the boundary conditions can not be fully defined as some information is not shown or the attention was not devoted to perform additional measurements for the simulations. To improve the quality of the validation, some experiments were performed in parallel with this work using the facility located at Universitat Jaume I.

2.2 Experimental datasets selected

In this section we introduce the experimental datasets selected from the literature for validation and discussion. The experiments of Hosokawa et al. 2009, Hibiki et al. 2001b and our experiments were used to obtain a global understanding of the validation process. This covers a variety of diameters, ratios of pipe diameters and bubble size, bubble injection methods and measurement techniques to obtain the data (see Fig. 2.1).

The pipe used in Hosokawa et al. 2009 is a relatively small diameter pipe and the wall effect is expected to be more important. The pipe used in Hibiki et al. 2001b has a similar diameter as the one introduced in this work. The latter has a

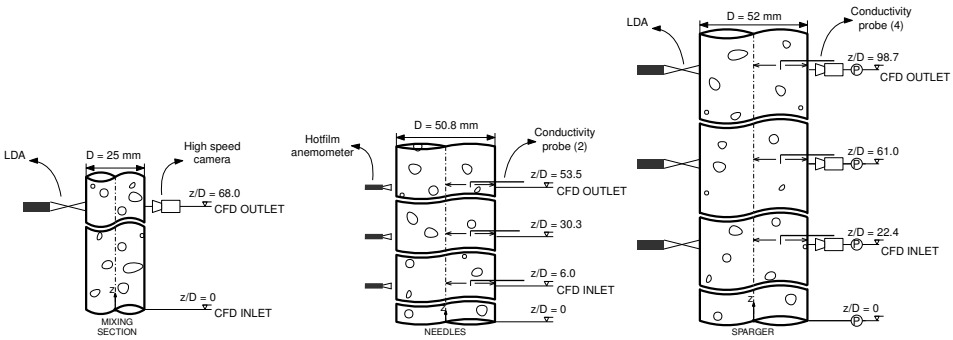

(a) Hosokawa et al. 2009 **(b)** Hibiki et al. 2001b **(c)** Present work

Figure 2.1: Experimental configurations of the three two-phase flow systems used.

considerable larger length that will serve us to better analyse the axial evolution of the flow. Also, it results interesting to compare two similar systems with different air flow injection mechanisms and measurement techniques. Table 2.2 gives an overview of the flow characteristics that determines the three experimental cases selected.

Table 2.1: Relationship between experiments and labels.

Experiment	Label
Hosokawa et al. (2009)	H050018
Hibiki et al. 2001b	HK05003
Present work	PW05002
Present work	PW05003
Present work	PW05004

Table 2.2: Flow conditions for each scenario.

Label	j_l	j_g (m/s)	μ_{inlet} (m/s)	σ_{inlet} (mm)	z/D (mm)
H050018	0.5	0.018	2.91	0.42	68
HK05003	0.491	0.0275	2.40	0.36	6 53.5
PW05002	0.5	0.02	2.777	0.602	22.4 61.0 98.7
PW05003	0.5	0.03	2.776	0.643	22.4 61.0 98.7
PW05004	0.5	0.04	2.976	0.577	22.4 61.0 98.7

Note that additional flow conditions are dealt separately in Section 6.5 as they were obtained in a first study with TFM.

Hosokawa et al. 2009 provided experiments in a pipe of 25.0 mm of diameter and 1700 mm of length with the air injected through the holes of diameter 1 mm in a mixing section.

The experiments of Hibiki et al. 2001b with a pipe diameter of 50.8 and length 3061 mm contain a great number of variables of the dispersed phase to analyse as discussed later. The air was injected by a square 20×20 array of hypodermic needles of random lengths resulting in a random distribution of bubbles.

In addition to these experiments, we presented in this work experimental results based on the facility described in Monrós-Andreu et al. (2013) and Monrós-Andreu et al. (2017) in a pipe of diameter 52 mm and length 5500 mm. A sparger to inject the air flow is used. The details about the experimental facility and measurements are detailed below.

Fig. 2.2 shows the corresponding BSD for each case for the top measurement port.

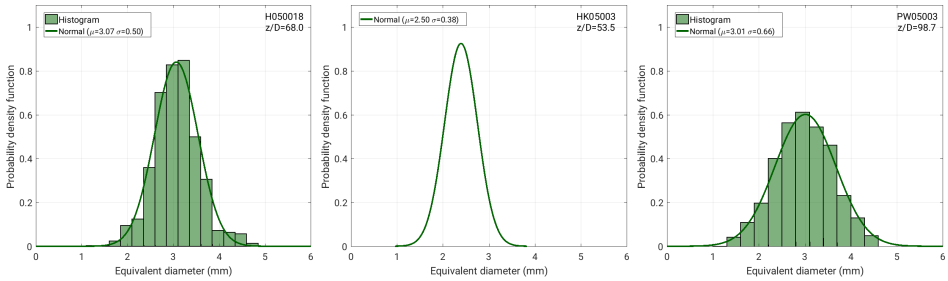

Figure 2.2: Bubble size distribution at the top measurement section (CFD outlet) for H050015 and PW05003 measured by IP and HK05003 estimated from the Sauter mean diameter and an aproximated size deviation.

The BSD was fitted in the literature for bubbly flow, to normal (Laakkonen et al. 2007), log-normal (Lage et al. 1999; Parthasarathy et al. 1996; Ribeiro Jr. et al. 2004; Kazakis et al. 2008; Besagni et al. 2016), or gamma (Lim et al. 1990; Uga 1972) distributions. For the experiments dealt in this work, where relatively low superficial gas velocities are given, the bubble size data fitted well to a normal distribution. The Kolmogorov-Smirnov test at 5% significance level was applied for PW05003 (p=0.79) as we have access to the sample data. In the table, the mean and deviation parameters of a normal distribution fitting the BSD for the inlet (CFD inlet in Fig.2.1) are shown.

2.3 Description of the specific experimental facility used for this thesis (PW series)

To supplement the information present in the existing experimental works and to extend the possibilities of validation with this new solver, we performed a new set of experiments (PW) to fulfil the following requirements:

- The pipe has the necessary length to observe the flow characteristics evolution even under low void fraction conditions.
- The data has enough information to test the solver and the involved models with high spatial resolution at different axial locations as bubble velocity, void fraction, interfacial area concentration, chord length, Sauter mean diameter, bubble frequency, liquid velocity and turbulence. In addition, bubble size distributions were obtained at different port measurements.
- The data contains error bars to quantify the accuracy and precision, which is valuable to analyse the computational results.
- The probability density function of the variables is available and it will be used to analyse the results.

The experimental facility is located at the Laboratory of Hydraulics of the Universitat Jaume I and consists of an upward flow experimental loop (Fig. 2.3) with three axial locations used for the measurements: z/D=22.4, z/D=61.0 and z/D=98.7.

Osmotized water (200-300 $\mu S\,m^{-1}$) is circulated by a centrifugal pump and stored in a 500 L reservoir tank that is kept at a constant temperature (20 °C) thanks to a heat exchanger. The water flow rate introduced in the system was measured by an electromagnetic flow meter (M1000, Badger Meter Inc). An air flow-meter controller (EL-FLOW 250 lNpm, Bronckhorst Hi-Tech) was used to adjust and measure the gas flow-rate.

Four-sensor conductivity probes and Laser Doppler Anemometry (LDA) techniques were adopted to extract information from the air-water flow field. The measurement system consisted of three mounted four-sensor conductivity probes, mechanical traverses, a measurement circuit, a digital high-speed acquisition board, and the software used for signal processing. The four-sensor conductivity probe was attached to the mechanical traverse mounted on a custom designed flange, and it could be moved along the radial direction of the test section using controlled step motors. The measurement circuit was used to measure the voltage difference between the exposed tip and the grounded terminal. A high-speed acquisition board (National Instrument Crop., SCXI-1325) and a PC were used to acquire the signals of the four-sensor probe, with the help of a control program developed under the LabView (National Instrument Crop.) software environment. Probe

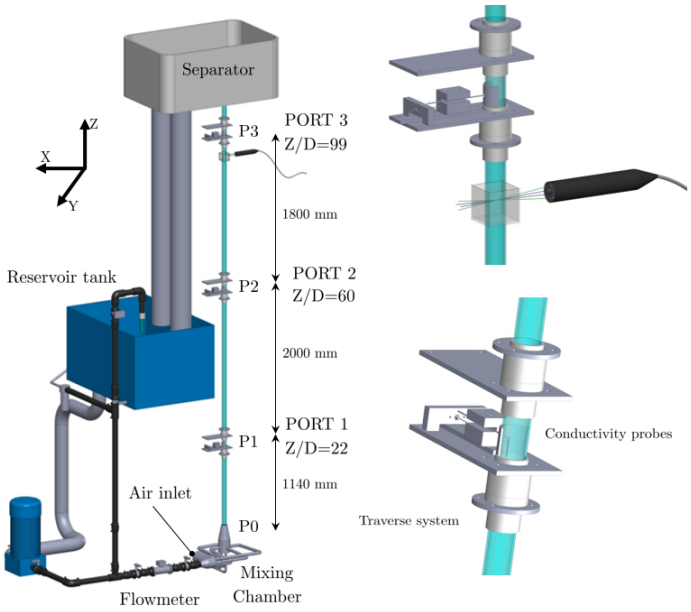

Figure 2.3: Experimental facility.

voltage signals were simultaneously recorded for PW over 30 seconds at 60 kHz individual probe tip sampling rate (720 kHz total sampling rate considering the three sensors).

Pressure was measured thanks to pressure transducers with a range 0-1 bar for the two lower ports, and 0-200 mBar for the mid and top ports (all transducers with an 0.1% relative error). High-speed cameras were located at low and top ports and are used to measure the BSD. A frame is shown in Fig. 2.4 for different conditions.

2.4 Liquid mean velocity and turbulence measurements

The most popular technique for the measurement of velocity and turbulence fields in continuous phases are based on optical techniques (LDA) and heat transfer phenomenology such as Thermal Anemometry (TA). Optical techniques require seeding the flow with microscale tracers that reflect the impinging light, so the flow velocity is indirectly measured. Since its first proposal (Durst et al. 1976b), several researchers have used this technique for the measurement of flow velocity either in single-phase (Durst et al. 1995) and two-phase flows (Lance et al. 1991;

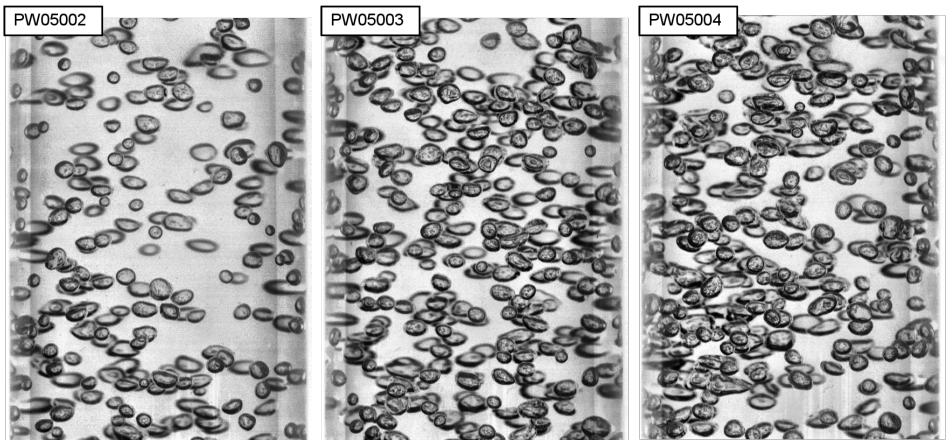

Figure 2.4: Images obtained by the high-speed camera.

Mudde et al. 1997a). Given its accuracy, this technique is the preferred among researchers for most purposes. However, several problems limit its application and measurements in high-void fraction conditions (over 20%) is unpractical (Mudde et al. 1997a).

On the other hand, thermal techniques provide local measurements that rely on the fact that the heat transfer coefficient of a sensing solid immersed in a fluid depends on the flow speed (Bauer 1965b). TA based on hot-wires has been used to measure flow velocity and turbulence in single-phase flows (Jørgensen 2001), and also in two-phase flows (Mendez Díaz 2008), where it also serves as a phase identifier. In practice, a wire is heated by an electrical current, and its electrical resistance is measured. As this property is temperature dependent, the measurement of the wire resistivity allows for the computation of the flow speed. This technique provides measurements with high dynamic range at high-acquisition rates. However, the non-linearity of its signal requires for extensive calibrations that may change over time due to slight contamination of the working fluid.

The experiments H050018 and PW used two-channel LDA to measure the liquid velocity and turbulence, whereas TA was used in HK05003. The velocity fluctuations are quantified differently among these contributions. H050018 provided the turbulence kinetic energy profiles directly without specifically define the methodology, while HK05003 showed the turbulence intensity.

In the experiments performed in this work, the turbulence intensity is provided using the measurement of the LDA as:

$$I = \frac{u'}{|\mathbf{U}|} = \frac{1}{|\mathbf{U}|}\sqrt{\frac{1}{3}({u'_{\mathrm{a}}}^2 + {u'_{\mathrm{r}}}^2 + {u'_{\theta}}^2)} \tag{2.1}$$

where $\mathbf{U}$ is the mean velocity vector and u' is the turbulent fluctuations of the velocity in the axial (a), radial (r) and azimuthal (θ) directions. Let us note that only axial and azimuthal components of velocity field were actually measured with the two-channel LDA. In this analysis, the radial velocity fluctuation was assumed to be equal to the azimuthal velocity fluctuation ($u'_r = u'_\theta$). This approximation is based on the fact that both components are of the same order in pipe flows (Trip et al. 2012).

2.5 Void fraction, bubble frequency, bubble velocity, interfacial area concentration and bubble size

With respect to the measurement of gas phase properties, there is a huge variety of measurement systems. In the experiments selected for this work, needle probe (NP) techniques and image processing (IP) from high-speed cameras (HSC) were used. NP present a moderate degree of intrusiveness and temporal resolution, and constitute the most accurate technique to get local information with high spatial resolution. HSC provides more direct results with fewer assumptions, but is limited to scenarios with few bubbles in order to avoid bubble occlusion.

In H050018 void fraction and bubble velocity profiles were obtained by means of stereoscopic images of bubbles from two cameras. HK05003 measured with a double-tip resistivity probes, the void fraction, bubble velocity, interfacial area concentration and Sauter mean diameter.

2.5.1 Signal processing in needle probes

Since pioneering work of Neal et al. (1963) and Miller et al. (1970) on conductivity and optical fiber probes, respectively, the phase discrimination probes have been widely utilized in two-phase flow studies as local measuring devices. It can be found in the literature different techniques used in the raw signal processing and square signal transform from acquired voltage signal process (Cartellier 1998; Barrau et al. 1999; Kim et al. 2000; Dias et al. 2000; Fu 2001). Signal processing technique is therefore necessary to extract the required information from the raw signal. It is essential to select the right interface signal from the outputs of different sensors of the four-sensor probe in the measurement with the four-sensor probe signal processing algorithm. The sequential signals detected by different sensors not

always corresponds to the same interface and the residence time in the same gas or liquid phase is not exactly the same for different sensors, especially for small bubbles.

The accurate determination of bubble interface start time and bubble interface end time during its movement through the four sensor tips will lead to an accurate velocity vectors determination. So as first step, we need to assign raw signal data to each tip where it belongs to, signal related to liquid phase or signal related to gas phase.

For a single tip voltage signal, it can be observed that when the incoming bubble interface is detected (gas phase data start), voltage signal increases so slow compared to the corresponding leaving bubble interface voltage signal. This behaviour is due to the change of capacitance between tips when the medium changes (mainly due to measurement circuit inherent capacitance) and the tip wetting and dewetting process.

One way to avoid the problem in bubble start point mentioned above is to consider a relatively high threshold level and use an exponential/polynomial fit to data near the rising time determined by the previous threshold. Similar procedure as suggested by (Dias et al., 2000). Exponential fit shows a quite good agreement for all tested signals. The ending point of each bubble is considered as the maximum voltage before signal decay.

In the PW series, four-sensor conductivity probes (Fig. 2.5) were used. Besides the aforementioned variables we show the chord length, bubble frequency or missing ratio. The high speed camera is used to obtain the equivalent bubble diameter with IP.

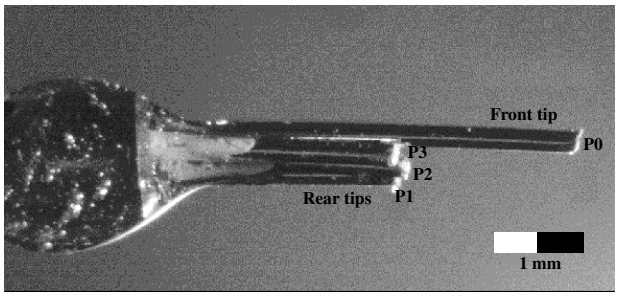

Figure 2.5: Detailed image of a four-sensor conductivity probe used.

An example of the signals obtained in a four-conductivity probe sensor is shown in Fig. 2.6. Four voltage signals appear corresponding to every tip. The voltage of each tip remains at a low value when the tip is immersed in water, and increases smoothly as it pinches a bubble. Later, it sharply decays when the bubble leaves.

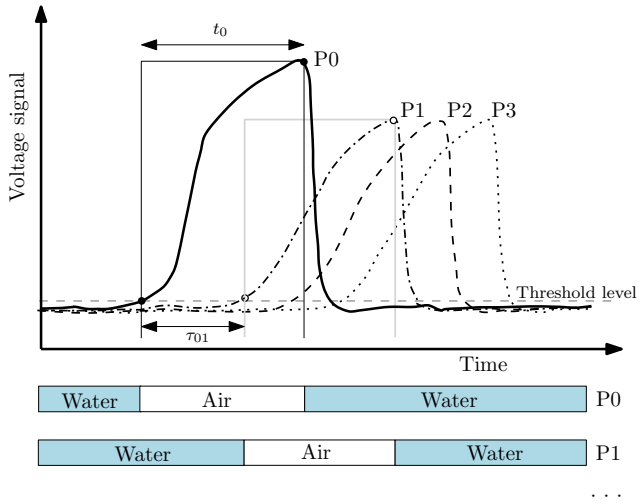

Figure 2.6: Example signal of a detected bubble.

A description of how the data is obtained is detailed in the next sections for the sake of clarity as it is used in the rest of the work.

2.5.2 Void fraction

The mean local volume fraction of the bubbles or time-averaged void fraction at the position of the probe can be well estimated from the signal produced by each bubble. It can be calculated as the fraction of time that the sensor is exposed to gas phase (t_0) over the total sampling time (Ω). These values were measured in different radial positions to obtain the void fraction profile.

$$\alpha_{\mathrm{d}} = \frac{1}{\Omega} \sum_{i=1}^{N_p} t_{0,\mathrm{i}} \tag{2.2}$$

where $t_{0,\mathrm{i}}$ stands for the passing time of the i-th bubble by the front tip and N_p the number of bubbles passing by the probe.

When IP is used, as in the H050018 case, the radial profiles of void fraction are obtained averaging the gas-phase density function, obtained from the reconstructed bubbles, in the specified annular control volumes.

2.5.3 Bubble frequency

The bubble frequency N_t at each local point is computed as the number of bubbles detected per unit time by the front sensor (P0) (number of rising edges in the corresponding binarized signal).

2.5.4 Bubble velocity

The time delay for the paired signals between two needles, say front tip (k=0) and a rear one (k=1,2 or 3), allows for the estimation of the velocities of individual bubbles. The bubble estimated velocity, V_{0k} can be computed from the corresponding distance between tips, S_{0k}, such as:

$$V_{0\mathrm{k}} = \frac{S_{0\mathrm{k}}}{N_p} \sum_{i=1}^{N_p} \frac{1}{\tau_{0\mathrm{k,i}}} \, , k = 1, 2, 3 \tag{2.3}$$

where $\tau_{0\mathrm{k,i}}$ stands for the time delay between the rising time of central tip and the rising time of rear tip k (Fig. 2.6) for a given interface. For HK05003, where dual probes were used, the estimated bubble velocity (assumed parallel to the flow direction) is obtained from the dual conductivity probe with a front tip (k=0) and a rear one (k=1) as $V_{\mathrm{z,NP}}$=V_{01}.

$$V_{\mathrm{z,NP}} = V_{01} = \frac{S_{01}}{N_p} \sum_{i=1}^{N_p} \frac{1}{\tau_{01,\mathrm{i}}} \tag{2.4}$$

The bubble velocity parallel to the sensor probe was computed in PW as the average of individual velocities obtained from Eq. 2.3 with the four probes, one front tip (k=0) and three rear tips (k = 1,2,3) (Tian et al. 2014):

$$V_{\mathrm{z,NP}} = \frac{V_{01} + V_{02} + V_{03}}{3} \tag{2.5}$$

The bubble velocity obtained by IP in H050018 is directly calculated from the distance traveled by the center of gravity of the bubbles from frame to frame.

2.5.5 Interfacial Area Concentration

The interfacial area concentration is defined by the total interfacial area per unit mixture volume. Up to now, several investigations and experimental measurements have been carried out using double or four sensor probe methodology, proving the consistency of this method for a_I measurements. From the pioneer work of Kataoka et al. (1986) on the local interfacial area derivation from velocity measurements, Kim et al. (2001) proposed a miniaturized probe and made it capable of measuring both large and small bubbles.

The interfacial area concentration was obtained in HK05003 with dual probes as Hibiki et al. (1998):

$$a_I = 2N_t \frac{1}{V_z} I(\omega_0), \quad I(\omega_0) = \frac{\omega_0^3}{3(\omega_0 - \sin\omega_0)} \tag{2.6}$$

where ω_0 is the maximum angle between the velocity vector of the i-th interface and the z-direction obtained by Eq. 2.7. This assumes that the root mean square of the fluctuations of the interfacial velocity, σ_z, is equal in all directions.

$$\frac{3}{2\omega_0^2}\left(1 - \frac{\sin 2\omega_o}{2\omega_0}\right) = \frac{1 - (\sigma_z^2/V_z^2)}{1 + 3(\sigma_z^2/V_z^2)} \tag{2.7}$$

The four-sensor probes used in PW make possible the calculation of the normal interfacial velocity $\mathbf{V}_{n,i}$ (Kataoka et al. 1986; Revankar et al. 1993) avoiding the assumptions related to the bubble interface orientation. Shen et al. (2013) proposed an explicit equation for the instantaneous local interfacial area and local interfacial velocity vector using four sensor conductivity probes from Kataoka et al. (1986) methodology for local interfacial area computation, which take into account both receding and oncoming bubble interfaces. Corre et al. (2002) numerically demonstrated that is necessary to consider interfacial area from the missing bubbles and suggested a correlation (Eq. 2.9) based on the bubble missing ratio, (m_r), which is an experimentally measurable parameter. The missing ratio is defined as the detected bubbles by the front tip, but not detected by the rear tips, and the total bubbles detected. Individual bubbles detected by all four sensor tips will be categorized as paired.

Local values of a_I for the four-sensor probes used in the experiments performed for this work, can be calculated as:

$$a_I = a_{I,cor} \frac{1}{\Omega} \sum_{i=1}^{2N_p} \frac{1}{|\mathbf{V}_{n,i}|} \tag{2.8}$$

where $a_{I,cor}$ is defined as:

$$a_{I,cor} = \frac{1}{\sqrt{1 - \sqrt{2.4 m_r - 1.5 {m_r}^2}}} \tag{2.9}$$

2.5.6 Chord length

The chord length, of the bubbles passing through the probe, is defined as the product of the bubble velocity and the bubble transit time from the pulse duration of the front sensor, which provides the less affected signal by bubble probe interaction. The calculation of the chord length implies the assumption of a vertical rising of the bubbles. It can be defined as:

$$c_l = V_z t_0 \tag{2.10}$$

2.5.7 Bubble size distribution and mean diameters

Bubble size distribution of a population is an important factor to determine in the experiments and is required to characterize the bubbly flow. Depending on the needs, arithmetic mean diameter, d_{10}, volume mean diameter, d_{30}, or volume-surface diameter (Sauter mean diameter), d_{32}, are usually employed. It is important to note that the mean bubble diameter will follow the pattern $d_{10}<d_{30}<d_{32}$ for the distributions that are typically employed such as the normal or log-normal distributions (Ribeiro Jr. et al. 2004; Zaepffel 2011). In addition to the mean diameter, the variance is needed to define the BSD. This information is crucial to seed the bubbles in the simulation and to apply properly the hydrodynamic forces, breakup and coalescence rates, and bubble bounces. It is also needed at several locations for a complete description of the BSD evolution as the flow advances.

Unfortunately, it is difficult to characterize the sizes of bubbles in an experiment. The most reliable method to measure the bubble diameter is IP, but this technique is limited to low void fractions or conditions with absence of clusters, as bubble occlusions prevent a proper measurement.

When using IP, the sphere-volume equivalent diameter, d_{eq}, can be obtained from the volumes of the reconstructed bubbles (Lage et al. 1999; Ellingsen et al. 2001; Lau et al. 2013; Besagni et al. 2016). The BSD of equivalent diameters is defined from the different samples as d_{eq} can be obtained from the images assuming oblate ellipsoids . Lage et al. (1999) stated that the ellipsoidal bubble hypothesis and the optical error determining the equivalent bubble diameter could be in the range from 10 to 15%. From the distribution of d_{eq} we can estimate any mean diameter d_{pq} using the generalized equation (Mugele et al. 1951) described in Eq. 2.11 in terms

of equivalent diameter, with values of p and q being tipically positive integers, in particular we use in this work the mean diameteres $d_{10,\mathrm{IP}}$ and $d_{32,\mathrm{IP}}$:

$$(d_{pq,\mathrm{IP}})^{p-q} = \frac{\int_0^\infty d_{eq}^p f(d_{eq})\mathrm{d}d_{eq}}{\int_0^\infty d_{eq}^q f(d_{eq})\mathrm{d}d_{eq}} = \frac{\sum_i^n d_{eq,i}^p f_i}{\sum_i^n d_{eq,i}^q f_i} \tag{2.11}$$

where $f(d)$ is the normalized density function for a bubble population and f_i the relative frequency.

These diameters can be, in addition, estimated with NP ($d_{10,\mathrm{NP}}$ and $d_{32,\mathrm{NP}}$) using measured variables as chord length or void fraction and interfacial area concentration.

The chord length measured with NP is a direct indicator of the bubble size being a representative variable to consider. However, is not possible to transform directly the obtained chord length distribution to the bubble size distribution without assuming a given shape or using correlations to relate sizes and shapes. Many works can be found in the literature using different assumptions to obtain the BSD as a backward transformation process (Besagni et al. 2016; Clark et al. 1988; Liu et al. 1998) or statistical parameters as the mean bubble diameter (Clark et al. 1988; Liu et al. 1998) from chord length measurements. Statistical calculation gives a relationship between the measured mean chord length and the mean diameter seen by the probe, independent of the size distribution (Clark et al. 1988; Liu et al. 1998). Following the representation of Clark et al. (1988), we consider the interaction of a bubble of radius R with the probe tip (see 2.7). Focusing the attention to the ring of wide dr, the bubble centres will pass with increasing probability proportional to r.

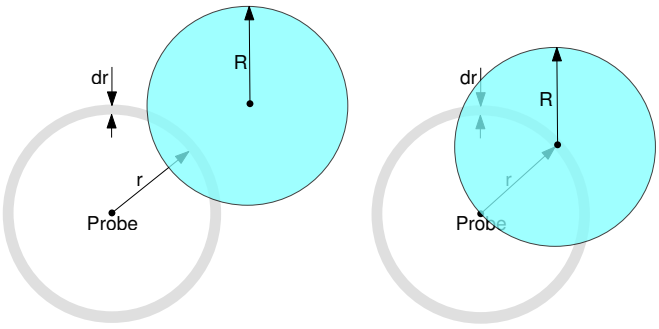

Figure 2.7: Bubble interaction related with an infinitesimal dr.

The probability will result:

$$P(r|R) = \begin{cases} \frac{2r}{R^2} & \text{if } 0 \leq r \leq R, \\ 0 & otherwise. \end{cases} \tag{2.12}$$

If we consider now an ellipsoid with the major semi-axis, b, and the aspect ratio, E, the other variables will result:

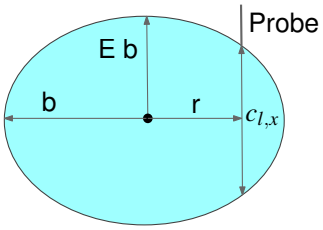

Figure 2.8: Probe and chord lenght relation.

The chord length can be then expressed as:

$$c_{l,x} = 2E\sqrt{b^2 - r^2} \tag{2.13}$$

The probability density function of chord lengths for a given bubble of radius R is:

$$P(c_{l,x}|b) = P(r|b)\left|\frac{dr}{dc_{l,x}}\right| = \frac{2r}{b^2}\frac{c_{l,x}}{4E^2 r} = \frac{c_{l,x}}{2E^2 b^2} \tag{2.14}$$

The probability of chord lengths of bubbles hitting the probe with a probability density function is defined as P_p:

$$P_c(c_{l,x}) = \int_0^\infty P_c(c_{l,x}|b)P_p(b)db = \int_{c_{l,x}/2E}^\infty P_p(b)db \tag{2.15}$$

A mean diameter, can be obtained by integrating the probability density function of chord lengths , assuming that the mean of the size distribution of bubbles touching the probes is:

$$b_{10} = \int_0^\infty bP_p(b)db \tag{2.16}$$

Then, we can relate the mean chord length and the mean major semi-axis, b_{10} related with the aspect ratio:

$$c_l = \int_0^\infty c_{l,x} P_c(c_{l,x}) dc_{l,x} = \frac{4E}{3} b_{10} \tag{2.17}$$

Finally we can obtain the relation between the mean equivalent volumetric diameter and the mean semi-axis as:

$$V_{b,ellipsoid} = V_{b,sphere} \tag{2.18}$$

$$\frac{\pi}{6} 2^3 E b_{10}^3 = \frac{\pi}{6} d_{10}^3 \tag{2.19}$$

$$b_{10} = \frac{d_{10}}{2E^{1/3}} \tag{2.20}$$

Manipulating Eq. 2.20 and introducing in Eq. 2.17 we have:

$$d_{10,\mathrm{NP}} = 1.5 c_l E^{-2/3} \tag{2.21}$$

As a result, assuming an ellipsoid with constant E, the semi-axes can be obtained. The aspect ratio is not known in principle but a global value can be estimated or measured by IP to use this equation.

The Sauter mean diameter can be obtained indirectly from local measurements of α and a_I using NP.

$$d_{32,\mathrm{NP}} = \frac{6\alpha}{a_I} \tag{2.22}$$

The main inconvenient of estimating a bubble size with NP could be that the assumptions considered estimating the size are not strictly the same as in the experiments. For instance, in turbulent flows the bubbles are not rising vertically, or in pipes, the probes located close to the wall hit the bubbles in a pre-determined location and not randomly. This can produce an important deviation as will be shown latter in Section 5.9, thanks to the use of the validation methodology performed in this work.

In practice, the inlet size distribution for the simulations was determined from the data available in the experiments. The experiments of HK05003 only provided the Sauter mean diameter. When the Sauter mean diameter is provided experimentally, is not possible to characterise the bubble size distribution without any

assumption. Therefore, similarly to Buffo et al. (2013) we assumed a standard deviation, σ, 15% of the mean value as stated in Laakkonen et al. (2006) and Petitti et al. (2010). With the Sauter mean diameter known, and the assumed value of the standard deviation, the mean of the distribution, μ, can be obtained from the following equation for a normal distribution:

$$d_{32,\mathrm{IP}} = \frac{\mu^3 + 3\mu\sigma^2}{\mu^2 + \sigma^2} \tag{2.23}$$

In H050018, the BSD is only measured at the top section z/D=68.0 and there is no data related to the bubble size at the inlet. As the injection is performed by using a mixing chamber, it is not possible to obtain the BSD with no measurements. Nevertheless, we can estimate the inlet values under the assumption that breakup and coalescence mechanisms can be neglected and the only change in size is due to the pressure changes, as we explain in the next subsection.

2.6 Measurements of bubble size distribution at different heights

A study has been conducted for this work to investigate the sizes at different heights. From the point of view of the simulation we need to account for the different sizes of the bubbles and its evolution. It will be determinant for the modelling of the closures. From the point of view of the measurement in the experiments it is required to examine in depth the current sizes in the system and how the size evolves. A bubble increase in size is expected but it is not usually shown in the literature. Although there are several methods to obtain bubble size, the measurements of d_{32} and d_{10} performed with needle probes can give considerably errors for pipe flows as demonstrated in this work.

The different sizes in a pipe between two heights excluding the breakup and coalescence mechanisms are due to the pressure changes. This change is given by the ideal gas law and is expressed as an expansion factor f_{ij}:

$$f_{ij} = (P_j/P_i)^{\frac{1}{3}} \tag{2.24}$$

where P_j and P_i are the absolute pressure at, for instance, the outlet port and inlet port respectively.

If the bubbles change its size by the factor f_{ij}, this means a proportional increase of the bubble size and it is equivalent to multiply a random variable by a constant

value. Then, the mean or expected value is also multiplied by the constant value, and the same is applied to the standard deviation:

$$E[f_{ij}d_{eq}] = f_{ij}E[d_{eq}] \tag{2.25}$$

$$\mathrm{Var}[f_{ij}d_{eq}] = f_{ij}^2\mathrm{Var}[d_{eq}] \tag{2.26}$$

Then a BSD can be estimated as a scaled distribution of the BSD at a different height. A normal distribution at a given height would have the following statistical parameters:

$$\mu_i = f_{ij}\mu_j \tag{2.27}$$

$$\sigma_i = f_{ij}\sigma_j \tag{2.28}$$

The BSD at z/D=22.4 and z/D=98.7 was measured by IP for PW05002, PW05003 and PW05004. Approximately 500 bubbles were manually measured for every port (Fig. 2.9). For the measurements, several points in the bubble borders are selected and an ellipse is fitted to the selected points by using a least-squares algorithm that provides with both axis and orientation angle. The semi-axis are used to obtain d_{eq} for each bubble.

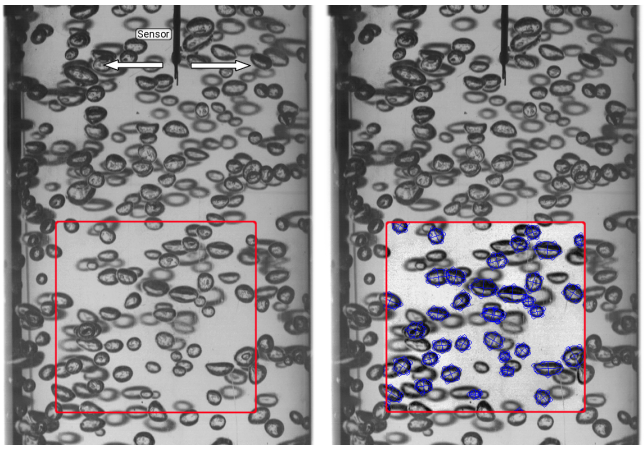

Figure 2.9: Example of some processed bubbles in an arbitrary region for an image frame in the lower measurement port.

The BSD of the equivalent diameters at z/D=22.4 and z/D=98.7 are shown in Fig. 2.10. The figure includes a theoretical BSD at z/D=98.7 based on the BSD

at z/D=22.4, using the parameters defined in Eq. 2.27 and Eq. 2.28, and the pressures on these heights.

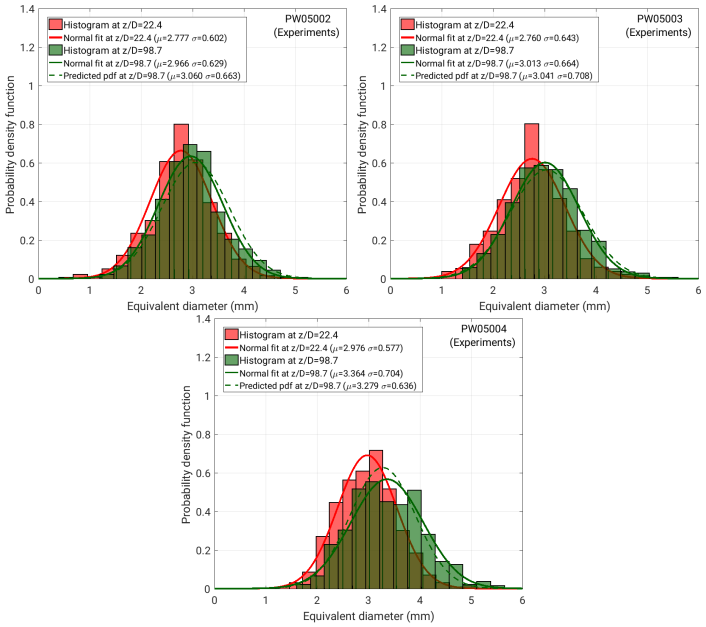

Figure 2.10: Experimental bubble size distributions.

2.7 Variables measured with needle probes and potential types of theoretical variables

Experimental measurement of dispersed phase characteristics is a complex task that involves several approximations and data processing. Also, the comparison of simulation results with experimental data is not as straightforward as one could expect.

Measuring with needle-probe sensors implies necessarily that not all the bubbles can be considered, producing a statistical bias in the measurements. Some bubbles will pass without being intersected by the probe and other bubbles intersected should be discarded as there is not enough information for the processing. For example, the bubble does not hit all the tips of the probe. Furthermore, from the bubbles that are paired, in the experiments we only know the signal, so the variables should be obtained assuming a set of hypotheses as mentioned above.

On the one hand, when not all the tips are hit by the bubble, it can be considered missed. This means, that a bias is produced as these circumstances are not random. Using the missing ratio it can be in principle corrected. For instance, the correlation used for the interfacial area concentration proposed by Corre et al. (2002).

On the other hand, in a non-uniform size flow like the one shown in Fig. 2.11 the bubbles will hit the probe with different probability depending on its size. This will result in a bias where the bigger bubbles will be more likely to be hit than smaller ones. In addition to the size, the variables measured as for example bubble velocity, will be given from the bigger bubbles.

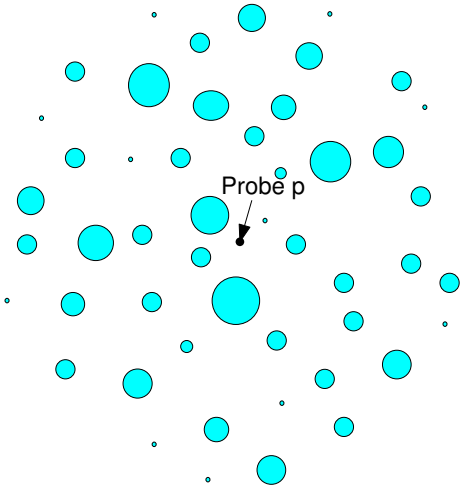

Figure 2.11: Probe surrounded by bubbles of different size.

The probability of a bubble of a given size to pass through a probe point can be explained following the works of Clark et al. (1988) and Liu et al. (1995):

$$\frac{P(b)}{P_s(b)} = \frac{\pi b^2}{\pi b_{max}^2} = \frac{b^2}{b_{max}^2}, \quad P(b) = \frac{b^2}{b_{max}^2} P_s(b) \tag{2.29}$$

The normalized probability density function of sizes of the bubbles touching the probe is defined as:

$$P_p(b) = \frac{P(b)}{\int_{-\infty}^{\infty} P(b)\mathrm{d}b} \tag{2.30}$$

Then, introducing Eq. 2.29 in Eq. 2.30, we obtain the relationship between the distribution of the bubbles in the system and the bubbles hitting the probe:

$$P_p(b) = \frac{b^2 P_s(b)}{\int_{-\infty}^{\infty} b^2 P_s(b) \mathrm{d}b} \tag{2.31}$$

This allows transforming from chord length distributions to the system distribution through the knowledge of the distribution seen by the probes. This transformation is dependent on the distribution. In Liu et al. (1995) the size distribution of bubbles in the system is obtained analytically from the chord length distributions for Gamma and Rayleigh probability functions and related with Monte-Carlo simulations. However, the analytical translation in the normal or log-normal distribution of the experiments is further complicated.

In summary, for the measures from multi-sensor probes, we know that not all the bubbles hit the probe with the same probability and that not all the bubbles hit all the sensor of tips of the probe. From this, the different possibilities of a bubble with respect to the probe for a given polydispersed flow are explained in Fig. 2.12. As a result a bubble can be non-intersected or intersected by the probe, and in turn paired or missed.

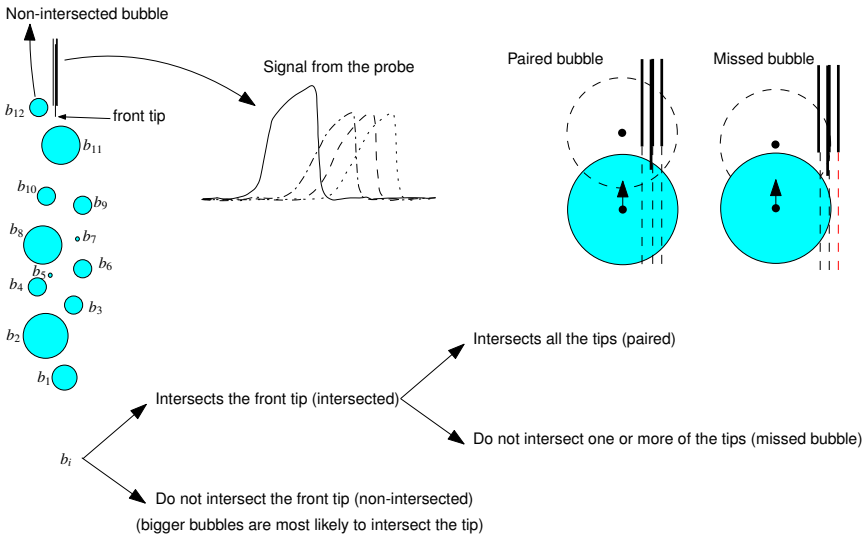

Figure 2.12: Scheme of bubble interaction with the probe.

The data obtained in the experiments comes from the signal generated by the paired bubbles as the other data is missed. Fig. 2.13 show the potential types of

variables that could be obtained. For instance system variables, probe variables, pair variables or reconstructed variables.

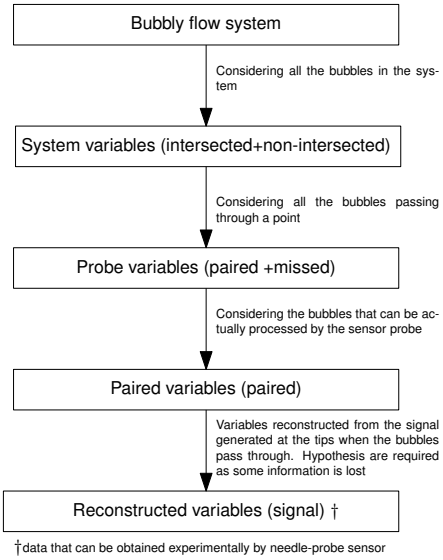

Figure 2.13: Description of the variables as a function of the considered data.

A rigorous validation should consider this effects in order to properly compare the results with the experiments. This permits to evaluate the possible discrepancies that exists because of the assumptions considered or inherent aspects of this technique.

Chapter 3

Two-phase flow modelling

A general view of the relevant issues to solve the two-phase flow problem is shown in this chapter. The theoretical frameworks and numerical methods found in the literature are very diverse and should be investigated to perform the objectives established for this work. An exhaustive review about two-phase flow modelling was carried out to establish the basis of the present study.

3.1 Introduction

In two-phase flow, two fluids or materials are coexisting separated by an interface evolving in space and time. To compute numerically a scenario like this, different mathematical formulations can be found involving from jump conditions to averaging procedures. Because these operations, information that is lost to a greater or lesser degree (e.g. unclosed terms that arise) is compensated by modelling. The two-phase flow modelling term in this thesis refers mainly to the collection of models, correlations or coefficients that are used within the different methods, and the methods themselves.

The methods and formulations for VOF, CFD-DEM and TFM will be described in the corresponding following chapter. This chapter is focused on describing main issues when modelling two-phase flow, and in particular bubbly flow. First, basic concepts related to the phase representation are described. The interfacial forces as drag, lift, virtual mass or wall lubrication are reviewed and discussed. The same is done hereafter for contact forces as particle-particle and particle-wall.

In addition, two-phase flow models require special attention to the turbulence modelling as the effect of the interface and the wake plays an important role in

both, the carrier phase velocity and the dispersed phase behaviour. For instance, the fluctuations of the continuous phase in interfacial forces should be considered for accurate simulations.

Finally, bubbly flows are commonly polydispersed. Then, the description of the size distribution is required. In TFM, the dispersed phase has a continuum description. To represent the size distribution it is needed the use of a Population Balance Equation (PBE) that calculates this distribution in space and time. The techniques to solve the PBE are analysed in this chapter. Finally, the non-linearity of the closures in a polydisperse flow is analysed.

3.2 Dispersed phase representation

An indicator function of a given phase φ over space and time can be defined as:

$$\mathbf{I}_{\varphi}(x,t) = \begin{cases} 1 & \text{if } \mathbf{x} \in \varphi, \\ 0 & \text{if } \mathbf{x} \notin \varphi. \end{cases} \tag{3.1}$$

The indicator function of Eq. 3.1 will serve us to define the flow equations for different methods. The numerical methods can be characterised as resolved or unresolved methods depending on the detail of resolution of the flow at the interface as shown in Fig. 3.1.

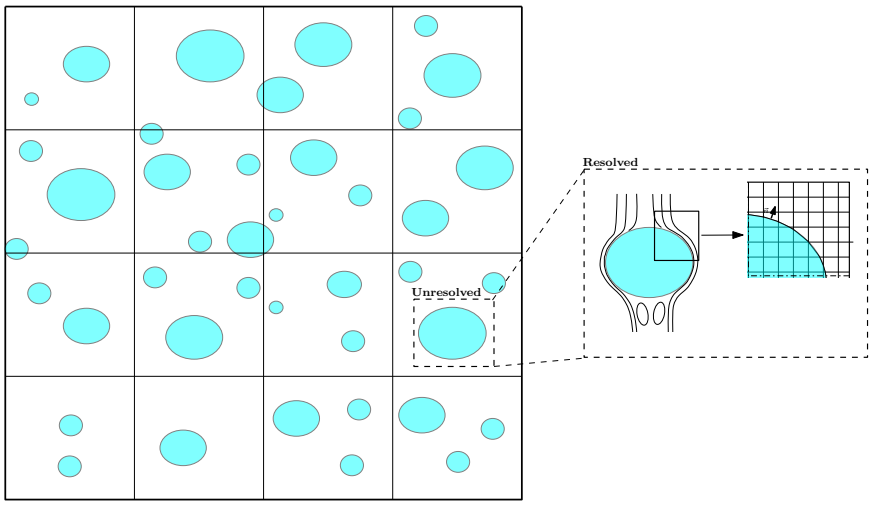

Figure 3.1: Bubble representation as a function of the grid.

Interfacial front tracking, volume of fluid, immersed boundary method or CFD-DEM (for resolved particles) are an example of solvers that need to refine the grid at the interface. In contrast, it is not always necessary to solve the flow in detail as with two-fluid model, Eulerian-Lagrangian or CFD-DEM for unresolved particles. For instance, with the use of correlations for interfacial forces it is possible to obtain relevant information for a given flow.

In the VOF method, the equations are volume averaged and the interface is tracked using $\mathbf{I}_\varphi$. A unique set of equations for the whole domain is obtained and the microscale effects on the border of the two materials can be considered (Hirt et al. 1981).

The representation of a dispersed phase in a Lagrangian framework as in the CFD-DEM, allows the motion of each bubble in the carrier phase. $\mathbf{I}_\varphi$ can be obtained by the knowledge of the position of the bubble in space and time. The carrier phase motion is solved by the volume averaged Navier-Stokes equations including the averaged properties of the disperse phase (disperse-continuous phase interaction and volume fraction) (Norouzi et al. 2016a).

In the TFM approach, the local instantaneous equations of each phase are averaged to obtain an Euler-Euler two-phase flow description, as stated in Drew et al. (1971b) and Drew (1982). The equations are multiplied by the indicator function before applying averaging techniques. The averaging process introduces phase fraction ($\alpha_\varphi = \overline{\mathbf{I}_\varphi(x,t)}$) and unclosed terms representing the property transfer between the phases (Rusche 2002; Weller 2005).

The averaging procedures mentioned result in unclosed terms that necessarily increase when the resolution level is lower. These terms are crucial for the prediction of two-phase flow simulations and must be modelled.

3.3 Interfacial force modelling

The fluid-particle or fluid-fluid interaction has been extensively studied during the years. In these studies, separate effects from a microscopic point of view, are analysed to obtain macroscopic model formulations. The interfacial closures laws obtained aim to define the fluid-particle interaction as a function of physical constant or variables. These relations can not be always achieved because of its complexity or because of the difficulty to isolate the effects. Nevertheless, under specific scenarios, interfacial closures laws can be defined with an acceptable degree of confidence. The resolution level of the approach (CFD-DEM, TDM-3D, TFM-1D) used for the simulation will have an important role in the effectiveness of their definition.

The Interfacial Methods (IM) calculate directly the forces between fluid and the interface, but do not contain the unclosed terms for the forces as for TFM. The surface tension acting on the bubble surface is directly calculated with this method. The surface tension forces is exerted by a continuous fluid on a particle and using the Continuum Surface Force model (CSF) results:

$$F_s = \sigma\kappa(x)\mathbf{n} \tag{3.2}$$

When the surface tension force is not computed, the interfacial forces term arises and constitute the closure equations for the forces acting on a bubble. The motion of a bubble can be determined from the Newton's second law considering a total interfacial force acting on the bubble:

$$m_\mathrm{b}\frac{\mathrm{d}\mathbf{u}_\mathrm{b}}{\mathrm{d}t} = \mathbf{f}. \tag{3.3}$$

The term $\mathbf{f}$ represents the forces acting on the bubble (hydrodynamic forces resulting from the liquid-bubble interaction, body force, etc.) and is usually described by a set of uncoupled terms (Auton 1984; Maxey 1983) mainly drag ($\mathbf{f}_\mathrm{D}$), lift ($\mathbf{f}_\mathrm{L}$), virtual mass ($\mathbf{f}_\mathrm{VM}$), buoyancy ($\mathbf{f}_\mathrm{B}$) and pressure gradient ($\mathbf{f}_\mathrm{P}$). The equation results (Auton et al. 1983):

$$\mathbf{f} = \mathbf{f}_\mathrm{D} + \mathbf{f}_\mathrm{L} + \mathbf{f}_\mathrm{V} + \mathbf{f}_\mathrm{B} + \mathbf{f}_\mathrm{P} \tag{3.4}$$

The different contributions are analysed in the subsequent subsections. The reader is referred to Magnaudet et al. (2000) for a review about the description of the bubble motion in inhomogeneous flow. Eq. 3.4 can be solved directly for every particle using a Lagrangian description of the bubbles as in CFD-DEM. The different contributions of Eq. 3.3 are considered in the momentum equation of the TFM as a result of the averaging procedures of the phase equations and represents the interfacial closure term (Drew et al. 1971b; Ishii 1975; Drew 1982).

3.3.1 Drag force

The drag force is the hydrodynamic resistance exerted on a body by the surrounding fluid when a relative motion is given. It constitutes the most important closure as determines the terminal velocity of particles. The determination of the drag force is still an unsolved problem of fluid dynamics that started Newton (1687) with his theory about air resistance. Stokes (1851) derived the drag force for a flow past a sphere with validity at very low Reynolds numbers. Under these conditions, the flow is very slow, so the inertial forces are much smaller than the viscous forces and an analytical solution is possible. Since the Stokes work, the

experimental determination of drag has been extensively investigated. The first investigations on this field were devoted to spheres and infinity cylinders in high-viscosity fluids. The reader is referred to Veysey et al. (2007) for an extensive review of experimental and theoretical literature on this field.

At high Reynolds numbers, the drag force is defined with Eq. 3.5 attributable to Lord˜Rayleigh (1876), noting that the drag force is proportional to the square of the velocity.

$$\mathbf{f}_D^{\mathrm{h}} = \frac{1}{2} C_D \rho_{\mathrm{c}} A_p (\mathbf{U}_{\mathrm{c}} - \mathbf{U}_{\mathrm{b}}) |\mathbf{U}_{\mathrm{c}} - \mathbf{U}_{\mathrm{b}}| \tag{3.5}$$

In the above equation, A_p is the projected area of the bubble. It is usual to present the drag force assuming that the bubbles are spherical, then:

$$A_p = \pi r_b^2 = \frac{1}{4} \pi d_b^2 \tag{3.6}$$

Therefore, substituting Eq. 3.6 in Eq. 3.5 for spherical particles or bubbles, it results:

$$\mathbf{f}_D^{\mathrm{h}} = \frac{1}{8} C_D \rho_{\mathrm{c}} \pi d_b^2 (\mathbf{U}_{\mathrm{c}} - \mathbf{U}_{\mathrm{b}}) |\mathbf{U}_{\mathrm{c}} - \mathbf{U}_{\mathrm{b}}| \tag{3.7}$$

Many works rely on this equation over the last and current centuries to obtain experimentally or numerically the drag coefficient, C_D. Initially the drag coefficient was determined for an isolated body in an infinite medium obtaining analytically or experimentally a given expression for $C_{\mathrm{D},\infty}$.

The pioneering researches were focused to determine experimentally the drag coefficient of single bubbles rising in a quiescent liquid (Hadamard 1911; Grace 1973; Peebles et al. 1953; Žun et al. 1996; Tomiyama et al. 1998).

For spherical bubbles, different drag coefficients were obtained. Hadamard (1911) presented a coefficient for a spherical bubble valid for Re$\leq$1:

$$C_{\mathrm{D},\infty} = \frac{16}{Re}, \tag{3.8}$$

and Levich (1962) for high Reynolds number:

$$C_{\mathrm{D},\infty} = \frac{48}{Re} \tag{3.9}$$

The drag correlation was studied formerly for particles and a standard drag coefficient for a rigid spherical particle was obtained by Schiller et al. (1935):

$$C_{\mathrm{D},\infty} = \frac{24}{Re}(1 + 0.15Re^{0.687}) \tag{3.10}$$

This correlation gives also reasonable results for spherical bubbles when the interface is contaminated (Tomiyama et al. 1998). The drag coefficients for bubbles are usually based on Eq. 3.10.

The later researches were focused on study the influence of the bubble shape in the drag coefficient . Usually, if non-spherical bubbles are considered, the value of this coefficient is bigger than that of the spherical one. Then, the drag coefficient is selected according to the maximum value.

Tomiyama et al. (1998) obtained the following correlations for different degrees of contamination:

- Pure system (water distilled two or more times):

$$C_{\mathrm{D},\infty} = \max\left[\min\left(\frac{16}{Re}(1 + 0.15Re^{0.687}), \frac{48}{Re}\right), \frac{8}{3}\frac{\mathrm{Eo}}{\mathrm{Eo}+4}\right] \tag{3.11}$$

- Contaminated system (tap water):

$$C_{\mathrm{D},\infty} = \max\left(\frac{24}{Re}(1 + 0.15Re^{0.687}), \frac{8}{3}\frac{\mathrm{Eo}}{\mathrm{Eo}+4}\right) \tag{3.12}$$

- Slightly contaminated (intermediate contamination):

$$C_{\mathrm{D},\infty} = \max\left[\min\left(\frac{24}{Re}(1 + 0.15Re^{0.687}), \frac{72}{Re}\right), \frac{8}{3}\frac{\mathrm{Eo}}{\mathrm{Eo}+4}\right] \tag{3.13}$$

In a more recent contribution, Dijkhuizen et al. (2010a) proposed an expression for $C_{\mathrm{D},\infty}$ for pure liquids as a function of the Reynolds and Eötvös numbers:

$$C_{\mathrm{D},\infty} = \sqrt{C_{\mathrm{D}}(Re_{\mathrm{d}})^2 + C_{\mathrm{D}}(Eo)^2}, \tag{3.14}$$

$$C_{\mathrm{D}}(Eo) = \frac{4Eo}{Eo + 9.5}, \tag{3.15}$$

where $C_D(Re_\mathrm{d})$ is described by the correlation of Mei et al. (1994):

$$C_D(Re_\mathrm{d}) = \frac{16}{Re}\left[1 + \frac{2}{1 + 16/Re + 3.315/\sqrt{Re}}\right]. \tag{3.16}$$

In addition to single bubbles rising, several researches have been focused to analyse the influence on the drag coefficient of bubbles rising in a swarm. The findings of these works are usually a correction factor, $C_{f,swarm}$, applied to the drag coefficient of a single bubble.

Tomiyama et al. (1995) proposed a modified drag force coefficient trough an empirical correlation for drift velocity of the swarm and the balance of forces. The expression is given by:

$$C_{f,swarm} = \alpha_\mathrm{c}^{3-2n} \tag{3.17}$$

Simonnet et al. (2007) found that, for bubble diameters less than 7 mm, the relative velocity decreases with α_d until a critical value of around 0.15, where the local void fraction is independent of the bubble diameter. The following expression is valid for d_b <7 mm and α <0.15. This correlation was obtained up to a liquid superficial velocity of 0.1 m/s:

$$C_{f,swarm} = \alpha_\mathrm{c}^{-1} \tag{3.18}$$

DNS simulations, were also used to obtain this coefficient as in Roghair et al. (2013), showing a dependency of the swarm correction on the Eötvös number. Their study led to a correlation valid for high void fractions.

$$C_{f,swarm} = 1 + \frac{22}{E_o + 0.4}\alpha_\mathrm{d}\alpha_\mathrm{c} \tag{3.19}$$

Tomiyama et al. (2002a) defined the drag coefficient as a function of the aspect ratio E:

$$C_{\mathrm{D},\infty} = \frac{8}{3}\frac{Eo}{E^{2/3}(1-E^2)^{-1}Eo + 16E^{4/3}}F^{-2} \tag{3.20}$$

where

$$F = \frac{\sin^{-1}\sqrt{1-E^2} - E\sqrt{1-E^2}}{1-E^2} \tag{3.21}$$

The correlation of Vakhrushev et al. (1970) is used to define the aspect ratio of a bubble in an infinite stagnant liquid E_0 as function of the Tadaki number ($Ta = Re_{\mathrm{d}} Mo^{0.23}$):

$$E_0 = \begin{cases} 1, & Ta < 1 \\ [0.81 + 0.206 \tanh(2(0.8 - \log_{10} Ta))]^3, & 1 \leq Ta \leq 39.8 \\ 0.24, & Ta \geq 39.8 \end{cases}$$

whith the Morton Number being $Mo = g\rho_{\mathrm{c}}^2 \Delta\rho \nu_{\mathrm{c}}^4 / \sigma^3$ and σ being the interfacial surface tension.

A correction to this aspect ratio was applied later in Hosokawa et al. (2009), to consider the wall effect on E as a function of the distance to the wall (y) and the pipe diameter (D):

$$\frac{E}{E_0} = \max\left(0.65, 1.0 - 0.35\frac{y}{D}\right) \tag{3.22}$$

The effect of shear rate on the drag coefficient is accounted for by Magnaudet et al. (1997) with the following correction coefficient:

$$C_{f,\mathrm{shear}} = \left(1 + 0.55 Sr^2\right), Sr = \frac{d_b \omega}{|\mathbf{U}_{\mathrm{r}}|}. \tag{3.23}$$

where ω is the magnitude of the gradient of the carrier phase velocity.

3.3.2 Lift force

The fluid moving past the surface of a body, exerts in addition to the drag, the so-called lift force . While the drag acts opposite to the motion, the lift force acts perpendicular to the motion. In the case of bubbles, the presence of shear flows is subjected to a lift force that pushes the bubble in a direction perpendicular to the streamwise direction. Several researches have developed lift force equations and correlations based on analytical, numerical or empirical observations. A literature survey about lift force modelling can be found in Hibiki et al. (2007).

A first approach to develop a lift force on a sphere was made by Saffman (1965). In this work an analytical expression was obtained for low Reynolds numbers. Some years later Žun (1980), Drew et al. (1987), and Auton et al. (1988) described

the migration of spherical bubbles towards the wall with the expression for the shear-induced lift force:

$$\mathbf{f}_L^{\mathrm{h}} = \mathrm{C_L}\rho_{\mathrm{c}}\mathrm{V_b}\mathbf{U}_r \times (\nabla \times \mathbf{U}_{\mathrm{c}}) \tag{3.24}$$

This force has been traditionally used in two-phase flow in pipes and ducts to explain the lateral migration of bubbles. In the subsequent years the researches were conducted, specially with experiments and front-tracking DNS simulations. With the aim to determine a C_L that describes the behaviour of bubbles of different shapes and sizes, with a focus in the change of the sign of C_L for bubbles of different size.

The lift equation (Eq. 3.24) was first obtained with constant coefficients. Auton et al. (1988) showed a lift coefficient of 0.5 for a spherical bubble or particle. Various values are recorded in the literature ranging from 0.01 to 0.5 (Hibiki et al. 2007).

Some authors as Tomiyama et al. (2002b) have detected in a single-particle system a sign change on $C_{\mathrm{D},\infty}$ for big bubbles. The lift coefficient of (Tomiyama et al. 2002b) takes into account the influence of the shear rate for the different bubble sizes:

$$C_{\mathrm{L},\infty} = \begin{cases} \min\left(0.288\tanh(0.121Re), f\right) & \mathrm{Eo}_d < 4 \\ f & 4 \leq \mathrm{Eo}_d \leq 10 \\ -0.29 & \mathrm{Eo}_d > 10 \end{cases} \tag{3.25}$$

$$f = 0.00105\mathrm{Eo}_d^3 - 0.0159\mathrm{Eo}_d^2 - 0.0204\mathrm{Eo}_d + 0.474 \tag{3.26}$$

where Eo_d is a modified Eötvös number with characteristic length the maximum horizontal dimension of the bubble that can be estimated as in the same work as a function of a spherical bubble diameter.

Finally, system correlations for the lift force is also available. Wang et al. (1987) obtained from the radial momentum equation as it can be applied to bubble systems for fully developed axisymmetric pipe flow Hibiki et al. (2007).

$$C_{\mathrm{L}} = 0.01 + \frac{0.49}{\pi}\cot^{-1}\left(\frac{\log\zeta + 9.3}{0.20}\right) \simeq 0.02 + 0.6(\log\zeta + 10.67)^{-2.605}, \tag{3.27}$$

$$\zeta \equiv e^{-\alpha_\mathrm{d}} \frac{d_\mathrm{b}}{\mathbf{U}_\mathrm{r}} \frac{\partial \mathbf{U}_\mathrm{c}}{\partial r} \left(\frac{d_\mathrm{b}}{D} \frac{1}{Re_\mathrm{d}} \frac{\mathbf{U}_\mathrm{d}}{1.18(\sigma g/\rho_\mathrm{c})^{\frac{1}{4}}} \right)^2 . \tag{3.28}$$

The values are in a range from 0.01 to 0.1 in the experimental conditions considered by the original authors.

3.3.3 Virtual mass force

The virtual mass force is related to the mass of liquid *carried* by the bubble. This force was first quantified by Lord˜Kelvin (1873) who obtained a resultant force in the direction of the pressure gradient. For an accelerating solid sphere concluded that the force was proportional to 1.5 the volume of the sphere. In practice, it represents a force proportional to the bubble acceleration and opposite to its motion.

The virtual mass force is commonly defined as Drew et al. (1987):

$$\mathbf{f}_V^\mathrm{h} = \mathrm{V_b} \rho_\mathrm{c} \mathrm{C_V} \left(\frac{\mathrm{D}\mathbf{U}_\mathrm{c}}{\mathrm{D}t} - \frac{\mathrm{d}\mathbf{U}_\mathrm{b}}{\mathrm{d}t} \right) \tag{3.29}$$

The application of potential flow theory to flow around a spherical bubble in an infinite medium gives a value of 0.5 for C_V according to Lamb (1895), Auton et al. (1988), and Drew (1982). Several works related to the virtual mass force coefficient were focused on the shape, resulting in coefficients dependent on the aspect ratio, showing an increase of the coefficient with the aspect ratio (Lamb 1895; Clift et al. 1978; Tomiyama et al. 2004). In particular (Clift et al. 1978; Zenit et al. 2009):

$$C_\mathrm{V} = \frac{(E^2-1)^{1/2} - cos^{-1}E^{-1}}{cos^{-1}E^{-1} - (E^2-1)^{1/2}E^{-2}} \tag{3.30}$$

Numerical simulations with IM can be found in the literature1 analysing the virtual mass coefficient. Dijkhuizen et al. (2005) showed values close to 0.5 for spherical bubbles.

In a CFD-DEM solver, the main concern is related to its implementation when integrating the motion. In fact, the virtual mass force is dependent to the bubble velocity that is being calculated. Implicit and explicit implementations of the force can be found in the literature.

3.3.4 Pressure gradient force

In addition to the virtual mass force, a pressure gradient force arises due to the pressure gradient in the fluid. It can be expressed as:

$$\mathbf{f}_V^{\mathrm{h}} = \mathrm{V_b}\rho_{\mathrm{c}} \left(\frac{\mathrm{D}\mathbf{U}_{\mathrm{c}}}{\mathrm{D}t} \right) \tag{3.31}$$

This force plays an important role for scenarios where the bubbles pass by considerable carrier phase velocity gradients over time, as for example two-phase flow through an horizontal T-junction.

3.3.5 Wall lubrication force

The wall lubrication force reflects the drainage of the fluid around the bubble. It represents the force that the liquid drainage around a bubble moving near a wall have on the bubble. A two-dimensional solution was derived for flow between a cylinder and a wall:

$$\mathbf{f}_W^{\mathrm{h}} = -\frac{\rho_{\mathrm{c}} \mathrm{V_b} C_{\mathrm{W}}}{r_{\mathrm{b}}} \left| U_{\mathrm{r}} \right|^2 \mathbf{n_w} \tag{3.32}$$

where $\mathbf{n_w}$ is the unit vector normal to the wall in its direction.

The model of Antal et al. (1991) has been used traditionally for TFM. In Antal et al. (1991), constants were evaluated by comparison to a three-dimensional DNS of viscous flow past a single bubble with uniform velocity using PHOENICS code. The simulations were done for two relative velocities (0.1 and 0.2 m/s) finding a match to obtain the coefficients in the following equation:

$$C_{\mathrm{W}} = \max \left[C_{\mathrm{W1}} + C_{\mathrm{W2}} \frac{r_{\mathrm{b}}}{y} \right] \tag{3.33}$$

where y is the distance to the wall with the following coefficients obtained by Antal et al. (1991):

$$C_{\mathrm{W1}} = -0.104 - 0.06 |\mathbf{U}_{\mathrm{r}}| \tag{3.34}$$

$$C_{\mathrm{W2}} = 0.147 \tag{3.35}$$

During the last decades different values can be found in the literature, as for example the default values on the commercial code ANSYS CFX or in Krepper et al. (2005). In practice, this force is used in TFM as a wall-force to adjust the void fraction radial distribution near the wall with ad-hoc values of the coefficient. In a wall peak configuration of two-phase flow in pipes, the position of the peak will be governed by the lift and wall lubrication force. Note, that the turbulent dispersion force will play a role in the profile shape but not mainly defining the peak position. Without considering any additional force, one can compensate the lift force through these coefficients to adjust the values to the experiments. Among others, the absence of forces as bubble-wall collision model, an overestimation of the lift force, misleading boundary condition could affect the results, and tuning the wall lubrication force could be required.

3.4 Particle collision

In addition, to interfacial forces, there are in two-phase flow other forces produced in the bubbles as the contact forces. These are produced by the contact of the particles with other particles or with other bodies in the system as solid walls. The particle-wall or bubble-wall interaction is of great importance for wall-bounded systems based on experimental observations or analytical considerations. The particle-wall collision is responsible of two-effects (Alajbegovic et al. 1999): a wall force that moves the particles to the flow stream and a dissipation of the kinetic energy due to inelastic collisions. This is appreciated for bubbles by Vries (2001), depending on the bubble size and the distance to the wall where the bubble was injected, the bubble bounces repeatedly or departs away from the wall after the collision.

In DEM approaches, hard-sphere and soft-sphere models are the most common approaches, originally applied to molecular dynamics. The soft-sphere model (Cundall et al. 1979) consists of a spring, a dash-pot and a slider. These elements generally need the definition of stiffness k, as well as damping coefficient η and friction coefficient μ_f. The force according to a linear contact-stiffness model is given by normal and tangential components:

$$\mathbf{f}_n^c = -k\delta_n - \eta u_n \tag{3.36}$$

$$\mathbf{f}_t^c = -k\delta_t - \eta u_t \tag{3.37}$$

where δ_n and δ_t are the normal and tangential overlapping or displacement.

If the particle is sliding, for instance, the following is true:

$$|\mathbf{f}_t^c| > \mu_f |\mathbf{f}_n^c|, \tag{3.38}$$

the tangential force becomes:

$$\mathbf{f}_t^c = -\mu_f |\mathbf{f}_n^c|, \tag{3.39}$$

Regarding the consideration of this force in TFM, it is usually neglected in almost every simulation found in the literature. However, this effect is in some way introduced through the wall lubrication and dispersion forces. An averaged wall force due to particle-wall was described by Alajbegović et al. (1994), Alajbegovic et al. (1999), and Lahey Jr et al. (2000), assuming rigid particles and negligible rotational effects. The probability of the collision events is also modelled with this approach. The momentum transfer for the wall collision term is:

$$\mathbf{M}_{wc}^{\mathrm{c}} = -6\rho_{\mathrm{d}} \frac{(1+e_w) r_m^2}{d_b^3 (1+e_w)} \mathbf{n_w} \left(\alpha_{\mathrm{d}} {u'_{\mathrm{d,w}}}^2 + (y - r_b) {u'_{\mathrm{d,w}}}^2 \frac{\delta \alpha_{\mathrm{d}}}{\delta w} + \right.$$
$$\left. + y\alpha_{\mathrm{d}} \frac{\delta {u'_{\mathrm{d,w}}}^2}{\delta w} + \frac{2\sqrt{1+e_w^2}}{\sqrt{\pi}} y\alpha_{\mathrm{d}} \sqrt{{u'_{\mathrm{d,w}}}^2} \frac{\delta u'_{\mathrm{d,w}}}{\delta w} \right) \tag{3.40}$$

where w refers to the wall direction, $u'_{\mathrm{d,w}}$ is the velocity fluctuation of the disperse phase in the wall direction and $\mathbf{n_w}$ is the unit vector towards the wall, y the distance to the wall of the cell center, r_b is the radius of the bubble and e_w the wall restitution coefficient.

3.5 Turbulence modelling

Turbulence is a characteristic of almost all the fluids. In turbulent flow, the instantaneous velocities (and pressure) can be derived in a time-averaged term and a fluctuating one:

$$\mathbf{u}_{\mathrm{c}} = \mathbf{U}_{\mathrm{c}} + \mathbf{u}'_{\mathrm{c}} \tag{3.41}$$

Fig. 3.2 show graphically the different parts for a unsteady motion in a turbulent flow.

The prediction or modelling of turbulence is always a major challenge. In single-phase flow one may require an accurate description of the turbulence as it will

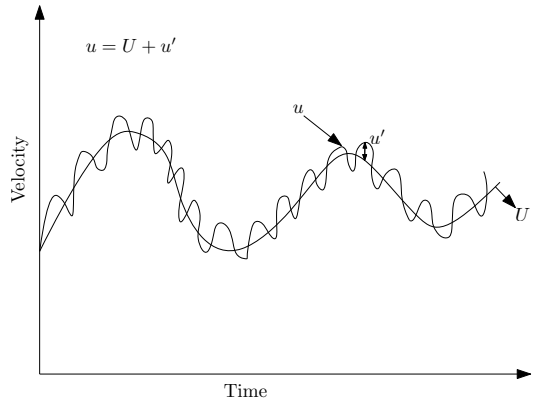

Figure 3.2: Decomposition of velocity into mean and fluctuating parts.

determine an accurate description of the field. The difficulties when modelling turbulence arises from its characteristics features (Tennekes et al. 1972; Davidson 2001): irregularity, diffusivity, large Reynolds Numbers, three- dimensional flow, dissipation and continuum. The idea of dividing the velocity in a time-averaged and a fluctuating part is useful to obtain the corresponding models. If we want to solve the Navier-Stokes equation directly, a Direct Numerical Simulation (DNS) is required. These simulations would require a fine mesh and small time-steps in order to resolve all the turbulent scales. Hence, its use is in practice very limited due to the computational costs. A Large Eddy Simulation (LES) can be used to reduce the computational time. A spatial filtering is applied and then the eddies under the filter size are modelled and the others are directly solved.

A cheap approach is to use the Reynolds-Averaged Navier Stokes (RANS) method that considers the turbulent scales influence on the mean flow. The averaging of the Navier-Stokes equation results in the closure problem, as the Reynolds stress tensor related with the fluctuations appears. To close this system, different approaches can be taken as: algebraic eddy viscosity, one-equation, two-equation and Reynolds stress models.

Focusing the attention into the two-equation model, two quantities are considered, the turbulent kinetic energy and the dissipation rate. These quantities are related to obtain the Reynolds stress tensor. The κ-ε two-equation model for single-phase flow reads (Launder et al. 1974):

$$\frac{\partial}{\partial t}(\kappa_\mathrm{c}) + \nabla \cdot (\mathbf{U}_\mathrm{c}\kappa_\mathrm{c}) = \nabla \cdot \left[\left(\nu_\mathrm{c} + \frac{\nu_{t,\mathrm{c}}}{\sigma_\kappa}\right)\nabla\kappa_c\right] + \mathbf{R}_\mathrm{c} : (\nabla\mathbf{U}_\mathrm{c}) - \epsilon_\mathrm{c} \tag{3.42}$$

$$\frac{\partial}{\partial t}(\varepsilon_{\mathrm{c}}) + \nabla \cdot (\alpha_{\mathrm{c}} \mathbf{U}_{\mathrm{c}} \varepsilon_{\mathrm{c}}) = \nabla \cdot \left[\alpha_{\mathrm{c}} \left(\nu_{\mathrm{c}} + \frac{\nu_{t,\mathrm{c}}}{\sigma_{\varepsilon}} \right) \nabla \varepsilon_{c} \right] + \frac{\varepsilon_{\mathrm{c}}}{\kappa_{\mathrm{c}}} \Big(C_{1\varepsilon} \mathbf{R}_{\mathrm{c}} : (\nabla \mathbf{U}_{\mathrm{c}}) - C_{2\varepsilon} \varepsilon_{\mathrm{c}} \Big) \quad (3.43)$$

where turbulent Reynolds stress can read as:

$$\mathbf{R}_{\mathrm{c}} = \nu_{t,\mathrm{c}} \left(\nabla \mathbf{U}_{\mathrm{c}} + (\nabla \mathbf{U}_{\mathrm{c}})^{\mathrm{T}} - \frac{2}{3} \mathbf{I} (\nabla \cdot \mathbf{U}_{\mathrm{c}}) \right) - \frac{2}{3} \mathbf{I} \kappa_{\mathrm{c}} \quad (3.44)$$

In the equations below, $\nu_{t,\mathrm{c}}$, is the eddy viscosity:

$$\nu_{t,\mathrm{c}} = C_{\mu} \frac{\kappa_{\mathrm{c}}^2}{\varepsilon_{c}} \quad (3.45)$$

The values of the constants in the κ-ε equations are the default values found in Launder et al. (1974):

Table 3.1: Constant values of the κ-ε model

C_{μ}	$C_{1\varepsilon}$	$C_{2\varepsilon}$	σ_{κ}	σ_{ε}
0.09	1.44	1.92	1.0	1.3

In two-phase flow, the presence of the interface, influences the flow structure and consequently the turbulence determines the interfacial forces and for instance the dynamics of the bubbles. To the difficulties for turbulence modelling, the effect of the interface is added. The bubbles produce an *impulse* in the fluid producing a perturbation on the fluid and a wake with a complex turbulence structure. Most of these mechanisms are still unknown even at a microscopic level and is obviously a difficult task for modelling.

In the literature one can find studies related with the modelling of the wake itself (Vries 2001) or models for the modelling of the bubble induced turbulence (BIT). It will be also mentioned in this thesis: bubble pseudo-turbulence (BPT). Note that from a macroscopic point of view, the bubbles could in average act as a sink from some void fractions. But, every bubble generates local fluctuation because of its motion, then the terms *induced turbulence* or *turbulence produced* will be referred in this work to this effect. The term pseudo-turbulence is used as its nature is similar to the turbulence.

Two different approaches are commonly used to model the bubble turbulence (see Rzehak et al. (2013)): bubble-induced contribution to the effective viscosity as in Sato et al. (1975) and the addition of a bubble-induced source term arising from the averaging, to the transport equations of the turbulence model.

The model of Sato et al. (1975) considers in addition to the shear turbulence an additional bubble induced eddy viscosity defined as:

$$\nu_{ind,\mathrm{c}} = C_{\mathrm{ind}} \alpha_{\mathrm{d}} d_b |\mathbf{U}_{\mathrm{d}} - \mathbf{U}_{\mathrm{c}}|, \tag{3.46}$$

with a value of C_{ind} of 0.6.

Two-phase flow turbulence model are described in Kataoka et al. (1989), Morel (2016), and Troshko et al. (2001a). According to these models the interfacial effects are considered explicitly in the transport equations for these turbulent variables.

The total mixture turbulent kinetic energy is obtained by the summation of the κ_k-equation and considering the gas-phase turbulence negligible in comparison with the liquid-phase turbulence (Kataoka et al. 1989)). The following equation is obtained for κ_{c}:

$$\begin{aligned} \frac{\partial}{\partial t}(\alpha_{\mathrm{c}}\kappa_{\mathrm{c}}) + \nabla \cdot (\alpha_{\mathrm{c}}\mathbf{U}_{\mathrm{c}}\kappa_{\mathrm{c}}) = \nabla \cdot \left[\alpha_{\mathrm{c}} \left(\nu_{\mathrm{c}} + \frac{\nu_{t,\mathrm{c}}}{\sigma_\kappa}\right) \nabla \kappa_c\right] \\ + \alpha_{\mathrm{c}}\mathbf{R}_{\mathrm{c}} : (\nabla \mathbf{U}_{\mathrm{c}}) - \alpha_{\mathrm{c}}\epsilon_{\mathrm{c}} \\ - \mathbf{M}^{\mathrm{h}}(\mathbf{U}_{\mathrm{d}} - \mathbf{U}_{\mathrm{c}}) - (p_{\mathrm{d}} - p_{\mathrm{c}})\frac{\delta \alpha_d}{\delta t} - \gamma \Gamma a_I \end{aligned} \tag{3.47}$$

The three last terms in the RHS of Eq. 3.47 are related to the interfacial effects on the turbulence kinetic energy. The last two terms are related to the change of interfacial area or growth.

The turbulent dissipation rate equation used is based on the Kolmogorov's hypothesis (Pope 2000). Hence, the production and dissipation rates of ϵ_c are considered proportional to the production and dissipation rates of κ_{c} with a factor of ω_{c}=$\varepsilon_{\mathrm{c}}/\kappa_{\mathrm{c}}$ according to Launder et al. (1974). Conversely, the destruction of the turbulence produced by the interfacial effects must be related to the characteristic time scale of the pseudoturbulence produced by the bubbles (López de Bertodano 1998; Troshko et al. 2001a) with a dissipation frequency ω_b that needs to be modelled. The turbulence dissipation rate equation results:

$$\begin{aligned} \frac{\partial}{\partial t}(\alpha_{\mathrm{c}}\varepsilon_{\mathrm{c}}) + \nabla \cdot (\alpha_{\mathrm{c}}\mathbf{U}_{\mathrm{c}}\varepsilon_{\mathrm{c}}) = \nabla \cdot \left[\alpha_{\mathrm{c}} \left(\nu_{\mathrm{c}} + \frac{\nu_{t,\mathrm{c}}}{\sigma_\varepsilon}\right) \nabla \varepsilon_c\right] \\ + \omega_{\mathrm{c}}\Big(C_{1\varepsilon}\alpha_{\mathrm{c}}\mathbf{R}_{\mathrm{c}} : (\nabla \mathbf{U}_{\mathrm{c}}) - C_{2\varepsilon}\alpha_{\mathrm{c}}\varepsilon_{\mathrm{c}}\Big) \\ - \omega_b\Big(\mathbf{M}^{\mathrm{h}}(\mathbf{U}_{\mathrm{d}} - \mathbf{U}_{\mathrm{c}}) + (p_{\mathrm{d}} - p_{\mathrm{c}})\frac{\delta \alpha_d}{\delta t} + \gamma \Gamma a_I\Big) \end{aligned} \tag{3.48}$$

where $C_{1\varepsilon}$, $C_{2\varepsilon}$ and σ_ε are defined as in Launder et al. (1974) and Troshko et al. (2001a). In the literature, one can be found different dissipation frequencies of the production terms produced by the bubbles, ω_b. Morel et al. (1997) suggested Eq. 3.49. This is based on the relation of proportionality between interfacial turbulence production and dissipation of Elghobashi et al. (1983) and defining the characteristic time τ with the diameter of the bubble as the length scale (Morel et al. 1997; Yao et al. 2004b).

$$\omega_b = \frac{C_{3\varepsilon}}{\tau} = \frac{C_{3\varepsilon}}{(d_{32}^2/\varepsilon_\mathrm{c})^{\frac{1}{3}}} \tag{3.49}$$

The constant $C_{3\varepsilon}$ was set to 1.0 in Yao et al. (2004b) for adiabatic scenarios similar to the ones studied in this work. However, it varies depending on the scenario. Values of 1 and 0.6 were used for DEDALE (Grossetête 1995) and DEBORA (Manon et al. 2000) experiments respectively.

Troshko et al. (2001a) used the following equation to compute ω_b:

$$\omega_b = \left(\frac{2C_{vm} d_b}{3C_d |\mathbf{U}_\mathrm{d} - \mathbf{U}_\mathrm{c}|} \right)^{-1} \tag{3.50}$$

In Eq. 3.47 and Eq. 3.48 note that the $\mathbf{M}^\mathrm{h}$ term includes the contribution of all the interfacial forces. In practice, for TFM it is usually established the contribution of the drag force (Troshko et al. 2001a):

$$\mathbf{M}^\mathrm{h}(\mathbf{U}_\mathrm{d} - \mathbf{U}_\mathrm{c}) = \frac{3}{4}\frac{C_\mathrm{d}}{d_b}\alpha_\mathrm{d}\rho_\mathrm{c}|\mathbf{U}_\mathrm{d} - \mathbf{U}_\mathrm{c}|^3 > 0 \tag{3.51}$$

Morel et al. (1997) proposed a similar contribution for the term of production of turbulence, including the virtual mass force:

$$S_\kappa = (\mathbf{M}_\mathrm{d,D} - \mathbf{M}_\mathrm{d,VM}) \cdot \mathbf{U}_\mathrm{r}, \tag{3.52}$$

Lee et al. (1989) used in their predictions the source terms:

$$S_\kappa = \alpha_\mathrm{d} C_{1\kappa} \frac{\partial p}{\partial z} |\mathbf{U}_\mathrm{r}|, \tag{3.53}$$

$$S_\varepsilon = C_{3\varepsilon} S_\kappa \frac{\varepsilon_\mathrm{c}}{\kappa_\mathrm{c}}, \tag{3.54}$$

where

$$C_{1\kappa} = 0.03 - 0.344 \times 10^{-5} Re_{\mathrm{c}} + 0.243/(1 + e^{(Re_{\mathrm{c}} - 60{,}000)/2{,}000}). \tag{3.55}$$

The constant value for $C_{3\varepsilon}$ is assumed to be equal to $C_{2\varepsilon}$ as discussed in Lee et al. (1989) for bubbles rising freely with gradients of $\mathbf{U}_{\mathrm{c}}$, κ_{c} and ε_{c} considered to be zero.

3.6 Turbulence on interfacial forces

In a turbulent flow, the fluctuating component of the carrier phase velocity has an influence in the force acting on a bubble. Essentially they are captured in turbulent eddies and moved with it. Simulations like CFD-DEM can consider the turbulent effects in the interfacial forces while the fluctuations are computed. In TFM, the turbulence effect on the interfacial forces are usually neglected or are considered only in the drag through the turbulent dispersion force. The influence of the turbulence on the interfacial forces was evaluated by Behzadi et al. (2001) for mixing layer and sudden expansion scenarios concluding that the turbulent effects on lift and virtual mass forces are negligible for these cases. However, in the literature, there is no many investigations showing its influence in other systems. Indeed, when the lateral forces are predominant as in the case of wall-bounded systems we may expect an important influence on the lift and wall interaction effects.

Burns et al. (2004) presented the Favre Averaged Drag (FAD) model for turbulent dispersion force. This was derived by performing a time averaging to the phase averaged equations obtained from ensembled averaging. With this model, phase-weighted variables are used. The Favre averaging results in the following time-velocities:

$$\widetilde{\mathbf{U}}_{\varphi} = \overline{\mathbf{U}_{\varphi}} + \overline{\mathbf{u}''_{\varphi}} \tag{3.56}$$

$$\overline{\mathbf{u}''_{\varphi}} = \frac{\overline{\mathbf{u}'_{\varphi}\alpha'_{\varphi}}}{\alpha_{\varphi}} \tag{3.57}$$

The last term, describes the relation between the void fraction fluctuations due to the velocity fluctuations.

The averaging of the instantaneous drag force is performed and the time averaged drag expressed in terms of Eq. 3.56, after linearisation and including the velocity fluctuations and area density fluctuations (Burns et al. 2004), results:

$$\mathbf{M}_{\mathrm{d,t}} = C_i(\widetilde{\mathbf{U}}_d - \widetilde{\mathbf{U}}_c) + \mathbf{M}_{\mathrm{TD}} \tag{3.58}$$

where C_i is defined as:

$$C_i = \frac{1}{8} C_d a_I \rho_{\mathrm{c}} |\mathbf{U}_{\mathrm{d}} - \mathbf{U}_{\mathrm{c}}|, \tag{3.59}$$

where a_I is the interfacial area concentration. Note that this results in a volumetric force.

After simplifications derived from the consideration of general dispersed multiphase flow, the turbulent dispersion term can be expressed in a general form as:

$$\mathbf{M}_{\mathrm{TD}} = C_i\Big(\frac{\overline{\alpha'_d u'_{\mathrm{d}}}}{\alpha_{\mathrm{d}}} - \frac{\overline{\alpha'_c u'_{\mathrm{d}}}}{\alpha_{\mathrm{c}}}\Big) \tag{3.60}$$

Although this expression should be manipulated to be applied to TFM, could be specially useful for CFD-DEM simulations (or other method relying on in a representation of the bubble) as we can transform the turbulent effects considered inherently in the method to a turbulent force for a comparison between the approaches.

If the eddy diffusivity hypothesis is applied to Eq. 3.60, the following equation is obtained:

$$\mathbf{M}_{\mathrm{TD}} = C_i \frac{\mu_t}{\sigma_\alpha}\Big(\frac{\nabla\alpha_{\mathrm{c}}}{\alpha_{\mathrm{d}}} - \frac{\nabla\alpha_{\mathrm{d}}}{\alpha_{\mathrm{c}}}\Big), \tag{3.61}$$

where σ_α is the turbulent Prandtl number for volume fraction dispersion. Usually assumed equal to unity.

Finally, for the specific case of dispersed two-phase flow, the FAD model for turbulent dispersion force is:

$$\mathbf{M}_{\mathrm{TD}} = -C_i \frac{\mu_t}{\sigma_\alpha}\Big(\frac{1}{\alpha_{\mathrm{d}}} - \frac{1}{\alpha_{\mathrm{c}}}\Big)\nabla\alpha_{\mathrm{d}} \tag{3.62}$$

Reeks (1991) and Reeks (1992) derived a turbulent diffusion force for TFM and López de Bertodano (1992) and López de Bertodano (1998) derived the equation

in terms of a two-phase turbulence model κ-ε. This force is called from now on, the turbulent dispersion force and considers the effect of the turbulent fluctuations in the carrier phase on the dispersed phase. The formulation of López de Bertodano (1992):

$$\mathbf{M}_{\mathrm{TD}} = -\rho_{\mathrm{c}} C_{\mathrm{TD}} \kappa_{\mathrm{c}} \nabla \alpha_{\mathrm{d}} \tag{3.63}$$

Originally a value of 0.1 for C_{TD} was chosen by López de Bertodano (1992). However, and in a later contribution, López de Bertodano (1998) proposed the following correlation:

$$C_{\mathrm{TD}} = C_{\mu}^{1/4} \frac{1}{St(1+St)}, St = \frac{\tau_d}{\tau_e} \tag{3.64}$$

The turbulent Stokes number, St, is defined as the ratio of the time constant of the bubbles ($\tau_d = 4d_b/(3C_{\mathrm{D}} |\mathbf{U}_{\mathrm{r}}|)$) and the effective time constant of the turbulent eddies obtained from:

$$\frac{1}{\tau_e} = \sqrt{\frac{1}{\tau_t^2} + \frac{1}{\tau_R^2}} \tag{3.65}$$

This force is in fact similar to the one of Burns et al. (2004) in Eq. 3.62. This can be expressed as Eq. 3.65 and the only difference is in the turbulent dispersion coefficient.

The turbulent dispersion model using Favre averaging is performed in Burns et al. (2004) only for the drag force. Previously, Behzadi et al. (2001) used a turbulent description of interfacial forces as lift, virtual mass in addition to the drag.

The average turbulent lift force can be obtained applying the same averaging and assumptions as with the drag force to the lift force (Behzadi et al. 2001). The first term represents the mean part and the others the turbulent in the same way as applied before for drag force:

$$M_{\mathrm{l,t}} = \mathrm{C_l}\rho_{\mathrm{c}}\Bigg(\alpha_{\mathrm{d}}\widetilde{\mathbf{U}}_{\mathrm{r}} \times (\nabla \times \widetilde{\mathbf{U}}_{\mathrm{c}}) - \overline{\mathbf{u}''_{\mathrm{c}}} \times (\nabla \times \widetilde{\mathbf{U}}_{\mathrm{c}}) + \alpha_{\mathrm{d}}\widetilde{\mathbf{U}}_{\mathrm{r}} \times (\nabla \times \overline{\mathbf{u}''_{\mathrm{c}}}) + \\ + \alpha_{\mathrm{d}}(C_t - 1)\Big(\nabla k - (u'_{\mathrm{c}} \cdot \nabla)u'_{\mathrm{c}}\Big) + \alpha_{\mathrm{d}}(\overline{\mathbf{u}''_{\mathrm{d}}} - \overline{\mathbf{u}''_{\mathrm{c}}}) \times (\nabla \times \overline{\mathbf{u}''_{\mathrm{c}}}) + \\ + \widetilde{\mathbf{U}}_{\mathrm{r}} \times (\nabla \times (\overline{\alpha}_{\mathrm{c}}\overline{\mathbf{u}''_{\mathrm{c}}})) - \widetilde{\mathbf{U}}_{\mathrm{r}} \times \overline{\nabla\alpha'_{\mathrm{d}} \times u'_{\mathrm{c}}} - (\overline{\alpha}_{\mathrm{d}}\overline{u''_{\mathrm{d}}} + \overline{\alpha}_{\mathrm{c}}\overline{u''_{\mathrm{c}}}) \times (\nabla \times \overline{\mathbf{u}''_{\mathrm{c}}}) + \\ + \overline{u''_{\mathrm{c}}} \times (\nabla \times (\overline{\alpha}_{\mathrm{c}}\overline{\mathbf{u}''_{\mathrm{c}}})) - \overline{\mathbf{U}''_{\mathrm{r}}} \times \overline{\nabla\alpha'_{\mathrm{d}} \times u'_{\mathrm{c}}}\Bigg) \quad (3.66)$$

In this equation, in addition, are usually neglected the double correlation terms $\overline{(u'_{\mathrm{c}} \cdot \nabla)u'_{\mathrm{c}}}$ and $\overline{\nabla\alpha'_{\mathrm{d}} \times u'_{\mathrm{c}}}$ as in Behzadi et al. (2001), Chahed et al. (1998), and Oliveira (1992).

The average turbulent virtual mass force will result:

$$M_{\mathrm{vm,t}} = C_{\mathrm{vm}}\rho_{\mathrm{c}}\Bigg(\alpha_{\mathrm{d}}\Big(\frac{D_{\mathrm{d}}\widetilde{\mathbf{U}}_{\mathrm{c}}}{Dt} - \frac{D_{\mathrm{c}}\widetilde{\mathbf{U}}_{\mathrm{c}}}{Dt}\Big) - \frac{D_{\mathrm{c}}\overline{\mathbf{u}''_{\mathrm{c}}}}{Dt} - (\overline{\mathbf{u}''_{\mathrm{c}}} \cdot \nabla)\widetilde{\mathbf{U}}_{\mathrm{c}} + \\ + \overline{\mathbf{u}''_{\mathrm{c}}\nabla \cdot \mathbf{u}''_{\mathrm{c}}} - \nabla \cdot \overline{\alpha_{\mathrm{d}}\mathbf{u}''_{\mathrm{c}}\mathbf{u}''_{\mathrm{c}}} + \nabla \cdot \overline{\alpha_{\mathrm{d}}\mathbf{u}''_{\mathrm{d}}\mathbf{u}''_{\mathrm{d}}}\Bigg) \quad (3.67)$$

3.7 Size distribution modelling

According to the particle size, a dispersed multiphase flow can be classified as monodisperse (uniform size) or polydispese (non-uniform size) flow. In many simulations we can assume the bubble size is uniform either because the population dispersion of the size is small enough to consider an unique size, or because considering an average size of the population does not compromise on the quality of the results. However, in some simulations we need to consider the flow as polydisperse to account for the effect of the different sizes in the modelling.

In bubbly flows, the bubble size is an important parameter to numerically predict the flow characteristics and it is needed to adequately describe the size distribution in space and time, which implies a greater complexity of the models, specially in lower resolution level methods as Two-Fluid Model.

In case of TFM, the evolution of the bubble size distribution in space and time is described by means of a PBE (Ramkrishna 2000) derived through the consideration

of averaging the statistical Boltzmann equation. This equation based on a length-based number density function (NDF) of the dispersed phase $n(L;\mathbf{x},t)$ reads:

$$\frac{\partial n(L)}{\partial t} + \nabla \cdot (n(L)\mathbf{U}_\mathrm{d}) = -\frac{\partial}{\partial L}(G(L)n(L)) + B(L) - D(L) \tag{3.68}$$

where $G(L)$ is the growth rate, $B(L)$ and $D(L)$ are, respectively, the birth and the death rates of bubbles of size L due to coalescence and breakage. It is worth noticing that these terms depend also on the position and on time, even if this dependency was not explicitly indicated in the equation to keep the notation simpler. A simplification of the PBE implies that the velocity $\mathbf{U}_\mathrm{d}$ is the average velocity of the dispersed phase, obtained from the momentum equation of the TFM. Using this velocity represents an approximation, as assume that all the bubbles in a given computational cell move at the same velocity. This is reasonable only for bubbles that only slightly deviate from the average size on that cell.

Nevertheless, analytical methods to solve the PBE require and extensive computational effort and for this reason numerical methods are usually applied resolving the PBEs. The pioneering technique consisted on solving this numerically, discretising the population balance equation (DPB) or the class method (CM) (Kumar et al. 1996a; Kumar et al. 1996b) with the potential disadvantage of requiring a high number of equations.

An approximation to solve this with a reduced number of equations is to transport equations related to some statistical moments or Method Of Moments (MOM) that describe the two-phase flow characteristics. These are the statistical moments. Particle number density, average particle volume, interfacial area concentration, and local volume fraction correspond to zero-order moments through third-order moments. The particles are considered as nodes that compose a discretized probability density function. Each node consists of an abscissa and weight. The weight defines the probability of finding a particle that has the value of its abscissa. The quadrature approximation can be dynamic and the number of nodes may decrease or increase to fit complex probability density functions. This method is usually used to reduce the computational requirements without compromising accuracy (McGraw 1997; Marchisio et al. 2003a; Marchisio et al. 2003b; Sanyal et al. 2005). Compared with discrete methods to solve the PBE as classes method (CM) or Multiple Size Group (MUSIG) (Lo 1996), MOM can consider a wide range of bubble sizes with a reduced number of equations. Different methods of MoM exists as Quadrature Method Of Moments (QMOM) and its direct (DQMOM) or conditional (CQMOM) versions. QMOM was the pioneering, with this approach a set moments are transported and the weights and abscissas reconstructed through an eigenvalue solution. DQMOM is a simplification of QMOM, with this approach instead of transporting the moments, the weights and abscissas are directly considered in the equations, avoiding the moment reconstruction and inversion of

QMOM. As a result of the process, robustness can be lost. Lastly, CQMOM provides a general approach as can be considered as the multivariate extension of QMOM.

In the literature we can found simulations of bubbly flows with a two-fluid model using DQMOM (Cheung et al. 2013; Silva et al. 2011) and CQMOM tested by Buffo et al. (2013) for a rectangular bubble column.

A cheapest approximation of the PBE in terms of computational time can be obtained solving a one-group Interfacial Area Transport Equation (IATE) (Kocamustafaogullari et al. 1983). With IATE, the PBE is integrated analytically. The IATE is a very interesting model and may be considered as a simplified version of a PBM in which only one additional transport equation, an IAC transport equation, is usually used. Events such as coalescence, breakage and nucleation can be modelled with the IAC and PBM models. The PBM ideally captures all these phenomenons, but is computationally expensive since several transport equations need to be solved.

On the other hand, in CFD-DEM, the bubbles can be represented individually or by parcels. If each bubble is represented as an individual entity any additional method is needed to represent the size of the bubbles. If parcels are considered, particles with common properties are defined as a group. Note that, the break up and coalescence processes can be modeled in a deterministic way to compute the drainage time.

3.8 Non-linearity effects on interfacial forces

The simulation of a two-phase flow system, requires a consistent choice of the formulation of the approach, the modelling of the interfacial forces and the approximation used for the bubble size distribution. A classical formulation of TFM usually involves the consideration of a homogeneous flow, turbulent effects not considered in all the interfacial forces and an ad-hoc wall force to compensate the lift force.

When homogeneous flow is considered and the PBE is solved approximately with IATE, MOM or CM, a unique velocity field for the dispersed phase is assumed. The PBE provides the bubble size distribution field but a mean bubble size (usually the Sauter mean diameter) is used to compute the interfacial forces. This is accurate when the forces can be approximated as a linear function of the diameter. The correlations to model the interfacial forces described are usually far from the linear description that is needed with these assumptions. This is schematized in Fig. 3.3, for several scenarios and using the drag coefficient of Eq. 3.13 and lift coefficient of Eq. 3.25. The mean size of the BSD at the inlet is shown for each experiment. An

approximate range of bubble sizes that concerns the sizes found in the experiments is marked.

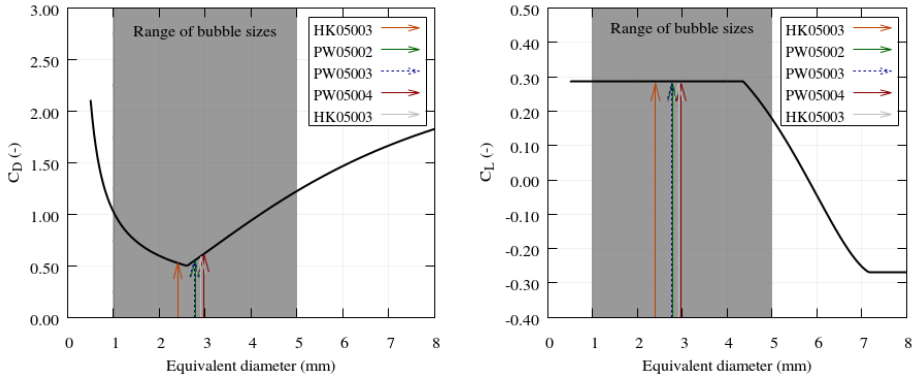

Figure 3.3: Drag and lift coefficients with arrows showing the mean size for different conditions.

In the figure, we can appreciate that mean sizes of the experiments are close to the minimum, in the limit between the drag force dominated by the Reynolds and Eötvös numbers. This means that considering a mean size will result in an underestimated drag coefficient, in contrast to consider the whole BSD. For the lift force coefficient, the transition to negative values starts around 4.3 mm under these conditions. Then, an overestimated lift force will be obtained by considering a mean size as the Eötvös dominated regime will not be taken into account.

The terminal velocity of the bubbles can be obtained analytically from the balance of drag and buoyancy:

$$V_t = \sqrt{\frac{4(\rho_c - \rho_d)gd_b}{3C_d\rho_c}} \tag{3.69}$$

Then we represent for the experiments PW05003 and PW05004 the terminal velocity as a result of apply the drag coefficient of Tomiyama for contaminated systems (Eq. 3.12):

In the same figure we show the BSD at the low and top ports from the measurement described in Section 2.6. At first glance the effects of the non-linearity of the drag coefficients are appreciated. In addition, as a result of the expansion of the bubbles a different BSD is given at the top. This means that the proportion of bubbles that are dominated by the Reynolds term of the drag coefficient, will decrease as the bubbles grow. It results in an axial void fraction dependent on the BSD,

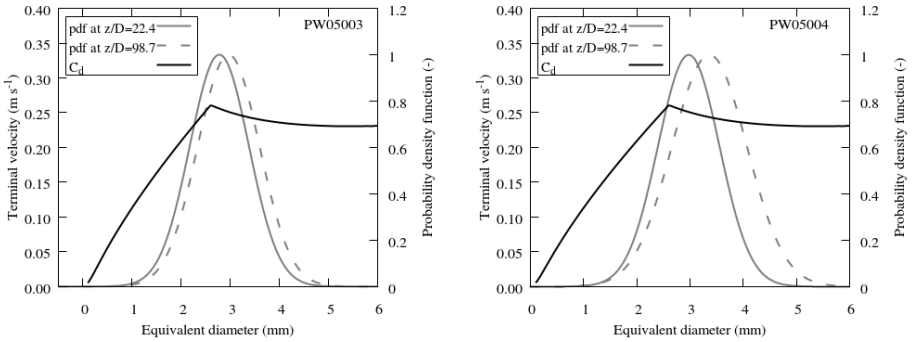

Figure 3.4: Terminal velocity from the Tomiyama drag (Eq. 3.13) correlation for contaminated systems and experimental bubble size distribution at low and top heights.

consequently the axial cross-section average void fraction will evolve axially in a non-linear manner.

In addition, the non-linearity is also present in the bubble-wall contact forces, as revealed by experimental observations and methods.

Chapter 4

Volume Of Fluid method (VOF)

The simulation of bubbles using an interfacial method as VOF are used in the present work to obtain high resolution results of single bubbles. This data is of interest to perform a later validation with other methods at lower resolution level as CFD-DEM. Two scenarios are investigated in this chapter: initially spherical bubbles at rest, and bubbles generated due to growth and detachment from an orifice. The continuous phase velocity fields, terminal velocity of the bubble, bubble shape and size are obtained and compared with experiments. Finally, the path and wake of the bubbles is analysed.

4.1 Introduction

The interface interaction between two different fluid phases is a complex process with many challenges involved as breakup, coalescence or the influence of contaminants. The numerical methods for interface tracking have provided historically a high level of detail for simulating two-fluid interfacial flows. These permit to resolve the interface obtaining a detailed description of the flow around the bubble at the expense of computational resources.

The simulations with IM are useful to understand the behaviour of bubbles with size in the order of those present in bubbly flow, providing important feedback to lower resolution level simulations. Simulations at a microscopic level description of the dispersed phase are very enlightening though limited to small domains and number of bubbles. Particularly interesting are the works of Dijkhuizen et al. (2010b) who studied the bubble behaviour of isolated bubbles, Roghair et al. (2013) who presented results of simulations for dense bubbly flow up to 31 bubbles

or Tryggvason et al. (2009) who simulated a vertical channel in a periodic domain with around 36 bubbles in the turbulent downflow case.

The rising of individual bubbles has been extensively investigated in the past. Several researches performed simulations with VOF about bubbles rising. These simulations consisted on a bubble initially spherical in a domain. Chen et al. (1999b) studied in its work using VOF, an isolated initially spherical bubbles rising in a liquid with Re = 100 and Bo = 50, later Hua et al. (2007) expanded the study in viscous liquid to a wide range of bubbles with Re up to 150 and Bo up to 200. Similar simulations are performed in Dijkhuizen et al. (2005). Other researches were focused to model the formation and growth of a bubble (Kumar et al. 1970; Jamialahmadi et al. 2001; Cano-Lozano et al. 2017). In the literature several analytical and numerical models (Oguz et al. 1993) can be found. Simulations with 2D-VOF with air injection from an orifice (Islam et al. 2015) were also performed.

The results obtained with these simulations were generally accurate, and therefore this technique was used in this work to obtain results that will be used later to compare the performance of the CFD-DEM. To understand better the bubble dynamics, in this chapter we study the rising of the bubble from the injection. Then, through this scenario one can compare the formation process and the perturbation of the fluid field in order to validate the model. In addition, after the detachment of the bubble, the path of the bubbles is investigated in order to study the path instabilities and the interactions with the wake produced. The path of the bubbles has been classified by the different authors as rectilinear, helical (spiraling) or zigzaging. The rectilinear path is followed by small bubbles that remain almost spherical. The reasoning behind what makes the bubble to separate from an ideal path has been unknown for years. This phenomena is referred as Leonardo's paradox by Prosperetti (2004) because of the observation recorded by Leonardo da Vinci. Different authors noted a spiralling motion of the bubbles and determining critical criteria for the onset of the instability. It is explained nowadays due to a two-threaded wake (Mougin et al. 2001; Vries 2001; Prosperetti 2004; Shew et al. 2005) of opposite direction produced by the bubbles and resulting in a wake-induced lift. Mougin et al. (2001) investigated numerically the path instability considering the bubble as a spheroidal body of fixed shape showing a double threaded wake for rectilinear, zigzag and spiral path. Observations shown by Vries (2001) provide an interesting experimental investigation of the path and wake of bubbles. The same reference provides an interesting review and findings about path instabilities. Shew et al. (2005) presented the possible mechanism for the onset of zigzag and helical instability. Tripathi et al. (2015), studied the rise of an initially static and spherical bubble with numerical results using Gerris (Popinet et al. 2003) showing path instabilities, the terminal velocity and the path trajectory of bubbles in the range of Ga from 70 to 100 and Eo from 0.5 to 10. Recently, Cano-Lozano et al. (2015) and Cano-Lozano et al. (2016) performed 26 DNS of

deforming bubbles in the regime close to the transition to path instability, rising in still liquid, with Ga from 60 to 350 and Eo from 0.1 to 10.

In summary, this chapter contains the description of the mathematical formulation, the modelling and setup of the case, a study of the bubble growth, formation and detachment and bubble size after detachment for different gas flow rates, perturbation flow field after detachment and study of the bubble wake path and instability.

4.2 Mathematical formulation

The VOF technique is based on a whole-domain formulation of the Navier-Stokes. Thus, the differential equations apply to the whole domain occupied using the transport of the volume fraction field and the material properties. In general, it relies on the capability of the advection method of the volume fraction.

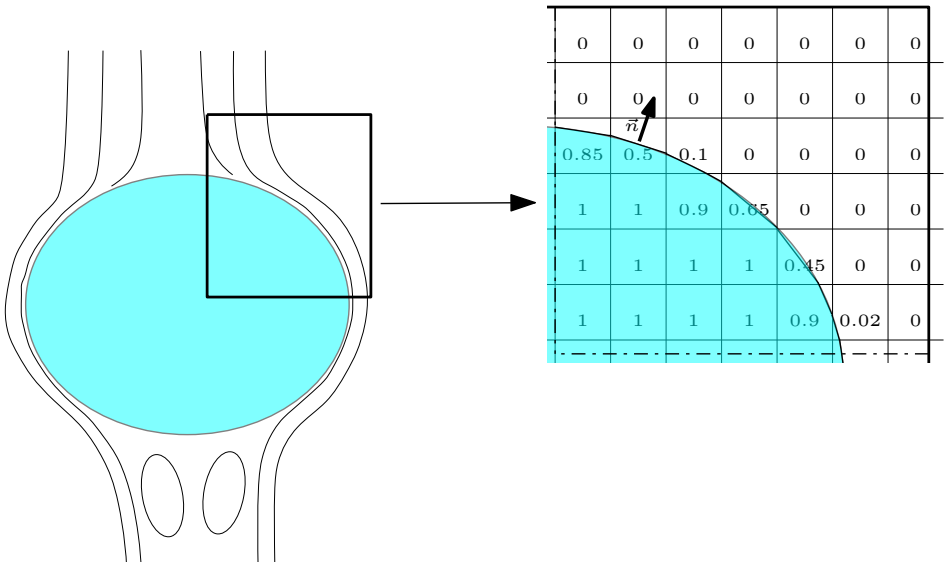

Figure 4.1: Schematic representation of the VOF and the interface capturing.

The VOF method solves the momentum (4.2) and continuity (4.1) equations for one field, being these equations the same for both phases. The volume fraction of the two fluids are used to calculate the weighted physical properties. The

mass conservation equation for both phases and the interface can be expressed as Prosperetti et al. (2007):

$$\nabla \cdot \mathbf{U} = 0, \tag{4.1}$$

and the Navier-Stokes momentum equation:

$$\frac{\partial \rho \mathbf{U}}{\partial t} + \nabla \cdot (\rho \mathbf{U}\mathbf{U}) = -\nabla p + \nabla \cdot \mu(\nabla \mathbf{U} + \nabla \mathbf{U}^T) + \rho \mathbf{g} + \mathbf{F_s}, \tag{4.2}$$

where $\mathbf{F_s}$ is the surface tension force. The surface tension force is accounted by the Continuum Surface Force model (CSF) solved using the properties at the interface. In the code, this is calculated at reconstructed surfaces from the transport of the volume fraction, knowing the surface tension between phases and the geometry data of the interface. This force reads:

$$\mathbf{F_s} = \sigma \kappa(x) \mathbf{n}, \tag{4.3}$$

being $\mathbf{n}$ the unit vector normal to the interface obtained by:

$$\mathbf{n} = \frac{\nabla \alpha}{|\nabla \alpha|}, \tag{4.4}$$

and κ the curvature of the interface:

$$\kappa(x) = \nabla \cdot \mathbf{n}. \tag{4.5}$$

The fluid fraction, α, of each cell is computed from the following transport equation:

$$\frac{\partial \alpha}{\partial t} + \nabla \cdot (\alpha \mathbf{U}) = 0 \tag{4.6}$$

Details about the numerical solution of this method can be found in Hirt et al. (1981) and Prosperetti et al. (2007).

4.3 Modelling and setup

The domain for the simulation is a square channel with dimensions $21 \times 21 \times 100$ mm. At the bottom of the domain the air is injected from a nozzle of different diameters. A nozzle edge of 2 mm is defined to maintain the same conditions of wettability as in the experiments. A bubble is produced from the detachment with a given radius and detachment position. This is used to define a hypothetical scenario where the bubble is initially spherical and at rest, at the beginning of the simulation. Both scenarios are schematised in Fig. 4.2a and Fig. 4.2b. For the nozzle case the air is injected with a uniform velocity at the bottom of the nozzle. The bubbles are generated through the different stages of the injection: expansion, elongation and detachment. In addition, from a given case we analyse the results of a simulation with an initial spherical bubble. The simulation consisted of the same rectangular domain with a bubble defined at the same position with the given equivalent diameter and position of the bubble detached.

In Table 4.1 we summarise the simulations that were defined for this work. The type of the simulation is labelled as "Nozzle" or "Sphere" depending on the way to introduce the air in the system. Different turbulence models are tested and labelled as Large Eddy Simulation (LES) or Reynolds Averaged Simulations (RAS) .

Table 4.1: Conditions used for the simulation.

Label	Type	Turb. model	Q_g ($\mathrm{cm^3\,s^{-1}}$)	d_0 mm	d_{eq} mm	B_o
N1	Nozzle	LES	0.1875	2	4.10	2.29
S1	Sphere	LES	-	-	4.10	2.29
N2	Nozzle	LES	0.75	2	4.48	2.7
N3	Nozzle	LES	0.375	4	5.08	3.5
N4	Nozzle	LES	0.75	4	5.37	3.9
N5	Nozzle	LES	1.5	4	5.89	4.7
S5a	Sphere	LES	-	-	5.89	4.7
S5b	Sphere	RAS	-	-	5.89	4.7
N6	Nozzle	LES	3	4	6.63	5.9

The phyisical properites of air and water are selected according to the experiments of Dietrich et al. (2013b) and Dietrich et al. (2013a) as shown in Table 4.2.

Table 4.2: constant properties at temperature of 293 K

ρ_c ($\mathrm{kg\,m^{-3}}$)	ρ_d ($\mathrm{kg\,m^{-3}}$)	γ ($\mathrm{N\,m^{-1}}$)
998	1.205	0.073

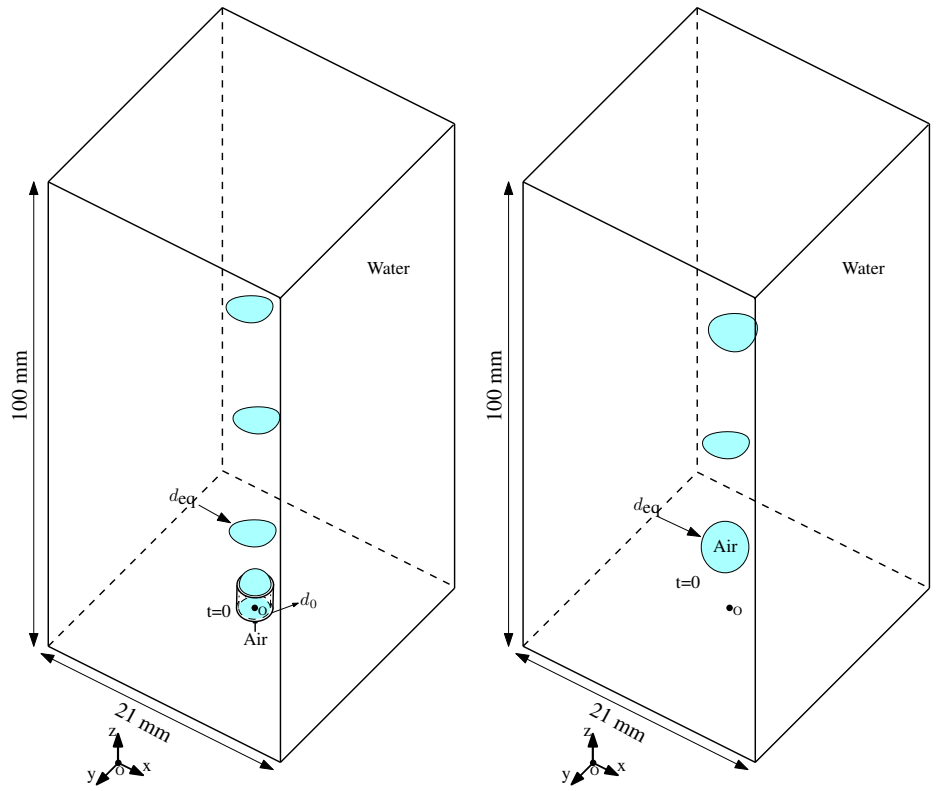

(a) Nozzle **(b)** Sphere

Figure 4.2: Configuration for the VOF simulations depending on the way to introduce the air.

The solver interFoam of the OpenFOAM® version 4.x is used for these simulations. A fixed regular mesh was created using the blockMesh tool. The mesh was treated with the OpenFOAM® utilities for mesh manipulation to create the nozzle. As a result, a mesh of around 39 million of cells was created. Fig. 4.3 shows an image of the mesh of the domain and the mesh representing the bubble for a given time step.

The time step is dynamic and based on a Courant number restriction with a maximum value of 1. In this work the use of a fixed mesh was preferred instead of a dynamic or adaptive mesh. Although dynamic mesh based methods can usually provide a reduction in computational time, the computation of adaptive mesh can produce very small cells leading to really small time steps if the simulation is dependent on the Courant number. In addition, the mesh defined each time step

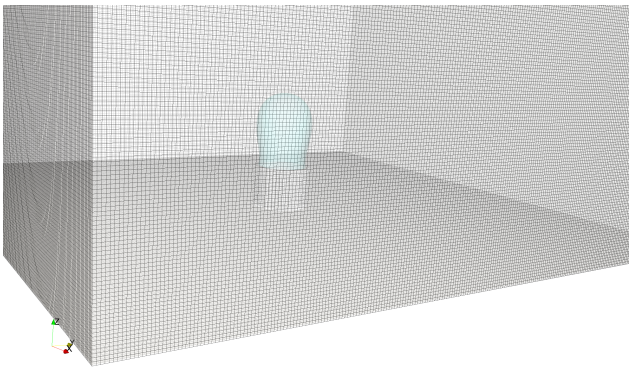

Figure 4.3: Mesh representation.

can solve the interface refining the region near the interface. It is difficult to define each time step a proper mesh to capture the turbulence structure that take place by the bubble path. For instance, the production and decay of the turbulence on the back of the bubble.

Different turbulence models are used to investigate the influence of the turbulence in the bubble velocity and path. In particular the Smagorinsky subgrid model is used for LES and a κ-ε turbulence model is employed for RAS.

The simulations were run in a Intel(R) Xeon(R) CPU E5-2450 @2.10GHz using 16 processors in a decomposed domain with the Scotch algorithm (Pellegrini et al. 1996). The case was run until the bubble reached the top of the domain for the sphere tests, except for N5 that was run longer as the first two bubbles coalesced. The data is stored each 0.0025 seconds generating a total data of around 500 GB for each case. The simulations required a wall-clock time of around 10 days excluding the time for reconstructing the case and the post-processing.

4.4 Bubble formation an detachment

The growth and detachment of a bubble is analysed by studying the bubble formation, including the dynamics of the formation and the bubble size after the detachment. An accurate representation of this process is a main indicator that the calculated surface tension force was calculated with accuracy.

The resulting bubble equivalent diameter was obtained from the volume of the bubble after the detachment. Jamialahmadi et al. (2001) developed a correlation to predict the bubble size that results from the air injection in a submerged nozzle

in different solutions. The correlations were obtained using The Radial Basis Function (RBF) neural network architecture for predicting the bubble diameter:

$$\frac{d_b}{d_0} = \left[\frac{5.0}{Eo_0^{1.08}} + \frac{9.261 Fr^{0.36}}{Ga^{0.39}} + 2.147 Fr^{0.51}\right]^{\frac{1}{3}} \tag{4.7}$$

The correlation depends on the following dimensionless numbers in terms of the injection orifice:

$$Eo_0 = \frac{\rho_c g d_0^2}{\gamma} \tag{4.8}$$

$$Fr = \frac{U_o^2}{d_0 g} \tag{4.9}$$

$$Ga = \frac{\rho_c^2 d_0^3 g}{\mu_c^2} \tag{4.10}$$

In the simulations, the bubble volume is computed from the data of volume fraction and the volume of each cell. The bubble can be represented using an iso-surface which gives the information only of the bubble surface. In addition, a threshold filter can be applied to select specific cells with presence of the air phase. Fig. 4.4 shows an example of the volumes that represents a bubble having values of volume fraction greater than 0 and a iso-surface plotted by a value of volume fraction of 0.5.

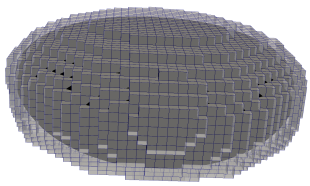

Figure 4.4: Bubble representation with iso-surface and threshold filters of ParaView.

For the selected cells with the threshold filter, the following expression is used to obtain the equivalent diameter over the cells forming the bubble.

$$d_{eq} = \left(\frac{6}{\pi}\sum(\alpha V_{cell})\right)^{\frac{1}{3}} \tag{4.11}$$

The results for the different air flow rates specified in Table 4.1 are shown in Fig. 4.5. An error band is shown, together with the correlation as an absolute mean average error of 3.12% between predicted and experimental data was reported in the correlation of Jamialahmadi et al. (2001). Experimental data from Dietrich et al. (2013a) is also included in the figure. The work performed by Dietrich et al. (2013a) noted an average error of 8.13% from 94 experimental data. In this figure a good trend of the simulated values is appreciated. The mean absolute error for the diameters obtained in the simulation is of 1.94%. The error band represents the deviation of the correlation with the experimental measures.

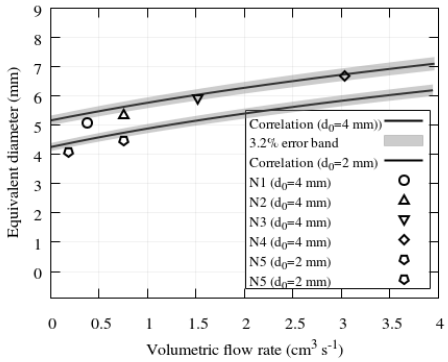

Figure 4.5: Equivalent bubble diameter and correlations for nozzle diameters of 2 and 4 mm.

The bubble shape and size of the simulations shown above are represented in Fig. 4.6 for images of bubbles when first bubbles reaches an equivalent position for the different flow rates.

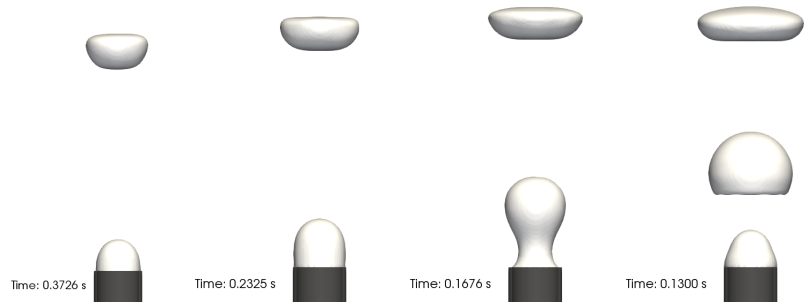

(a) N3 d_{eq}=5.08**(b)** N4 d_{eq}=5.37 mm**(c)** N5 d_{eq}=5.89 mm**(d)** N6 d_{eq}=6.63 mm mm

Figure 4.6: Bubble iso-surfaces for different gas flow rates for a nozzle of 4 mm.

Finally, for N5 we compare in Fig. 4.7 the evolution during the bubble formation, comparing the results obtained with high-speed camera in Dietrich et al. (2013a) for the same air flow rate. The three stages commented in the literature are appreciated in the experiments and numerical results.

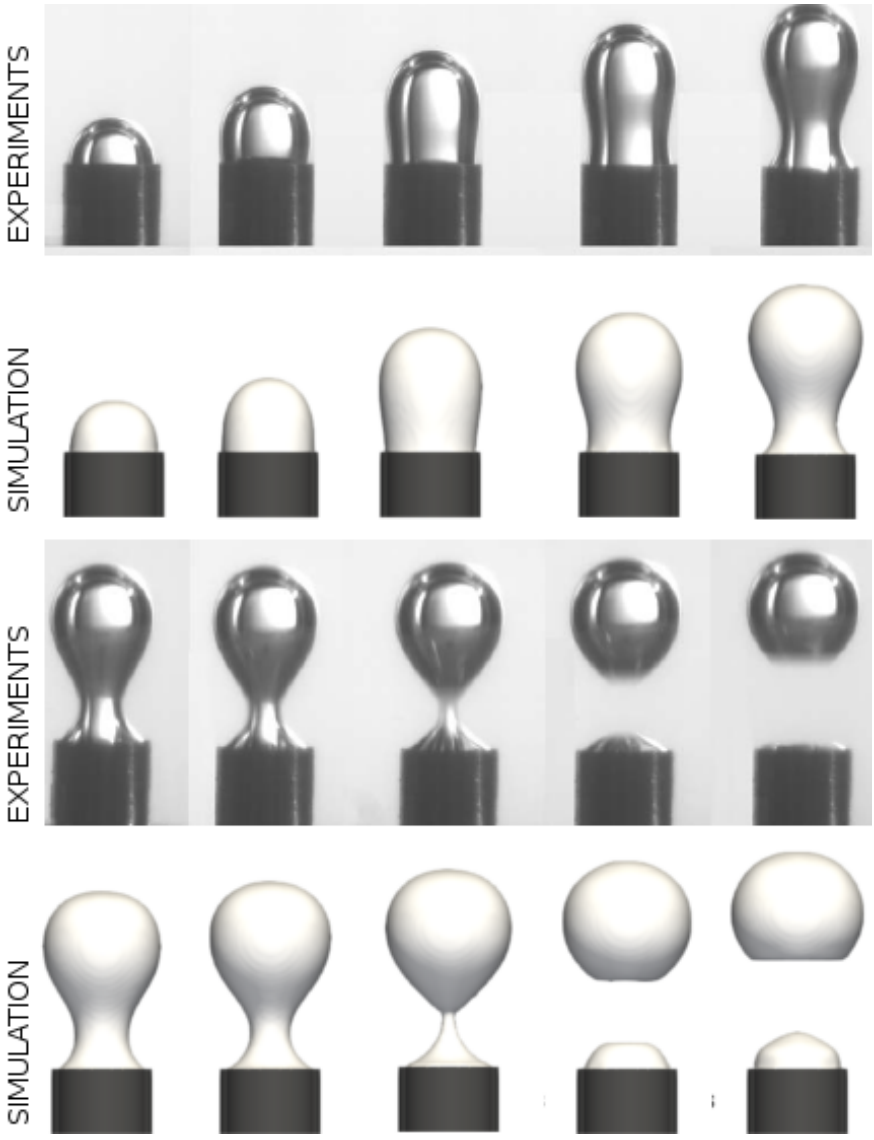

Figure 4.7: Experimental and numerical comparison of different stages of bubble growth and detachment. Experiments reproduced from Dietrich et al. (2013b) with permission of Springer.

4.5 Flow field perturbation after detachment

The influence of the bubble on the liquid is studied first as it is a key factor that defines the bubble dynamics, in terms of bubble path and velocity. The flow field around the bubble is shown representing the velocity vectors in a middle plane and comparing with the experiments measured with PIV in Fig. 4.8.

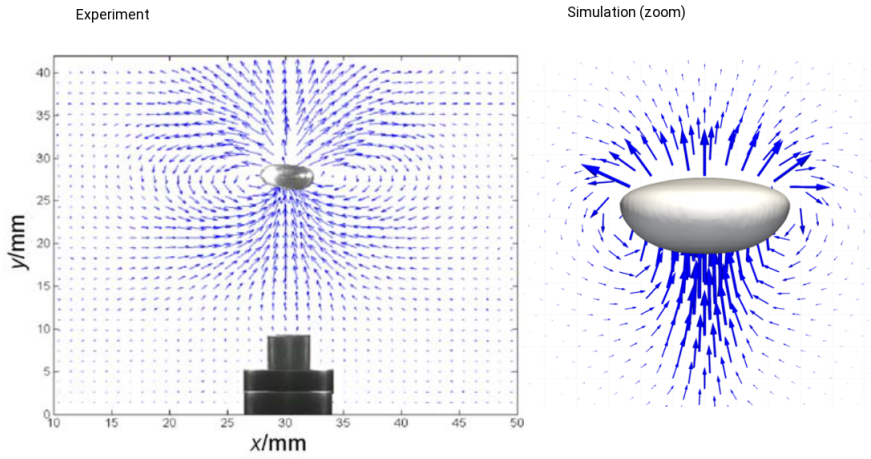

Figure 4.8: Comparison of fluid velocity vectors for experiments and simulation of a bubble detached from a nozzle. Experiment reproduced from Dietrich et al. (2013b) with permission of Springer.

As shown in the figure, the simulation captures a similar trend of the flow around the bubble and the wake. In addition, a couple of small vortexes of opposite direction are noted at each end of the bubble.

4.6 Bubble path and wake

The path followed by the bubbles and the wake produced is studied for the bubble detached from the nozzle and the initially spherical bubble. The opposite vortexes are observed appearing periodically and producing a change on the orientation of the bubble and a non-rectilinear path as the reported experimentally in the literature.

Fig. 4.9 shows for the scenario S5a the iso-surface of the bubbles and the velocity vectors representing the wake produced. Shape oscillations are noted in combination with the generation of clockwise and counterclockwise vortexes. The occurrence of the new vortexes takes place between the shape oscillation cycles. At 0.2450 seconds, the onset of the instability of the path is detected.

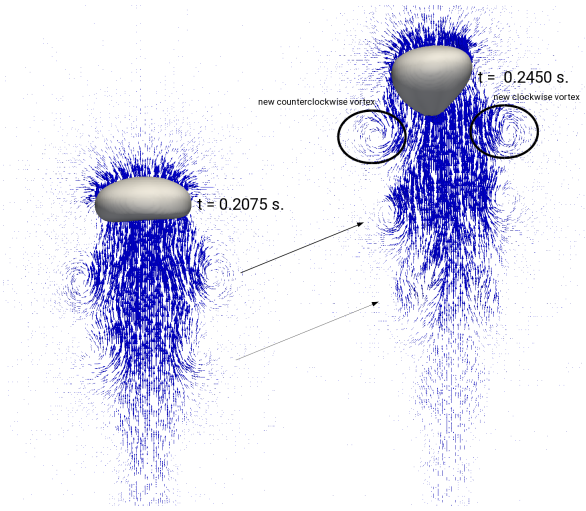

Figure 4.9: Bubble iso-surface and velocity vectors at the middle plane for S5a.

As a curious fact, it is interesting to note the behaviour of the same simulation using a RAS turbulence model as κ-ε (case S5b). With this simulation, the vortexes can not be properly predicted (see Fig. 4.10) and the bubbles follow a rectilinear path for the bubble sizes tested. This confirms the hypothesis of the wake effect on the path instability.

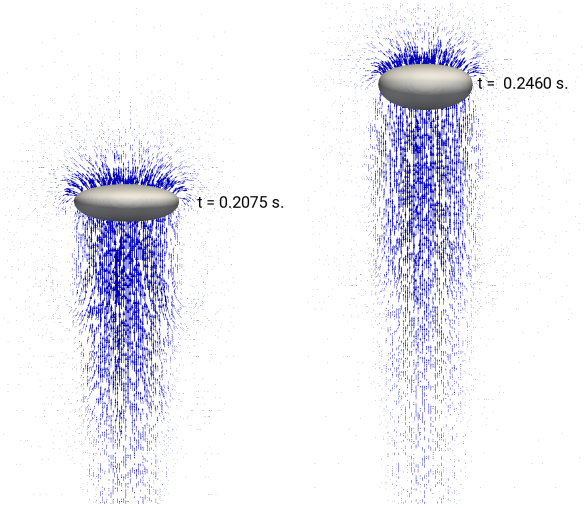

Figure 4.10: Bubble iso-surface and velocity vectors at the middle plane for S5b.

The horizontal projection of the path followed by the bubbles in these simulations is shown in Fig. 4.11. For the case of a bubble from the nozzle is appreciated that the acceleration of the bubble at the detachment of the nozzle anticipates the conditions for the change of trajectory in comparison with the initially spherical bubble.

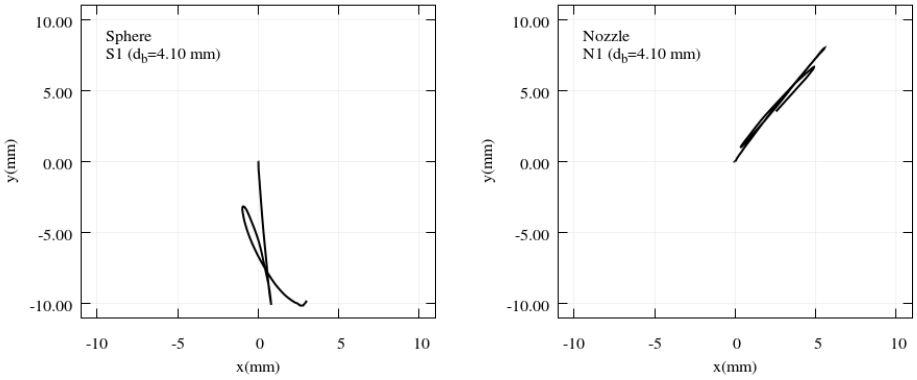

Figure 4.11: Horizontal projection of bubbles with diameter 4.10 mm for the sphere and nozzle cases.

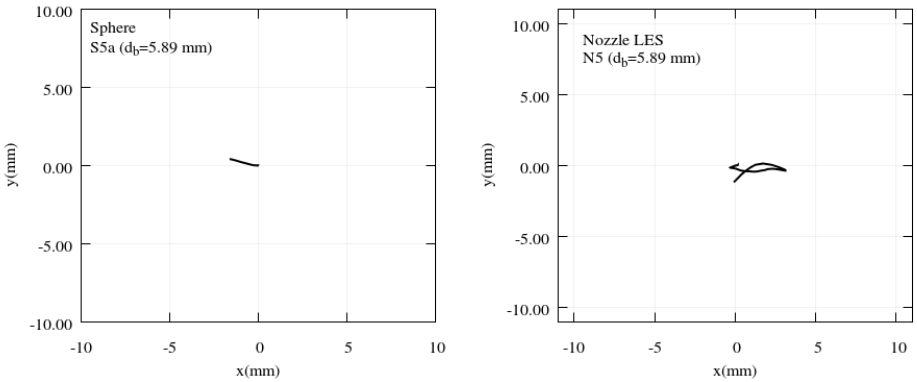

Figure 4.12: Horizontal projection of bubbles with diameter 5.89 mm for the sphere and nozzle cases.

The path and wake of bubbles were investigated in Vries (2001) as commented before. In this work zigzagging and helical paths were detected. In Fig. 4.13 the path the horizontal projection of a bubble of diameter 2 mm is shown.

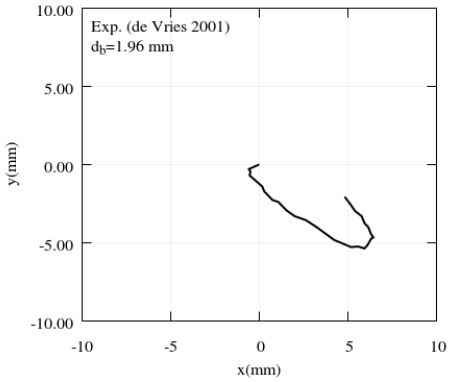

Figure 4.13: Horizontal projection of an experimental bubble path.

It is proposed in this work the comparison of the distance of the bubble centroid to the centreline:

$$d_c = \sqrt{C_{i,x}^2 + C_{i,x}^2} \tag{4.12}$$

This distance is plotted as function of height in Fig. 4.14 for N1, S1, N5 and S5a. In addition, d_c is obtained for the experiments of Vries (2001) with data obtained in equidistant steps along the 40 cm recorded.

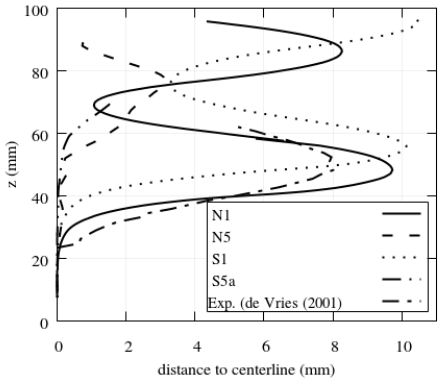

Figure 4.14: Distance of the bubble to the centreline as a function of height.

4.7 Velocity of a bubble rising

The velocity of the bubbles is analysed in this section. The scenarios N1 and N5 are used for the study. The former has a low gas flow rate that results in bubbles separated sufficiently to not influence the bubble coming behind. This is shown in Fig. 4.15, where the velocity vectors in the middle plane are shown.

The geometric centroid, C_b, is calculated at different times to determine the path of the bubbles. The iso-surface of the bubbles consists of a set of elements with vector position, $\mathbf{v_i}$, by each element. The centroid is obtained as:

$$\mathbf{C}_\mathrm{b} = \frac{1}{n}\sum_{i=1}^{n}\mathbf{v_i} \tag{4.13}$$

The velocity vector of the time step is computed as:

$$\mathbf{V}_\mathrm{b} = \frac{\Delta\mathbf{C}_\mathrm{b}}{\Delta t} \tag{4.14}$$

In Fig. 4.16 we represent an analysis of the bubble velocity for the scenarios N1 and N5. The terminal velocity ($V_{\mathrm{b,z}}$) and the magnitude of the velocity vector are represented ($|\mathbf{V}_\mathrm{b}|$) in addition to the integrated value of the surface velocity at the iso-surface of the bubble. For N1 the bubble starts a shape oscillation after the detachment that can be appreciated in the bubble velocities. After some oscillations the bubble change its orientation and the terminal velocity starts a velocity cycle due to the zigzagging movement but the magnitude of the velocity vector remains almost constant. The bubble velocity of a bubble with the same size using the correlation of Tomiyama et al. (1998) for pure systems (Eq. 3.11) will give a terminal velocity of 0.235 m/s. In the simulation, the mean value of one entire cycle after the onset of the instability path results in 0.225 m/s. In the case of N5, a bubble shape oscillation is responsible of the velocity oscillations and discrepancies are only noted at the end of the simulations. The velocity with Eq. 3.11 gives a value of 0.232 m/s but the mean value of the last cycle gives a value of 0.334 m/s. This could be explained as the bubble has not yet started the instability motion.

The same comparison is shown for S1 and S5a in Fig. 4.17. For these simulations, the bubble is introduced in the system as a sphere, so the effects of the nozzle, as for example the acceleration increase in the detachment, are not considered.

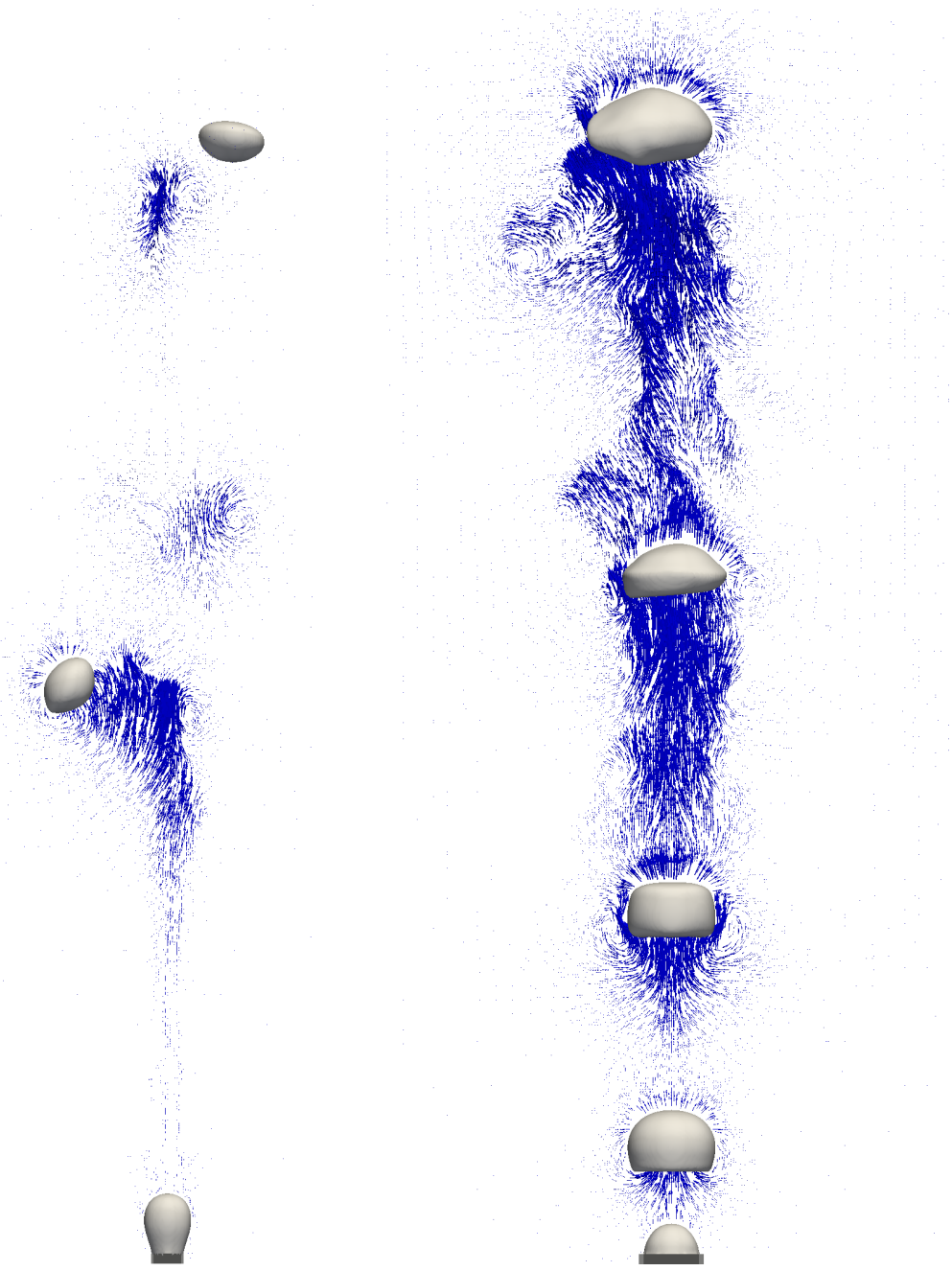

Figure 4.15: Velocity vectors for N1 and N5.

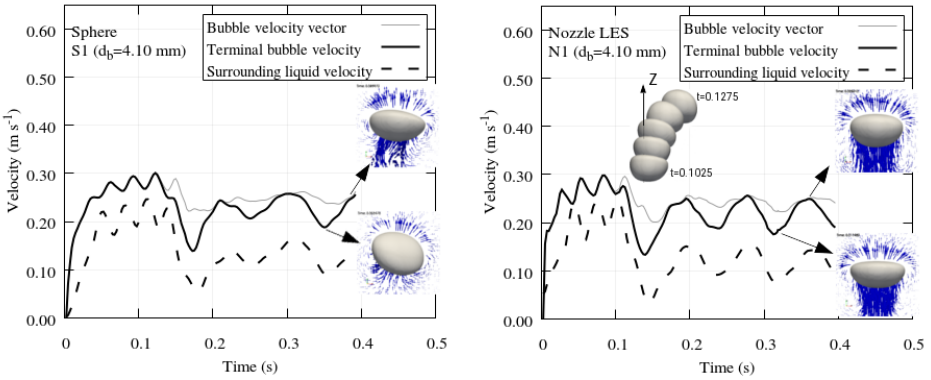

Figure 4.16: Velocities for a bubble of 4.10 mm for the sphere and nozzle cases.

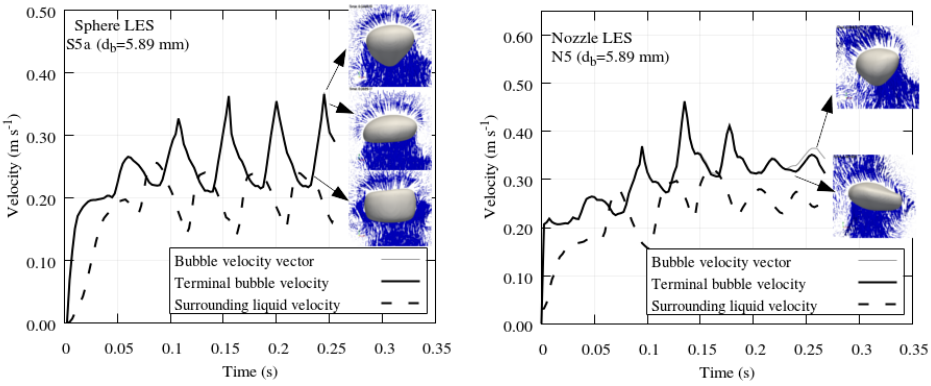

Figure 4.17: Velocities for a bubble of 5.89 mm for the sphere and nozzle cases.

4.8 Conclusions

The study performed in this chapter demonstrates the performance of the VOF technique for bubbles with relatively small size. Through this technique, the growth and bubble detachment from an air injection from an orifice was properly captured. The comparison with experiments showed that the bubble size and shape were obtained accurately in the simulation. In addition, the instantaneous velocity field was displayed matching the experiments.

Later, the acceleration of a bubble after the detachment and the acceleration from a sphere initially at rest were compared. The bubbles reached a terminal velocity that was, in turn, used to compare with the terminal velocity described by a drag correlation. For the bubbles analyzed we also noted a spiraling rising path,

the comparison with experimental data revealed a very similar evolution of the distance to a given centreline.

This chapter demonstrates the influence of the effects at the interface and how the wake affects the bubble. The results shown in this section are useful to verify the performance of CFD-DEM simulations when applied to single bubbles.

Chapter 5

Computational Fluid Dynamics - Discrete Element Method (CFD-DEM)

In this chapter the development of a new solver based on the CFD-DEM formulation is performed in combination with an exhaustive study of the experimental techniques and validation. The development of the solver implied the investigation of several aspects that are particularly relevant for bubbly flow in pipes but were not usually required for traditional CFD-DEM simulations. In contrast, a rigorous validation was made possible by means of a new methodology to obtain the computational results with conditions similar to reality, extracting the relevant information of simulations with virtual sensor probes. This made it possible to use the solver not only as a method to reproduce the experiments, but as a tool to understand and investigate the experimental data and measurements. The solver was capable to predict several upward bubbly flow scenarios without the need of tuning coefficients including the axial evolution of the flow characteristics from a given inlet condition.

5.1 Introduction

The first main objective of this chapter is the development of a confident solver to predict vertical bubbly flow for pipes under different diameters and conditions with accurate results without the need of tuning coefficients. The solver relies on the CFD-DEM approach for unresolved particles. A spherical shape is assumed for this simulation but the effects of the bubble shape is introduced through the force correlations. Fig. 5.1 shows an image of the experiment and the simulation at the bottom measurement port for PW05003.

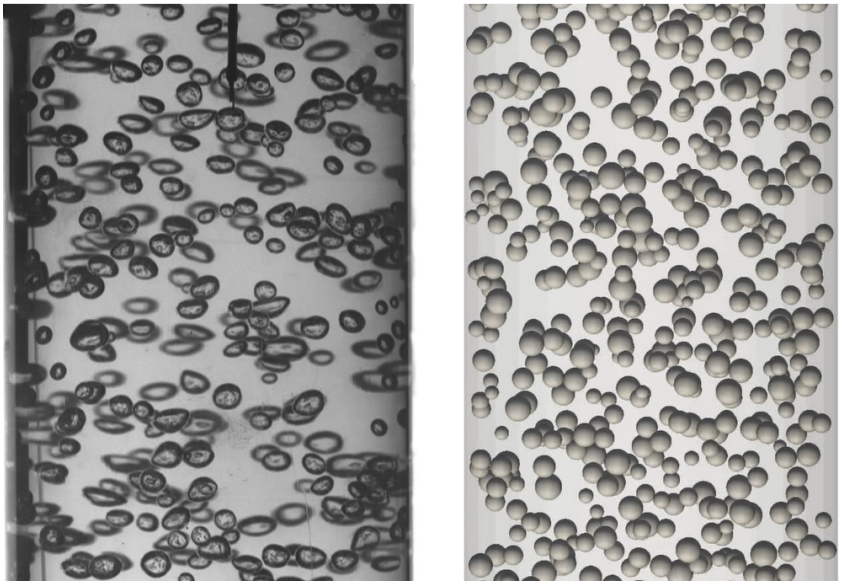

Figure 5.1: Experimental image from high speed camera and simulation screenshot.

The solver includes developments as the coupling between phases, the required interfacial forces, a two-equation turbulence model for two-phase flow and the consideration of the bubble-bubble and bubble-wall interaction with a soft-sphere model. Also, developments related to particular issues to perform a proper simulation of the bubbly flow as an equivolumetric sub-element method to distribute the bubble on the grid, injection algorithm, bubble expansion and turbulence effects on both liquid and bubbles. Due to the high importance and complexity of modelling accurately the two-phase flow, we intentionally limited this work to low void fraction scenarios where the break-up and coalescence effects can be neglected. For instance, from the data analysed by the camera, no evidence of coalescence or breakup was found for this condition. This allowed investigating in

depth the bubble dynamics resulting suitable to interpret accurately the results and validations.

The second main objective aims at providing a critical overview of the datasets and the employed methodologies, specially regarding the data corresponding to the dispersed phase properties. This requires to have an adequate knowledge on how the experiments have been conducted, the signal processing procedure followed to obtain the data, and how to fairly compare these results with the simulations.

Given most of the experimental data found in the literature has been obtained using needle probes, we developed a novel methodology to obtain computational results within a similar way. This methodology, called Virtual Needle Probe System (VNPS), consists on placing probes in the simulations acting as phase identifiers to later process the signal generated with the same program as the one used to process the experimental signal. This implies that the same assumptions and processing schemes as in the experiments are adopted and that a more comprehensive comparison can be performed. Hence, this research shows an extensive validation of the variables that define the two-phase flow characteristics.

The experimental facilities and measurement techniques were described previously in Chapter 2. In the corresponding sections, the experimental techniques utilized were described, in order to emphasize the difficulties of the measurements, the particularities of the data from different experiments and a classification of the variables depending on the information lost in the measurement. On that basis, we developed a system to obtain the dispersed phase variables by means of the probe sensor concept implemented in the simulations for a fair comparison with the experiments.

Different experiments of bubbly flow in adiabatic vertical pipes were used in this study as the experiments of Hibiki et al. (2001b) and Hosokawa et al. (2009) in pipes with diameters of 50.8 and 25.0 mm respectively. In addition, new experiments were performed to obtain complementary data, necessary for an extensive validation, using a larger pipe of 52 mm of the experimental facility described in Monrós-Andreu et al. (2013) and Monrós-Andreu et al. (2017) (see Fig. 2.1). Details about the conditions used (PW05003, HK05003 and H050018) were shown in Table. 2.2.

The main mathematical formulation and methods are described in Section 5.2. The development of the solver has been performed in the context of the CFD-DEM approach for unresolved particles extending its use to bubbly flows. This solver has been developed and implemented in the framework of the open-source package OpenFOAM®, so its libraries and methods served as a basis to develop this new solver.

Section 5.4 is focused on the methods to assign the volume fraction and momentum in the mesh used to solve the liquid phase. In fact, this is an important step as determines the coupling between the phases. This has been done in the past in different ways by different authors. While analytic methods are accurate, they are not suitable when arbitrary unstructured grids are used. A classical method consists on assigning the bubble volume and momentum to the cell where the particle centre is located. This method can lead to considerable local errors and inaccuracies that were crucial for our simulations as shown in this work. Instead, a new sub-element method was introduced, based on dividing the sphere into equivolumetric volumes to improve the stability and accuracy of the solver.

In Section 5.5, the terminal velocity and dynamics of a single bubble rising was analyzed including its behaviour for a turbulent scenario. The scenarios simulated with VOF in the previous chapter are also used.

Section 5.6 dealt with the method to seed the bubbles in a circular pipe for a given polydisperse flow. The injection of bubbles in the simulation should reproduce the experimental conditions adequately in terms of flow rate, BSD, bubble velocity and injection position. In this way, one can obtain the same void fraction and bubble frequency profiles as in the experiments. This can be performed easily for time-averaged variables, but is not trivial when using a DEM and is required to seed the bubbles as a function of time. For this reason, we developed a generic injection algorithm for polydispersed flow to deal with the injection adequately. Three different inlet patterns were compared to analyse the influence of the bubbles on the liquid along the axial distance.

In Section 5.7, the effects of the bubble size distributions on the flow behaviour are analysed. First, the assumption of monodispersity and polydispersity is analysed to study its influence on the computational results. Also, the bubble expansion due to the pressure change as a function of the pipe height was investigated measuring experimentally the bubble size at different measurement ports. The increase on size and volume through the pipe can determine the flow structure, therefore a simplified model for the bubble expansion has been integrated in the bubble tracking of the CFD-DEM solver.

The bubbles generate random velocity fluctuations in the flow that were modelled in this work using a two-phase flow κ-ε turbulence model. At the same time, the turbulence has an effect on the bubbles motion that was described with a Continuous Random Walk (CRW) model. This was studied in conjunction in Section 5.8. The effect of the pseudoturbulence and bubble dispersion can be noted on the resulting void fraction profile and probability density function of dispersed phase velocity. The liquid velocity seen by the bubble along its path was also compared with the experimental instantaneous velocity.

Finally, in Section 5.9, a complete validation is presented for the three different experiments mentioned, which involved the tracking of around 30000 bubbles each time step for the most restrictive case. The validation was performed with all the available variables for radial profiles at different heights, and for the axial evolution of the cross-section average values. The section ends with a critical assessment on validation procedures against needle probes experimental data.

5.2 Mathematical formulation and methods

In this section we show the main formulation of the solver. It starts by introducing the DEM formulation for the dispersed phase. Then, the Eulerian formulation for the continuous phase is summarised. Finally, the numerical methods employed and simulation setup are presented.

5.2.1 DEM formulation

The motion of the i-th bubble is computed by integrating the Newton's second law of motion:

$$m_i \frac{\mathrm{d}\mathbf{u}_{\mathrm{b}_i}}{\mathrm{d}t} = \mathbf{f}_i^{\mathrm{b}} + \mathbf{f}_i^{\mathrm{h}} + \sum_{j=1}^{\mathrm{IL}_i} \mathbf{f}_{ij}^{\mathrm{c}}. \tag{5.1}$$

In the left-hand size of this equation m stands for the bubble mass and $\mathbf{u}_{\mathrm{b}}$ for its instantaneous velocity. The first term on the right-hand side stands for the body force or buoyancy force due to the influence of the gravitational field on the bubbles:

$$\mathbf{f}_i^{\mathrm{b}} = \mathrm{V}_{\mathrm{b,i}}\mathbf{g}(\rho_{\mathrm{b}} - \rho_{\mathrm{c}}), \tag{5.2}$$

being V_{b} the bubble volume, $\mathbf{g}$ the gravity vector, and ρ_{c} and ρ_{b} are the carrier phase and bubble density. The bubble volume, is computed from the bubble diameter d_{b}:

$$\mathrm{V}_{\mathrm{b}} = \frac{\pi d_{\mathrm{b}}^3}{6} \tag{5.3}$$

The second term in Eq. 5.1 represents the hydrodynamic forces resulting from the liquid-bubble interaction. The last term considers the collisional forces between pairs of bubbles or between bubbles and the walls. This is performed along the

range of influence on each bubble with the data of bubbles or wall, stored in an interaction list (IL).

The hydrodynamic forces considered are the drag, lift, virtual mass and wall lubrication force. The pressure gradient force has not been considered as its influence is considered negligible for this scenario.

$$\mathbf{f}_i^{\mathrm{h}} = \frac{3}{4d_{\mathrm{b,i}}}\mathrm{V_{b,i}}\rho_{\mathrm{c}}\mathrm{C_{d,i}}(\mathbf{u}_{\mathrm{c}}-\mathbf{u}_{\mathrm{b,i}})|\mathbf{u}_{\mathrm{c}}-\mathbf{u}_{\mathrm{b,i}}| + \mathrm{V_{b,i}}\rho_{\mathrm{c}}\mathrm{C_{l,i}}(\mathbf{u}_{\mathrm{c}}-\mathbf{u}_{\mathrm{b,i}})\times(\nabla\times\mathbf{u}_{\mathrm{c}}) + \mathrm{V_{b,i}}\rho_{\mathrm{c}}\mathrm{C_{v,i}}\left(\frac{\mathrm{D}\mathbf{u}_{\mathrm{c}}}{\mathrm{D}t}-\frac{\mathrm{d}\mathbf{u}_{\mathrm{b,i}}}{\mathrm{d}t}\right) - \mathrm{V_{b,i}}\rho_{\mathrm{c}}\mathrm{C_{w,i}}\left|\mathbf{u}_{\mathrm{c}}-\mathbf{u}_{\mathrm{b,i}}\right|^2\mathbf{n}_{\mathrm{w}}. \quad (5.4)$$

In this equation, $\mathrm{C_d}$, $\mathrm{C_l}$, $\mathrm{C_v}$ and $\mathrm{C_w}$ stand for the drag, lift, virtual mass and wall lubrication force coefficients. The instantaneous liquid velocity, $\mathbf{u}_{\mathrm{c}}$, used to compute the forces was calculated as the sum of the mean liquid velocity, $\mathbf{U}_{\mathrm{c}}$, and the fluctuating velocity component, $\mathbf{u}'_{\mathrm{c}}$. On the other hand $\mathbf{u}'_{\mathrm{c}}$ was computed with a Continuous Random Walk (CRW) stochastic model described later in Section 5.8 together with the turbulence modeling.

The contact forces are usually modelled with a soft-sphere model (Cundall et al. 1979) consisting of a spring, a dash-pot and a slider. These elements generally need the definition of stiffness, as well as damping coefficient and friction coefficient. In this first approximation viscous damping and tangential forces were not included in the analysis, so the force is restricted to normal collisions of a spring system. The force according to a linear contact-stiffness model is given by:

$$\mathbf{f}_{ij}^{c} = -k_{ij}\delta_{ij}\mathbf{n_{ij}}, \quad (5.5)$$

where δ_{ij} and k_{ij} are the overlapping and stiffness respectively between two particles or between a particle and the wall, and $\mathbf{n_{ij}}$ the unit vector.

Finally, after expanding and manipulating the Eq. 5.1 results:

$$(m_{\mathrm{b,i}} + \mathrm{V_{b,i}}\rho_{\mathrm{c}}\mathrm{C_{v,i}})\frac{\mathrm{d}\mathbf{u}_{\mathrm{b,i}_i}}{\mathrm{d}t} = \mathrm{V_{b,i}}\mathbf{g}(\rho_{\mathrm{b}}-\rho_{\mathrm{c}}) + \frac{3}{4d_{\mathrm{b,i}}}\mathrm{V_{b,i}}\rho_{\mathrm{c}}\mathrm{C_{d,i}}(\mathbf{u}_{\mathrm{c}}-\mathbf{u}_{\mathrm{b,i}})|\mathbf{u}_{\mathrm{c}}-\mathbf{u}_{\mathrm{b,i}}| + \mathrm{V_{b,i}}\rho_{\mathrm{c}}\mathrm{C_{l,i}}(\mathbf{u}_{\mathrm{c}}-\mathbf{u}_{\mathrm{b,i}})\times(\nabla\times\mathbf{u}_{\mathrm{c}}) + \mathrm{V_{b,i}}\rho_{\mathrm{c}}\mathrm{C_{v,i}}\frac{\mathrm{D}\mathbf{u}_{\mathrm{c}}}{\mathrm{D}t} - \mathrm{V_{b,i}}\rho_{\mathrm{c}}\mathrm{C_{w,i}}\left|\mathbf{u}_{\mathrm{c}}-\mathbf{u}_{\mathrm{b,i}}\right|^2\mathbf{n}_{\mathrm{w}} - \sum_{j=1}^{\mathrm{IL}_i}k_{ij}\delta_{ij}\mathbf{n}_{\mathrm{ij}}. \quad (5.6)$$

5.2.2 Eulerian formulation (CFD)

The carrier phase motion is solved by the volume averaged Navier-Stokes equations for incompressible flow. The local averaged continuity and momentum equations are:

$$\frac{\partial}{\partial t}\alpha_{\mathrm{c}} + \nabla \cdot (\alpha_{\mathrm{c}}\mathbf{U}_{\mathrm{c}}) = 0, \tag{5.7}$$

$$\frac{\partial}{\partial t}\alpha_{\mathrm{c}}\mathbf{U}_{\mathrm{c}} + \nabla \cdot (\alpha_{\mathrm{c}}\mathbf{U}_{\mathrm{c}}\mathbf{U}_{\mathrm{c}}) = -\alpha_{\mathrm{c}}\nabla p + \nabla \cdot \mathbf{R}_{\mathrm{c}} - \mathbf{M}^{\mathrm{h}}, \tag{5.8}$$

where p is the density-normalized pressure, $\mathbf{M}^{\mathrm{h}}$ is the volumetric average of the interfacial forces and α_{c} is the carrier phase volume fraction, generated by each bubble along its path on the cell. The method to compute these coupling terms is described in Section 5.4. The Reynolds stress, $\mathbf{R}_{\mathrm{c}}$, is defined in Section 5.8.

5.2.3 Particle force coefficients

Eq. 5.6 establishes the full force balance onto the i-th bubble. This equation depends upon four coefficients that need to be specified in order to solve it. Next, the different correlations selected to model the interfacial coefficients and the definition of the stiffness coefficients are presented.

Interfacial forces coefficients

The drag coefficient of Tomiyama et al. (1998) for an air-water contaminated system reads:

$$C_{\mathrm{d},\infty} = \max\left(\frac{24}{Re}(1 + 0.15Re^{0.687}), \frac{8}{3}\frac{\mathrm{Eo}}{\mathrm{Eo}+4}\right) \tag{5.9}$$

The dimensionless numbers for each bubble in the equation above are given by:

$$Re = \frac{|\mathbf{u}_{\mathrm{b}} - \mathbf{u}_{\mathrm{c}}|d_{\mathrm{b}}}{\nu_{\mathrm{c}}} \tag{5.10}$$

$$\mathrm{Eo} = \frac{g(\rho_{\mathrm{c}} - \rho_{\mathrm{d}})d_{\mathrm{b}}^2}{\gamma} \tag{5.11}$$

where ν_{c} is the molecular viscosity, and γ the surface tension.

This results in the terminal velocity curve of Fig. 5.2. In this figure, an approximate range of the diameters present in the experiments is marked. In the simulation, the drag coefficient will influence the individual velocity of each bubble. Hence, according to the non-linearity of the drag force, small changes in size from the inlet to the top of a pipe, can influence variables related with the bubble velocity as the volume fraction.

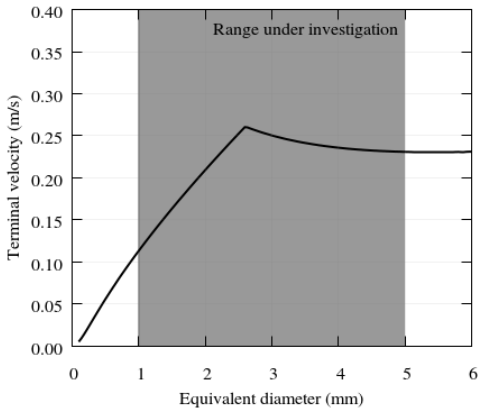

Figure 5.2: Terminal velocity for an air-water system for a fully contaminated system using the drag coefficient of Tomiyama et al. (1998).

The previous drag coefficient was obtained for experiments performed in a stagnant liquid. In the literature an increase on the drag coefficient as a function of the strain rate, Sr, was reported (Legendre et al. 1998; Magnaudet et al. 2000; Sugioka et al. 2009). The relation found by Legendre et al. (1998) is used to describe the drag force:

$$C_\mathrm{d} = C_{\mathrm{d},\infty}(1 + 0.55\mathrm{Sr}^2), \quad \mathrm{Sr} = \frac{d_\mathrm{b}\omega}{|\mathbf{u}_\mathrm{b} - \mathbf{u}_\mathrm{c}|}, \tag{5.12}$$

where ω is the magnitude of the carrier phase velocity gradient.

The lift coefficient of Tomiyama et al. (2002b) was used to take into account the influence of the shear rate for the different bubble sizes present in the simulations:

$$C_\mathrm{l} = \begin{cases} \min\left(0.288\tanh(0.121Re), f\right) & \mathrm{Eo}_d < 4 \\ f & 4 \leq \mathrm{Eo}_d \leq 10 \\ -0.29 & \mathrm{Eo}_d > 10 \end{cases}, \tag{5.13}$$

$$f = 0.00105\mathrm{Eo}_d^3 - 0.0159\mathrm{Eo}_d^2 - 0.0204\mathrm{Eo}_d + 0.474, \tag{5.14}$$

where Eo_d is a modified Eötvös number with characteristic length the maximum horizontal dimension of the bubble that can be estimated as in the same work as a function of a spherical bubble diameter.

The wall lubrication force (Antal et al. 1991) is a hydrodynamic force usually taken into account to simulate two-phase flow in pipes. This force reflects the drainage of the fluid around the bubble and represents the force that the liquid drainage around a bubble moving near a wall has on the bubble. A two-dimensional solution was derived for flow between a cylinder and a wall by Antal et al. (1991). The constants obtained in this work were evaluated by a 3D DNS of viscous flow past a single bubble with uniform velocity using PHOENICS code. The simulations were done for two relative velocities (0.1 and 0.2 $\mathrm{m\,s^{-1}}$) finding the following equation:

$$\mathrm{C_w} = \max\left[0, \mathrm{C_{w1}} + \mathrm{C_{w2}}\frac{r_b}{y}\right], \tag{5.15}$$

where y is the distance of the bubble center to the wall. The fitting coefficients can be expressed as:

$$\mathrm{C_{w1}} = -0.06\,|\mathbf{u}_\mathrm{c} - \mathbf{u}_\mathrm{b,i}| - 0.014, \tag{5.16}$$

and

$$\mathrm{C_{w2}} = 0.147. \tag{5.17}$$

Finally, the application of potential flow theory to flow around a spherical bubble in an infinite medium gives a value of 0.5 for C_V according to Lamb (1895), Auton et al. (1988), and Drew et al. (1987).

Stiffness coefficient

In order to calculate the stiffness of the spring system (Eq. 5.5), we assume a_i and b_i the semi-minor axis and semi-major axis of the i-th bubble, respectively.

The stiffness of the bubbles was determined as a function of the increase of the surface area due to the bubble deformation. Assuming that in the deformation the bubble conserves the volume, the surface energy changes due to surface deformation, ΔA, for a given surface tension, γ. For the computation of the stiffness, is assumed that the bubbles have a spherical shape unless they are colliding. Once

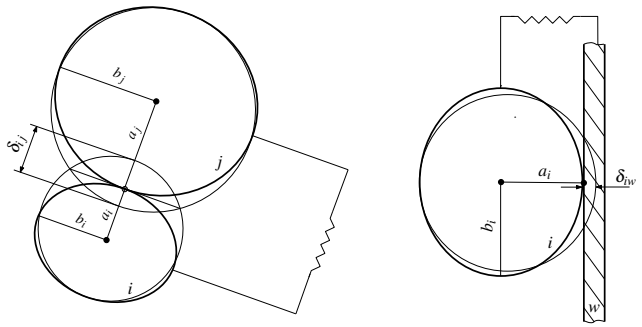

Figure 5.3: Ellastic collision scheme for the soft-sphere model.

they collide, their shape deforms to an oblate spheroid with its minor-axis along the collision direction (see Fig. 5.3). The bubble deformation is accounted for by the normal overlapping defined as:

$$\delta_{ij} = 0.5(d_{b,i} + d_{b,j}) - l_{ij}, \tag{5.18}$$

where l_{ij} is the distance between the bubble centers. The semi-axis a_i is defined as a_i=$r_{b,i}$-$0.5\delta_{ij}$. The semi-axis b results in b_i=$\sqrt{r_{b,i}^3/a_i}$.

Combining the works done by the bubble deformation and the spring system (Eq. 5.5) it results:

$$\int_0^{\delta_{ij}} k_{ij}\delta_{ij}d\delta_{ij} = \gamma(\Delta A_i + \Delta A_j) \tag{5.19}$$

Consequently, the stiffness between the two bubbles can be calculated as:

$$k_{ij} = \frac{2\gamma(\Delta A_i + \Delta A_j)}{\delta_{ij}^2} \tag{5.20}$$

The value of k_{ij} is calculated dynamically for each bubble movement if the bubble is interacting with other bubbles or walls. The wall is considered as a rigid body, j index is replaced by w in the above equations for solving the overlapping of the bubbles with the wall.

5.2.4 Numerical methods and simulation set up

The solution procedure consists on solving the CFD and DEM parts explicitly. Thus, the pressure-velocity calculation procedure for the Navier-Stokes equations is solved first and then the bubbles are tracked during a given number of sub-cycles until the Eulerian time step, Δt, is reached. During the tracking, in each sub-step, $\mathbf{u}'_c$ is computed from the CRW stochastic model, and $\mathbf{U}_c$ is updated according to the interpolated values at the current position of the bubble to obtain $\mathbf{u}_c = \mathbf{U}_c + \mathbf{u}'_c$ needed to compute the hydrodynamic forces and calculate the new bubble velocity. The coupling terms are calculated averaged on time during the path to provide the required $\mathbf{M}^h$ and α_c to solve pressure and velocity in the next steps. In each sub-step the bubble radius r_b is updated to consider the bubble size changes due to the pressure according to Eq. 5.34 from the simplified model described later.

Eq. 5.8 and Eq. 5.7 were solved with the Pressure-Implicit with Splitting of Operators (PISO) algorithm (Issa 1986) including the modifications to consider the volume fraction and momentum exchange. Eq. 5.35 and Eq. 5.37 defining the turbulence model are incorporated in the algorithm and will be discussed later.

A modified version of the tracking algorithm of Macpherson et al. (2009) was developed and implemented in the solver to incorporate the modifications described in this work. A second-order leapfrog integrator was used to numerically solve Eq. 5.6, alternating a linear move and collision in time. This integrator is symplectic and the energy error remains bounded for sufficiently small time steps. The collisions are performed using the Arbitrary Interaction Cells Algorithm (AICA) already implemented in OpenFOAM® (Macpherson et al. 2008). With this algorithm the bubble-bubble and bubble-wall interactions are evaluated for the bubbles in the given referred cells. The referred cells are defined at the beginning of the simulation according to a specified r_{cut} value larger than the maximum bubble radius expected. The soft-sphere model is then applied for the bubbles that are overlapping.

The meshes were created by means of the blockMesh tool of OpenFOAM®, resulting in an unstructured hexahedral mesh with an O-grid structure. The meshes were created with an axial mesh size of 1.5 times the maximum bubble diameter considered. The number of elements of the mesh results in 209280, 171200 and 57600 hexahedrals for PW05003, HK05003 and H050018 respectively.

The value of Δt selected for the simulation was kept fixed to a value of 7.5×10^{-4} s and a number of 10 sub-cycles was considered. This time step matches the stability criteria for both phases in terms of Courant number, phyisical contraints for the collisions and response time. In addition it is sufficiently small to apply the VNPS as the signal from the virtual probes is produced each sub-step. The simulations for the three scenarios were run until a total time of 35 seconds was reached as in the real experiments, to obtain statistically converged results.

5.3 Dispersed phase variables calculation

Experimental measurement of dispersed phase characteristics is a complex task that involves several approximations and data processing. Also, the comparison of simulation results with experimental data is not as straightforward as one could expect. Here we perform a critical analysis of the so-called validation procedure and propose an adequate methodology for a rigorous comparison between simulation results and experimental data. This new methodology is briefly summarised in the scheme of Fig. 5.4, and takes profit of the full potential of CFD-DEM simulations.

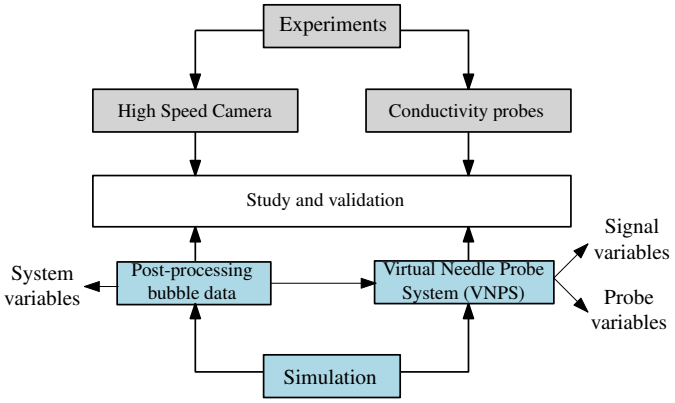

Figure 5.4: Validation setup for simulation.

First, a Virtual Needle Probe System (VNPS) was implemented into the CFD-DEM code. These virtual probes mimic the actual NP used in the experimental facilities. They will be placed in the same measurement locations as the NP, providing signals similar to those obtained by the NP, so they can be processed by doing the same approximations and assumptions as in the experimental processing of NP signals. The data generated by the processing of VNPS signals will be referred to as the *signal variables*. Second, in the context of the VNPS, the bubble data can be obtained at a sampling location coincident with a probe by capturing the properties of the bubbles that pass through the sampling point, leading to the so-called *probe variables*. Finally, the code allows for the knowledge of the location, diameter and velocity of every bubble. Then, the characteristics of the dispersed phase in the simulation are known. The averaged data obtained from this knowledge will be referred to as *system variables*. These variables are summarized in Fig. 5.5.

The VNPS consists in a set of probe-points placed in space so that their relative locations coincide with those of the tips of a real needle probe. Their role is to serve as phase indicators to generate a synthetic signal. During the simulation, and for

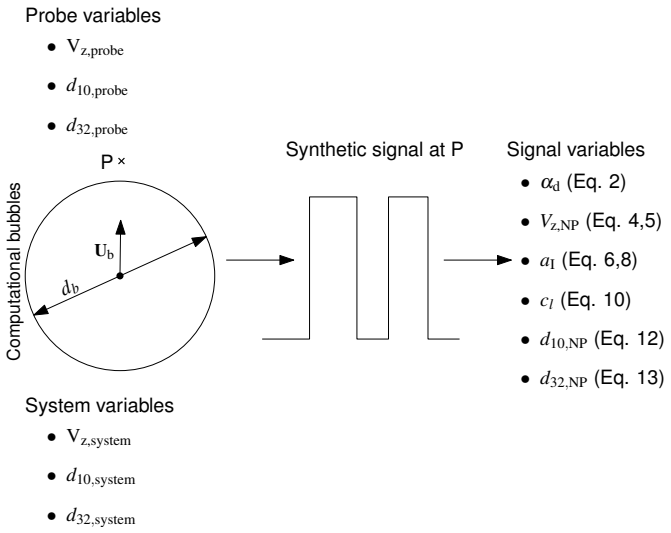

Figure 5.5: Scheme of the different type of variables obtained for validation.

the tracking process of every bubble, a value of 1 or 0 is assigned to a probe point depending on if its location is inside or outside a bubble, respectively (see Fig. 5.6). Afterwards, the data can be post-processed with the same program as the one used to process experimental output signal, once the regenerated square-wave signals is obtained. With this methodology time-averaged values of void fraction, velocity, interfacial area concentration, Sauter mean diameter, chord length or number of bubbles detected can be directly obtained from the simulation. The radial and axial distances between tips are shown in Fig. 5.6. The distances are measured in the real probes obtaining values of 1.77 mm for δ_z and 0.26 mm for δ_x and δ_y.

In addition to the signal variables, the actual values of the variables owned by each bubble are obtained when they are crossing the probes. These variables can be computed averaged in time for the N_p bubbles crossing the probe. The definition of the variables used in this work are the following:

$$\mathrm{V_{z,probe}} = \frac{1}{N_p}\sum_{i=1}^{N_p}\mathrm{U_{b,z}} \tag{5.21}$$

$$d_{10,\mathrm{probe}} = \frac{1}{N_p}\sum_{i=1}^{N_p} d_b \tag{5.22}$$

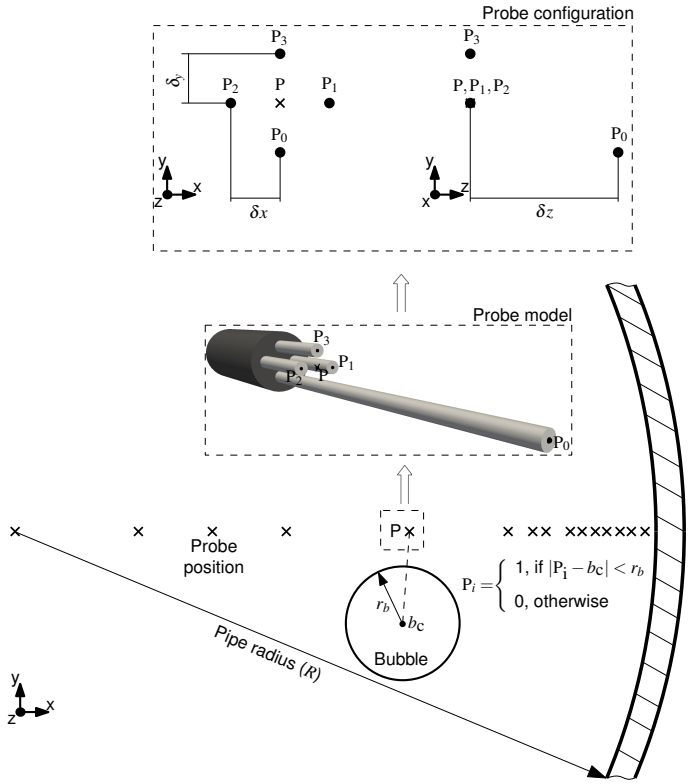

Figure 5.6: Virtual Needle Probe System (VNPS). Example of a four-probe sensor with a square configuration.

$$d_{32,\text{probe}} = \frac{\sum_{i=1}^{N_p} d_b^3}{\sum_{i=1}^{N_p} d_b^2} \tag{5.23}$$

Along with this, one can compare the discrepancies between *signal* and *probe variables* for a more complete understanding of the validation with the experiments. In fact, if the digital processing scheme and assumptions are accurate, then *signal* and *probe variable* should be equal.

The *system variables* give different values as the *probe variables* because bigger bubbles are more likely to be hit by the probes (Clark et al. 1988; Liu et al. 1998). Then, a different post-processing to VNPS was applied to process the data owned

by each computational bubble during the time-steps of the calculation independent to the probes. This data can be represented directly with scatter plots or as an average in a volume over the time. For the latter, the region where this variable is calculated can vary and can include from a given arbitrary volume to a ring or disk as an example. The average is performed for the number of bubbles in the region, N_s, during the time as follows:

$$\mathrm{V_{z,system}} = \frac{1}{N_s} \sum_{i=1}^{N_s} \mathrm{U_{b,z}} \tag{5.24}$$

$$d_{10,\mathrm{system}} = \frac{1}{N_s} \sum_{i=1}^{N_s} d_b \tag{5.25}$$

$$d_{32,\mathrm{system}} = \frac{\sum_{i=1}^{N_s} d_b^3}{\sum_{i=1}^{N_s} d_b^2} \tag{5.26}$$

When different sizes of bubbles are present in the system as for polydispersed flow, there is a discrepancy between the bubbles actually seen by the probe and the bubbles existing in the system.

5.4 Void fraction and momentum exchange assignment

The bubble volume and momentum exchange assignment is important for the coupling between the phases as determines the velocity-pressure results and the solver stability. Furthermore, it determines the local values of the bubble forces. Therefore, an efficient consideration of the local void fraction and momentum exchange becomes mandatory.

From the pioneering work of Crowe et al. (1977) who accounted for the mass, momentum, and energy coupling between phases, through the Particle-Source-In Cell (PSI) model, several methods have been proposed. According to Norouzi et al. (2016b) the void fraction, and therefore the momentum term, in a cell can be calculated by exact analytical (Wu et al. 2009a; Peng et al. 2014; Wu et al. 2009b) or approximate non-analytical methods. Among the second type, they can be classified as Particle Center Method (PCM) (Xu et al. 1997), porous cubes (Deen et al. 2004; Link et al. 2005), statistical approaches (Xiao et al. 2011), sub-element (Gui et al. 2008; Hilton et al. 2010; Norouzi et al. 2016c) and spherical control volume (Kuang et al. 2008). The first type of methods has the advantage of

being accurate but hardly suitable for non-regular meshes as the used for the pipes under investigation. Hence, the non-analytical approach would be most effective for this case. These techniques usually obtain satisfactory results at the expense of computational time.

The algorithm shown in Vaidya et al. (2006) and Macpherson et al. (2009) is implemented in OpenFOAM® to track particles along the cells. The motion was done for unstructured, arbitrary polyhedral meshes leading with 3D meshes of complex geometries. The assignment of void fraction and momentum exchange during the tracking is based on the PCM, giving satisfactory results for scenarios where the cell volumes are regular and much larger than the volume occupied by the particles. In the PCM method all the bubble volume is assigned to the cell where the particle centre is located. As reported by Peng et al. (2014) it may lead to an error up to 50% where the particle centre is near the cell boundaries or to numerical instabilities due to dramatic changes in void fraction. The sub-element method is used to improve precision and accuracy, dividing the particle in a number of elements in such a way that each sub-element contributes its volume to the cell where the sub-element centre is located during its path.

5.4.1 Description of the new equivolumetric sub-element method

Similarly to the sub-element method, we have developed an equivolumetric sub-element method to track a fixed number of representative volumes or sub-elements of each bubble. To generate an optimal distribution we divide strategically the sphere with the equivolumetric partitioning algorithm defined in Yang et al. (2006). The method is performed in three main steps. First, an initial division of the sphere into two solid hemispheres is accomplished. Later each semi-sphere is divided into n hemispheric shells of equal thickness $\delta r{=}r_b/n$ (note that the first shell results in a small hemisphere). Finally, in the last step, the basic elements are generated from the hemispheric shells. An example of the partition of the i-th shell is shown for a sphere of radius π in Fig. 5.7.

The i-th shell is sliced into i polar divisions, and labelled by index j=1,2,...,i. Then every polar slice is cut into pieces given by k=1,2,...,6(j-1). According to this method, a sphere is partitioned exactly into a $2n^3$ cuts of equivalent volume depending on the number of n shells specified for each sphere.

The angles β_{ij} and α_{ijk} described in Fig. 5.7 determine the polar and azimuthal coordinates of the resulting cuts:

$$\alpha_{ijk} = \frac{2k\pi}{6(j-1)} \tag{5.27}$$

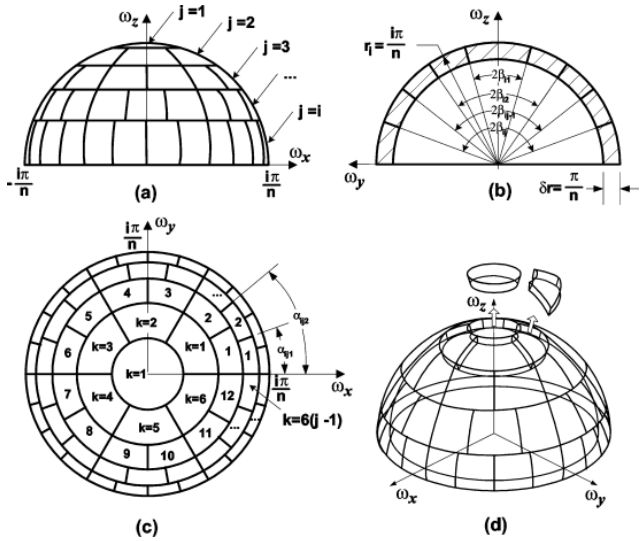

Figure 5.7: ©2006 IEEE. Equivolumetric and uniform convergent partition of hemispherical shell (Yang et al. 2006).

$$\beta_{ij} = cos^{-1}\left(\frac{3(i-j)(i+j-1)}{1+3i(i-1)}\right) \tag{5.28}$$

apply this equivolumetric partition of the bubble to the simulation, the bubbles are divided dynamically when they are seeded. A common δr is fixed for all the bubbles and the bubbles are partitioned according to the number of shells obtained (n=$r_b/\delta r$) and applying a ceiling function (next largest integer). Figure 5.8 shows an example for a bubble of 2.5 mm radius divided by 3 shells. The residence time of each element in the cells is computed to determine the contribution of momentum and volume fraction into the grid.

Considering that many bubbles may be present in a cell, the exchange momentum in a cell for a given sub-cycle can be calculated as:

$$\mathbf{M}^{\mathrm{h}} = \frac{1}{\rho_{\mathrm{c}} V_{\mathrm{cell}}} \sum_{i=1}^{N_b} \sum_{j=1}^{N_{cs,i}} \frac{\mathbf{f}_i^{\mathrm{h}}}{N_{s,i}}, \tag{5.29}$$

where V_{cell} is the cell volume, N_b the number of bubbles entirely or partialy in the cell, $N_{cs,i}$ the number of sub-elements belonging to the i-th bubble inside the cell, and $N_{s,i}$ the number of sub-elements that compose the i-th bubble.

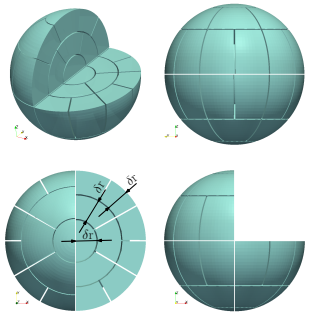

Figure 5.8: Views of the equivolumetric partition for a bubble of diameter 2.5 mm.

The carrier phase volume fraction is calculated in the same way as:

$$\alpha_{\mathrm{c}} = 1 - \frac{1}{V_{\mathrm{cell}}} \sum_{i=1}^{N_b} \sum_{j=1}^{N_{cs,i}} \frac{\mathrm{V_{b,i}}}{N_{cs,i}} \tag{5.30}$$

5.4.2 Validation and convergence study

In order for the unresolved CFD-DEM method to be valid, the volume cell must be larger than that of the particles. The cases under investigation in the present work are highly restrictive according to the diameter pipe and bubble size. This means that the mesh size should be sufficiently small to capture the hydrodynamics on the pipe and sufficiently large to satisfy the requirements of the method. Employing the δr parameter defined before, we studied the maximum ratio of total volume occupied by the bubbles and volume cell (or void fraction) obtained at each time step, which suggest the worst-case scenario where, for instance, the smallest cell volume concurs with the biggest bubble. This has been checked for the three conditions shown in this work. Figure 5.9 shows the probability density function of the maximum local void fraction for different values of δr for the mesh used in PW05003.

The results suggest that the maximum local void fraction decrease as the value of δr is decreased, until reaching minimum values. For δr=1.8 mm, maximum void fraction values above were obtained in the domain, in fact, this caused convergence problems stopping the simulation. This situation was observed for other tests of δr from this value. o analyzed We alsthe special situation where δr is sufficiently large to result in only a sub-element per bubble, which would be equivalent to a PCM method. These simulations stopped earlier and stability problems related to the unrealistic changes in time of local void fractions were detected. In contrast,

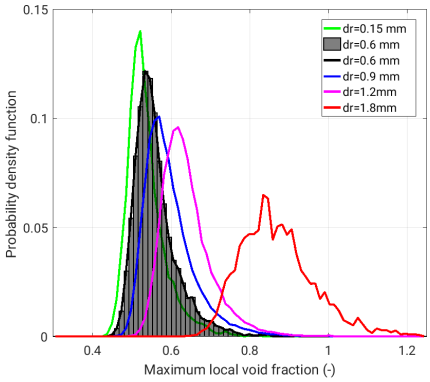

Figure 5.9: Maximum local void fraction among the time steps for different δr values for PW05003.

small values of δr results in greater number of sub-elements that allows a more accurate assignment of bubble volume into the cells, improving the convergence and the accuracy of the calculation of pressure and velocity fields.

Finally, a value of δr of 0.6 was used for convenience for this simulation, as it gives a good balance between computational time and performance. Furthermore, to validate the calculation of void fraction of this method we made use of the local definition of void fraction (Eq. 2.2) with the VNPS to compute averaged void fraction in the probes locations and compared with the time-averaged values of the interpolated values in the cells (Fig. 5.10).

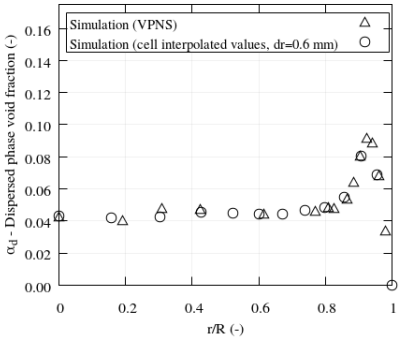

Figure 5.10: Cell interpolated values of void fraction for values compared with the void fraction obtained with the Virtual Needle Probe System (VNPS).

5.5 Single bubble rising in a quiescent liquid

The dynamics of a single bubbles is analyzed in this section. The same domain as the one used for the simulations with VOF is considered. The N1 and N5 case described in that section (Section 4.7) is used for the simulations with CFD-DEM.

5.5.1 Mesh sensitivity

First, mesh tests similar to the previous one is performed but fixing the δr for different mesh sizes. The mesh configurations are shown in Table 5.1:

Table 5.1: Mesh configuration for single bubble simulations with CFD-DEM

Label	Δx mm	V_b/V_{cell} (d_b=4.10)	V_b/V_{cell} (d_b=5.89)
M1	7.05	0.10	0.30
M2	5.25	0.25	0.74
M3	4.20	0.49	1.44
M4	3.50	0.84	2.49
M5	2.80	1.64	4.87

The different bubbles and the volume fraction contribution in the cells for a given time step are analysed. For M4, the volume of the cell is lower than the bubble volume, then the sub-elements of the bubble can fill the computational cell giving situations with void fraction greater than 1. Note that for M3 the size is smaller than the bubble diameter but not the volume. For this case a sufficiently small size of δ_r will satisfy the requirements of the solver.

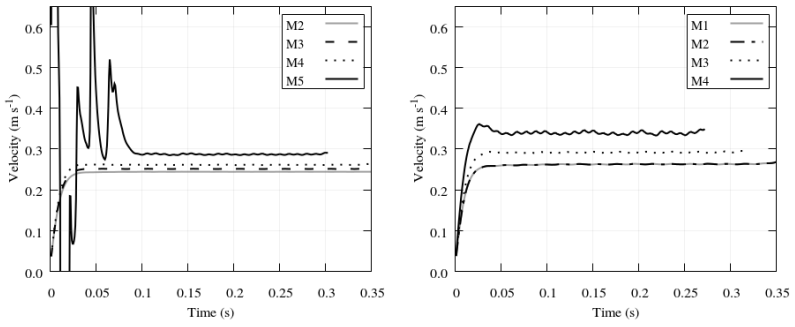

Figure 5.11: Terminal velocity for d_b=4.10 and d_b=5.89 for different meshes.

To verify the mentioned before, the terminal velocity is compared for the different meshes in Fig. 5.11. For M1, M2 and M3 we obtain the same results while for M4 there is initially instabilities and latter a steady state point overestimated. The

formulation of CFD-DEM for unresolved particles is used for the solver and then for M4 high velocity gradients begin to appear and as it relies on force correlations, the interfacial forces are not properly applied, in particular the virtual mass force makes the simulation to be unstable.

5.5.2 Bubble velocity and acceleration

The bubble velocity as function of time is now compared with the results with VOF in 5.12. The terminal velocity reached by both solvers are in a good agreement and the acceleration produced from the sphere initially at rest. Note that shape effects as path instabilities are not considered with this solver, and then discrepancies in time exists between both.

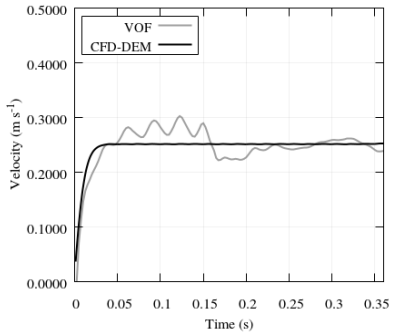

Figure 5.12: Terminal velocity comparison of a single bubble with CFD-DEM and VOF.

5.5.3 Test case with initially agitated liquid

In this section, the rising velocity and path for turbulent scenarios is investigated. We suppose that the liquid is initially agitated with corresponding initial values of κ and ε that are decaying as the bubbles rise. With this test we can study the influence of the turbulence in the bubble's motion produced because of the consideration of the CRW (details given later).

In Fig. 5.13 the terminal velocity is shown for a bubble of size 4.10 mm for two different cases of initial turbulence.

The path that the bubble follows for both turbulence quantities is shown in Fig.5.14 for a bubble of size 4.10 mm for the two different cases of initial turbulence. The results show how the bubbles are moved by the eddies, with a more pronounced path for the case with higher values of turbulence kinetic energy.

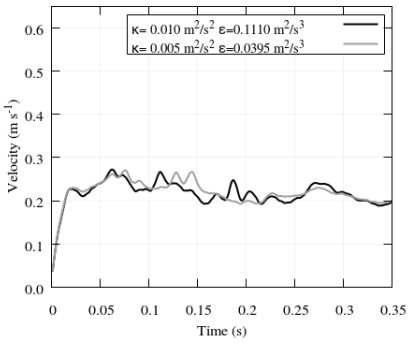

Figure 5.13: Terminal velocity comparison of a single bubble for different values of κ and ε.

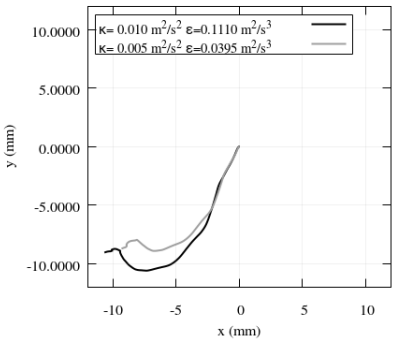

Figure 5.14: Horizontal projection of the path of isolated bubbles under different turbulence conditions.

5.6 Injection model and fluid flow influence

Next, for PW05003 we study how to introduce the bubbles at the inlet. The position in which the bubbles are injected in the domain determines the dispersed phase evolution due to the local momentum exchange from the bubbles to the fluid. In fact, the void fraction and bubble density radial profiles should be in accordance to the experiments at the inlet. Hence, in the present simulations the seeding of bubbles over time must be done under these constraints on their time-averaged values. In this section we propose an algorithm for the random-polydisperse seeding of bubbles in circular pipes that accomplishes with the statistical properties of given BSD, void fraction and bubble frequency profiles. This algorithm can be easily extended for include more constraints if needed.

To demonstrate the strength of the proposed algorithm, we make use of it to study the effects of bubble injection distribution on flow evolution. Thus, the flow characteristics and evolution of the case PW05003 have been examined when using three different injection patterns. In addition to the pattern with a profile from the bubble frequency of the experiments, a uniform distribution, and random radius and polar angle will be studied as illustrated in Fig. 5.15.

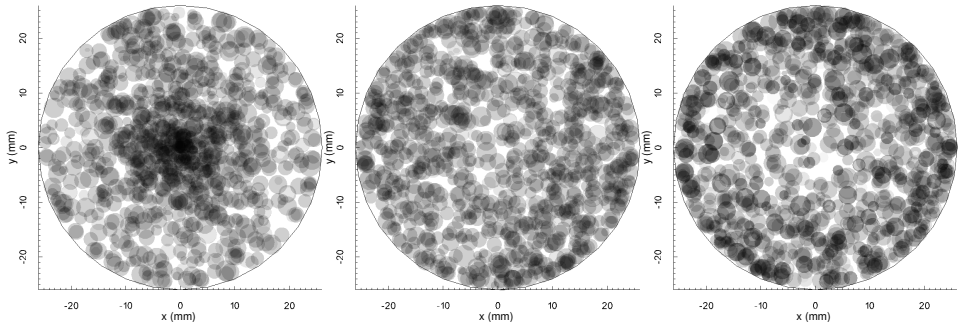

(a) Random r and θ **(b)** Unfiformly distributed **(c)** Profile from experiments

Figure 5.15: Injection patterns tested for PW05003. Bubbles at injection during 1 s with a sampling period of 0.075 s.

5.6.1 Injection algorithm to seed the bubbles

Considering a circular section of radius R in polar coordinates with r (radial coordinate) and θ (angular coordinate), a uniform distribution of injection points over [0,R] and [0,2π] respectively, gives an accumulation of bubbles near the centre as the area is proportional to the squared distance of r to the centre. To obtain an area-uniform random distribution, the probability density function of the random variable should be $f(r) = 2r/R^2$. Instead of a uniform distribution, is more convenient to seed the bubbles according to a given radial condition. For a given experimental sample of bubbles, if we know the radial distribution of bubbles detected per unit time the probability density function can be expressed as:

$$f(r) = N_t(r)\frac{2r}{R^2} \tag{5.31}$$

Based on $f(r)$ we developed the algorithm shown in Fig. 5.16 to seed the bubbles in the system following a BSD in a corresponding polar position vector $\mathbf{r}$ with random radial, ξ_r, and angular, ξ_θ, positions.

This algorithm provides the seeding of bubbles during a given injection time t_i. An average time step volume, V_i, is defined at the beginning of the simulation from

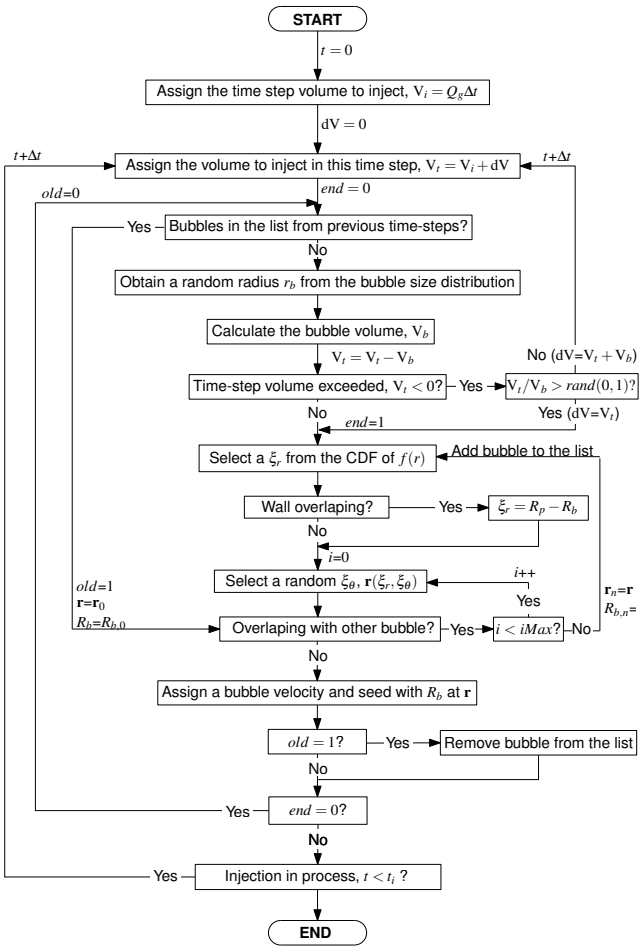

Figure 5.16: Injection algorithm diagram.

the air volumetric flow rate, Q_g, and Δt. Each Eulerian time step, a volume V_t is calculated, and bubbles with a size from a given BSD are consecutively generated until the total volume of these bubbles reach V_t. A deviation between V_i and V_t is expected as each bubble size is obtained randomly from the BSD, and the resulting volume V_t does not match V_i with accuracy, specially for low time steps. A correction variable, dV, is introduced in the algorithm to store the exceeding or missing volume for a given time step, to correct V_t in the next time step.

The radial coordinate is randomly obtained from the defined $f(r)$, while the angular one is randomly uniformly distributed. The geometrical constraints of the bubble sizes and the pipe wall are considered in order to avoid unrealistic over-

lapping between two bubbles or with the wall. Each time-step a bubble can be discarded if overlaps another bubble previously seeded close to it. In order to speed up the algorithm, an iterative process to try the seed at different random azimuthal positions for a given radial position is performed until a maximum number of tries, $iMax$, predefined by the user.

The discarded bubbles are stored in a list to try their injection in the next time step. This step is necessary to keep the statistic consistent over time. Position and diameters are stored in a data list where the First-In, First-Out (FIFO) rule is applied to try first the seed of the oldest bubbles in the list. In Fig. 5.16, the index n refers to the tail or the list and the index 0 to the head.

5.6.2 Boundary conditions and flow influence of the injection patterns

In this subsection we analyze the performance of the injection algorithm for PW05003. The bubbles were introduced in the system according to the data specified in the experiments related to the air flow rate.

In order to check the volume actually injected, we show in Fig. 5.17 the superficial gas velocity over time. The superficial gas velocity in the simulation at the inlet was calculated from the volume injected at each Eulerian time step during the simulation and compared with the target value specified from the air flow-meter of an experiment. The average of the time step values can be compared with the target value of the experiments, verifying that the injection process in the simulation was performed properly.

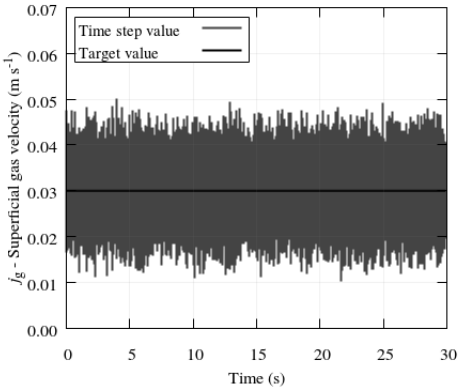

Figure 5.17: Superficial gas velocity at inlet in the simulation compared with the target value j_l=0.03 m s^{-1}.

It is necessary to remark that a deviation is expected in the experiments between the air flow rate given by the flowmeter and the actual value measured by the probes (typically provided by the authors in the experiments), that should be taken into account when analysing the computational results. The air flow rate measured at the probes, $Q_{\mathrm{g,probes}}$, is compared with Q_{g}. The former is obtained from the cross-sectional averaged α_{d} and V_z. The resulting value of $Q_{\mathrm{g,probes}}$ is around 7% lower than Q_{g} for PW05003.

The data measured at z/D=22.4 is considered for the inlet of our simulation, so the experimental measures of N_t were used to estimate $f(r)$ for the injection in the simulation. In Fig. 5.18 we compare with experimental data and the results of the simulation immediately after the injection. The comparison for N_t and α_{d} profiles shown that the injection was performed representing the experimental data provided.

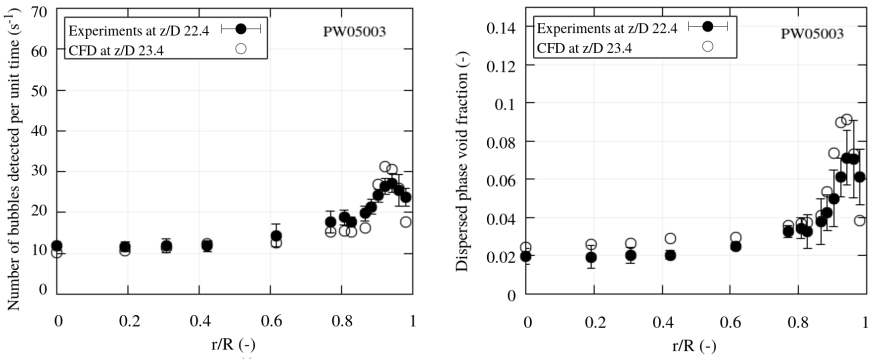

Figure 5.18: Radial profiles at the simulation inlet to test the injection algorithm.

The three injection patterns shown in Fig. 5.15 were used to analyse the axial evolution of the carrier phase velocity and void fraction at the centre of the pipe (r/R=0) and near the wall (r/R=0.94). In Fig. 5.19 we can appreciate how the velocity is affected by the bubbles, especially for the random r and θ position pattern.

The simulations predict, that even for the more restrictive pattern injection checked, the influence of the injection is smoothed as the flow advances and eventually lost after a certain evolution distance. For this particular experimental facility, the mid-port location is set at z/D=61.0, so one can expect that the experimental results for this flow configuration do not depend upon the injection. But other flow configuration, or even different port locations in case for other experimental facilities, may lead to results that depend on the injection so, in general, a proper radial injection seeding is mandatory for accurate validation.

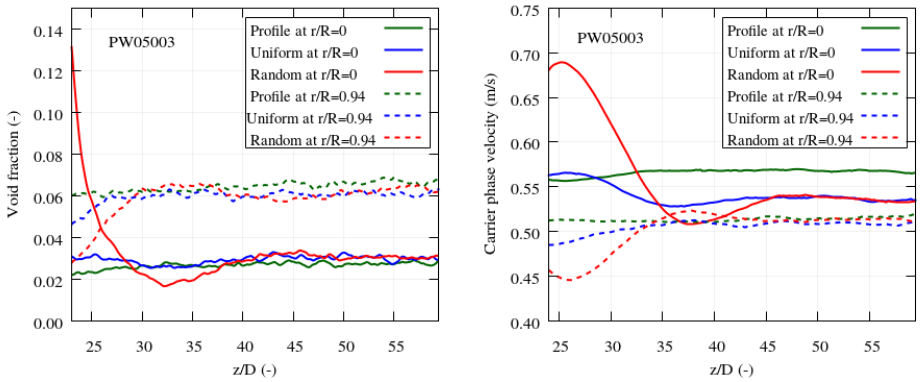

Figure 5.19: Axial evolution of void fraction and carrier phase velocity at several radial locations according to the different injection analysed.

Also, note that for some flow configurations, coalescence and breakup become an important phenomenon. For these cases, the accumulation of bubbles due to a non-accurate injection algorithm would lead to unrealistic coalescence and breakup rates. In summary, a proper seeding of the bubbles at the inlet is of great interest for an adequate validation of the code. Consequently, this injection model was applied in our simulations and can be used in the simulations in pipes or circular sections from a given point where enough information is known or estimated.

5.7 Bubble size distribution and axial evolution

According to the particle size, a disperse multiphase flow can be classified as monodisperse (uniform size) or polydispese (non-uniform size) flow. In many simulations we can assume the bubble size is uniform either because the dispersion of the BSD is small enough, or because the assumption of monodispersity does not actually compromise the quality of the results. But in general, flow characteristics depend on BSD polydisperse nature so it must be included for detailed and accurate simulations.

In bubbly flows the bubble size is an important parameter to numerically predict the flow characteristics and it is needed to adequately describe the size distribution in space and time. If we want to predict the axial evolution of bubbly flow, in the air-water systems dealt here, we must take into account the pressure changes along the pipe that have a significant influence on bubble size and bubble volume. The axial evolution of the pressure for the PW05003 scenario is illustrated in Fig. 5.20 to show this change. The simulation was compared with the experiments to ensure that the pressure values are accurate to apply an expansion model.

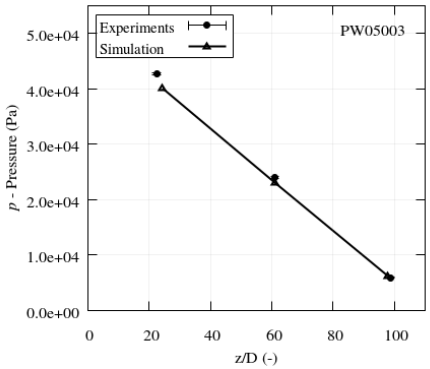

Figure 5.20: Axial evolution of cross-section average pressure.

5.7.1 Simplified model for bubble expansion

The modelling of the gas decompression was performed updating the radius of the bubble each time step during the tracking. The volume increase and the radius, can be estimated based on the Young-Laplace equation and the ideal gas law. The Young-Laplace equation defines the pressure inside a gas bubble, p_{b}, assuming it remains mechanically stable as:

$$p_{\mathrm{b}} = p_{\mathrm{H}} + \frac{2\gamma}{r_{\mathrm{b}}}, \tag{5.32}$$

being p_{H} the hydrostatic absolute pressure computed from the pressure field p:

$$p_{\mathrm{H}} = p_{\mathrm{atm}} + \rho_{\mathrm{c}} p + \alpha_{\mathrm{c}} \rho_{\mathrm{c}} g h, \tag{5.33}$$

where h is the height of fluid column. Assuming an isothermal expansion and introducing the ideal gas law, one can obtain the following relationship, between the bubble radius at current time step, $r_{\mathrm{b,t}}$, and the bubble radius at previous time step, $r_{\mathrm{b,t\text{-}1}}$:

$$r_{\mathrm{b,t}}^3 p_{\mathrm{H,t}} + 2\gamma r_{\mathrm{b,t}}^2 - r_{\mathrm{b,t\text{-}1}}^3 \left(p_{\mathrm{H,t\text{-}1}} + \frac{2\gamma}{r_{\mathrm{b,t\text{-}1}}} \right) = 0. \tag{5.34}$$

5.7.2 Axial evolution study and validation

In order to assess and validate the model, we show first in Fig. 5.21 the axial evolution of the BSD for PW05003, comparing the equivalent diameter and chord length distributions at z/D=22.4 and z/D=98.7. The BSD was measured experimentally by image processing at different heights appreciating the expected bubble size expansion, and in the same way it is noted by the chord length distribution measured by the probes. Based on the BSD at z/D=22.4 we included a theoretical distribution at z/D=98.7 assuming the pressure change on bubble size and using the pressure measured at these ports. The estimated distribution is, in fact, a scaled distribution by the factor f_{ij} (Eq. 2.24) that matches the experimental data at z/D=98.7 with good agreement. In the simulation the BSD were extracted from the total bubbles in the system at a given height and the chord length distribution with the *signal variable* of the VNPS. Chord length and bubble size distribution at the given heights are similar as the measured.

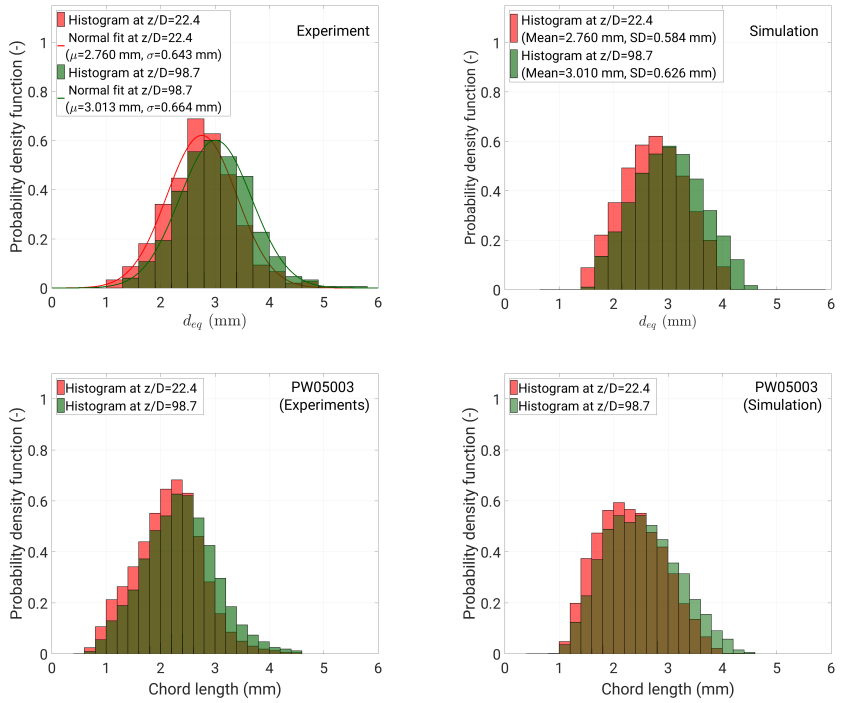

Figure 5.21: Bubble size and chord length distributions for experiments and simulations.

The significant changes in terms of volume and bubble size may influence on the bubble evolution along the pipe. For the sake of argument, we examined in de-

tail the PW05003 case (Fig. 5.22), comparing at the top measurement port, void fraction radial profiles for three scenarios: a monodisperse case with size the mean of the distribution, a uniform size at inlet that includes the bubble expansion and a polydispersed flow with the 95% of the bubble sizes considered from the experimental size distribution at z/D=22.4 including, in like manner, the bubble expansion.

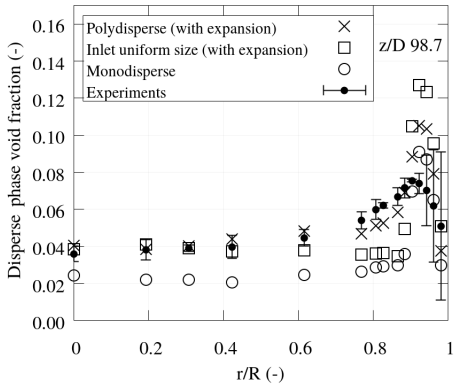

Figure 5.22: Dispersed phase void fraction at z/D=98.7 for PW05003 comparing three cases: polydisperse with expansion (95% of the bubble sizes of the BSD), inlet uniform size with expansion (mean size of the BSD) and monodisperse (mean size of the BSD).

Note that the monodisperse case underpredicts the void fraction as shown in the figure as the bubble expansion can not be considered to maintain the monodisperse constraint. The difference between the polydisperse and the inlet uniform size reveal significant discrepancies on the void fraction close to the wall, because of differences in force balances, interactions with the wall and contributions of volume in space from different bubble sizes. In addition to the void fraction, the effect of the polydispersity on other variables (i.e. bubble frequency, interfacial area concentration, chord lengths or Sauter mean diameter) result more significant and may lead to an erroneous interpretation of the results when comparing with the experiments. Therefore, the flow must be considered as polydisperse for an accurate comparison, even if coalescence or breakup is negligible.

5.8 Bubble dispersion and pseudoturbulence

5.8.1 Carrier phase turbulence model

The bubbles motion produces random velocity fluctuations along their trajectories in the carrier phase. This can be considered as a pseudoturbulence according

to Wijngaarden (1998) and means an increase of turbulent velocity fluctuations due to the pass of bubbles. This produces an excess energy that needs to be considered in the turbulence models. A κ-ε turbulence model for gas-liquid two-phase flow similar to Kataoka et al. (1989), Morel (2016), and Troshko et al. (2001a) is used in this work. According to these models the interfacial effects are considered explicitly in the transport equations for these turbulent variables. The total mixture turbulent kinetic energy is obtained by the summation of the κ_k-equation and considering the gas-phase turbulence negligible in comparison with the liquid-phase turbulence (Kataoka et al. 1989). The following equation is obtained for κ:

$$\begin{aligned}\frac{\partial}{\partial t}(\alpha_{\mathrm{c}}\kappa_{\mathrm{c}}) + \nabla\cdot(\alpha_{\mathrm{c}}\mathbf{U}_{\mathrm{c}}\kappa_{\mathrm{c}}) = \nabla\cdot\left[\alpha_{\mathrm{c}}\left(\nu_{\mathrm{c}}+\frac{\nu_{t,\mathrm{c}}}{\sigma_\kappa}\right)\nabla\kappa_c\right] \\ + \alpha_{\mathrm{c}}\mathbf{R}_{\mathrm{c}}:(\nabla\mathbf{U}_{\mathrm{c}}) - \alpha_{\mathrm{c}}\epsilon_{\mathrm{c}} \\ - \mathbf{M}^{\mathrm{h}}(\mathbf{U}_{\mathrm{d}}-\mathbf{U}_{\mathrm{c}}) - (p_{\mathrm{d}}-p_{\mathrm{c}})\frac{\delta\alpha_d}{\delta t} - \gamma\Gamma a_I, \quad (5.35)\end{aligned}$$

where $\nu_{t,\mathrm{c}}$ is the eddy viscosity, ε_{c} is the turbulent dissipation rate, and Γ is the rate of change of interfacial area. The turbulent Reynolds stress is defined as Serizawa et al. (1975) and Troshko et al. (2001a)

$$\mathbf{R}_{\mathrm{c}} = \nu_{t,\mathrm{c}}\left(\nabla\mathbf{U}_{\mathrm{c}} + (\nabla\mathbf{U}_{\mathrm{c}})^{\mathrm{T}} - \frac{2}{3}\mathbf{I}(\nabla\cdot\mathbf{U}_{\mathrm{c}})\right) - \frac{2}{3}\mathbf{I}\kappa_{\mathrm{c}} \quad (5.36)$$

The three last terms in the RHS of Eq. 5.35 are related to the interfacial effects on the turbulence kinetic energy. In particular the last two terms are included to be consistent with the expansion of the bubble described previously.

The turbulent dissipation rate equation used is based on the Kolmogorov's hypothesis (Pope 2000). Hence, the production and dissipation rates of ϵ_c are considered proportional to the production and dissipation rates of κ_{c} with a factor of ω_{c}=$\varepsilon_{\mathrm{c}}/\kappa_{\mathrm{c}}$ according to Launder et al. (1974). Conversely, the destruction of the turbulence produced by the interfacial effects must be related to the characteristic time scale of the pseudoturbulence produced by the bubbles (López de Bertodano 1998; Troshko et al. 2001a) with a dissipation frequency ω_b that needs to be modelled. The turbulence dissipation rate equation results:

$$\frac{\partial}{\partial t}(\alpha_c \varepsilon_c) + \nabla \cdot (\alpha_c \mathbf{U}_c \varepsilon_c) = \nabla \cdot \left[\alpha_c \left(\nu_c + \frac{\nu_{t,c}}{\sigma_\varepsilon} \right) \nabla \varepsilon_c \right] + \omega_c \Big(C_{1\varepsilon} \alpha_c \mathbf{R}_c : (\nabla \mathbf{U}_c) - C_{2\varepsilon} \alpha_c \varepsilon_c \Big) - \omega_b \Big(\mathbf{M}^h (\mathbf{U}_d - \mathbf{U}_c) + (p_d - p_c) \frac{\delta \alpha_d}{\delta t} + \gamma \Gamma a_i \Big), \quad (5.37)$$

where $C_{1\varepsilon}$, $C_{2\varepsilon}$ and σ_ε are defined as in Launder et al. (1974) and Troshko et al. (2001a). The dissipation frequency of the production terms produced by the bubbles (ω_b) was modelled in this work as suggested by Morel et al. (1997) (see Eq. 5.38). This is based on the relation of proportionality between interfacial turbulence production and dissipation of Elghobashi et al. (1983) and defining the characteristic time τ with the diameter of the bubble as the length scale (Morel et al. 1997; Yao et al. 2004b). Note that in our simulations the characteristic time can be defined, for accuracy, with the actual bubble diameter d_b and not the Sauter mean diameter as in the mentioned works.

$$\omega_b = \frac{C_{3\varepsilon}}{\tau} = \frac{C_{3\varepsilon}}{(d_b^2/\varepsilon_c)^{\frac{1}{3}}} \quad (5.38)$$

The constant $C_{3\varepsilon}$ was set to 1.0 in Yao et al. (2004b) for adiabatic scenarios similar to the ones studied in this work.

Finally, the law of the wall of Troshko et al. (2001a) and Troshko et al. (2001b) for two-phase turbulent boundary layers was implemented in the solver to obtain a more accurate description of the turbulence near the wall.

5.8.2 Bubble dispersion model

On the other hand, when using a RANS turbulence model, the average velocity $\mathbf{U}_c$ is solved. To compute adequately the forces including the liquid-phase turbulence effect, the instantaneous carrier phase velocity seen by the bubbles is modelled. The fluctuating velocity component $\mathbf{u}'_c$ has been modelled in the past using discrete random walk (DRW) (Buwa et al. (2006) and Gosman et al. (1983)) and continuous random walk (CRW) (Thomson (1987)) stochastic models. The latter solves the Langevin equation and provides a more realistic solution of the particle path than DRW. It should be noted that Large Eddy Simulation (LES) simulations could be used, in principle, to model the turbulence and compute the velocity fluctuations. However, the application of those models implies considerable grid restrictions that are inconsistent with the application of the unresolved CFD-DEM approach for the conditions of this work. Then, we use the two-equation turbulence for simplicity and to reduce the computational costs.

The velocity fluctuations can be obtained directly for homogeneous turbulence through a Markov chain based on the Langevin equation. In wall-bounded flows, the turbulence is expected to be inhomogeneous. Wilson et al. (1981) and Iliopoulos et al. (1999) proposed a normalized Langevin equation to consider the inhomogeneous turbulence. In addition, a drift correction was included to consider in the Markov chain the inhomogeneity and to avoid non-physical diffusion (MacInnes et al. 1992; Bocksell et al. 2006). For instance, it provides that tracer particles will follow streamlines on average (Dehbi 2008) but particles with a large Stokes number will have little influence from the fluid motion.

The normalized Langevin equation for isotropic inhomogeneous turbulence can be expressed as Dehbi (2008) to obtain the $\mathbf{u}'_{\mathrm{c}}$ for each bubble during the time. In this work the drift correction term is considered non-inertial for bubbles, and the equation results:

$$\mathrm{d}\left(\frac{\mathbf{u}'_{\mathrm{c}}}{u_{\mathrm{rms}}}\right) = -\left(\frac{\mathbf{u}'_{\mathrm{c}}}{u_{\mathrm{rms}}}\right)\frac{\mathrm{d}t}{\tau} + \sqrt{\frac{2}{\tau}}\mathrm{d}\boldsymbol{\xi} + \frac{1}{3u_{\mathrm{rms}}}\nabla\kappa_{\mathrm{c}}\mathrm{d}t, \tag{5.39}$$

where $\mathrm{d}\boldsymbol{\xi}$ is a succession of uncorrelated Gaussian random numbers with zero mean and variance $\mathrm{d}t$ for each direction.

From the definition of mean kinetic energy of the turbulence and for isotropic turbulence (Pope 2000):

$$u_{\mathrm{rms}} = u_{\mathrm{x,rms}} = u_{\mathrm{y,rms}} = u_{\mathrm{z,rms}} = \sqrt{\frac{2}{3}\kappa_{\mathrm{c}}} \tag{5.40}$$

In the boundary layer, Dehbi (2008) used a different Langevin equation to account for the anisotropy turbulence. The root-mean-square values in the boundary layer were obtained from DNS data in the channel flow simulation performed for particles. In turbulent bubbly flow in vertical pipes as the investigated in this work, DNS data set of two-phase flow pipe flow (in order to include the turbulence generated by the bubbles) for different Reynolds number would be needed but are not available in the literature. In addition, considering the bubble size distribution of this scenarios, the bubbles should not be affected strongly by the anisotropy turbulence. Therefore, Eq. 5.39 is applied in the whole domain.

5.8.3 Validation of the turbulence and dispersion models and influence on the results

Finally, we analyse the effects of both, CRW and two-phase flow turbulence model on the liquid instantaneous velocity and on the dispersed phase characteristics. Figure 5.23 shows the instantaneous liquid velocity $\mathbf{u}_c$ obtained with the LDA at z/D=98.7 and r/R=0 and the computational results. In the simulation, the bubbles passing by a location coincident with the LDA measurement over time, are selected as they store the actual value of $\mathbf{u}_c$. Higher peaks are appreciated above average in the experiments because of the velocity bias McLaughlin et al. (1973) and Zhang (2010) and is attributed to the LDA measurement technique.

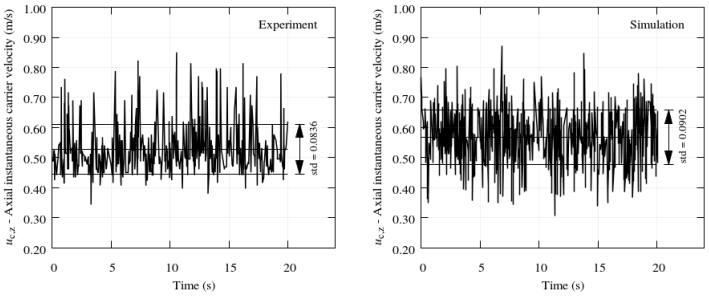

Figure 5.23: Experimental and computed axial instantaneous carrier phase velocity.

The bubble velocity distribution was analysed at the same position (z/D=98.7 and r/R=0) in Fig. 5.24. When no CRW is included (left figure), the bubble velocity distribution is dominated by the drag correlation. Then, the different velocities are explained mainly by the different bubble sizes. This results in an apparent underprediction on the bubble velocity fluctuations. When the CRW is included (central figure), the bubble velocity distribution is clearly wider and looks similar to the experimental one (right figure).

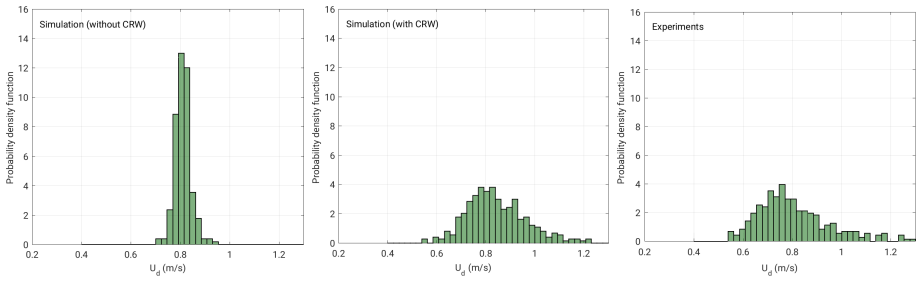

Figure 5.24: Comparison between experiments and simulations of the probability density function of the dispersed phase velocity obtained by VNPS at z/D=98.7 and r/R=0 for PW05003. Simulations performed with and without CRW.

The influence of the instantaneous liquid velocity through the CRW model has a major impact for the time-averaged void fraction profiles as illustrated in Fig. 5.25. The CRW was not considered for some tests ($\mathbf{u}_c$=$\mathbf{U}_c$) and the turbulence produced by the bubbles (BPT in the figure) was neglected (canceling the last three terms in Eq. 5.35 and Eq. 5.37) for different combinations as shown in the figure. It is well noticed the effect near the wall. When the liquid velocity fluctuations were not considered the void fraction peak is further accentuated and minimum values are found close to this area. In contrast, using the dispersion model and a turbulence model considering the bubbles effects, a more accurate profile is obtained.

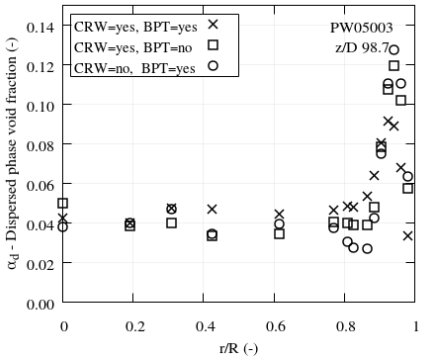

Figure 5.25: Dispersed phase void fraction at z/D=98.7 for PW05003 comparing the influence of the turbulence effects with CRW and BPT.

In order to gain a deeper insight into the effects of the CRW into the void fraction profile, we analyse the path followed by bubbles of similar diameter (2.7-2.8 mm) seeded at the inlet in the vicinity of the wall (r/R>0.9) for the PW05003 case. These paths are shown in Fig. 5.26.

The figure represents the normalized axial distance against the normalized distance to wall of the bubble centre. The figure on the left side shows the paths followed when CRW is not included. In this case, the bubbles studied tend to an equilibrium position that results mainly from a force balance between lift and elastic collisions against the wall. In contrast, when the CRW is used (right figure), the fluctuation effects are clear. Some bubbles leave the equilibrium state presumably because of the dispersion effects and, furthermore, because an increase in the number of collisions with the wall and in the collision energy, leaving the bubble beyond the range of influence of the lift force. This produced a temporal migration of some bubbles close to the centre and is more significant as the bubble increase its size with the height. Furthermore, we can compare the presence of bubbles in the range of r/R between 0.75 to 0.9 for both cases and the corresponding void fraction shown before in Fig. 5.25.

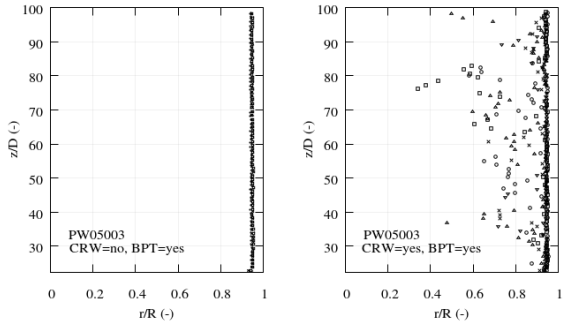

Figure 5.26: Distance to wall along the axial distance of 5 randomly selected bubbles of size 2.7 to 2.8 mm and seeded at r/R>0.9 for simulations with and without the CRW stochastic model. Each symbol represents the distance to wall of each bubble.

In addition, we select bubbles from small to large diameters present in the simulation. The normalized distance is plotted against the distance to wall for bubbles of different size (Fig. 5.27 and Fig. 5.28). In the figure, one can appreciate how smaller bubbles tend to rise close to the wall. In contrast, bigger bubbles travel throughout the pipe. As a consequence, they contribute on the void fraction more further from the wall without this meaning a lateral migration deriving from a negative lift force coefficient. Furthermore, the axial bubble size increase makes some bubbles more favorable to bounce during their rising.

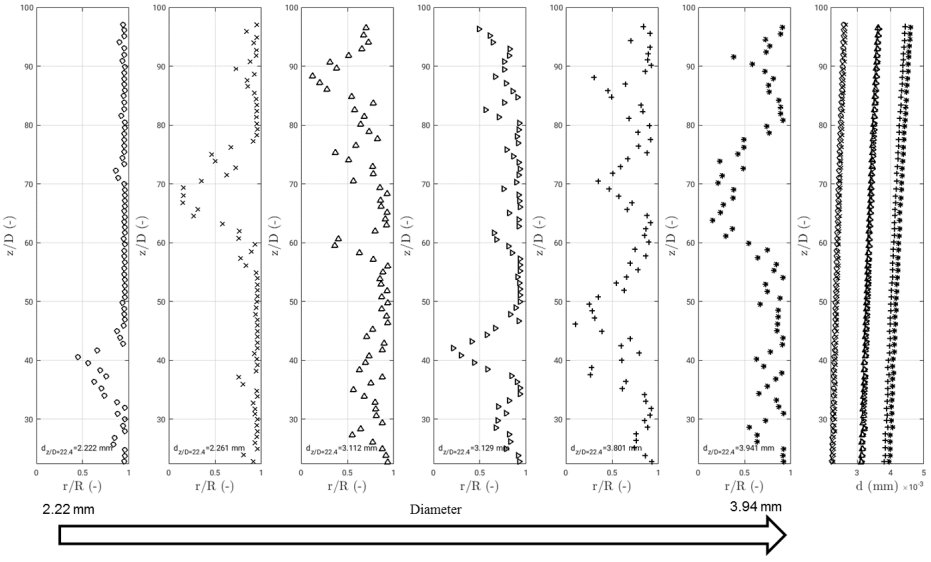

Figure 5.27: Distance to wall along the axial distance for *bigger* bubbles.

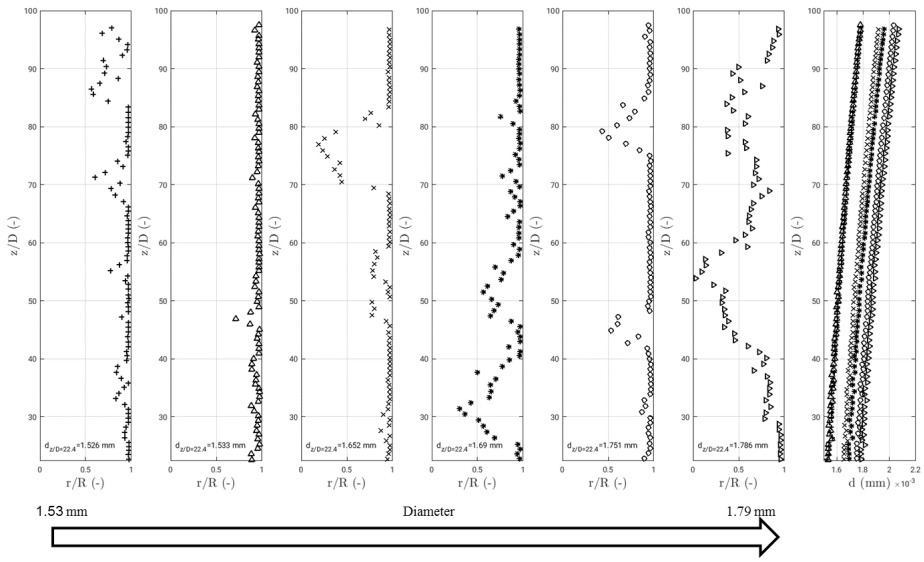

Figure 5.28: Distance to wall along the axial distance for *smaller* bubbles.

Close to the wall, bubble bounces are also appreciated in the experiments. As an example, Fig. 5.29 shows the rise of a bubble interacting with the wall.

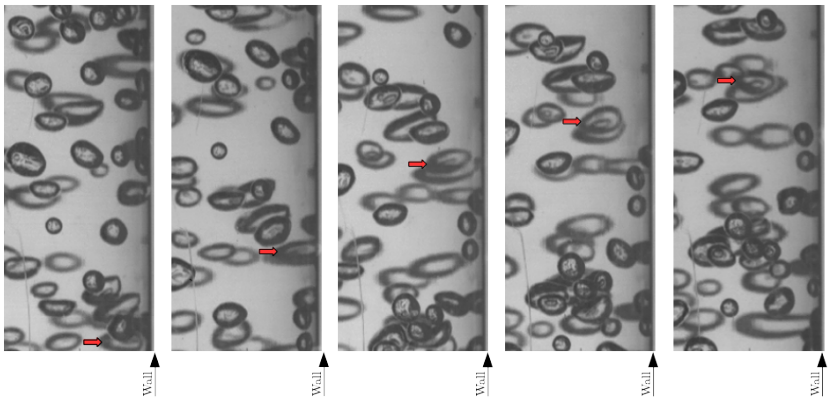

Figure 5.29: Image sequence of a boubble interacting with the wall.

In the images is appreciated how the bubble pointed out with an arrow collides with the wall. In fact, it is shown how the bubble's side in contact with the wall is detached. After that, the bubble moves far from the wall. This effect is mentioned by Alajbegovic et al. (1999), noting that the bubble-wall force would be responsible of moving the bubbles to the flow stream. This behavior is also noted

by Vries (2001). The latter studied the bubble-wall interactions demonstrating how a bubble can bounce repeatedly against the wall, or depart away from the wall, depending on the bubble size.

The lateral forces are responsible for the void fraction radial profile and the path of the bubbles. We analyze in Fig. 5.30 the radial component of lift and wall lubrication force at the bubble centroid. These results show that the wall lubrication force is negligible, for this case, in comparison to the lift force. Close to the wall positive values of lift force are found as expected, with different contributions depending on the bubble size.

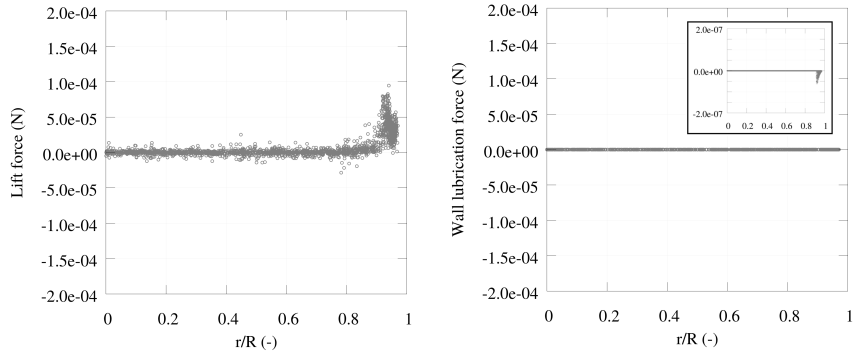

Figure 5.30: Computational results of radial component of lift and wall lubrication forces at the bubble centroid position.

Negative values of the lift forces are also appreciated although only positive values of the lift coefficients are given. This is produced by the existence of local velocity gradients in the opposite direction to the average gradient.

In Fig. 5.31 we evaluate the influence that the wall lubrication force of Antal has in the system when its applied directly in a CFD-DEM solver. As a result of comparing one simulation including the wall lubrication force and the other neglecting this. Neglecting the wall lubrication force does not compromise the results as it usually happens in TFM. For instance, for this case, it shows that a rigorous implementation of this wall lubrication force results in similar results.

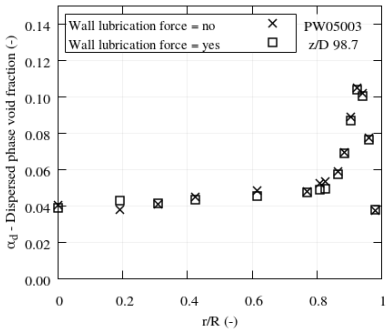

Figure 5.31: Influence of the wall lubrication force on the void fraction.

5.9 Results and discussion

The solver was finally used to predict and analyse the two-phase flow characteristics for the experiments and conditions displayed in Table 2.2. Variables as dispersed phase void fraction, dispersed and continuous velocity, interfacial area concentration, chord length, Sauter mean diameter or number of bubbles detected were compared. The dispersed phase data obtained with the VNPS is located at the same place as the experiments allowing a direct comparison. The continuous phase variables are located in the cell centre of the mesh and a linear interpolation was applied to obtain an estimated value at the same location of the experimental data.

The next sections show the comparison of radial profiles and cross-section average values. In the experiments, error bars were included when available. For PW05003 the error bars correspond to a 95% confidence interval obtained in the measurements through repeated observations.

5.9.1 Continuous phase radial profiles

The hydrodynamics of the liquid phase were evaluated with velocity and turbulent intensity profiles (Fig. 5.32). In addition, the velocity profile without gas (SP refers to the corresponding single-phase case in the figure) is shown, when provided by the authors, to highlight the influence of the bubbles on the carrier phase velocity. The computational results of velocity are in good agreement with the experiments in all the scenarios tested. The results for the turbulence intensity show a similar trend and are reasonably well predicted. The effect of the turbulence produced by the bubbles was compared with the single-phase case and fits the different experiments without the need of changing any coefficient in the two-phase turbulence model. In addition, the profiles maintain the same tendency between the different ports or

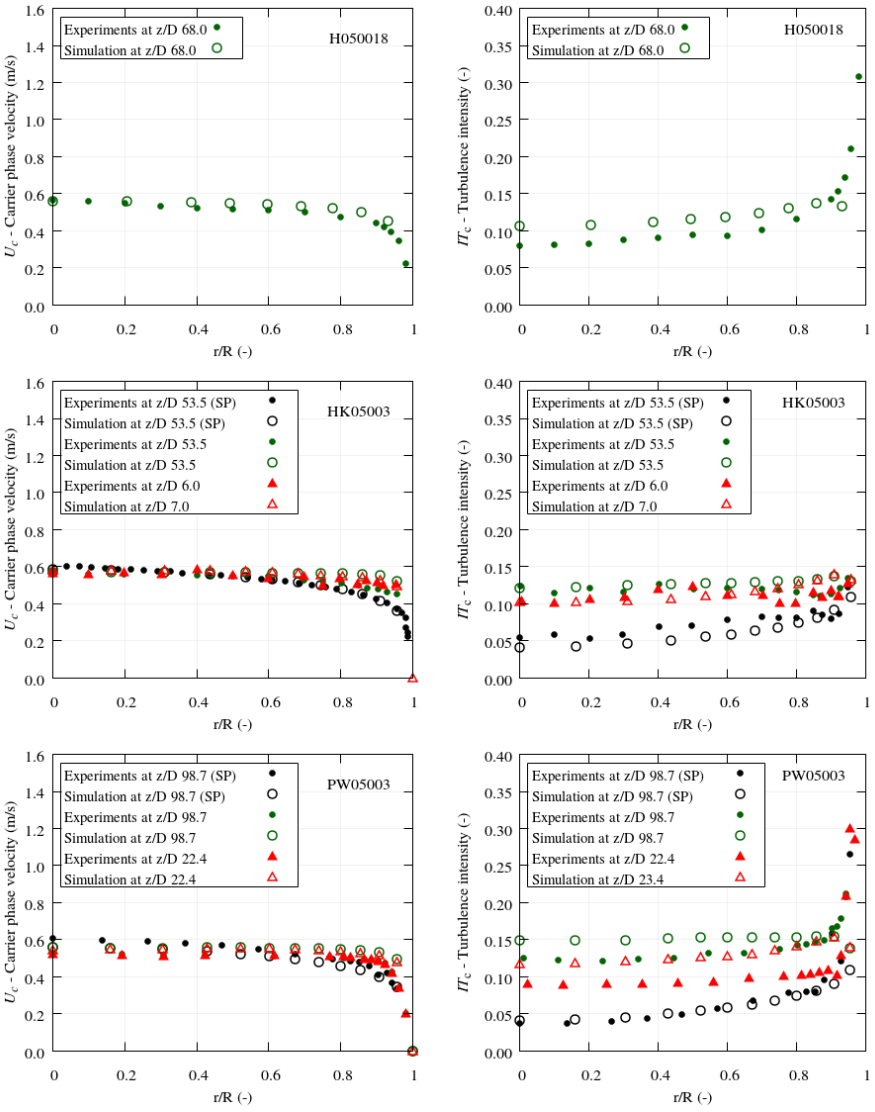

Figure 5.32: Carrier phase velocity and turbulence intensity comparison between experimental data and computational results.

heights as appreciated for HK05003 and PW05003. Close to the wall, for the results measured with LDA (H050018 and PW05003), the turbulence is underestimated.

In H050018 this occurs especially in a region with low void fraction, indicating that the discrepancies are due to the generation of turbulence in the vicinity of the wall. Nevertheless, this is a common problem with the single-phase κ-ε turbulence model. More complicated RANS or LES models can be used in simulations to improve the prediction of near-wall phenomena. This generally involves a sufficiently fine grid near the wall to resolve the wall-boundary layer. For two-phase flow, is not always possible to apply a near-wall refinement if we use in this scenarios the CFD-DEM approach for unresolved particles as we need to preserve the restrictions between the ratio of bubble and grid cell volumes.

5.9.2 Dispersed phase radial profiles

The dispersed phase variables that can be obtained experimentally are compared numerically following the techniques defined in Section 5.3. Variables as void fraction, bubble frequency, velocity, chord length and interfacial area concentration are shown in this section. In those cases in which the profiles are not provided by the authors, only the computational results are shown.

The time evolution of the cross-section average void fraction of the cell values of the simulations is shown in Fig. 5.33 (left). The void fraction between the three scenarios at different measurement ports provides useful information about the behaviour of the bubbly flow. The figures show where the bubbles arrive to a certain height, the pass frequency and the bubble expansion effect. The void fraction cross-section average values vary with time as the bubbles are passing through, contributing with a certain volume fraction depending on its size. In H050018 the number of bubbles in the system is low enough to leave the cells almost empty between time steps and the cross-section average vary considerably.

The void fraction profiles in Fig. 5.33 (right row) indicate, on the one hand that the different scenarios result in, for instance, a different significant void fraction profile between them. On the other hand, the void fraction profile evolves similarly as the experiment. For HK05003 the void fraction close to the inlet differs from the experiments mainly because the discrepancies between the experimental air flow rate and the measurement of the probes. Nevertheless, the profile at the outlet is predicted in good agreement with the experiments. For PW05003 the peak is more pronounced because of Q_{g} is around 7% higher than $Q_{\mathrm{g,probes}}$ as mentioned before. Furthermore, a discrepancy near the wall in the void fraction is expected as we assumed spherical bubbles in contrast with the ellipsoidally shaped bubbles present in the experiments.

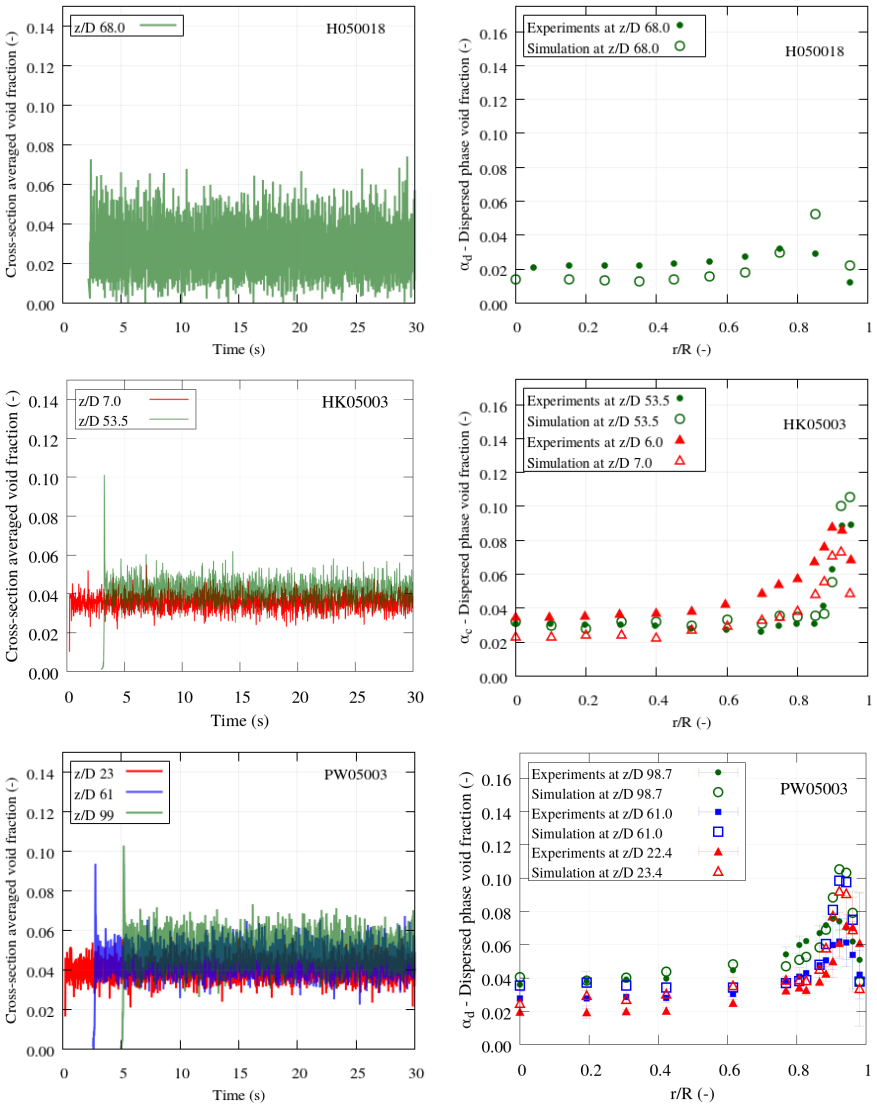

Figure 5.33: Evolution of the cross-section average void fraction at different heights and void fraction comparison between experimental data and computational results.

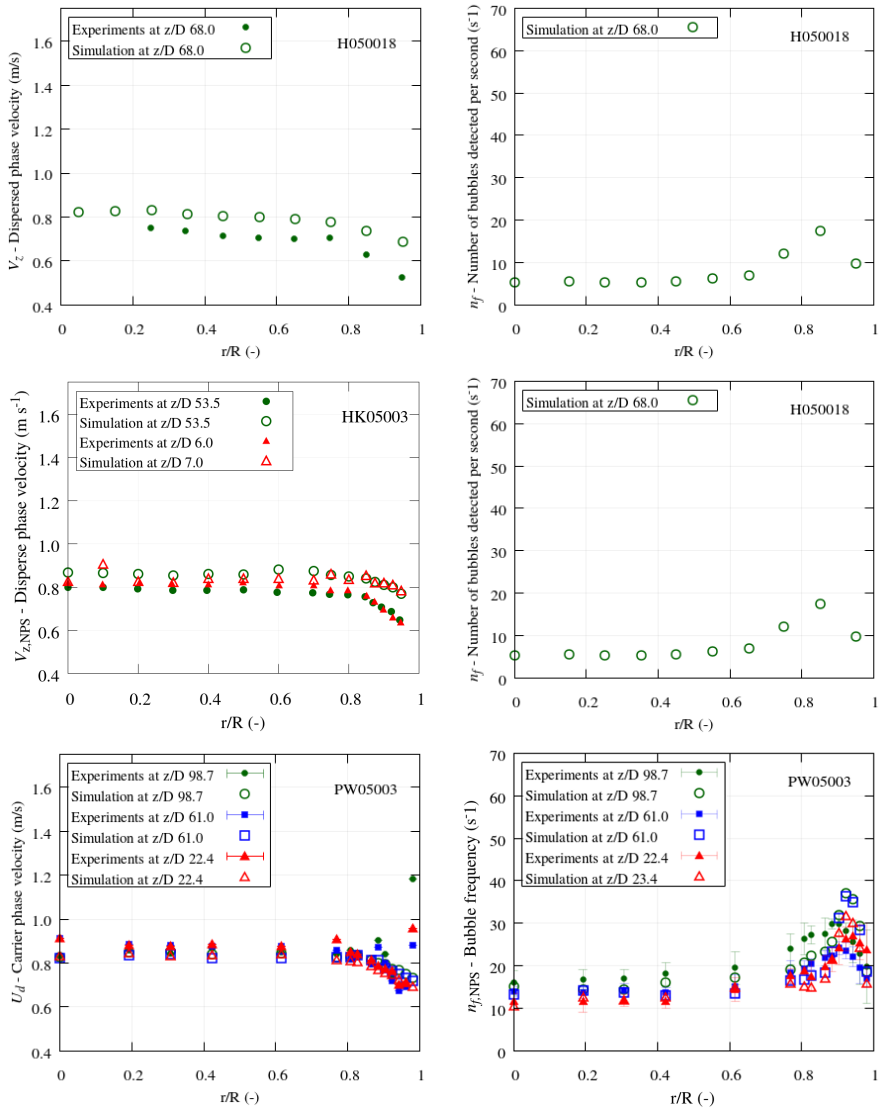

Figure 5.34: Dispersed phase velocity and bubble frequency comparison between experimental data and computational results.

Although the effect of the shape is included in the interfacial forces, the contribution of volume in space and time of an ellipsoid near the wall produces a smoother profile of void fraction. This is shown in Fig. 5.35 for bubbles close to the wall with different aspect ratios.

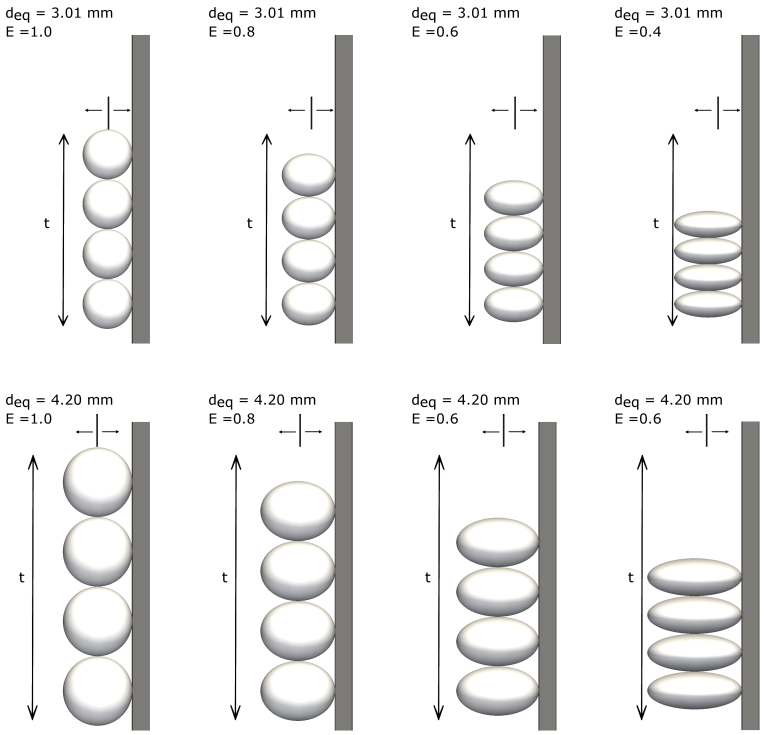

Figure 5.35: Illustration of a train of bubbles rising vertically sliding on the wall for different aspect ratio values.

The void fraction radial distribution assuming a train of bubbles is shown Fig. 5.36, verifying the effect mentioned.

The bubble velocity is compared in Fig. 5.34 (left). HK05003 and PW05003, used probes to measure this variables, so $V_{z,NP}$ is used in the simulation to compare the results. In contrast, in H050018 the velocity was measured by IP and then the comparison is performed with $V_{z,system}$. In general the three cases shows an overall good agreement in terms of trend and accuracy. The case HK05003 gives higher values of velocity near the wall for both carrier phase and dispersed phase velocities, but the predicted profiles in general agree quite well with the measured data.

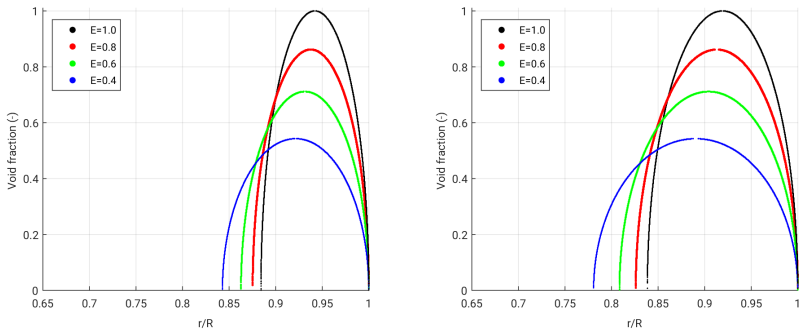

Figure 5.36: Void fraction profile that would result from a train of bubbles with d_{eq} 3.01 (left) and 4.2 (right) with aspect ratio from 0.4 to 1.0, rising parallel to the wall of a pipe with diameter 52 mm.

In addition to void fraction and bubble velocity, we are interested on the number of bubbles intersecting the probes that depends on the bubble size. We use the VNPS to compare the results with the experiments which implies the same probability of bubbles intersected by the probe. Moreover, a good agreement between experiments and simulations for bubble frequency and void fraction, is a good indicator of a suitable BSD passing through the probes. Figure 5.34 (right) shows the bubble frequency validation for PW05003 with satisfactory match. This indicates an increase of the number of bubbles detected between the low and top ports.

The interfacial area concentration was compared in Fig. 5.37 (left). The results are consistent and the trend agree well with experiments. Slightly differences in the values are presumably expected because of ellipsoids have in average a greater surface area compared with spherical bubbles seeded in the simulation.

The chord length profiles are shown in Fig. 5.37 (right). The comparison with the experimental data was performed for PW05003 but is shown for H050018 and HK05003 for convenience. As noted by Liu et al. (1998), among others, the bubble shape has a direct influence on the chord length, then the values can differ from experiments and simulations. In the figure, the effect of the bubble expansion, is also evident in the measurements of chord lengths. The radial profiles may suggest, at first glance, a rapid change on bubble size according to the chord lengths for the two cases with more deviation in the BSD (H050018 and PW05003).

Finally, Fig. 5.38 shows the comparison for the missing ratio for an individual case of PW05003 and not the mean, to emphasize into the local effects. As might be expected, the missing ratio values are larger in the experiments than in the simulations where the bubbles cross the probes ideally. However, similar tendencies

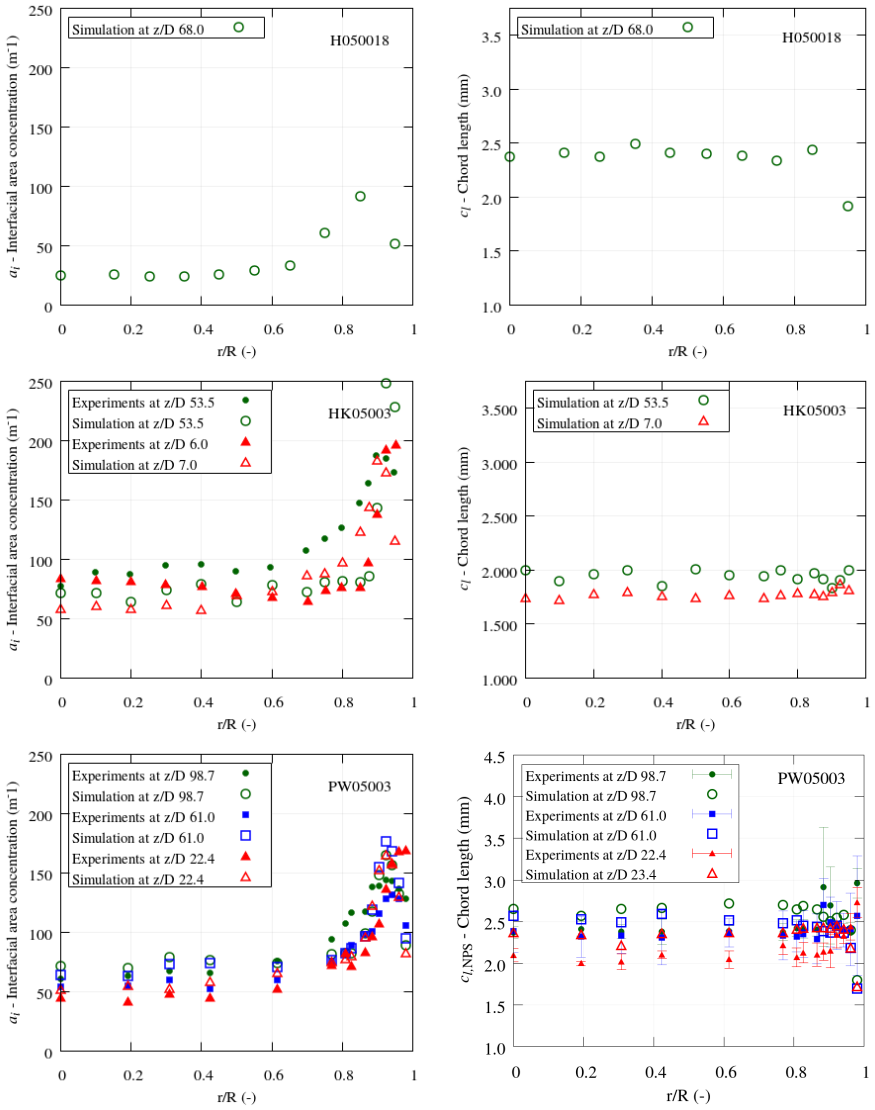

Figure 5.37: Interfacial area concentration and chord length comparison between experimental data and computational results.

were appreciated. Close to the wall, relative maximum values were obtained in radial positions where the bubble edge location is more probable to be hit (in this case 0.87 and approximately 1 r/R). Between this range lower values were obtained as the probability to hit a bubble center increase and, thus, the probability that the four probes detect the bubbles. This indicates that the bubble size is similar in both, experiments and simulations.

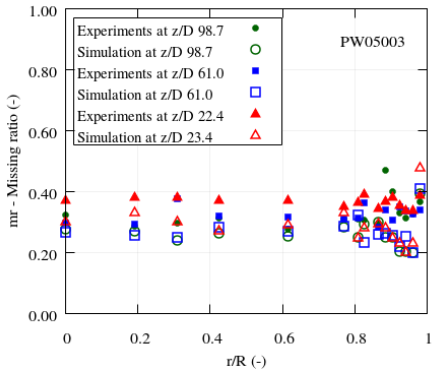

Figure 5.38: Missing ratio comparison between experimental data and computational results from Virtual Needle Probe System (VNPS) for PW05003.

5.9.3 Cross-section average evolution

The axial evolution for cross-section average variables was evaluated for PW05003 in this section. The axial evolution of the cross-section averaged void fraction is compared with the experimental data in Fig. 5.39.

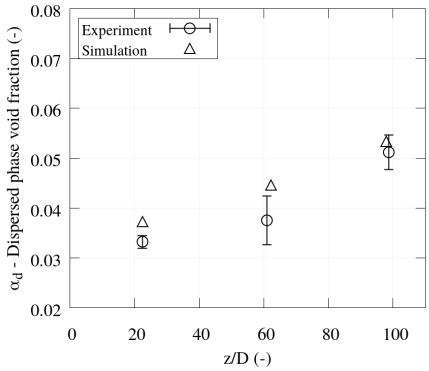

Figure 5.39: Axial evolution of area averaged void fraction for experiment and simulation using needle probes.

The void fraction value at the inlet in the simulation is slightly above the experimental one because of the differences between Q_{g} and $Q_{\mathrm{g,probes}}$ mentioned before. The axial evolution was predicted in good agreement compared with the experiments as shown in the figure.

The evolution of bubble frequency is also of great interest. Note that is not straightforward to anticipate if the total number of bubbles at different heights remains constant or by contrast any coalescence and breakup occurred. This is related with the probability to intersect a bubble in a probe. For instance, assuming only a change in size due to bubble expansion, the probability for the bubble to be intersected by the probe would increase necessarily with the increment in bubble size. Fig. 5.40 illustrates the case of a bubble with a radius increasing with height. In this case, the probability of a bubble to intersect the probe would also increase. Therefore, more bubbles would be detected at the top measurement port even if the total number of bubbles remains constant.

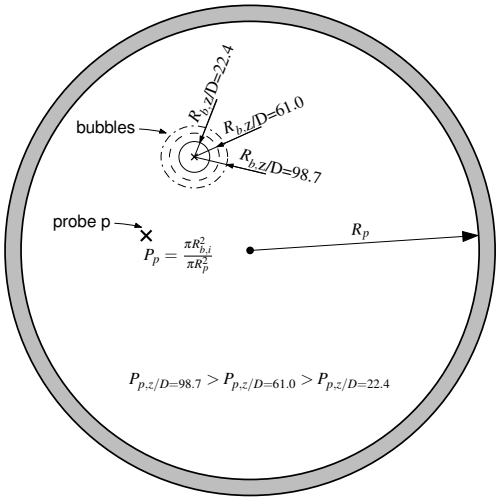

Figure 5.40: Schematic representation of the probability of detecting a given bubble by a probe as the bubble increase its size as a function of height.

The probability of detecting a bubble distribution with a probe with negligible area is:

$$P_p = \frac{\pi(\mu^2 + \sigma^2)}{\pi R^2} \tag{5.41}$$

If we assume a normal size distribution affected by the expansion, the sizes along the pipe would have a distribution with mean $\mu_i{=}f_{ij}\mu_j$ and variance $\sigma_i{=}f_{ij}\sigma_j$ that can be defined with the corresponding expansion factor (Eq. 2.24). The

ratio of probabilities between two heights where pressure is known, would give the following relation for the number of bubbles detected:

$$n_{f,i} = f_{e,ij}^2 n_{f,j} \tag{5.42}$$

In Fig. 5.41 the bubble frequency for the experiment and simulation is detailed. The theoretical prediction using Eq. 5.42 is included in the figure. An increase is shown between low (inlet) and top (outlet) ports of around 20% that could be attributable only to the bubble expansion and not to changes on size due to breakup and coalescence. The experiments are in good agreement with this prediction and the simulations are in overall good agreement.

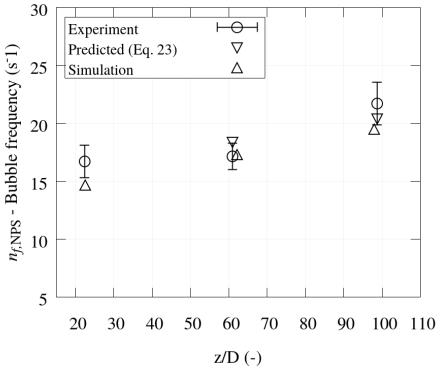

Figure 5.41: Axial evolution of area averaged bubble frequency for experiment and simulation using needle probes.

5.9.4 A critical assessment on validation procedures against needle probes experimental data

The previous section described the comparison of experimental and computational results with analogous assumptions. These assumptions produced a deviation of the obtained values with respect to the values of the variables currently on the system. Then, using the validation methodology described in this work we performed a comparison with the *system*, *probe* and *signal variables* described in Section 2.7 to analyse the case PW05003. The following study is focused for this experiment using four-sensor probes, but it can be applied to dual probes.

The deviations on the measured diameter are due to different causes. On the one hand, the missing bubbles tend to be those with smaller chord lengths, then the resulting chord length distribution does not match the expected one and the mean diameter calculated is overestimated. Figure 5.42 illustrates this for a four-

conductivity probe. In this figure one can appreciate two scenarios: a paired bubble where all the tips hit it, and a missed bubble where one tip is on the limit beyond which the bubble is considered missed. For instance, the missed bubbles will always tend to hit with a chord length from the outermost of the bubbles that will depend on the distance of the tips. As a result, the mean of the chord length distribution obtained will be considerably higher. For the Sauter mean diameter, the interfacial are concentration is also affected. This is indeed taken into account in the definition of a_{I} for the four-conductivity probes by the correction $a_{I,cor}$ of Corre et al. (2002).

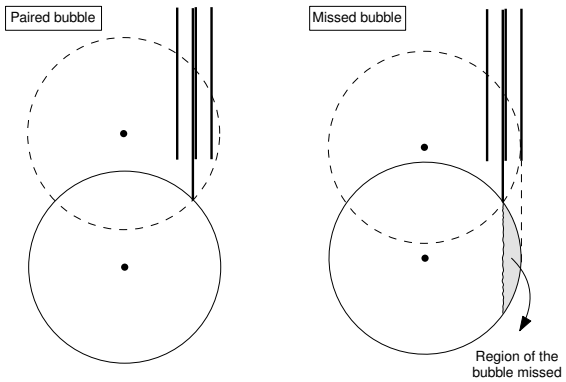

Figure 5.42: Illustration of a paired bubble and a bubble in the limit to be missed.

On the other hand, the measure of mean diameters from the chord length implies several assumptions as that the bubbles are rising vertically that is far from reality in turbulent bubbly flows, and may lead to an overestimation. In Fig. 5.43 (left) we show the actual chord length of a given bubble rising with a lateral component of velocity. Furthermore, the values are largely conditioned near the wall and classical statistical assumptions to obtain mean diameters ($d_{10,\mathrm{NP}}$ and $d_{32,\mathrm{NP}}$) could result in biased and misleading results. As shown in Fig. 5.43 (right) the probes hitting a bubble with a distance d_w smaller than $2r_b$ will have a biased statistics of the measure. For example, the chord lengths seen by the probe will not be randomly distributed in the range between 0 and $c_{l,max}$. Then, Eq. 2.21 will give unrealistic values for this range. Depending on if the probe position is placed at d_w, below or above, expected, underestimated or overestimated values will be given respectively (Kalkach-Navarro et al. 1993). In addition if a bubble is sliding along the wall, the measures will be conditioned to obtain repeatedly the values at a given d_w. This effect will be similar when computing the a_I as the measured normal velocity is also conditioned by the position. If a_I is measured by four-conductivity probes, $a_{I,cor}$ give non-accurate results as it was defined for scenarios with a random distribution in the probe. Then, in the region near the wall the missing ratio is dominated by the bubble position as shown in the missing ratio profiles in Fig. 5.38.

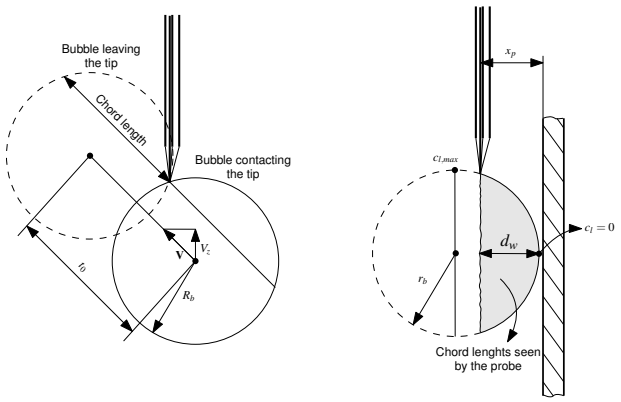

Figure 5.43: Schemes of potential source of error when measuring chord length .

Besides the above, the diameter of the bubbles seen in the probes are statistically from bigger bubbles than the existing in the domain. This will have an effect on the measured variables as chord length or velocity. In fact, we can find the relation between $d_{10,\text{system}}$ and $d_{10,\text{probe}}$ using the findings of Clark et al. (1988) and Liu et al. (1998). If we assume the BSD in the system follows a normal distribution described by Eq. 5.43, the BSD of bubbles touching a probe with negligible size can be estimated as Eq. 5.44.

$$f_{system}(d_{eq} \mid \mu, \sigma^2) = \frac{1}{\sqrt{2\sigma^2\pi}}\, e^{-\frac{(d_{eq}-\mu)^2}{2\sigma^2}} \tag{5.43}$$

$$f_{probe}(d_{eq} \mid \mu, \sigma^2) = \frac{d_{eq}^2}{\mu^2+\sigma^2}\frac{1}{\sqrt{2\sigma^2\pi}}\, e^{-\frac{(d_{eq}-\mu)^2}{2\sigma^2}} \tag{5.44}$$

The ratio between the mean diameters from the system and the detected by the probes integrating both probability density functions, results:

$$\frac{d_{10,probe}}{d_{10,system}} = 3 - \frac{2\mu^2}{\mu^2+\sigma^2} \tag{5.45}$$

In the simulations, the actual diameter passing through the probes, $d_{10,\text{probe}}$ is known and is compared with the obtained from the signal $d_{10,\text{NP}}$. Hence, this is particularly useful to evaluate the measurement methodology in a scenario similar as the given in the experiments. In Fig. 5.44 both variables are compared showing important discrepancies existing even in an ideal case as the presented in a simulation.

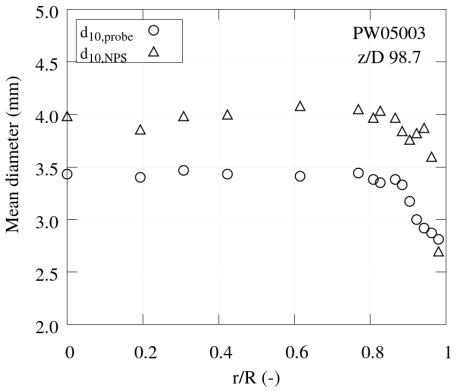

Figure 5.44: Computational results of mean diameters from *probe* and *signal variables* for PW05003 at z/D=99.8.

The profiles of $d_{10,\text{probe}}$ at the different measurement ports of the PW05003 simulation are shown in Fig. 5.45, to appreciate the evolution of the diameters with the height. As could be expected, smaller bubbles were found near the wall as a result of the bubble dynamics and force balances, for a case where only positive lift force coefficients are given (see Eq. 6.14). In particular the lift coefficient was mainly controlled by the Reynolds number in the whole system (d_{eq}<4.4 mm). However, this tendency was not fully detected for $d_{10,\text{NP}}$ in Fig. 5.44.

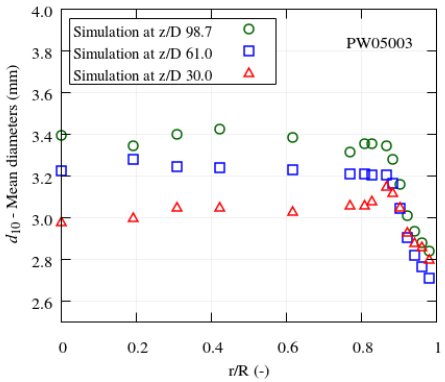

Figure 5.45: Computational results of mean diameters for different port measurement heights. Average performed directly with the diameters of all the bubbles passing by the probe.

The axial development of the mean diameters is shown in Fig. 5.47 for simulations and experiments. The computational results of the test case with inlet uniform size

shown in Section 5.7, was included to state the influence that the polydispersity could have on the computational results when using sensor-probes.

Cross-section average of the arithmetic mean diameter was obtained from different ways. The *system variable* $d_{10,\text{system}}$ represents the mean diameter actually in the system at different heights. It was obtained over all the bubbles passing at the given height. Different values are given by $d_{10,\text{probe}}$, that was obtained through the diameters seen by the probes, distinguishing in turn, the diameters from all the bubbles detected by the probe and the diameters from bubbles that were actually paired. The variable $d_{10,\text{NP}}$ was obtained for experiments and simulations with the chord length from the signal generated as in Eq. 2.21. The figure also includes the experimental variable $d_{10,\text{IP}}$.

The comparison revealed, first of all, for the inlet uniform size case that any discrepancies are appreciated between $d_{10,\text{system}}$ and $d_{10,\text{probe}}$ as the bias because of the size is not given when the size is uniform. The difference between these values and $d_{10,\text{NP}}$ is given even for this case. In the polydisperse case the discrepancies between $d_{10,\text{system}}$ and $d_{10,\text{probe}}$ is noted as the bigger bubbles are more likely to be hit by the probes. The ratio between both variables is studied for the top measurement port of PW05003. The curve of Eq. 5.45 for a fixed μ of 3.01 is plotted against σ. The same ratio is obtained for the simulation with the data of the bubbles at the height of the top port, and the experiment with the parameters of the BSD measured with IP. Fig. 5.46 show how this ratio increase with the standard deviation of the distribution, indicating that the more polydisperse is the flow, higher values of mean diameters seen by the probes will be measured. This ratio increase quadratically and can produce important discrepancies in the diameters measured with the probes with small changes on the standard deviation of the BSD.

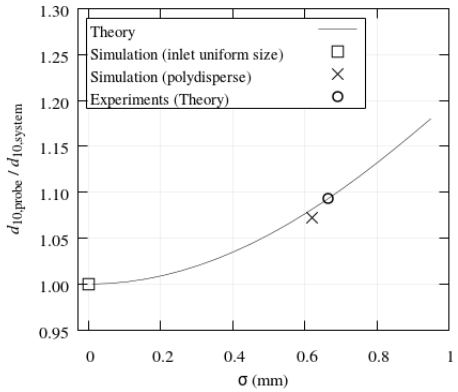

Figure 5.46: Ratio between the diameters seen by the probes and the diameters in the system as a function of the standard deviation of a normal distribution.

In Fig. 5.47 (left row), the values of $d_{10,\mathrm{NP}}$ should be coincident with $d_{10,\mathrm{probe}}$ but are overestimated with regard to $d_{10,\mathrm{probe}}$ for the above mentioned reasons. If we compare this values with $d_{10,\mathrm{system}}$ larger discrepancies are found. In the experiments, this effects were more pronounced as the polydispersity is expected to be higher but the trend is similar as in the simulations.

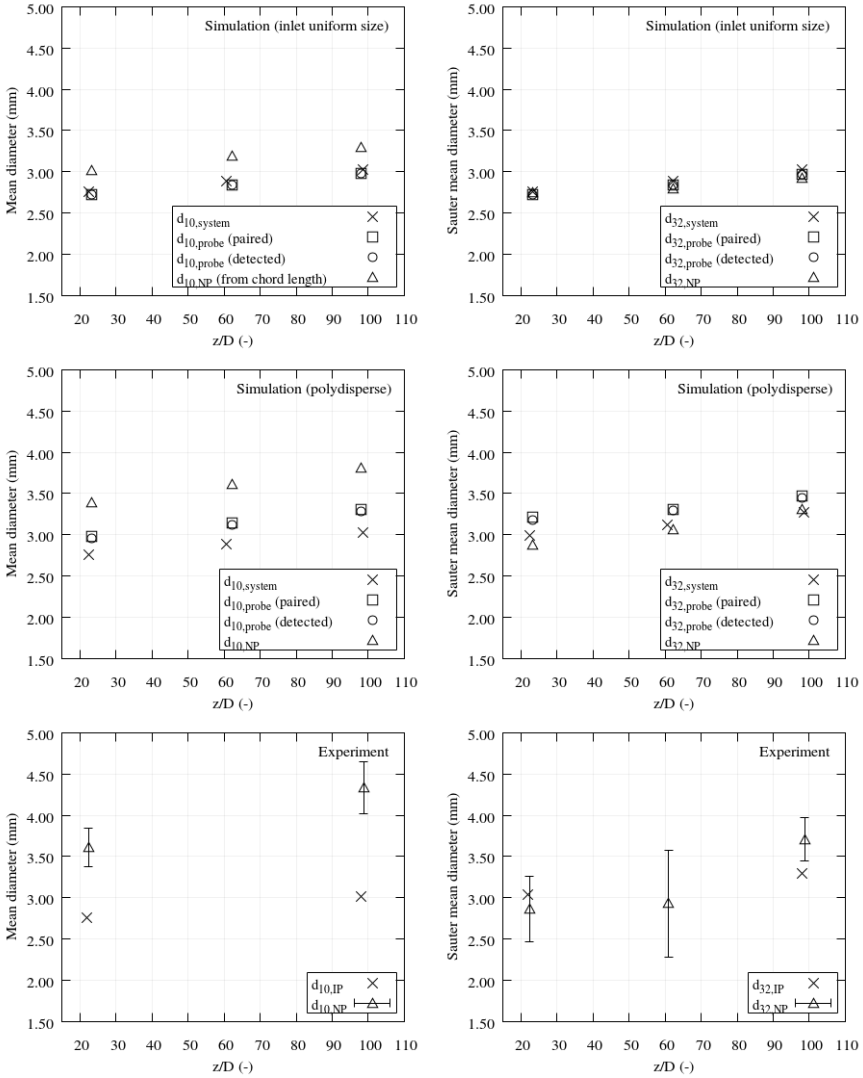

Figure 5.47: Axial evolution of area averaged mean diameters d_{10} and d_{32} for experiment and simulation.

The same study was performed with the Sauter mean diameters $d_{32,\text{system}}$, $d_{32,\text{probe}}$ and $d_{32,\text{NP}}$ in Fig. 5.47 (right row). The simulation with an inlet uniform size, give equivalent values of the three variables, and the values were similar to the arithmetic mean diameter of Fig. 5.47 as the bubble size deviation is almost zero at the different measurement heights. For the simulation with inlet polydisperse flow, the values of $d_{32,\text{system}}$ were similar to the experimental variable $d_{32,\text{IP}}$.

The Sauter mean diameter seen by the probes, $d_{32,\text{probe}}$, is higher than $d_{32,\text{system}}$ in the polydisperse case for the same reasons as shown for the arithmetic mean diameter. The values of $d_{32,\text{NP}}$ should be equal to $d_{32,\text{probe}}$ but in contrast are in good agreement with $d_{32,\text{system}}$. In this case, the bias near the wall is produced and the interfacial area of the bigger bubbles near the wall is not measured with uniform probability. Therefore, $a_{\text{I,corr}}$ produce, in average, overestimated values of a_{I} and then underestimated Sauter mean diameters. However, in this case both effects compensate and $d_{32,\text{NP}}$ and $d_{32,\text{system}}$ are in a good agreement.

As regards the bubble velocity, we compare $V_{\text{z,system}}$, $V_{\text{z,probe}}$ and $V_{z,NP}$. The results are shown in Fig. 5.48. In this case, $V_{\text{z,probe}}$ gives slightly lower values compared with $V_{\text{z,NP}}$. The trend of the bubble velocity near the wall is well predicted with the computed values of VNPS compared with $V_{\text{z,system}}$.

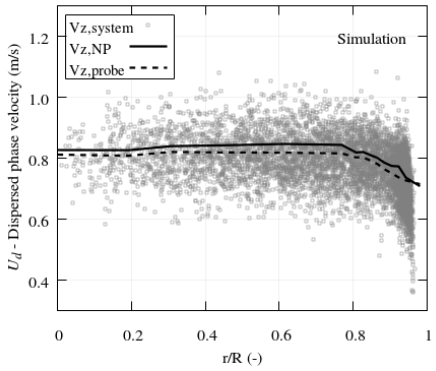

Figure 5.48: Computational results of bubble velocity for *system*, *probe* and *signal* variables for PW05003 at z/D=98.7.

Figure 5.49 show the cross-section average of the velocity and the comparison with the experiments. The values of $V_{\text{z,system}}$ are lower as the probe sees bigger bubbles and for this specific BSD it results in an underestimation of the velocity according to the drag correlation used. In contrast, $V_{\text{z,NP}}$ is in good agreement with the experiments as they were obtained with the same assumptions.

Finally, it should be emphasised that this study did not aim to propose new measurement techniques but emphasise on the existing methods to perform the

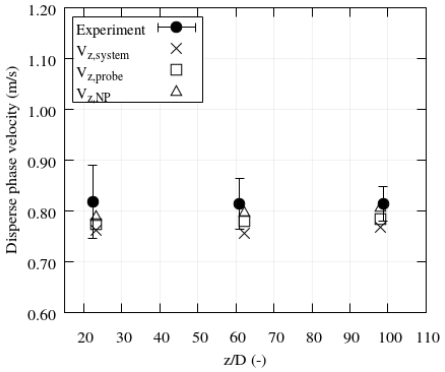

Figure 5.49: Axial evolution of bubble velocity for experiment and simulation.

validation of the solver and to study jointly results and experimental measurements itself from a critical point of view to reach unambiguous conclusions.

5.10 Conclusions

A new CFD-DEM solver has been developed using the OpenFOAM® library and proposed a novel validation scheme for a rigorous comparison between simulation results and experimental data. In order to exclude complex phenomena such as bubble breakup and coalescence, the present study was limited to specific bubbly flow conditions in vertical pipes. Then, the flow dynamics is expected to be governed by the bubble forces and the coupling between phases. Thus, the solver was configured to include these phenomena. The results of radial profiles and axial evolution have been validated against experiments from different authors, employing different pipe diameters and measurement techniques. With the solver setup proposed, it was noted a strong agreement between simulation results and experimental data for all conditions without the use of any tuning parameter.

The solver includes the coupling between phases, the required interfacial forces, a two-equation turbulence model for two-phase flow and the consideration of the bubble-bubble and bubble-wall interaction with a soft-sphere model. Several contributions were required, in addition, to develop the presented CFD-DEM solver. The first consisted of a new sub-element method to provide stability and precision on the exchange of momentum and volume fraction, basing on equivolumetric divisions of the spheres.

Once the coupling between the phases was performed accurately, we focused on the development of an algorithm to seed the bubbles as close as in the experiments as possible to provide a correct inlet condition. The new proposed algorithm

permits to adjust the locations, velocities and sizes of the bubbles to match any required inhomogeneous bubble size distribution. To illustrate the potential of this algorithm, it was shown that, under scenarios without breakup and coalescence, the flow characteristics are not dependent on the injection pattern above a certain height.

Furthermore, the changes in size and volume of the bubbles produced by the pressure variations were investigated experimentally, and were taken into account by means of a simplified model integrated in the bubble tracking through the Young-Laplace equation and the ideal gas law. The results indicated that this model was required to obtain accurate result. In addition, a polydisperse and a uniform inlet case were compared to demonstrate that considering the dynamics of the different sizes, and bubble expansion of the population led to better results.

With respect to the turbulence modelling, a two-phase flow κ-ε model was used as the CFD-DEM formulation limits the grid refinement in the near-wall region. In order to include the turbulent dispersion, a Continuous Random Walk stochastic model was used to compute the instantaneous liquid velocity seen by every bubble. Bubble pseudoturbulence was considered in the κ-ε including the effects of the bubble expansion. The instantaneous liquid velocity and the probability density function of the bubble velocity were properly captured using these models comparing with the experiments. The relevance of the turbulent effects was clearly shown in the void fraction profile and bubble paths. Noting that the dispersion was accounted in this work without the need of a turbulent dispersion force and any tuning coefficient.

An exhaustive validation has been made possible through a new method, Virtual Needle Probe System (VNPS), consisting of emulating the sensor probe experimental technique. This method provided a set of square signal for each probe location that was processed with the same program used to obtain the variables in the experiments. This allowed to extract dispersed phase variables from the simulation by matching the same approximations as in the analysis of the experimental data. In this way, dispersed phase variables from the simulation as void fraction, bubble velocity, bubble frequency, interfacial area concentration, mean chord length and distribution, arithmetic mean diameter, Sauter mean diameter and missing ratio can be directly compared to the experimental ones. The bubble size distribution was also compared with experimental data obtained from image processing. To complete the validation, the continuous phase velocity and turbulence intensity were compared as well. Experimental measurements and numerical results were obtained with satisfactory agreement for the radial profiles of the various experiments at different heights. In addition, cross-section average evolution were compared for the new experiments performed.

A rigorous analysis on validation methodology was provided, showing that important deviations between simulation and experiment can arise due to an inadequate

extraction of the variables from the simulation. To this end, we made the distinction of *system*, *probe* and *signal variables* as real dispersed phase data should be distinguished from the data that is actually detected, as the resulting measurement can be biased. Moreover, the assumptions made in experimental measurements using needle probes can lead to important discrepancies, and this solver was used to verify the experimental results obtained. For example, the estimated diameter from the chord length it was rather different that the diameter measured by image processing, and the same difference was given by the simulation.

In summary, this work allowed the simulation of bubbly flow systems with the representation of bubbles as discrete elements to analyse the two-phase flow characteristics in different pipes. Let us note that the proposed solver and validation methodology can be further extended to other flow regimes and include more complex phenomenology as non-sphericity of bubbles, near-wall modelling, and bubble breakup or coalescence. This study can be used for a direct comparison of simulations in pipes with the Two-Fluid Model using the same models as with the CFD-DEM approach that could be useful to interpret the effects of the assumptions made in the two-fluid model. In addition, the research shown in this work, can be extended in the future to simulations with approaches as front tracking or volume of fluid methods, using the same validation methodology and the injection algorithm for the seeding of bubbles according to a desired inhomogeneous bubble size distribution field.

Chapter 6

Two-Fluid Method (TFM)

This chapter presents simulations with TFM of vertical upward bubbly flow in pipes to study the modelling with this lower resolution level approach. To take into account the bubble size distribution a population balance equation is implemented through the quadrature method moments. Interfacial closures and pseudo-turbulence induced models are investigated and implemented. The results are first analysed with an incompressible model and using common models and later the results are investigated with a compressible model and the same models as for the previous CFD-DEM approach.

6.1 Introduction

The Eulerian-Eulerian framework is usually chosen for practical purposes of simulations and investigations in view of its relatively low computational cost. With this approach, the local instantaneous equations of each phase are averaged to obtain an Euler-Euler two-phase flow description (Drew et al. 1971a). Based on this approach, several contributions showed its applications to bubble columns (Gupta et al. 2013; Pan et al. 1999; Pfleger et al. 1999; Zhang et al. 2006). Vertical pipes have taken particular attention as they are present in several industries. This flow involves wall-bounded turbulent flows and requires an exhaustive modelling of interfacial forces between phases and the turbulence interaction by bubbles and liquid. Some of the works were carried out in vertical pipes (Hosokawa et al. 2009; Krepper et al. 2005) and horizontal pipes (Ekambara et al. 2008). In addition, many researches relating this approach have been done focusing on specific phenomena such as interfacial forces, breakup and coalescence or solving the bubble size using a PBE approach (Cheung et al. 2013; Wang et al. 2005; Buffo et al.

2013). Despite its general use, the coefficients of the correlations vary greatly from one investigation to other even for similar configurations.

Chronologically, the study with TFM was the very first method investigated in this thesis, previous to VOF, CFD-DEM or system codes. Then, the lack of universality of the model motivated the investigation of higher resolution level approaches. This is not to say that TFM fails to predict the results, as indeed it is used in this work to properly predict the results with an appropriate set of coefficients. However, we emphasise that the basic principles of the models are mainly applied with CFD-DEM but not always with TFM.

In this study we analyse this models from two points of view. The so-called *"tuning approach"*, and the *critical approach*. The former is a study based on common modelling found in the literature and investigating the sensitivity of the interfacial forces, correlations and pseudoturbulence produced by the bubbles. The latter is based on the same modeling as with CFD-DEM applied to TFM.

To perform this study we needed to implement a PBE in the code. This was solved using the Quadrature Method Of Moments (QMOM) approximation, including a growth rate term for the expansion. In addition, interfacial closures were investigated and implemented.

Solving the PBE requires high computational effort and therefore QMOM (McGraw 1997; Marchisio et al. 2003a; Marchisio et al. 2003b; Sanyal et al. 2005) was implemented to reduce the computational requirements without compromising accuracy. Comparing with discrete methods to solve the PBE as classes method (CM) Kumar et al. 1996a; Kumar et al. 1996b or Multiple Size Group (MUSIG) Lo 1996, QMOM can consider a wide range of bubble sizes with a reduced number of equations. A cheapest approximation of the PBE in terms of computational time can be done solving a one-group interfacial area transport equation (IATE) Kocamustafaogullari et al. 1983 where the PBE is integrated analytically, however with this approach the local probability distribution of the bubble size is not fully accounted.

Previous work related to simulations of bubbly flows with a two-fluid model using QMOM, which solves the equations for the weights and abscissae directly can be found in the literature for ANSYS in Cheung et al. 2013 or OpenFOAM® in Silva et al. 2011. For the implementation of the conditional quadrature method of moments (CQMOM) in OpenFOAM® Buffo et al. 2013 tested in a rectangular bubble column shown overall good results.

For this investigation the QMOM approach is implemented to solve a univariate PBE, relying on a robust moment inversion algorithm following Gordon 1968; Wheeler 1974; Marchisio et al. 2013. We focus the attention on polydispersed bubbly flow applications in vertical pipes. Cases with such characteristics and QMOM

are rarely presented in the literature. Simulations with this simple geometry let us to test the models under well-known boundary conditions and its validity is extensible to a large number of industrial applications.

The development described in this work is based on the existing twoPhaseEulerFoam with incompressible and compressible versions, 2.2.x and 4.x respectively. Interfacial force models, bubble induced turbulence and QMOM have been implemented.

6.2 Mathematical formulation and methods

This summarizes the model equations used in this work, which rely on the two-fluid methodology. In this approach, the local instantaneous equations of each phase are ensemble averaged to obtain an Euler-Euler two-phase flow description, as stated in Drew et al. 1971b and Drew 1982. The averaging process introduces the phase fraction α and unclosed terms $\mathbf{M}$ representing the property transfer between the phases. These unclosed terms are crucial to the prediction of the two-phase flow and must be modelled. Models for the closure terms are discussed in the following sections.

A continuous phase and a dispersed phase are computed. The mean momentum (Eq. 6.1) expressed in an incompressible "phase-intensive" form Oliveira et al. 2003; Weller 2005; Rusche 2002, and continuity (Eq. 6.2) equations for each phase φ can be written as

$$\frac{\partial \mathbf{U}_\varphi}{\partial t} + \mathbf{U}_\varphi \cdot \nabla \mathbf{U}_\varphi + \nabla \cdot \left(\frac{\tau_\varphi}{\rho_\varphi} + \mathbf{R}_\varphi \right) + \frac{\nabla \alpha_\varphi}{\alpha_\varphi} \cdot \left(\frac{\tau_\varphi}{\rho_\varphi} + \mathbf{R}_\varphi \right) = - \frac{\nabla p}{\rho_\varphi} + \mathbf{g} + \frac{\mathbf{M}_\varphi}{\alpha_\varphi \rho_\varphi}, \quad (6.1)$$

and

$$\frac{\partial \alpha_\varphi}{\partial t} + \nabla \cdot (\alpha_\varphi \mathbf{U}_\varphi) = 0, \quad (6.2)$$

where $\mathbf{U}$, τ, $\mathbf{R}$, p, $\mathbf{g}$ and ρ are the velocity, laminar stress tensor, Reynolds stress tensor, pressure, gravity and density, respectively with the conventional forms of τ and $\mathbf{R}$ as found in the previous references (also details can be found in Passalacqua (2013)). The subscript φ=c stands for the carrier phase (liquid), and φ=d for the dispersed phase (gas). The numerical method to overcome the instability when the phase volume fraction tends to zero is implemented as proposed by Oliveira et al. 2003.

6.2.1 Interfacial models

The interfacial momentum transfer term is given by the sum of various forces (Eq. 6.3) modelled as a function of flow parameters. These forces are conventionally divided into drag and non-drag forces:

$$\mathbf{M}_\mathrm{d} = -\mathbf{M}_\mathrm{c} = \mathbf{M}_\mathrm{d,D} + \mathbf{M}_\mathrm{d,VM} + \mathbf{M}_\mathrm{d,L} + \mathbf{M}_\mathrm{d,WL} + \mathbf{M}_\mathrm{d,TD}, \tag{6.3}$$

where $\mathbf{M}_\mathrm{d,D}$, $\mathbf{M}_\mathrm{d,VM}$, $\mathbf{M}_\mathrm{d,L}$, $\mathbf{M}_\mathrm{d,WL}$, $\mathbf{M}_\mathrm{d,TD}$ are the momentum exchange terms due to, respectively, the drag force, the virtual mass force, the lift force, the wall lubrication force and the turbulence dispersion force.

In the following subsections we give a description of each terms contained in the above equation.

Drag force

The drag force exerted by the fluid on a bubble determines the rise velocity. It is related to the slip velocity ($\mathbf{U}_\mathrm{r} = \mathbf{U}_\mathrm{d} - \mathbf{U}_\mathrm{c}$), and, for spherical bubbles of uniform size it can be calculated as Ishii et al. 1984

$$\mathbf{M}_\mathrm{d,D} = -\frac{3}{4}\alpha_\mathrm{d}\frac{C_\mathrm{D}\rho_\mathrm{c}}{d_\mathrm{b}}|\mathbf{U}_\mathrm{r}|\mathbf{U}_\mathrm{r}. \tag{6.4}$$

Following the work of Hosokawa et al. 2009 the drag coefficient C_D (Eq. 6.5) is corrected with respect to the single bubble drag coefficient $C_{\mathrm{D},\infty}$ multiplying by a factor considering the effect of bubble swarms. In addition, Magnaudet et al. 1997 revealed a strong change in the drag force for shear rates near or larger than one, and accounted for this effect by means of a correction term $C_{f,\mathrm{shear}}$. The resulting coefficient is then

$$C_\mathrm{D} = C_{\mathrm{D},\infty} C_{f,\mathrm{swarm}} C_{f,\mathrm{shear}}. \tag{6.5}$$

Three models for $C_{\mathrm{D},\infty}$ are tested. A drag correlation was derived by Schiller et al. 1935 for a sphere as a function of the dispersed phase Reynolds number $Re_\mathrm{d} = |\mathbf{U}_\mathrm{r}|\, d_b/\nu_\mathrm{c}$ being ν_c the molecular viscosity,

$$C_{\mathrm{D},\infty} = \frac{24}{Re_\mathrm{d}}(1 + 0.15 Re_\mathrm{d}^{0.687}), \tag{6.6}$$

and was used because of its simplicity to compute bubbly flows in different research works as Chen et al. 2004; Končar et al. 2008; Kumar et al. 2012. During the last

decades, several drag correlations have been proposed to model the drag coefficient in bubbly flows, mostly considering the influence of the shape of the bubble on the rising velocity. Tomiyama et al. 1998 defined the drag coefficient as a function of the aspect ratio E:

$$C_{\mathrm{D},\infty} = \frac{8}{3}\frac{Eo}{E^{2/3}(1-E^2)^{-1}Eo + 16E^{4/3}}F^{-2} \tag{6.7}$$

where

$$F = \frac{\sin^{-1}\sqrt{1-E^2} - E\sqrt{1-E^2}}{1-E^2} \tag{6.8}$$

The correlation of Vakhrushev et al. 1970 is used to define the aspect ratio of a bubble in an infinite stagnant liquid E_0 as function of the Tadaki number ($Ta = Re_{\mathrm{d}}Mo^{0.23}$):

$$E_0 = \begin{cases} 1, & Ta < 1 \\ [0.81 + 0.206\tanh(2(0.8 - \log_{10} Ta))]^3, & 1 \leq Ta \leq 39.8 \\ 0.24, & Ta \geq 39.8 \end{cases} \tag{6.9}$$

with the Morton Number being $Mo = g\rho_{\mathrm{c}}^2\Delta\rho\nu_{\mathrm{c}}^4/\sigma^3$ and σ being the interfacial surface tension.

Virtual mass force

The virtual mass force is related to the mass of liquid carried by the bubble. This term is calculated following Drew et al. 1987:

$$\mathbf{M}_{\mathrm{d,VM}} = \alpha_{\mathrm{d}}\rho_{\mathrm{c}}C_{\mathrm{VM}}\left(\frac{\mathrm{D}\mathbf{U}_{\mathrm{c}}}{\mathrm{D}t} - \frac{\mathrm{D}\mathbf{U}_{\mathrm{d}}}{\mathrm{D}t}\right) \tag{6.10}$$

The application of potential flow theory to flow around a spherical bubble in an infinite medium gives a value of 0.5 for C_{VM} according to Lamb 1895; Auton et al. 1988; Drew et al. 1987.

Lift force

The effect of the lateral force due to the lift was first modelled by Auton et al. 1988:

$$\mathbf{M}_{\mathrm{d,L}} = -\alpha_{\mathrm{d}}\rho_{\mathrm{c}}C_{\mathrm{L}}\mathbf{U}_{\mathrm{r}} \times \nabla \times \mathbf{U}_{\mathrm{c}}. \tag{6.11}$$

We use the lift correlation of Wang et al. 1987 for the "tuning approach" obtained from the radial momentum equation as it can be applied to bubble systems for fully developed axisymmetric pipe flow (Hibiki et al. 2007).

$$C_{\mathrm{L}} = 0.01 + \frac{0.49}{\pi}\cot^{-1}\left(\frac{\log\zeta + 9.3}{0.20}\right) \simeq 0.02 + 0.6(\log\zeta + 10.67)^{-2.605}, \quad (6.12)$$

$$\zeta \equiv e^{-\alpha_{\mathrm{d}}}\frac{d_{\mathrm{b}}}{\mathbf{U}_{\mathrm{r}}}\frac{\partial \mathbf{U}_{\mathrm{c}}}{\partial r}\left(\frac{d_{\mathrm{b}}}{D}\frac{1}{Re_{\mathrm{d}}}\frac{\mathbf{U}_{\mathrm{d}}}{1.18(\sigma g/\rho_{\mathrm{c}})^{\frac{1}{4}}}\right)^{2}. \quad (6.13)$$

The values are in a range from 0.01 to 0.1 in the experimental conditions considered by the original authors.

The lift coefficient of Tomiyama et al. (2002b) is used in the critical approach as for the CFD-DEM, the correlation is shown below for convenience:

$$C_{\mathrm{L}} = \begin{cases} \min\left(0.288\tanh(0.121Re), f\right) & \mathrm{Eo}_d < 4 \\ f & 4 \leq \mathrm{Eo}_d \leq 10 \\ -0.29 & \mathrm{Eo}_d > 10 \end{cases}, \quad (6.14)$$

$$f = 0.00105\mathrm{Eo}_d^3 - 0.0159\mathrm{Eo}_d^2 - 0.0204\mathrm{Eo}_d + 0.474, \quad (6.15)$$

Wall lubrication force

The effect of walls on the dispersed phase is modelled as in Antal et al. 1991, considering that the liquid drainage around a bubble moving near a wall carries the bubbles away from the wall. The force can be expressed as:

$$\mathbf{M}_{\mathrm{d,WL}} = -\alpha_{\mathrm{d}}\rho_{\mathrm{c}}C_{\mathrm{W}}\left|\mathbf{U}_{\mathrm{r}} - (\mathbf{U}_{\mathrm{r}}\cdot n_{\mathrm{w}})\right|^2 n_{\mathrm{w}}, \quad (6.16)$$

where

$$C_{\mathrm{W}} = \max\left[\frac{C_{\mathrm{w1}}}{d_{\mathrm{b}}} + \frac{C_{\mathrm{w2}}}{y}\right] \quad (6.17)$$

The values of C_{w1} and C_{w2} are discussed in Section 6.5.

Turbulent dispersion force

This force considers the effect of the turbulent fluctuations in the carrier phase on the dispersed phase. We adopt the formulation of López de Bertodano 1992:

$$\mathbf{M}_{\mathrm{d,TD}} = -\rho_{\mathrm{c}} C_{\mathrm{TD}} \kappa_{\mathrm{c}} \nabla \alpha_{\mathrm{d}} \tag{6.18}$$

Originally a value of 0.1 for C_{TD} was chosen by López de Bertodano 1992. However and in a later contribution López de Bertodano 1998, a new correlation was proposed:

$$C_{\mathrm{TD}} = C_{\mu}^{1/4} \frac{1}{St(1+St)}, St = \frac{\tau_d}{\tau_e} \tag{6.19}$$

The turbulent Stokes number, St, is defined as the ratio of the time constant of the bubbles ($\tau_d = 4d_b/(3C_{\mathrm{D}}\left|\mathbf{U}_{\mathrm{r}}\right|)$) and the effective time constant of the turbulent eddies obtained from:

$$\frac{1}{\tau_e} = \sqrt{\frac{1}{\tau_t^2} + \frac{1}{\tau_R^2}} \tag{6.20}$$

The turbulence coefficient obtained by Burns et al. 2004 will be also used in this chapter.

6.2.2 Turbulence models

A standard κ-ε turbulence model in combination with the "phase-intensiver form" momentum equations, is used to model the effect of turbulent fluctuations in the carrier phase. An equation for the turbulent kinetic energy

$$\frac{\partial \kappa_{\mathrm{c}}}{\partial t} + \nabla \cdot (\mathbf{U}_{\mathrm{c}} \kappa_{\mathrm{c}}) = \nabla \cdot \left[\left(\nu_{\mathrm{c}} + \frac{\nu_{t,\mathrm{c}}}{\sigma_\kappa} \right) \nabla \kappa_c \right] + P_\kappa - \epsilon_{\mathrm{c}} + S_\kappa, \tag{6.21}$$

and one for the turbulent dissipation rate:

$$\frac{\partial \varepsilon_{\mathrm{c}}}{\partial t} + \nabla \cdot (\mathbf{U}_{\mathrm{c}} \varepsilon_{\mathrm{c}}) = \nabla \cdot \left[\left(\nu_{\mathrm{c}} + \frac{\nu_{t,\mathrm{c}}}{\sigma_\varepsilon} \right) \nabla \varepsilon_c \right] + \frac{\varepsilon_c}{\kappa_c} \left(C_{1\varepsilon} P_\kappa - C_{2\varepsilon} \varepsilon_{\mathrm{c}} \right) + S_\varepsilon, \tag{6.22}$$

in its incompressible form are solved.

Two different approaches are commonly used to model the bubble turbulence (see Rzehak et al. 2013): bubble-induced contribution to the effective viscosity as in Sato et al. 1975 and the addition of a bubble-induced source term to the transport equations of the turbulence model. We analyse the last approach with two different models. Lee et al. 1989 used in their predictions the source terms:

$$S_\kappa = \alpha_\mathrm{d} C_{1\kappa} \frac{\partial p}{\partial z} \left| \mathbf{U}_\mathrm{r} \right|, \tag{6.23}$$

$$S_\varepsilon = C_{3\varepsilon} S_\kappa \frac{\varepsilon_\mathrm{c}}{\kappa_\mathrm{c}}, \tag{6.24}$$

where

$$C_{1\kappa} = 0.03 - 0.344 \times 10^{-5} Re_\mathrm{c} + 0.243/(1 + e^{(Re_\mathrm{c} - 60{,}000)/2{,}000}), \tag{6.25}$$

and the carrier Reynolds number $Re_\mathrm{c} = |\mathbf{U}_\mathrm{c}| \, D/\nu_\mathrm{c}$.

The constant value for $C_{3\varepsilon}$ is assumed to be equal to $C_{2\varepsilon}$ as discussed in Lee et al. 1989 for bubbles rising freely with gradients of $\mathbf{U}_\mathrm{c}$, κ_c and ε_c considered to be zero. Morel et al. 1997 proposed the following correlations:

$$S_\kappa = (\mathbf{M}_\mathrm{d,D} - \mathbf{M}_\mathrm{d,VM}) \cdot \mathbf{U}_\mathrm{r}, \tag{6.26}$$

$$S_\varepsilon = C_{4\varepsilon} \frac{S_\kappa}{\tau}, \tau = \left(\frac{d_{32}^2}{\varepsilon_\mathrm{c}} \right)^{1/3}, \tag{6.27}$$

where τ is the characteristic time for the bubble-induced source term. The ad-hoc constant value of $C_{4\varepsilon}$ vary depending on the scenario. In Yao et al. 2004a values of 1 and 0.6 were used for DEDALE (Grossetête 1995) and DEBORA (Manon et al. 2000) experiments respectively. A value of 1.92 is used in this work.

The numerical values of the constants in the κ-ε equations are the default values found in Launder et al. 1974 (Tab. 6.1).

Table 6.1: Constant values of the κ-ε model

C_μ	$C_{1\varepsilon}$	$C_{2\varepsilon}$	σ_κ	σ_ε
0.09	1.44	1.92	1.0	1.3

6.3 Population balance model (QMOM)

The evolution of the bubble size distribution in space and time is described by means of a PBE (Ramkrishna 2000). This equation is written in this work considering a length-based number density function (NDF) of the dispersed phase $n(L;\mathbf{x},t)$, and reads

$$\frac{\partial n(L)}{\partial t} + \nabla \cdot (n(L)\mathbf{U}_\mathrm{d}) = B(L) - D(L), \tag{6.28}$$

where $B(L)$ and $D(L)$ are, respectively, the birth and the death rates of bubbles of size L due to coalescence and breakage. It is worth noticing that these two terms depend also on the position and on time, even if this dependency was not explicitly indicated in the equation to keep the notation simpler. The velocity $\mathbf{U}_\mathrm{d}$ is the average velocity of the dispersed phase, obtained from the momentum equation of the two-fluid model. Using this velocity represents an approximation, because it relies on the assumption that all the bubbles in a given computational cell move at the same velocity, which is reasonable only for bubbles that only slightly deviate from the average size on that cell.

We model the coalescence and breakage following the work of Sanyal et al. 1999 and Petitti et al. 2010. In particular, the birth term due to coalescence is

$$B_\mathrm{c}(L) = \frac{1}{2}\int_0^\infty h\left((L^3-\lambda^3)^{1/3},\lambda\right) n\left((L^3-\lambda^3)^{1/3}\right) n(\lambda)\mathrm{d}\lambda, \tag{6.29}$$

while the term describing bubble death due to coalescence reads

$$D_\mathrm{c}(L) = \int_0^\infty = h(L,\lambda)n(L)n(\lambda)\mathrm{d}\lambda. \tag{6.30}$$

The birth term due to breakage is

$$B_\mathrm{b}(L) = \int_L^\infty \beta(L,\lambda)g(\lambda)n(\lambda)\mathrm{d}\lambda, \tag{6.31}$$

and the death term due to breakage reads

$$D_\mathrm{b}(L) = g(L)n(L). \tag{6.32}$$

The function $h(L,\lambda)$ represents the coalescence frequency, which depends on the collision frequency between two bubbles, while $\beta(L,\lambda)$ is the daughter distribution function, and $g(L)$ is the breakup kernel function. Expressions for these functions

depend on the flow conditions, and will be discussed only for the case under examination in this work.

6.3.1 Coalescence and breakup kernels

We briefly summarize here the expressions for the coalescence and breakage kernel functions, inviting the reader to refer to the corresponding literature for the details.

The expression for the coalescence kernel was developed by Coulaloglou et al. 1977 and corrected by Petitti et al. 2010, leading to

$$h(L,\lambda) = C_h \varepsilon^{1/3} (L+\lambda)^2 \sqrt{\lambda^{2/3} + L^{2/3}} \eta(L,\lambda), \tag{6.33}$$

where the coalescence efficiency $\eta(L,\lambda)$ is

$$\eta(L,\lambda) = \mathrm{e}^{-C_\eta \frac{\rho_c^2 \nu_c \varepsilon}{\sigma^2} \left(\frac{L\lambda}{L+\lambda}\right)^4}. \tag{6.34}$$

The expression for the breakup kernel (Narsimhan et al. 1979 Alopaeus et al. 2002 and Laakkonen et al. 2006) is:

$$g(L) = C_{1g} \varepsilon^{1/3} \operatorname{erf} \sqrt{\frac{C_{2g}\sigma}{\rho_c \varepsilon^{2/3} L^{5/3}} + \frac{C_{3g}\rho_c \nu_c}{\sqrt{\rho_c \rho_d} \varepsilon^{1/3} L^{4/3}}}. \tag{6.35}$$

Finally, the daughter distribution is described by the expression proposed by Andersson et al. 2006:

$$\beta(L,\lambda) = 180 \frac{L^8}{\lambda^9} \left(1 - \frac{L^3}{\lambda^3}\right)^2. \tag{6.36}$$

The values of the parameters used for the coalescence and breakup kernels are summarized in Tab. 6.2 (Laakkonen et al. 2006).

Table 6.2: Constant values for breakup and coalescence kernels

C_h	C_η	C_{1g}	C_{2g}	C_{3g}
4.6	6.0×10^9	6.0	0.04	0.01

6.3.2 Quadrature-based moment method

The direct solution of Eq. 6.28 would require the discretization of a four-dimensional space (4 independent scalar variables), in addition to time integration. This would represent a significant computational cost, in addition to the solution of the underlying multiphase model. A more convenient approach is to consider the moments of the NDF McGraw 1997; Marchisio et al. 2003a; Marchisio et al. 2003b; Marchisio et al. 2013, defined as

$$m_k = \int_0^\infty L^k n(L) \mathrm{d}L, \tag{6.37}$$

being k the order of the moment. Moments are averaged quantities obtained from the NDF. An infinite set of moments is theoretically required to exactly represent the NDF, however a truncated set is often sufficient to capture the peculiar features of the distribution which are of interest to engineers. For this reason, a moment method is used to find an approximate solution of the PBE in this work, paying particular attention in preserving the correct value of the the low-order moments of the NDF, which represent physical quantities of interest. In particular, m_0 is the total number of bubbles per unit volume, m_1 is their length, m_2 is related to the bubble surface area, and m_3 to their volume.

The application of Eq. 6.37 to the PBE in Eq. 6.28 leads to transport equations for the moments of the NDF, whose form is:

$$\frac{\partial m_k}{\partial t} + \nabla \cdot (m_k \mathbf{U}_\mathrm{d}) = \overline{B}_k - \overline{D}_k, \tag{6.38}$$

where the $\overline{B}_k$ and $\overline{D}_k$ represent, respectively, the moment of order k of $B(L)$ and $D(L)$. Note that the same velocity is used for all the moments in Eq. 6.38. This is a consequence of the assumption made when we decided to use the average velocity for each bubble size, however this is not strictly true, since, theoretically, each moment is advected with its own flux (Marchisio et al. 2013). Alternative methods, which rely on conditional moments were proposed to the address this problem Yuan et al. 2014 in the framework of quadrature-based moment methods.

The solution of Eq. 6.38 requires the two terms $\overline{B}_k$ and $\overline{D}_k$ to be calculated, which is not trivial in the general case, and represents the so-called *moment closure problem*. A widely adopted strategy to provide closures for the source terms of moment transport equations is the quadrature method of moments (McGraw 1997,

Marchisio et al. 2003a, Marchisio et al. 2003b and Marchisio et al. 2013). In this approach, the NDF is approximated as a summation of Dirac delta functions

$$n(L) \approx \sum_{i=0}^{\mathrm{N}} w_i \delta(L - L_i), \tag{6.39}$$

where w_i are the weights and L_i the abscissae of an appropriate Gaussian quadrature formula. A unique correlation is established between a set of $2N$ moments and a set of N weights and abscissae through an inversion algorithm, which allows weights and abscissae to be found from the set of transported moments by solving an eigenvalue problem as described by Gordon 1968 and Wheeler 1974. In this research, N has a value of 3 to have a satisfactory approximation of the number density function solving the minimum number of moment equations, in this case 6, as suggested by Marchisio et al. 2003a.

The substitution of Eq. 6.39 in the moment definition of Eq. 6.37 leads to the following expression for the approximated moments

$$m_k \approx \sum_{i=0}^{\mathrm{N}} w_i L_i^k, \tag{6.40}$$

which can be used to re-calculate the moments from the quadrature data. Similarly, considering the definition given for $B(L)$ and $D(L)$, Petitti et al. 2010 obtained

$$\begin{aligned} \overline{B}_k - \overline{D}_k = \frac{1}{2} \sum_{i=0}^{\mathrm{N}} w_i \sum_{j=0}^{\mathrm{N}} w_j h(L_i, L_j) \left(L_i^3 + L_j^3\right)^{k/3} \\ \sum_{i=0}^{\mathrm{N}} w_i g(L_i) \overline{\beta}_i^k - \sum_{i=0}^{\mathrm{N}} w_i g(L_i) L_i^k \\ - \sum_{i=0}^{\mathrm{N}} w_i L_i^k \sum_{j=0}^{\mathrm{N}} w_j h(L_i, L_j), \end{aligned} \tag{6.41}$$

being

$$\overline{\beta}_i^k = \int_0^L L^k \beta(L_i, L_j) \mathrm{d}L_j. \tag{6.42}$$

6.3.3 Numerical procedure

The solution procedure used in the code is summarized in Fig. 6.1. The numerical solution of the two-phase equations relies on a segregated algorithm extended to two-phase flows Oliveira et al. 2003. The coupled pressure-velocity problem is solved using the PIMPLE algorithm, which is a combination of the Pressure-Implicit with Splitting of Operators (PISO) (Issa 1986) and the Semi-Implicit Method for Pressure-Linked Equations (SIMPLE) (Patankar 1980) algorithms. The momentum equations are manipulated to stabilize the system of equation at the limits of the range of volume fractions, to avoid singularities Weller 2005 and both phases continuity equations are solved separately for the two phase fractions as evaluated for a flow around obstruction in Oliveira et al. 2003. The volume fraction equation is solved with the Multidimensional Universal Limiter with Explicit Solution (MULES) OpenCFD 2013 implemented in OpenFOAM®, an iterative implementation of the Flux Corrected Transport technique (FCT) to guarantee boundedness in the solution of hyperbolic problems (see Damián et al. 2014).

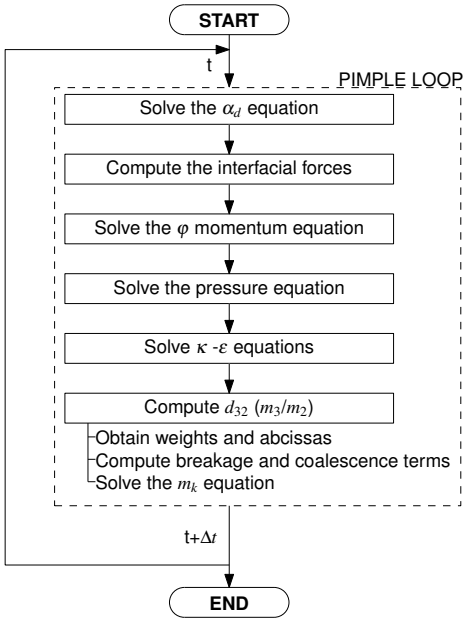

Figure 6.1: Solution procedure scheme.

The equations are solved sequentially and the set of moment equations solved in the last step of the loop to update the Sauter mean diameter field given by the relation of third and second low-order moments, $d_{32} = m_3/m_2$. The value of this quantity in each cell is used as the bubble diameter, d_b, to evaluate the sub-models.

Both phases are assumed to be incompressible and isothermal, with constant density and viscosity.

6.4 CFD setup

In order to validate the solver, three domains are modelled and simulated. The experiments of Monrós-Andreu et al. 2013. The experiments of Hibiki et al. 2001a provide data at z/D=6.0 and z/D=53.5 and therefore a pipe of 2.413 m was used. Measurements shown in Hosokawa et al. 2009 were carried out at 1.7 m (z/D=68.0) above the mixing section and this lenght is used to model the pipe.

The experimental data at the bottom measurement section are employed to set up the inlet boundary conditions for void fraction, Sauter mean diameter, turbulent kinetic energy, dispersed phase velocity, carrier phase velocity and the required moments. The computational results are shown in Section 5 together with the inlet values. The inlet boundary condition of the 6 moments are calculated with the non-central moments from the mean (μ) and standard deviation (σ) of the bubble size population of the experiments. The simulations are done considering a normalized distribution ($m_0 = 1$).

The mesh was created with the native OpenFOAM® mesh generation tool *blockMesh* fulfilling the requirements according to the NEA Best Practice Guidelines (BPG). After the mesh sensitivity analysis was carried out, a mesh of 938,400 elements with 5 mm of axial distance between nodes and 35 radial nodes as illustrated in Fig. 6.2. The maximum aspect ratio and skewness are 13.75 and 0.50 respectively.

The boundary conditions used in the simulations are listed in Tab. 6.3.

Table 6.3: Boundary conditions for inlet, outlet and wall patches.

Variable	Inlet	Outlet	Wall
$\mathbf{U}_\mathrm{d}$	Dirichlet	Neumann[a]	Slip
$\mathbf{U}_\mathrm{c}$	Dirichlet	Neumann	No-slip
p	Neumann	Dirichlet	Neumann
α_d	Dirichlet	Neumann	Neumann
κ_c	Dirichlet	Neumann	wall function
ε_c	Dirichlet	Neumann	wall function
$\nu_{t,\mathrm{c}}$	-	-	wall function
m_k	Dirichlet	Neumann	Dirichlet

[a]zero gradient

The equations were integrated with the finite-volume approach. The convective terms of the momentum and turbulent quantities equations were discretized with the second-order upwind scheme (linearUpwindV and linearUpwind schemes in

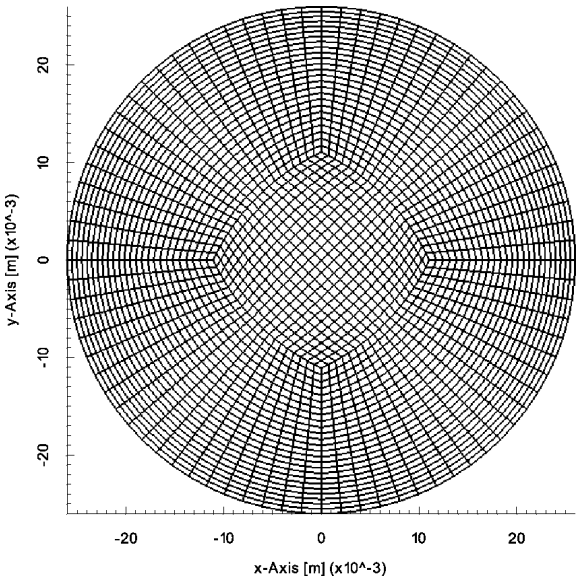

Figure 6.2: Cross-section mesh used for the experiments of Monrós-Andreu et al. (2013)

OpenFOAM, respectively). The convective terms of the moment transport equations were discretized using the first-order upwind scheme to avoid difficulties with moment realizability. The convective term of the equation for the phase fraction were discretized with a second-order total variation diminishing (TVD) scheme, a bounded central scheme stabilized with a limiter Sweby 1984 (limitedLinear01 scheme in OpenFOAM). Time integration was performed with the first-order Euler scheme. All the other terms were discretized with a second-order central scheme, since they do not present boundness problems.

In the next two sections we analyse this models from two points of view. The so-called *"tuning approach"*, and the *critical approach*. The former is a study based on typical modelling found in the literature and investigating the sensitivity of the interfacial forces, correlations and pseudoturbulence produced by the bubbles. The incompressible version of TFM is used. The latter is based on the same modeling as with CFD-DEM applied to a compressible version of TFM.

6.5 "Tuning approach"

This section discusses the performance of the models for the interfacial forces and bubble induced turbulence under different scenarios. For this approach, the bottom ports of the HK- and H- conditions are used and for G- the mid port. For this specific section we used different conditions with higher superficial velocities as the one used for the other scenarios (Table 2.2). This conditions are shown in Table 6.4.

Table 6.4: Flow conditions

Name	$(j_c)_{z=0}$ (m/s)	$(j_d)_{z=0}$ (m/s)	$\langle\alpha_d\rangle_{z/D,inlet}$ (-)	$\langle\mu\rangle_{z/D,inlet}$ (mm)	$\langle\sigma\rangle_{z/D,inlet}$ (mm)
G-JL05JG005	0.5	0.05	6.62×10^{-2}	3.47	0.66
G-JL10JG005	1.0	0.05	4.34×10^{-2}	3.74	0.87
G-JL10JG010	1.0	0.10	9.01×10^{-2}	3.59	0.90
G-JL10JG020	1.0	0.20	1.64×10^{-1}	3.81	1.09
G-JL20JG010	2.0	0.10	3.869×10^{-2}	3.58	0.23
HK-JL05JG005	0.491	0.0556	9.20×10^{-2}	2.34*	0.50*
HK-JL10JG005	0.986	0.0473	5.12×10^{-2}	2.26*	0.50*
H-JL10JG002	1.0	0.02	1.46×10^{-2}	3.52	0.44
H-JL10JG0036	1.0	0.036	3.30×10^{-2}	3.66	0.40

*estimated based on the experimental data

The strong dependency between models makes it difficult to consider each closure separately. The approach adopted is to first neglect any non-drag force and bubble-induced turbulence to predict a realistic slip velocity. Hence, the performance of the bubble-induced source terms models was studied for different voidage values and finally the non-drag forces will then be considered. The root-mean-square (RMS) deviation is shown in parentheses in each figure.

6.5.1 Drag force

A proper drag coefficient determines the slip velocity of the system being the key to model relevant phenomena. The relative velocity profiles for Schiller-Naumann, Tomiyama and Dikjhiuzen drag correlations are shown for the JL10JG005 conditions in Fig. 6.3 (left).

The slip velocity using different drag correlations have been shown to vary widely. Experimental results analysing the rising velocity of bubbles depends on purity of the phases, shape of the bubble, wall effects and turbulence among others.

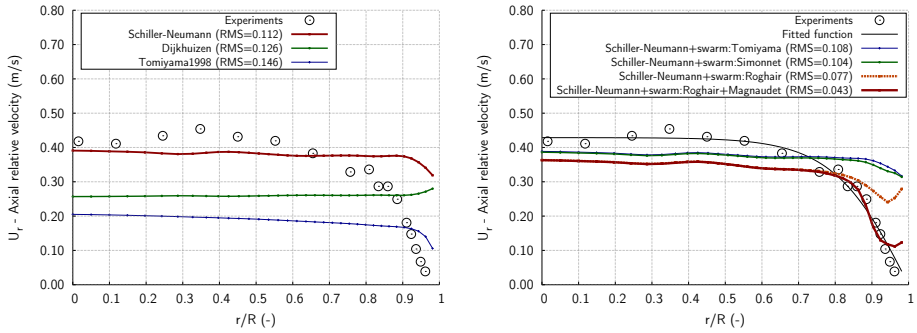

Figure 6.3: Slip velocity comparison with different drag correlations (left), different swarm and shear corrections (right) for G-JL10JG005 flow condition.

The corrections considering swarm and shear rate effects are included in the analysis for the drag correlation of Schiller-Naumann which is close to the experimental data as shown in Fig. 6.3 (right).

It is worth noticing that the relative velocity was chosen as the parameter to analyse the direct effect of the drag force rather than the void fraction for which only an indirect effect can be noticed.

6.5.2 Bubble induced turbulence

Turbulence is of high importance in fluid dynamics to predict the shape of velocity profiles. In two-phase flow defining proper values of κ and ε is crucial for models such as turbulent dispersion force and breakage and coalescence which depends on these turbulence quantities. Using the drag correlations obtained below, the bubble-induced source terms for κ and ε are tested under different scenarios with j_c=1.0 and j_d in the range of 0.05 – 0.20 m/s.

Fig. 6.4 shows the turbulent kinetic energy of the carrier phase, κ_c. These figures clearly show the difference between the simulations neglecting the influence of the bubbles on the turbulence and the evaluated models. The model proposed by Lee et al. (1989) underpredicts the turbulence kinetic values for all the scenarios tested. The one proposed by Morel et al. (1997) can reproduce the effect of the turbulence produced up to 0.8 normalized distance from the center of the pipe. Simulations for case G-JL10JG020 show that both models underpredict the values of turbulent kinetic energy. This last case is more critical since involves important changes on the size of the bubble from the bottom of the pipe to the top that influences the prediction of the bubble induced turbulence if they are not properly captured.

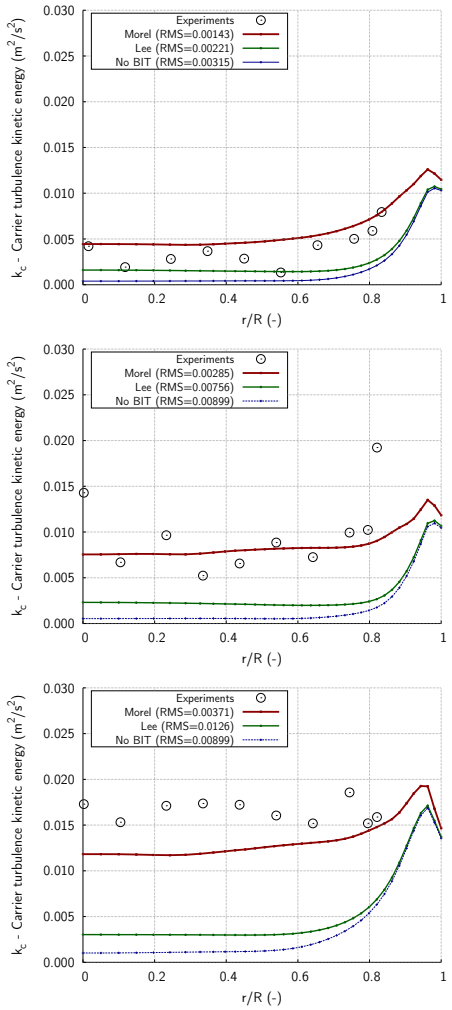

Figure 6.4: Turbulence kinetic energy profiles with different bubble-induced source terms for G-JL10JG005 (top), JL10JG010 (middle), JL10JG020 (bottom) flow conditions.

6.5.3 Non-drag forces

The effects of non-drag forces as lift, wall lubrication and turbulent dispersion are discussed in this section. For the wall lubrication force we use the coefficients used on the original paper of Antal et al. (1991), the default values on ANSYS

Table 6.5: Wall lubrication force coefficients.

Name	C_{w1}	C_{w2}
Antal	-0.104 - 0.06$\|\mathbf{U}_r\|$	0.147
ANSYS® CFX®	-0.01	0.05
Krepper	-0.0064	0.016
Proposed	-0.104 - 0.06$\|\mathbf{U}_r\|$	0.10

CFX (2014), Krepper et al. (2005) and a proposed set of coefficients fitting our experimental results as summarized in Tab. 6.5.

Fig. 6.5 shows the influence on the void fraction profile for each set of coefficients. It can be highlighted that no damping function is applied to the curl to compute the lift force in the near wall cell in these results.

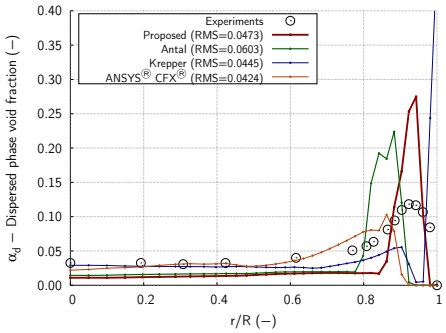

Figure 6.5: Void fraction profile comparison with different wall lubrication force coefficients for G-JL10JG005 flow condition.

The effect of the dispersion force for a given lift and wall lubrication force model is examined in Fig. 6.6 (left). These results show that the original value of 0.1 for the C_{TD} fits the experimental results used in the present work.

Finally, we show the results comparing the virtual mass force for values C_{VM}=0 and C_{VM}=0.5 in Fig. 6.6 (right). As expected, the influence of this force in steady state simulations can be neglected. However, we show this force does not cause any instability in the numerical procedure followed.

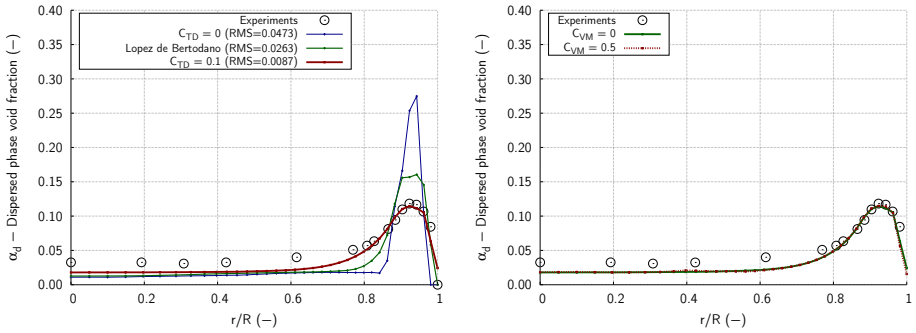

Figure 6.6: Void fraction profile comparison with different turbulent dispersion force coefficients for G-JL10JG005 flow condition

6.5.4 Results

Once the sensitivity analysis of the interfacial forces and bubble induced turbulence has been performed in the previous section, we analyse the results of the simulations with the conditions reported in Tab. 6.4, named G-JL05JG005, G-JL10JG005, HK-JL05JG005, HK-JL10JG005, H-JL10JG002 and H-JL10JG0036.

In the case of modelling the scenarios of Hosokawa et al. (2009), experimental profiles at a lower section is not provided and therefore, in our simulations, constant values were applied to the inlet boundary conditions. The solver is assessed by comparing dispersed and carrier phase characteristics of the flow with radial profiles at z/D=98.7, z/D=53.5 and z/D=68.0 respectively. The models and coefficients that best fit the experimental data according to the sensitivity analysis are used in these simulations for the interfacial forces and the bubble-induced source terms for the κ_c-ε_c turbulence equations and summarized in Tab. 6.6. The virtual mass force is neglected as the effects of the acceleration are not important in this type of bubbly flow problem and with this method.

Table 6.6: Overview of the interfacial force coefficient and bubble induced turbulence model.

C_{VM}	0
C_{D}	Schiller-Neumman + Roghair + Magnaudet-Legendre
C_{L}	Wang
C_{W}	Antal
C_{TD}	0.1
BIT	Morel

The radial profiles of the dispersed void fraction are reported in Fig. 6.7 (left). Bubbles migrate to the wall, leading to the formation of a peak in the gas concentration near the wall. The profiles obtained from the simulations have a similar trend, height and location of the peak to those obtained from the experiments.

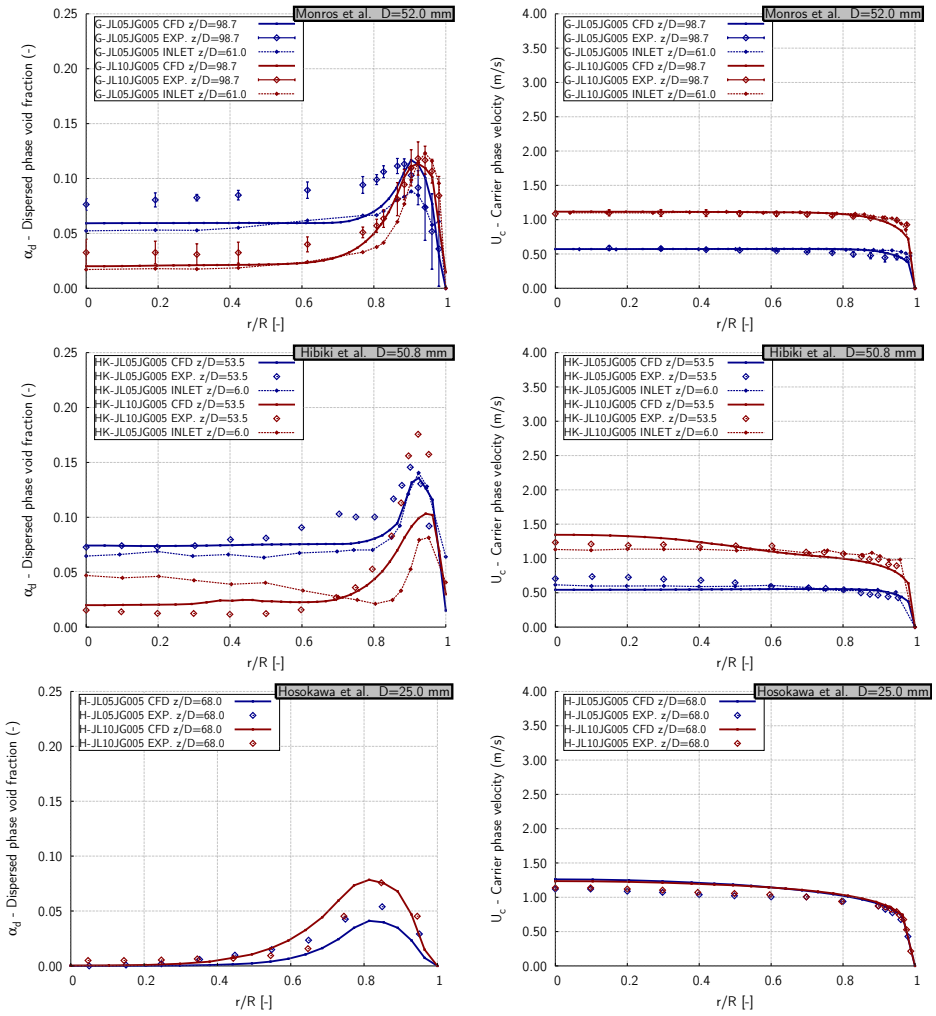

Figure 6.7: Void fraction and carrier phase velocity comparison between CFD results and experimental data.

Although the coefficients of the interfacial forces could be tuned to obtain a better fit for each scenario, we preferred to keep the model as general as possible to perform the validation with experiments from different authors. The results, and in particular the capability of the model for properly predicting the peak in the

gas concentration near the wall, have proven to be very sensitive to the models of the forces acting near the wall. The slight differences between the experimental and the numerical profiles in the region near the wall might be related to the imperfect values of the turbulence quantities predicted by the simple two-equation turbulence model supplemented with wall-functions used in this work. Another factor that might affect the results in this region of the pipe are the model for the wall lubrication and for the lift force. It is worth noting the difficulties in account for the effect of bubble assemblies in the interfacial forces. In pipe flows is expected that these forces will be affected by the presence of multiple bubbles. Further investigation of these phenomena at a fundamental level is required in order to develop averaged models capable of accounting for these effects. Fig. 6.7 (right) shows the radial velocity distribution of the carrier phase. The effect of the dispersed phase on the velocity profile of the continuum phase can be appreciated observing the flattened velocity profile. Velocities for all the cases are in overall good agreement with the experimental data.

The profile of the mean kinetic energy of the turbulence was quantified experimentally by mean of the velocity fluctuations as κ_c=1/2($\langle u_x'^2 \rangle + \langle u_y'^2 \rangle + \langle u_z'^2 \rangle$) (Pope 2000). The computational results compared with this value in Fig. 6.8 (left) are reasonably well predicted for Monrós-Andreu et al. (2013) and Hosokawa et al. (2009), both used LDA to obtain the turbulence kinetic energy measure.

In addition, extensive work with experimental techniques and CFD modelling is needed in the region near the wall ($r/R > 0.8$) to improve the turbulence modelling. It is worth noticing that within this narrow distance from the wall of around 5 mm, the LDA techniques can capture hardly these quantities for two-phase flow. In the other hand the κ-ε turbulence model relies in the wall functions to solve the turbulence and therefore the results are less accurate than with other turbulence models.

Fig. 6.8 (right), for the dispersed phase velocity profile, shows that the drag force predicts the rise velocity of the bubbles properly, it plays an important role as some sub-models depends on the slip velocity.

The Sauter mean diameter obtained experimentally as in Simonnet et al. (2007) is compared in Fig. 6.9. The experimental Sauter mean diameter profile in Hosokawa et al. is not provided and this validation is not shown. The trend of the profiles and the rapid change near the wall are properly captured for these conditions and guarantee the calculation of the interfacial forces as a function of the diameter.

The bubble size is studied in-depth for one condition with the information used to solve the PBE with QMOM. The evolution of the bubble size distribution from the axial location z/D=61.0 (inlet) to z/D=98.7 (outlet) for G-JL10JG005 is shown in Fig. 6.10. The set of weights and abscissae obtained from the moments solving the eigenvalue problem Wheeler (1974) are represented at radial positions r/R=0.0,

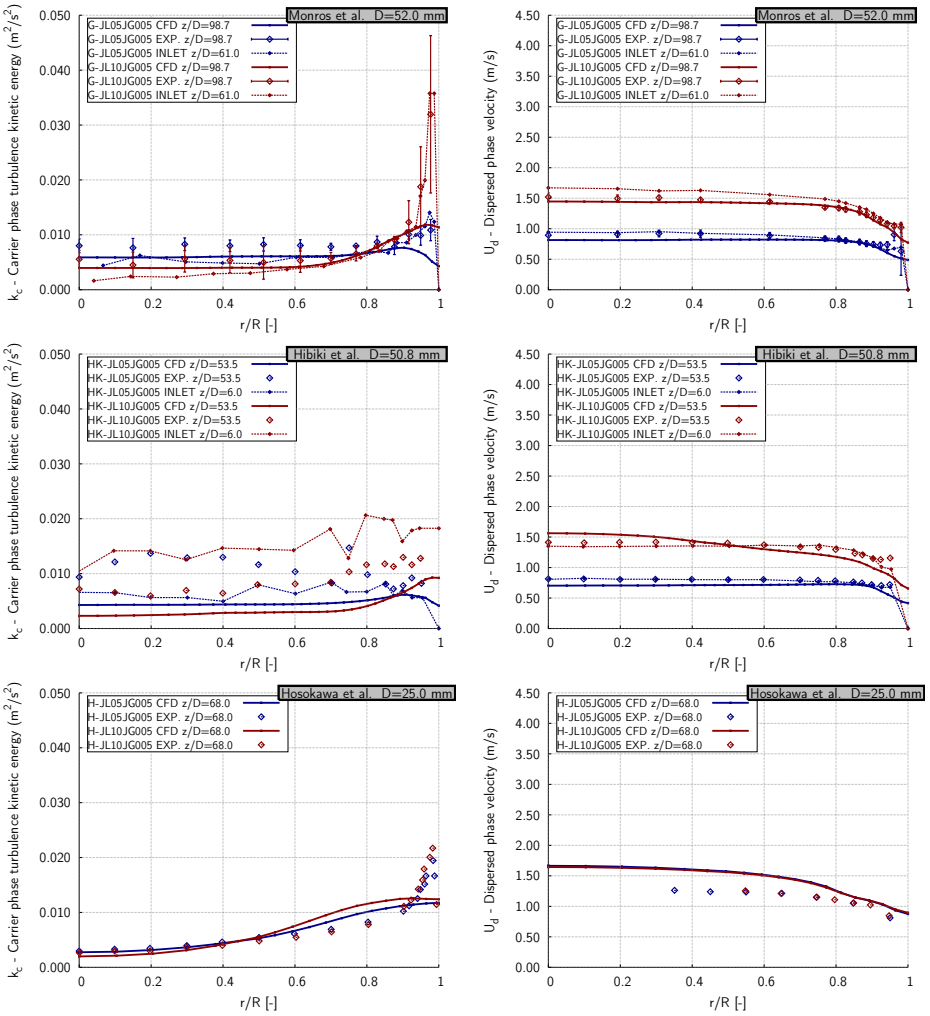

Figure 6.8: Turbulence kinetic energy and dispersed phase velocity comparison between CFD results and experimental data.

r/R=0.50 and r/R=0.96. An increase of bubble size from the inlet to the outlet is noted at these positions in agreement with the Sauter mean diameter.

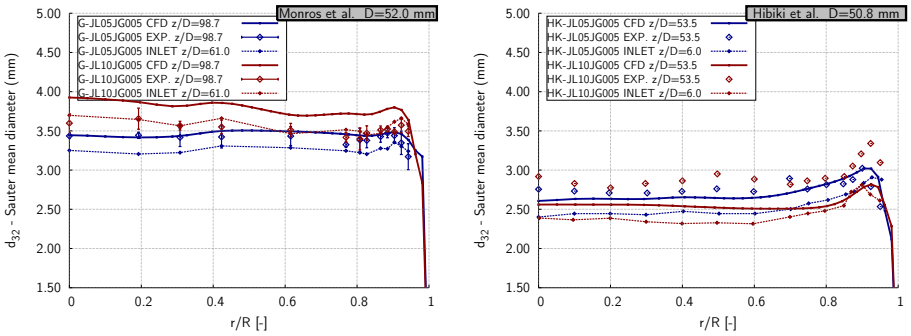

Figure 6.9: Sauter mean diameter comparison between CFD results and experimental data.

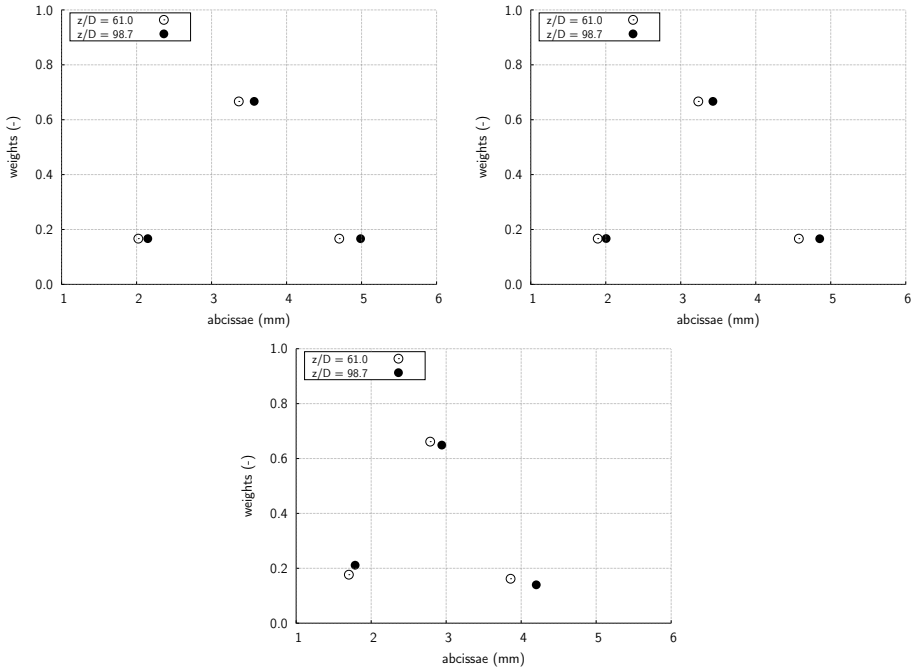

Figure 6.10: Bubble size distribution at inlet (void dots) and outlet (solid dots) showing the three nodes of the quadrature approximation at three different radial positions r/R=0.0 (left), r/R=0.50 (center) and r/R=0.96 (right) for the condition G-V10JG005.

6.6 Critical approach

This section shows an attempt to obtain the results of CFD-DEM with similar modelling. Similar modelling implies the same forces, turbulence modelling and correlations, and the compressibility of the dispersed phase. However, important discrepancies can be found because of the simplifications that are made to obtain the ensemble averaged equations. For this reason we focus in the bubble dynamics neglecting breakup and coalescence.

The models for the interfacial forces used in the CFD-DEM are summarised again in Table 6.7.

Table 6.7: Coefficients for interfacial force closures used in this work for CFD-DEM.

Drag force	Tomiyama et al. (1998)
Lift force	Tomiyama et al. (2002b)
Virtual mass force	Drew et al. (1987)
Wall lubrication force	Antal et al. (1991)

The wall lubrication force is not considered for this work for two main reasons: a) the CFD-DEM results shown that this force was negligible for these cases compared with the lift force and b) the use of this formulation in TFM could overestimate the force at nodes close to the wall.

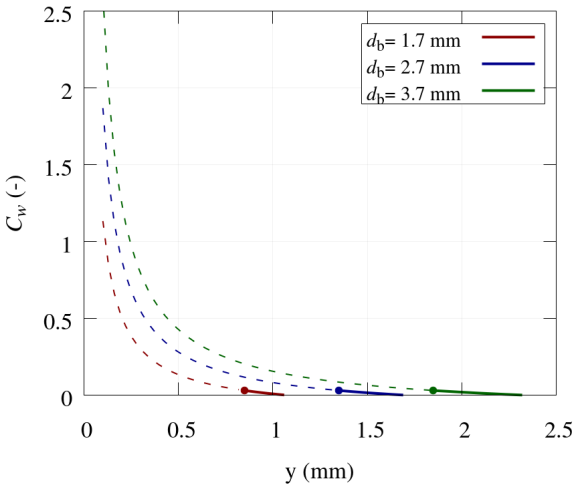

Figure 6.11: Wall lubrication force coefficient for three different bubble diameters assuming a relative velocity of $0.2\,\mathrm{m\,s^{-1}}$.

In Fig. 6.11 we show the coefficient of the wall lubrication force for three different bubble diameters. In the figure, the points show where the distance to the wall is equivalent to the bubble radius. This point represents the limit where the bubble is in contact with the wall. Dashed lines are plotted for distances to the wall to the left of this point. When the CFD-DEM method was used, the bubble centre was determined mainly by the bubble-wall contact force, then the coefficient falls around the range represented by the solid lines. Note, that the same model applied for TFM may result in an overestimated force.

Next, we have to consider the turbulent dispersion force. Note that in CFD-DEM it was not required as the turbulent effects was calculated directly in the forces. Then, in this section, the turbulence in the drag is considered with the turbulent dispersion force of Burns et al. (2004). In summary the interfacial force coeffficients used for this simulation with TFM are listed below:

Table 6.8: Coefficients for interfacial force closures used for TFM.

Drag force	Tomiyama et al. (1998)
Lift force	Tomiyama et al. (2002b)
Virtual mass force	Drew et al. (1987)
Turbulent dispersion force	Burns et al. (2004)

To perform this work it is also needed to account for the bubble-wall contact force. The next section deals with the development of a new wall force considering elastic deformation similar to the soft-sphere model of the CFD-DEM.

6.6.1 Bubble-wall interaction

As studied in the previous chapter with the CFD-DEM solver, the contact of the bubbles with the wall plays an important role to determine the lateral migration of the bubbles. When the bubbles impact against a wall they do deform and a deformation force must be considered also in TFM to explain the bubble dynamics. In this section we show the development of a TFM equivalent version of the soft-sphere model shown before for CFD-DEM, and taking into account the elastic deformation of the bubbles.

Deformation force onto bubbles in contact with the wall

Let us consider a spherical bubble of radius R_b rising near a plane wall (see Fig. 6.12). The z axis is chosen to be coincident with the main flow direction.

The coordinate y stands for the distance to the wall, whereas the coordinate x is orthogonal to the other two.

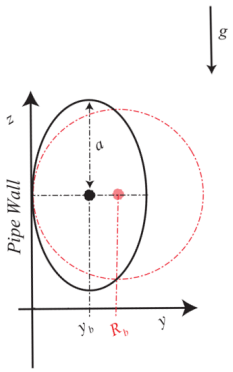

Figure 6.12: Coordinate system used for the calculations.

Consequently, the bubbles that are in touch with the wall are pressed against it and its shape is deformed. The deformation force or bubble-wall contact force, $\mathbf{f_{cf}}$, can be obtained (Zaruba et al. 2007) from the energy, δW, that is needed to make a differential change of its surface, S_b,

$$\delta W = \sigma \delta S_b. \tag{6.43}$$

As the bubble is deforming along the y-axis, the force can be obtained directly as

$$\mathbf{f_{cf}} = -\sigma \frac{\partial S_b}{\partial y_b} \mathbf{n_w}, \tag{6.44}$$

being $\mathbf{n_w}$ the unit vector in the y direction.

Assuming the shape of the deformed bubble as an spheroid so that the surface equation reads as

$$\frac{x^2}{a^2} + \frac{y^2}{y_b^2} + \frac{z^2}{a^2} = 1, \tag{6.45}$$

where a and y_b stand for the major and minor axes of the spheroid respectively. The volume of the spheroid is given by

$$V_b = \frac{4}{3} \pi y_b a^2, \tag{6.46}$$

where as its surface can be calculated as:

$$S_b = 2\pi a^2 \left(1 + \frac{y_b^2}{a^2 \sqrt{1 - \frac{y_b^2}{a^2}}} \operatorname{arctanh} \sqrt{1 - \frac{y_b^2}{a^2}} \right), \tag{6.47}$$

If the gas phase is treated as incompressible, the volume of the deformed bubble does not change with the deformation, so:

$$a = \frac{R_b^{3/2}}{\sqrt{y_b}}, \tag{6.48}$$

and the bubble surface is given simply by:

$$S_b = \frac{2\pi R_b^3}{y_b} \left(1 + \frac{y_b^3}{R_b^3} \frac{\operatorname{arctanh} \sqrt{1 - \frac{y_b^3}{R_b^3}}}{\sqrt{1 - \frac{y_b^3}{R_b^3}}} \right) \tag{6.49}$$

Introducing the radius normalized coordinates,

$$\beta \equiv \frac{y}{R_b}, \tag{6.50}$$

and

$$\beta_b \equiv \frac{y_b}{R_b}, \tag{6.51}$$

then the bubble surface can be computed as:

$$S_b = \frac{2\pi R_b^2}{\beta_b} \left(1 + \beta_b^3 \frac{\operatorname{arctanh} \sqrt{1 - \beta_b^3}}{\sqrt{1 - \beta_b^3}} \right). \tag{6.52}$$

Finally, the net deformation force can be written as:

$$\mathbf{f_{cf}} = \sigma \pi R_b f_d \mathbf{n_w}, \tag{6.53}$$

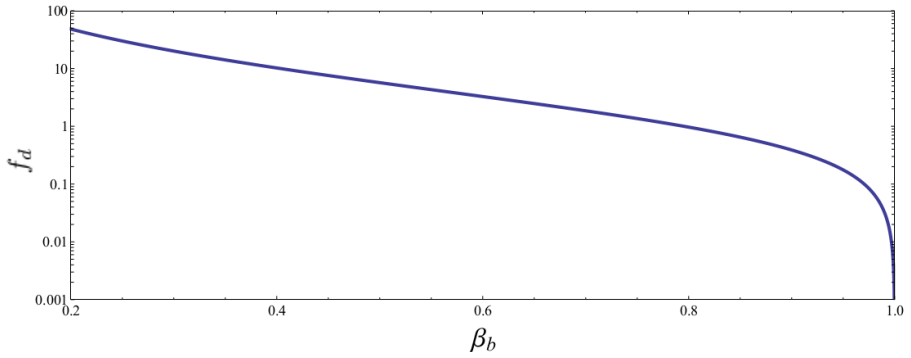

Figure 6.13: Plot of the normalized force function.

being f_d the normalized force function,

$$f_d \equiv \frac{1}{1-\beta_b^3}\left(\frac{2}{\beta_b^2}+\beta_b+\frac{\beta_b^4-4\beta_b}{\sqrt{1-\beta_b^3}}\operatorname{arctanh}\sqrt{1-\beta_b^3}\right). \tag{6.54}$$

As it can be seen in Fig. 6.13, the normalized force is zero for no deformation ($\beta_b = 1$) and increases fast with the bubble deformation.

Volumetric force

In order to obtain the Reynolds-averaged volumetric deformation force, $\mathbf{M}_{\mathrm{d,cf}}$, the following integral must be solved

$$\mathbf{M_{d,cf}} = \frac{1}{V_b}\int_{x_{min}}^{x_{max}}\int_{y_{min}}^{R_b}\Lambda\left(x_b,y_b;x,y\right)N\left(x_b,y_b\right)\mathbf{f_{cf}}dy_b dx_b. \tag{6.55}$$

In this equation, $\Lambda\left(x_b,y_b,x,y\right)$ stands for the chord-length of a bubble that is travelling vertically with its center being located at the coordinates (x_b,y_b). For spheroidal bubbles, this is given by

$$\Lambda\left(x_b,y_b;x,y\right) = \frac{2a\sqrt{1-\frac{(x-x_b)^2}{a^2}-\frac{(y-y_b)^2}{y_b^2}}}{L_b}, \tag{6.56}$$

being L_b the mean axial distance between bubbles. The term $N\left(x_b,y_b\right)$ in Eq. 6.55 stands for the Bubble Number Density Probability Function (BNPDF), and de-

scribes the probability of finding a bubble in a given location. As the deformation force does not depend on the coordinate x_b, and assuming a uniform distribution of bubbles, the integral above can be simplified to:

$$\mathbf{M_{d,cf}}\left(\beta\right) = \frac{\sigma\pi^2 R_b^2}{V_b L_b}\int_{1-\epsilon_{max}}^{1} \lambda f_d d\beta_b \mathbf{n_w}, \tag{6.57}$$

with

$$\lambda \equiv \frac{\pi}{2}\frac{\beta\left(2\beta_b - \beta\right)}{\beta_b^{5/2}}, \tag{6.58}$$

as long as $\beta \in [0, \beta_b]$.

As any interfacial force, the wall deformation force is expected to be dependant on the local void fraction. In order to introduce it in the formulation, let us recall that the void fraction profile for a uniform distribution of bubbles is given by:

$$\alpha_{\mathrm{d}} = \frac{R_b}{L_b}\left[\left(\beta - 1\right)\sqrt{\beta\left(2-\beta\right)} + \arccos\left(1-\beta\right)\right]. \tag{6.59}$$

Consequently, substituting L_b into Eq.6.57 the volumetric force can be expressed in terms of the local void fraction as:

$$\mathbf{M_{d,cf}} = \frac{\sigma\pi^2 R_b}{V_b}\alpha_{\mathrm{d}}\widetilde{M_d}\mathbf{n_w}, \tag{6.60}$$

Then, with the bubble volume expressed as a function of the bubble radius:

$$\mathbf{M_{d,cf}} = \frac{3\sigma\pi}{4R_b^2}\alpha_{\mathrm{d}}\widetilde{M_d}\mathbf{n_w}, \tag{6.61}$$

being $\widetilde{M_d}\left(\beta\right)$ the dimensionless volumetric force, given by

$$\widetilde{M_d} \equiv \frac{\int_{1-\epsilon_{max}}^{1}\lambda f_d d\beta_b}{\left(\beta-1\right)\sqrt{\beta\left(2-\beta\right)} + \arccos\left(1-\beta\right)} \tag{6.62}$$

Now we proceed to obtain a closed expression for the dimensionless volumetric force. A correlation function is proposed as an approximation to the exact numerical solution. The approximation is based on a balance between deformation and

buoyancy force. Note that the resulting formula is of general validity, for these assumptions, as it is applied to a dimensionless expression that does not depend on any empirical magnitude. This can be approximated by a function of the form:

$$\widetilde{M_d} \simeq A \sin\left(\frac{\pi\sqrt{\beta}}{\sqrt{2}}\right) \exp\left(-\frac{\beta^4}{\chi^4}\right). \tag{6.63}$$

In this equation, an amplitude function, $A\left(\epsilon_{max}\right)$, aims at describing the increase of the force intensity with the maximum deformation of the bubbles. The sinoidal function provides the main structure of the volumetric force with β, ensuring that it vanishes at both ends, $\beta = 0$ and $\beta = 2$. Finally, the decay function, $\chi\left(\epsilon_{max}\right)$, is inserted to account for the increasing asymmetry of the exact solution as the maximum bubble deformation increases and the smooth decay for $\beta \to 2$. Although the amplitude and decay functions were conceived as Taylor power series, a reduced number of terms showed to be important for the fitting so that:

$$A \equiv p_4 \epsilon_{max}^2 + p_5 \epsilon_{max}^4, \tag{6.64}$$

and

$$\chi^4 \equiv p_6 + p_7(\epsilon_{max}, -0.5)^2 + p_8(\epsilon_{max} - 0.5)^8, \tag{6.65}$$

with the following values for the fit parameters,

$$\begin{aligned} p_4 &= 1.63, \\ p_5 &= 16.5, \\ p_6 &= 1.91, \\ p_7 &= 167, \text{ and} \\ p_8 &= 146000. \end{aligned} \tag{6.66}$$

6.6.2 Results

The simulations are performed in TFM with this first approach of the bubble-wall contact force to obtain the same modelling as in CFD-DEM. Fig. 6.14 shows the comparison between approaches of the void fraction radial profile. The figure includes different hypothesis studied with CFD-DEM in the previous chapter, related with turbulence and size effects. This is included to highlight assumptions not considered with this TFM as inhomogeneity or turbulent effects in the lateral forces.

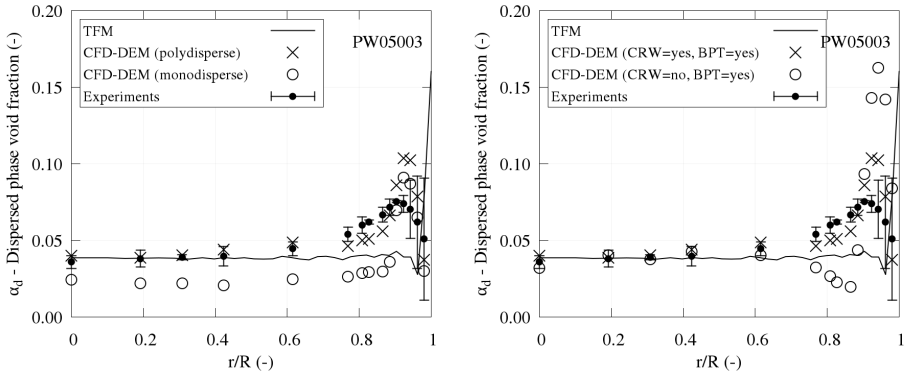

Figure 6.14: Comparison between the TFM and different hypothesis for CFD-DEM.

The results revealed that the TFM failed to predict the void fraction profile with this attempt. Future contributions will be focus to improve the bubble-wall contact force shown before, considering the turbulence effects on the collisions and improving the consideration of the bubble-wall interaction dynamics through the lateral forces. Note that these results also motivated the investigation of the CFD-DEM presented model obtaining satisfactory results with these models. In a turbulent flow, the fluctuating component of the carrier phase velocity has an influence in the force acting on a bubble. Essentially, they are captured in turbulent eddies and moved with it. Usually, the turbulence effect on the interfacial forces are neglected in TFM or are only considered in the drag through the turbulent dispersion force (López de Bertodano 1992; Burns et al. 2004). The influence of the turbulence on the interfacial forces was evaluated by Behzadi et al. (2001) for mixing layer and sudden expansion scenarios concluding that the turbulent effects on lift and virtual mass forces are negligible for these cases. However, in the literature, there are no many investigations showing its influence in other systems. Indeed, when the lateral forces are predominant as in the case of wall-bounded systems we may expect an important influence on the lift and wall interaction turbulent effects. These turbulence effects were considered directly in the CFD-DEM through the instantaneous velocities used to calculate the forces. Also, some bubbles leave the equilibrium state presumably because of the dispersion effects. Furthermore, because of an increase in the number and kinetic energy of the collisions with the wall, it leaves the bubble beyond the range of influence of the lift force. This produces a temporal migration of some bubbles close to the center. Then, future contributions should be focused on modelling this effects with TFM.

Chapter 7

System codes

System codes relying on one-dimensional TFM are widely used in industrial applications due to their simplicity, speed and historical background. We conclude with this approach, the validation scheme used in this thesis, feeding the analysis of its performance with the information acquired from the study of the experimental data and numerical methods with higher level of accuracy. A correlation for one-dimensional bubble size expansion is included. Finally a comparison of drift-velocity and drag coefficient approaches is performed and a new version proposed.

7.1 Introduction

Two-phase flow phenomena has been an object of study during several decades with a great impact in nuclear field. From the reactor to the turbines, one can find a wide variety of systems where two-phase flow plays a main role: BWR core, secondary loop or reactor heat removal system are examples of two-phase flow components. It is found not only in normal operating conditions, but also in eventual situations, like instabilities events, loss-of-coolant accidents or refueling. All the previous cases imply different conditions of pressure, temperature or mass flow.

This broad range of situations is considered in one dimensional thermal-hydraulic codes to set the appropriate flow regime in each situation. They include the two-fluid model (Ishii 1975), where averaged Navier-Stokes equations are solved for each phase including momentum, energy and continuity equations. Then, one can account for the interaction terms to consider the transfer of mass, momentum and energy at the interphase. This interfacial momentum term differs depending

on which flow regime is working. The proper regime is selected according to a flow regime map and the velocities of each phase. Different flow regime maps have been proposed by diverse authors (M.A. Vince 1982; M. Ishii 1982). This work investigates the performance of RELAP5/MOD3 predicting the results of experiments in an upward vertical bubbly flow for low velocity conditions. Bubbly flow at this conditions can be found in pressurizers, reactor pools or refuelling operations.

The one-dimensional Two-Fluid Model (1D TFM) has different approaches in system codes for the interfacial momentum transfer depending on the flow regime. In particular, for bubbly flows, the interfacial momentum transfer has the main responsibility (Brooks et al. 2012). Two approaches are usually used to define the interfacial drag force: the drift-velocity approach (DVA) and the drag coefficient approach (DCA). RELAP5/MOD3 uses DVA for bubbly flow in vertical pipes and DCA was used in the previous RELAP5/MOD2 version. The drift models, although more simple and effective than the drag coefficient approach, usually are only valid in the range of applicability for which they were obtained as they depend on flow and geometry.

The drag force calculated with DCA relies on correlations that are defined traditionally as a function of Reynolds and/or Eötvös numbers. In this work we make use of this approach in RELAP5/MOD3, by modifying the code, to verify the performance of both models and the comparison with the experiments.

The use of DCA incorporates a set of assumptions to calculate the drag term. The influence of these assumptions is also validated through the development of a modified version of the drag coefficient approach (DCA*) that consists of:

- A drag coefficient correlation that takes into account the effect of the bubble shape through the Eötvös number and the effect of the contaminants present in the system used.
- Bubble size distribution consideration by means of their statistical parameters including the axial evolution due to the gas expansion.
- Interfacial area calculated directly from the definition of the Sauter mean diameter.

In summary, three drag coefficient approaches are used. A drift-velocity approach named DVA, an existing drag coefficient approach DCA, and the proposed drag coefficient approach DCA*. These approaches are studied to compare the influence of the simplifications and assumptions on the results. This process is schematized in Fig.7.1.

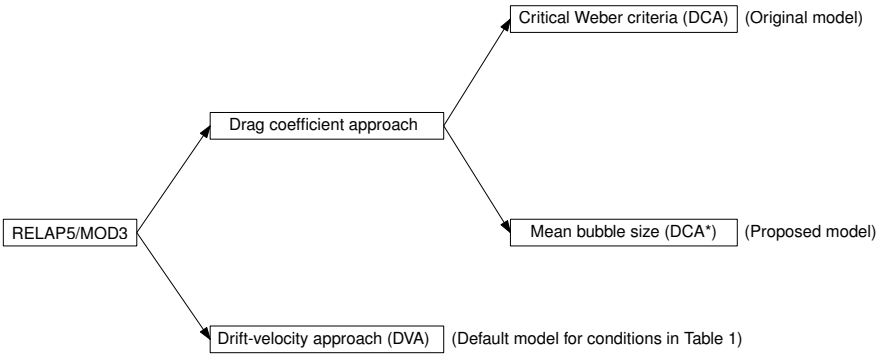

Figure 7.1: General overview of the drag force term approaches in this work.

This chapter aims on the one hand to investigate the performance of the code and the loss of information as a result of the information, and on the other hand to validate the axial evolution of the system code.

7.2 Mathematical formulation and setup

7.2.1 Drift-velocity approach (DVA)

The relative motion between the phases can be considered through a drift flux model (Zuber et al. 1965; Ishii et al. 2006b). In a drift flux model the mixture of the phases is solved as a whole. In RELAP5/MOD3, a drift-velocity approach is incorporated into the TFM to describe the interfacial drag force term. The area averaged interphase drag term is given as:

$$\mathbf{M}_d = C_i |V_r| V_r, \tag{7.1}$$

where C_i is the drag coefficient and V_r the relative velocity between both phases. The drag coefficient is obtained from a balance of the forces in the direction of the flow. It considers the interfacial drag, buoyancy and pressure drop, applies the assumptions that both phases have equivalent pressure and the action-reaction principle for the interfacial momentum terms (Brooks et al. 2012). The drag coefficient results:

$$C_i = \frac{\alpha(1-\alpha) g (\rho_\mathrm{c} - \rho_\mathrm{d})}{V_\mathrm{r}^2} \tag{7.2}$$

where α, g and ρ, are the void fraction, gravitational constant and density. In this equation, the relative velocity is replaced with the relation between local relative velocity and void weighted phase velocities assuming uniform relative velocity:

$$V_{\mathrm{r}} = \frac{v_{gj}}{1-\alpha} \tag{7.3}$$

From the definitions of Eq. 7.2 and Eq. 7.3, the drag coefficient in terms of drift flux is finally given as:

$$C_i = \frac{\alpha(1-\alpha)^3 g \Delta\rho}{v_{gj}^2} \tag{7.4}$$

The term v_{gj} refers to the drift velocity that depends on the flow geometry. For vertical pipe flows and conditions studied in this work, RELAP5/MOD3 uses the Chexal-Lellouche correlation (Chexal et al. 1985; Chexal et al. 1992):

$$v_{gj} = \sqrt{2}\Big(\frac{(\rho_c - \rho_d)\sigma g}{\rho_c^2}\Big)^{\frac{1}{4}} C_2 C_3 C_4 C_9, \tag{7.5}$$

where σ is the surface tension. The equation depends on many constants as C_2, C_3, C_4 and C_9 among others. This is a generalized correlation that was compared using steam-water, air-water, and refrigerant data on multiple flow configurations ranging from different orientations as vertical, horizontal or inclined, different geometries as pipes, channels, rod bundle and flow configurations as cocurrent or countercurrent flow. This correlation, although general, lacks the model specificity that is required for an accurate prediction (Griffiths et al. 2014). Moreover, this approach is not consistent with the TFM and its application is contrary to the field equations solved as noted by Brooks et al. (2012).

7.2.2 Drag coefficient approach (DCA)

The drag coefficient approach is based on the general drag interfacial term. This is defined as:

$$M_d = \frac{1}{8} C_d \rho_c a_i |v_d - v_c|(v_d - v_c) \tag{7.6}$$

In RELAP5/MOD3 for bubbly flow the drag coefficient was based on Ishii et al. (1979):

$$C_d = \frac{24}{Re}(1.0 + 0.1 Re^{0.75}) \tag{7.7}$$

The drag coefficient depends on the flow parameters, and the bubble size should be considered. The maximum bubble diameter, $d_{\max}$, is calculated from a critical Weber number:

$$We_{crit} = \frac{v_r^2 d_{b,max} \rho_c}{\sigma} \tag{7.8}$$

RELAP5/MOD3 specifies a value of 10 for bubbles for the We_{crit} (Nuclear Regulatory Commission 1995; Wallis 1969). In this equation, v_r^2 is not calculated as the difference between the phase velocities but refers to the velocity difference that gives the maximum bubble size (Nuclear Regulatory Commission 1995). The following equation is applied:

$$v_r^2 = \max\left[(v_d - v_l), \frac{We_{cri}\sigma}{\rho_l \min(D' \alpha_d^{(1/3)}, D_h)}\right], \tag{7.9}$$

where D' is set to 0.005 m for bubbly flow and D_h is the hydraulic diameter.

The bubble diameter is calculated from the maximum bubble diameter with the following assumption:

$$d_b = 0.5 d_{b,\max} \tag{7.10}$$

The interfacial area concentration is then given in terms of the mean bubble diameter (Nuclear Regulatory Commission 1995; Brooks et al. 2012):

$$a = \frac{6\alpha}{d_{32}} = \frac{3.6\alpha}{d_b}, \tag{7.11}$$

where d_{32} is the Sauter mean diameter of the distribution related to the bubble diameter d_b assuming a Nukiyama-Tanasawa distribution (Nuclear Regulatory Commission 1995), a distribution for droplet diameter for a spray.

7.2.3 Drag coefficient approach with specific drag closure and mean bubble size distribution (DCA*)

The previous drag coefficient approach contains a set of assumptions that may affect the prediction of the two-phase flow characteristics. In this work we propose a new approach to validate bubbly flow scenarios. The model consists on a drag coefficient correlation specific for the scenario, the consideration of the BSD and its axial evolution. Considering the BSD at each node implies that, on the one hand the influence of the bubble size in the terminal velocity can be incorporated through the drag force, on the other hand the interfacial area can be computed directly from the definition of the Suater mean diameter without any assumption.

For instance, the drag correlation of Tomiyama et al. (1998) for contaminated systems is used and implemented:

$$C_{\mathrm{D}} = \max\left[\frac{24}{Re}(1+0.15Re^{0.687}), \frac{8}{3}\frac{\mathrm{Eo}}{\mathrm{Eo}+4}\right] \tag{7.12}$$

This expression includes a region dominated by the Eötvös number. Then, is required the definition of the bubble size given in the experiments. The terminal velocity of the bubbles as function of the diameter using the drag force coefficients of Eq. 7.7 and Eq. 7.12 are compared in Fig. 7.2.

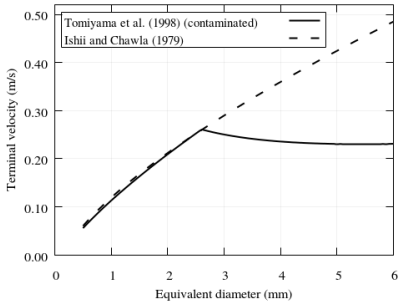

Figure 7.2: Terminal velocity for Tomiyama et al. (1998) and Ishii et al. (1979) drag correlations.

From the measurements of the BSD in the experiments we can define the size at the inlet boundary conditions. As the experiments are performed at atmospheric pressure, an increase of around 30% can be noted from the inlet to the outlet in

the experiments (z/D=22.4 to z/D=98.7). Given the change of the pressure field in the axial direction, the code will consider this axial evolution in terms of void fraction. For a rigorous implementation, the axial change on the bubble size must be considered.

The different of sizes in a pipe between two different heights, excluding the breakup and coalescence mechanisms, are due to the pressure changes. This change is given by the ideal gas law and can be expressed as an expansion factor, f_i, that is related in this work for convenience to the inlet values. At each node i we can calculate:

$$f_i = \left(\frac{\alpha_i}{\alpha_{\text{inlet}}}\right)^{\frac{1}{3}} \tag{7.13}$$

where α_i and α_{inlet} are the void fraction at the given node and the void fraction at the inlet respectively.

If the bubbles change its size by the factor f_i, this means a proportional increase of the bubble size and it is equivalent to multiply a random variable by a constant value. Then, the mean or expected value is also multiplied by the constant value (the same is applied to the standard deviation):

$$E[f_i d] = f_i E[d] \tag{7.14}$$

$$\text{Var}[f_i d] = f_i^2 \text{Var}[d] \tag{7.15}$$

Then the BSD can be estimated as a scaled distribution of the BSD at the different heights or nodes. A normal distribution at a given height would have the following statistical parameters:

$$\mu_i = f_i \mu_i \tag{7.16}$$

$$\sigma_i = f_i \sigma_i \tag{7.17}$$

Note, that breakup and coalescence has been neglected as any event was recorded for this cases from the observations with the high-speed camera. For other scenarios a one-dimensional approximation of a population balance equation would be required, but for this work this approximation has been preferred for convenience as a first approach.

A mean bubble diameter of the distribution can be defined from the numeric mean diameter definition:

$$d_b = d_{10} = \frac{\int_0^\infty d^1 f(d)\mathrm{d}d}{\int_0^\infty d^0 f(d)\mathrm{d}d} = \mu \tag{7.18}$$

The Sauter mean diameter of the distribution can be calculated knowing that the bubble size follows a normal distribution:

$$d_{32} = \frac{\int_0^\infty d^3 f(d)\mathrm{d}d}{\int_0^\infty d^2 f(d)\mathrm{d}d} = \frac{\mu^3 + 3\mu\sigma^2}{\mu^2 + \sigma^2} \tag{7.19}$$

The interfacial area concentration from the definition of Sauter gives the following:

$$a = \frac{6\alpha}{d_{32}} \tag{7.20}$$

7.2.4 Modelling and setup

The simulations are undertaken by modelling a pipe, whose length is equal to the experimental section from z/D=22.4 to z/D=98.7, with 99 uniform axial nodes. Boundary conditions are defined by time-dependent volumes at both inlet and outlet, followed by a time-dependent junction at the inlet and a branch at the outlet. In order to simulate non-condensable gases, one has to activate card 110 in the input. This card allows to define one or more (until eight) gases. In this work, only air has been defined.

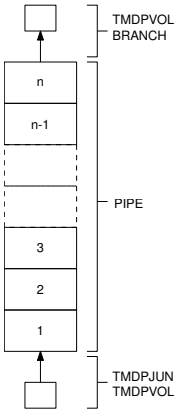

Figure 7.3: Model and nodalization of the pipe for RELAP5/MOD3.

RELAP5/MOD3.3 changes from single-phase to two-phase critical flow model when the non-condensable quality is greater than 1×10^{-6}. From this moment, the gas phase is treated as a mixture of vapour and non-condensable gas [RELAP Manual]. The simulations performed consist of a null transient of 100 seconds, so that the convergence, set at 1×10^{-3}, is completely achieved.

7.3 Results

The simulations are performed with DVA, DCA and the modified version DCA*. In this section we show first a comparison of the models and later a validation with experiments using the proposed model. Cross-section averaged experimental values are obtained from the radial profiles to compare the results of the simulations with the experiments.

7.3.1 Model comparison

The case PW05003 is used first to compare the different approaches. Fig. 7.4 shows the axial evolution of void fraction. The effect of the gas decompression is noted in the void fraction as a function of the height. DCA and DCA* gives similar results while DVA shows a lower void fraction values with a smoother axial evolution than the drag coefficient approaches. The discrepancies increase with the height, mainly because DCA* takes into account the bubble expansion of the distribution, and in consequence it has an impact in the drag coefficient and the interfacial area.

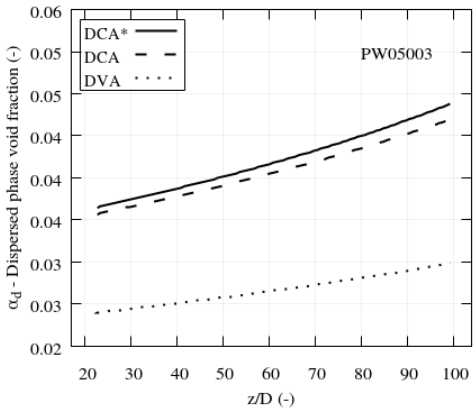

Figure 7.4: Comparison of void fraction axial evolution for the different drag approaches.

Fig. 7.5 shows the comparison of the disperse phase velocity. DVA with the Chexal-Lellouche gives a higher disperse phase velocity and consequently the void fraction values shown before are significantly lower. Slightly different trends are noted with DCA and DCA* with decreasing values of the velocity along the pipe.

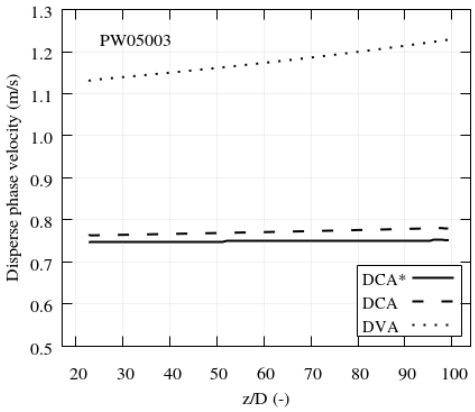

Figure 7.5: Comparison of disperse phase velocity axial evolution for the different drag approaches.

The bubble diameter is calculated for DCA and DCA* (see Fig. 7.6). Note that a proper calculation of the bubble diameter could be required to take into account breakup or coalescence phenomena.

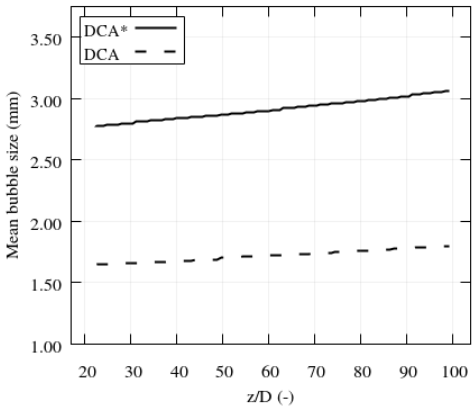

Figure 7.6: Comparison of mean bubble size axial evolution for the different drag approaches.

The interfacial area concentration is compared, in turn for DCA and DCA* as they are based on the drag coefficient approach. For instance, when heat transfer plays an important role as the simulations in nuclear installations, an accurate prediction of the interfacial area concentration is required. Fig.7.11 shows the comparison of these cases.

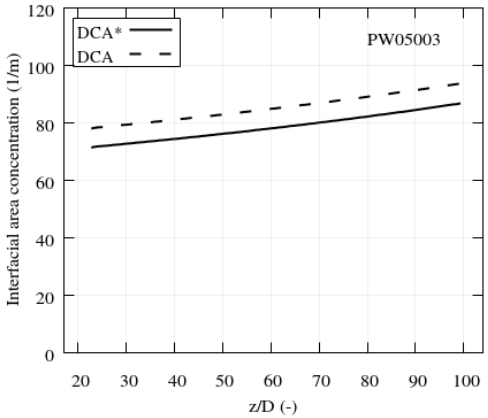

Figure 7.7: Comparison of interfacial area axial evolution for the different drag approaches.

Note that the values of the interfacial area are relatively close for both approaches. Significant discrepancies are appreciated between both approaches. The interfacial area equation for DCA is based on several assumptions but for DCA* is calculated directly from the Sauter mean diameter of the size distribution that is actually known. For DCA the bubble diameter is underestimated and the resulting interfacial area model compensates the values. In fact, a realistic calculation of d_b together with the area interfacial with DCA would give results of around the 50% of the values calculated with DCA*. These results and differences between bubble size and interfacial area can be explained by four main factors related with DCA:

- The use of the Nukiyama-Tanasawa size distribution.
- The criteria to determine the maximum bubble size from a critical Weber number.
- The assumption of obtaining the bubble diameter as a half o the maximum diameter.
- The calculation of v_r^2 with Eq. 7.9.

7.3.2 Validation with experiments

The previous section showed the differences existing when using the different approaches. It demonstrated for a given scenario that void fraction, dispersed phase velocity and interfacial area concentration can vary widely if a proper representation of the drag force and bubble size is not considered in the simulation. For instance, common models as DVA or DCA are not able to predict altogether the variables checked for this scenario due to the assumptions introduced.

In summary, the proposed drag coefficient approach (DCA*) considers the Tomiyama drag correlation for contaminated systems, the measured BSD with its axial evolution, and a direct calculation of the interfacial area concentration. All these effects represents more accurately the scenarios to simulate and the rest of the simulations are performed with this model. The cases PW05002, PW05003 and PW05004 described in Table. 2.2 are consequently analysed.

The mean bubble size and its axial evolution is shown in Fig. 7.8. Bigger bubble sizes are noted for PW05004 as higher gas flow rates through the sparger could result in an increasing diameter. However, is not observed a linear relation with PW05002 and PW05003. It could be explained due to the mechanism described by Kazakis et al. (2008) where, as the gas flow rate increase more pores are activated and hence more bubbles are formed. For higher values, larger bubbles can be produced from the activated pores or eventually if smaller pore sizes exists new smaller bubbles will appear.

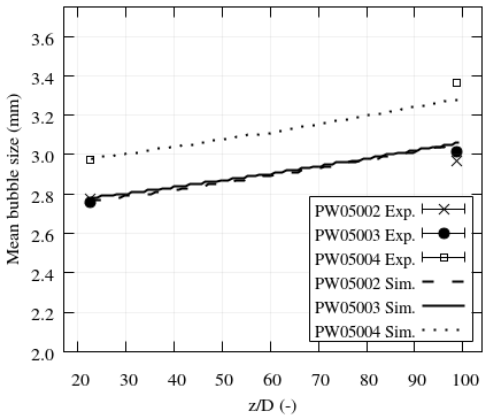

Figure 7.8: Comparison between computational results and experiments of the bubble mean size axial evolution.

The void fraction profiles are compared in Fig. 7.9. The computational results match the experiments accurately along the pipe. The results at the top measure-

ment port are well predicted for the three cases despite its non-linear evolution. This effect is more pronounced as the gas flow rate increase.

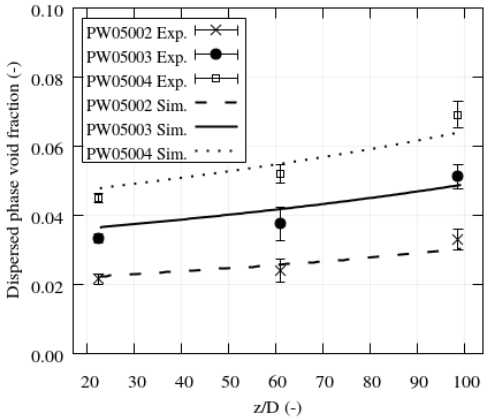

Figure 7.9: Comparison between computational results and experiments of the void fraction axial evolution.

In Fig. 7.10 the validation is done for the disperse phase velocity. The results are similar to the experiments both in magnitude and trend. The drag coefficients are obtained from experiments for single bubbles and therefore the influence that the bubbles have with each other is not taken into account. Therefore, the disperse phase velocity of the system could be different with these considerations.

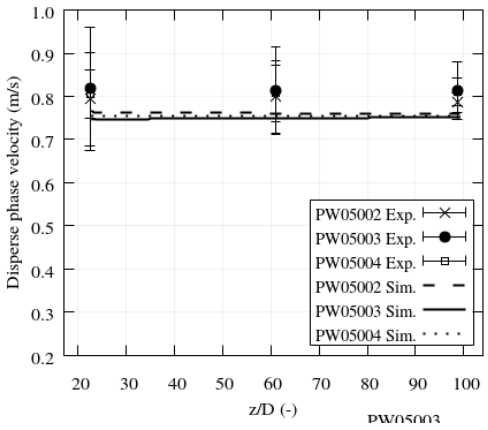

Figure 7.10: Comparison between computational results and experiments of the disperse phase velocity axial evolution.

Finally, the interfacial area concentration is analyzed in Fig. 7.11 noting how the interfacial are increase with the gas flow rate and the pipe height.

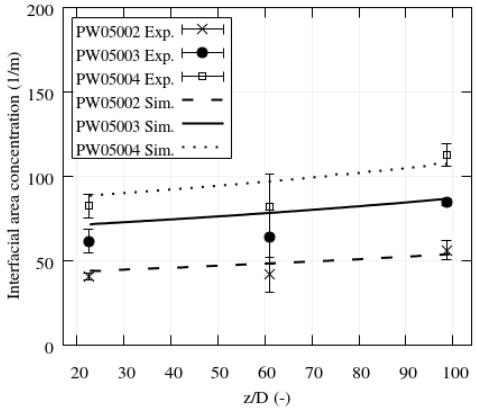

Figure 7.11: Comparison between computational results and experiments of the interfacial area concentration axial evolution.

7.4 Conclusions

A 1D TFM was used to simulate bubbly flow in adiabatic air-water upward bubbly flow to compare the results with experimental data at low velocity conditions. RELAP5/MOD3 was used to simulate these scenarios. This system code uses the drift-velocity approach (DVA) by default for the conditions tested. The differences with the experiments were considerable. Then the drag coefficient approach (DCA) used in previous versions for bubbly flow and vertical pipes was incorporated giving more reasonable results. However, the simulations with DCA were not able to predict all the variables compared.

A modified version of the drag coefficient approach implemented was proposed (DCA*). This included: a proper drag force for this scenario, the size effects in the drag force, bubble size distribution with axial evolution and direct calculation of the interfacial area. As a result of this implementations more accurate results in terms of magnitude and trend are obtained in overall, compared with regard to DCA. In addition, the validation performed with this model shown a good agreement with the experiment for several variables as: axial evolution of void fraction, disperse phase velocity, mean bubble size and interfacial area.

From this study the following conclusions are drawn:

- The Chexal-Lellouche drift correlation fails predicting bubbly flow in vertical pipes at low liquid velocities.
- The drag coefficient approach predicts relatively well the interfacial area at expenses of underestimating the mean bubble size around a 50%.
- The proposed drag coefficient approach is able to reproduce all the variables as the size distribution is considered and interfacial area is calculated directly from the size distribution.

While the present study was focused on investigate the different drag approaches using a system code, future investigations will incorporate the study of high velocity conditions similar to the present in nuclear reactors where break-up and coalescence takes place to investigate the modelling using 1D TFM and population balance equations.

Chapter 8

Preliminary studies on other bubbly flow system

Many industrial applications involving two-phase flow systems require the use of filters or grids to manage their processes. Despite the existence of numerous numerical studies related to two-phase flow, bubbly flow through obstacles with holes or narrow gaps have not been carefully studied and analysed. In this study two approaches at different resolution level as TFM or CFD-DEM are evaluated to analyse the appropriateness of these methods for this complex scenario.

8.1 Overview

This work studies the physics surrounding two-phase flow with two different approaches for predicting its dynamics at different resolution levels in a system with a perforated plate.

Although TFM has been used traditionally for engineering applications to predict two-phase flow and validated against experimental data in scenarios such as bubble columns or pipes, some industrial applications as two-phase flow systems with presence of filters or grids to manage its processes has not been widely studied. In this scenario, numerical methods could be useful to study interesting phenomena related with the bubble residence time as oxygen transfer rate or two-phase flow heat transfer, present for instance, in chemical or nuclear applications. However, the TFM approach could fail when the holes presented in the geometry are smaller than certain diameters of the bubble population size. The dispersed phase, passes

through them unrealistically as they are treated as a continuum media and the force balance is crucial.

The same scenario is computed with CFD-DEM, which calculates the motion of each bubble and takes into account the dispersed phase blockage of the perforated plate. Average void fraction and velocity distributions across and downstream of the obstacle are discussed.

8.2 Description of the simulation

Bubbly flow with bubbles passing trough a perforated plate is simulated with the classical TFM approach shown before and the novel CFD-DEM solver presented in this thesis and implemented in OpenFOAM®. Computational results from both approaches as void fraction distributions, averaged cross-section of the void fraction at different axial levels and velocities are shown in this work.

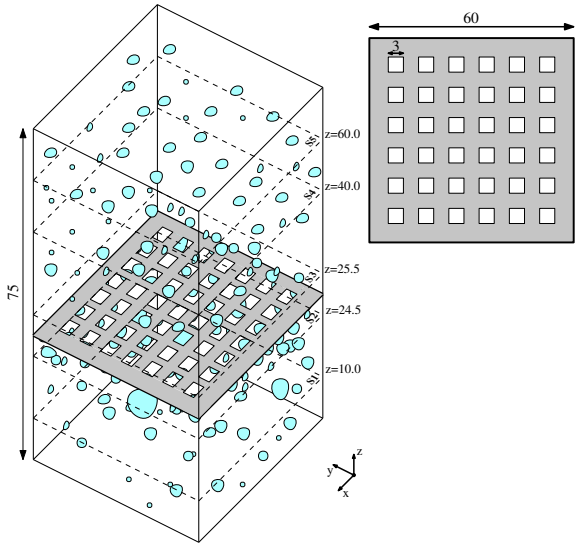

Figure 8.1: Description of the simulation domain (dimensions in mm).

In order to test the two solvers, a vertical square channel is simulated. A square hole perforated plate is located at 17 times the bubble size (d_b) from the inlet. The holes, of size $2d_b$, are distributed in the plate as shown in Fig. 8.1. The gas flow is introduced uniformly at the bottom of the channel in an initially quiescent medium. As a first approximation, we consider a monodispersed case with a bubble size of 1.5 mm which allows the bubbles to pass through the plate.

Cross-section planes at different positions along the domain are analyzed showing the void fraction, continuous and disperse phase velocities. In particular, the time evolution of the averaged cross section of the void fraction is studied with DEM at the five different axial distances shown in Fig. 8.1. S1 located close to the bottom of the channel, S2 before the plate, S3 after the plate, S4 and S5 significantly far from the plate. As a result, we can analyse the effect of the plate and the influence on the dispersed phase. Finally, TFM is also used to compare with the time-averaged results of the DEM simulation.

8.3 CFD-DEM results

The CFD-DEM simulation was run until a physical time of 10 seconds. The evolution of the bubbles at different times is shown in Fig. 8.2. The bubble residence time illustrates the influence of the plate on the system and it can be appreciated how the bubbles remain trapped temporally in the region just downstream from the plate.

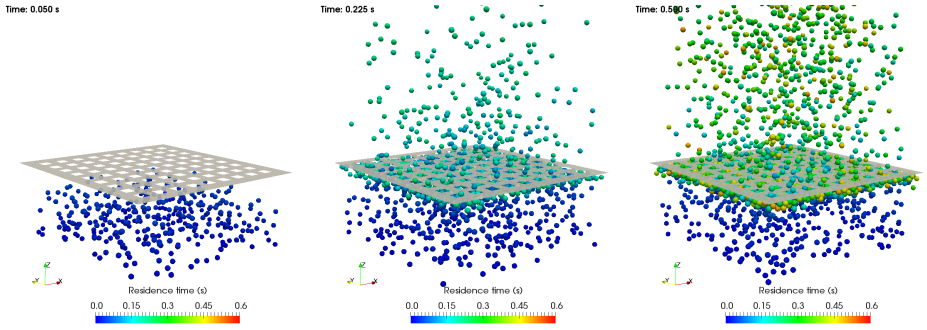

Figure 8.2: Time evolution of the bubbles position and residence time for the monodisperse scenario.

The influence of the bubbles on the liquid velocity is shown in Fig. 8.3 for different time snapshots. A decrease on the bubble velocity once it hits the plate is observed on the bubble, and it recovers its rising velocity once it passes the plate.

In Fig. 8.4 we show the dynamics at sections (see Fig. 8.1) close to the injection (S1) and far from the plate (S4 and S5). The system begins to become steady at around 1.5 seconds where the air flow through the holes is constant.

The accumulation of bubbles at a close distance downstream and upstream from the plate is quantified by means of the averaged cross section of the void fraction at the planes S2 and S3 in Fig. 8.5. Before the plate (S2), the void fraction increases as the bubbles arrives to the obstacle with the blockage limiting the air flow and

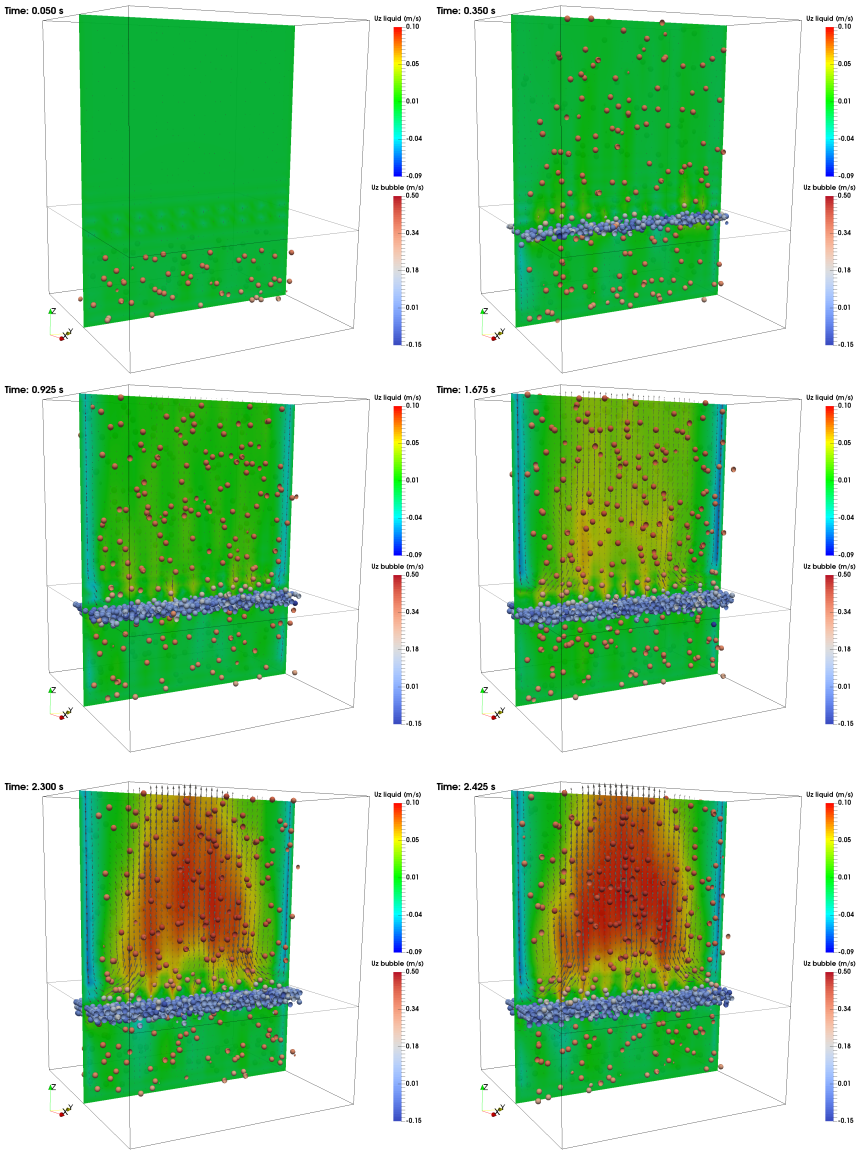

Figure 8.3: Time evolution of the bubbles clipped at center with the z-direction bubble velocity plotted and a cross-section passing through the center in the axial direction showing the liquid velocity and streamlines.

decreasing its rising velocity. After the plate (S3), the void fraction follows a similar pattern with values close to the inlet conditions.

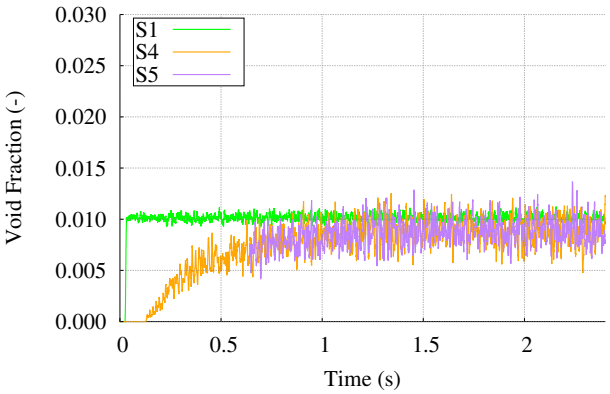

Figure 8.4: Time evolution of the bubbles position and residence time for the polydisperse scenario.

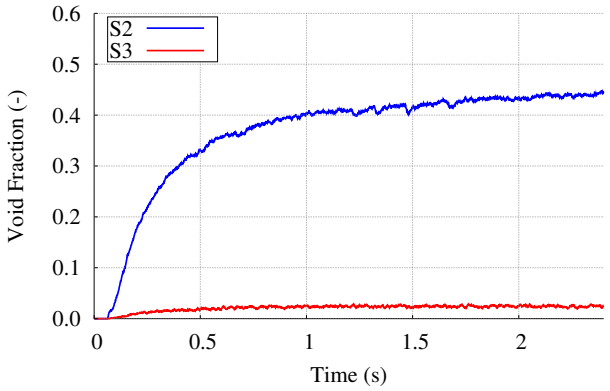

Figure 8.5: Time evolution of the bubbles position and residence time.

8.4 TFM results

The following provides the results obtained with the TFM approach. In Fig. 8.6 we show the liquid velocity (left) and the void fraction (right). We can note that the liquid velocity distributions downstream from the plate are significantly different compared with the obtained with CFD-DEM (Fig. 8.3). A similar vortex is noted after the plate and near the wall but the velocity in the core of the channel is predicted with discrepancies between both methods. The void fraction predicted with TFM show a local concentration of void fraction just before the plate in the

areas blocking the flow but not just at the holes where the dispersed phase flows without bubble size restrictions.

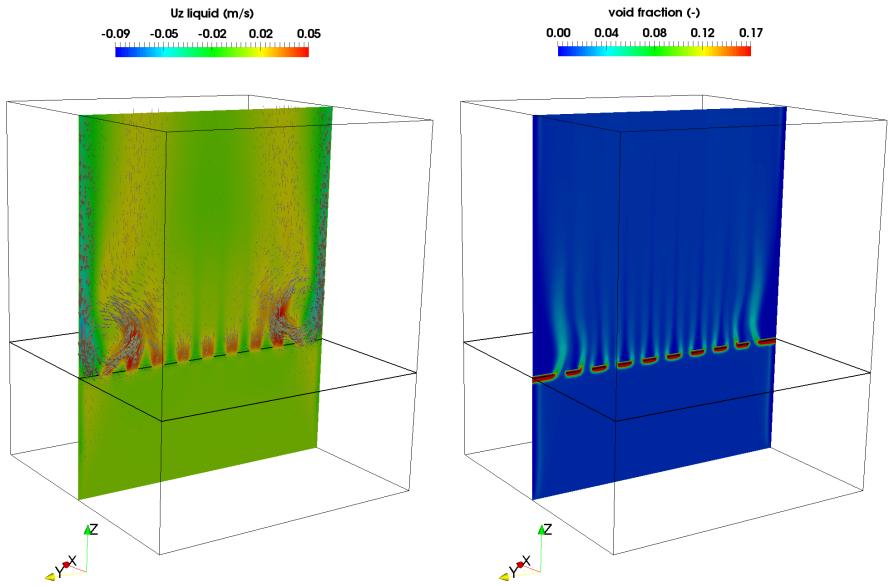

Figure 8.6: Cross-section plane and axial direction showing the liquid velocity and streamlines.

To analyse this, an axial cross-section plane at z=25.5 mm is illustrated at Fig. 8.7. In this figure we can clearly observe how the void fraction is higher close to the walls and almost zero at the hole center as the dispersed phase flows directly as a fluid from the areas with high void fraction downstream from the plate.

Finally, we compare the performance of the two solvers predicting the void fraction with the cross-section average void fraction along the channel in Fig. 8.8.

In the figure below, is highlighted the difference between the approaches which demonstrates that the classical formulation of the TFM underpredicts the accumulation of bubbles before the plate as a consequence of the blockage, compared with a more advanced technique.

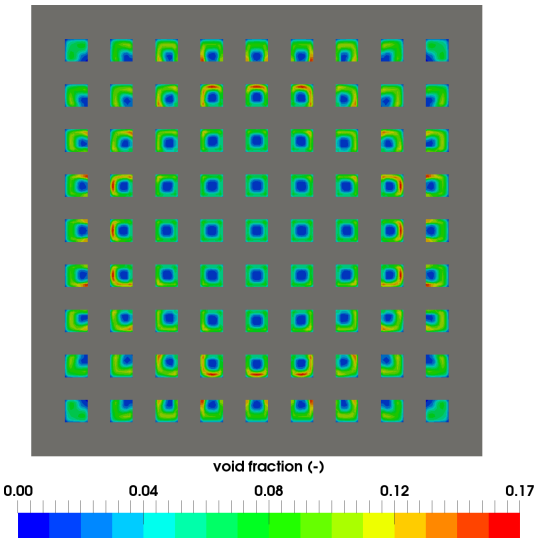

Figure 8.7: Time evolution of the bubbles position and residence time for the polydisperse scenario.

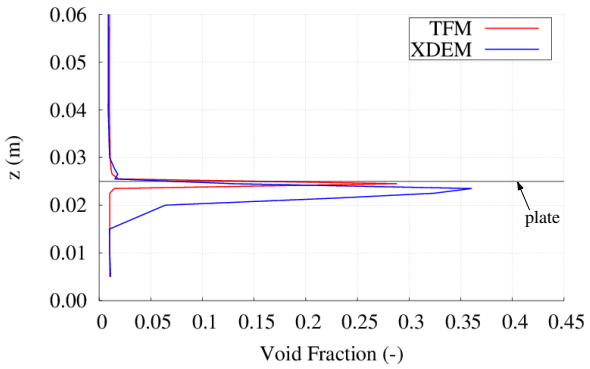

Figure 8.8: Cross-section average void fraction as a function of the height for TFM (red line) and CFD-DEM (blue line).

8.5 Experimental facility proposed and preliminary data

After verifying this scenario through both approaches, the experimental facility described in Fig. 8.9 is proposed.

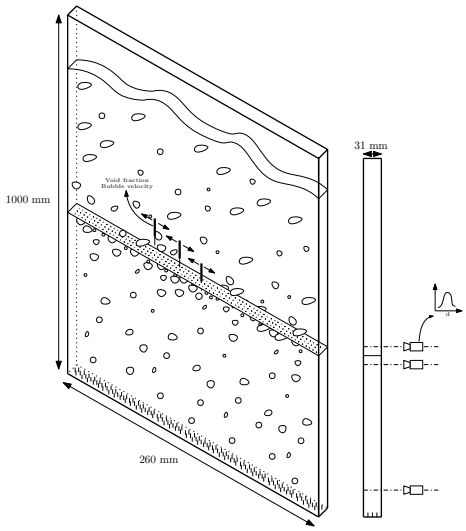

Figure 8.9: Experimental facility proposed.

The test rig counts of a 2D channel. A perforated plate or grid is located in the middle of the channel. Different grids of different hole size are designed and produced with a 3D printer (see Fig. 8.10). The facility is equipped with a needle probe system to measure the void fraction and velocity after and before the plate, a LDA to measure the velocity and turbulence and a high-speed camera located at different places to analyse the bubble size distribution after and before the plate. In this way we can detect the blockage of the bubbles depending on the size or break-up as a consequence of big bubbles passing through the grid.

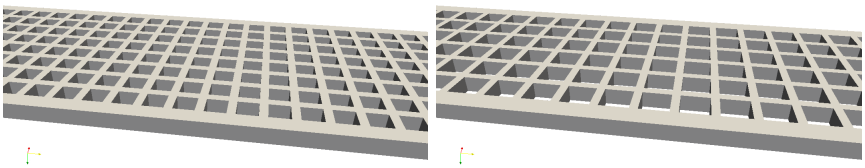

Figure 8.10: CAD models of two grids.

An example of the data obtained by the high-speed cameras is shown in Fig. 8.11. The first observations show a similar behavior as detected by the CFD-DEM. The bubbles are accumulated just before the grid. Periodically a group o bubbles passes trough the holes in pulse events.

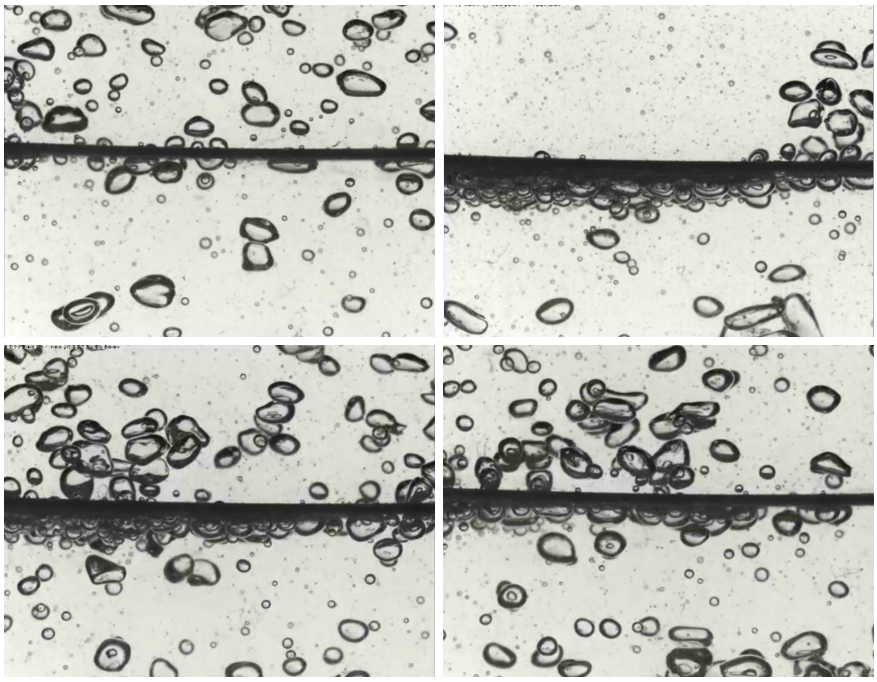

Figure 8.11: Images obtained by the high-speed camera at different time-steps.

In addition, bubble break up occurs for bigger bubbles flattened against the wall as shown in Fig. 8.12. In order to predict this phenomena with a CFD-DEM further modelling should be included.

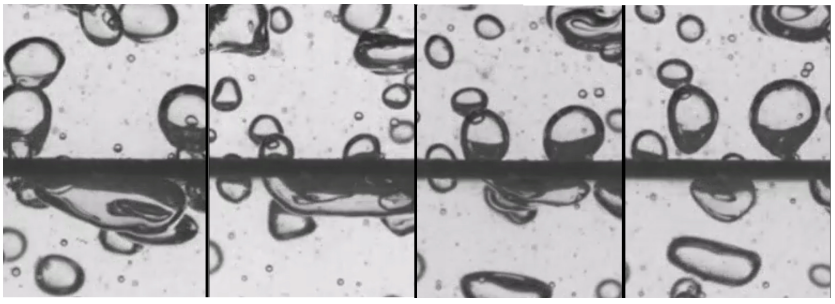

Figure 8.12: Bubble cut sequence.

8.6 Conclusions

A simulation of a vertical square channel with a square hole perforated plate has been simulated with two approaches as TFM and CFD-DEM. For the latter, the simulation shows an accumulation of bubbles just downstream of the plate produced by the collision of the bubbles with an obstacle as the perforated plate. After an initial transient period, the dispersed phase flow through the holes reaches a stationary condition and far enough downstream of the plate the cross-section average void fraction matches the values at the inlet. The performance of each solver has been analysed.

We can conclude that further investigation is needed into the TFM to be able to capture the effects of a blockage as a perforated plate. In addition, polydispersed bubbly flow will be computed with population balance approaches as Multiple Size Group (MUSIG) or Quadrature Method of Moments (QMOM) in order to study the effect of the plate in the bubble distribution. Experiments related with this kind of simulations and the use of advanced techniques as VOF will help to understand the physics of the bubbly flow under this situations to implement new models in TFM and eventually in CFD-DEM.

Chapter 9

Conclusions and future work

This work finishes with the conclusions that emerged from the investigations shown in previous chapters. Some recommendations are made to improve this study or to continue with it. In addition, future research is summarised.

9.1 Conclusions

Two-phase flow is a fascinating topic with many uncertainties and questions. Despite many efforts during recent decades, its modelling with computational techniques present nowadays many shortcomings to overcome. Whether by computational limitations or lack of knowledge most of the simulations can not be used as a predictive tool.

This work focused in the bubbly flow regime as it is the most simple of the existing regimes. It allows isolating effects and draw conclusions. The thesis aimed to investigate the numerical modelling of bubbly flow through a multiscale numerical study and experimental validations. With this methodology the extent of applicability of each technique has been evaluated. In order to achieve this objective, development of new models and implementations mainly in OpenFOAM® were required. As a result, an open-source multiscale framework was developed to create a solid basis of two-phase flow modelling in the bubbly flow regime.

In general, this research has strengthened the understanding of the bubbly flow by means of simulations at different resolution level. The combination of this numerical investigation at the same time that the experiments were performed, helped to address key aspects of the modelling of bubbly flow.

A Volume Of Fluid (VOF) method was used to investigate in detail the behaviour of single bubbles. A model for air injected from a nozzle, and a spherical bubble in a quiescent fluid was created. A fixed regular mesh was used to capture the turbulence produced by the wake. From this study we can conclude that:

- This technique can reproduce the formation stages of the bubbles, including the surrounding fluid flow produced and the rising pattern of the bubbles.
- The results shown an excellent agreement between the computed bubble size generated in the nozzle and an empirical correlation giving accurate results.
- The motion of single bubbles as terminal velocity, acceleration and shape oscillation is properly captured.
- Path instabilities patterns observed experimentally as zigzagging or spiralling are also detected in the simulations, but rarely found in the literature.
- The results can be used to better understand the wake structure and its influence on the path of the bubbles. These results, together with a CFD-DEM could reveal useful insights in the implementation of interface effects.
- These simulations could be extended to bigger scale to perform a multiscale comparison of the same scenarios with CFD-DEM and TFM.

A novel CFD-DEM for unresolved particles suitable for bubbly flow in pipes is presented in the thesis. Bubbles are represented as discrete elements and are tracked trough the carrier phase. Although this relies on correlations and the fluid flow is not resolved, it permitted to compute a hundred of bubbles using interfacial forces and pseudo-turbulence produced by the bubbles without many of the assumptions applied to TFM. The following conclusions arise from this investigation:

- Simulations of single bubbles with CFD-DEM can reproduce the bubble dynamics as terminal velocity and acceleration but excluding effects at the interface or instabilities.
- The proposed CFD-DEM solver for bubbly flow can provide reasonable results to simulate bubbly flow systems without tuning any parameter as validated for vertical pipes of different sizes. The formulation is based in basic principles allowing a better representation of the closures.
- All the variables that can be obtained from experiments were properly predicted. These variables were consistent between them.
- Bubble interactions with the wall produced a source of bubbles that migrates far from the wall because of the collisions. The radial fluctuations increased this phenomena.

- Wall lubrication force did not play a key role in the simulation. In addition, it is possible that this force could reduce the bubble approaching velocity to the wall and then the energy of the impact. It would result in an increment of bubbles close to the wall.
- To fairly compare the simulation results with the experimental data, it should be required an adequate knowledge on how the experiments have been conducted and the processing procedure followed. Although it seems clear, for two-phase flow the sensitivity on the boundary conditions or validation is much higher than for single-phase flow.
- The simulation results when compared to experimental data with needle probes must be obtained in the same way as the experiments to represent similar values, as demonstrated by means of virtual measurements (VNPS).
- Using VNPS it is possible to use the solver not only as a method to reproduce the experiments, but as a tool to understand and investigate the experimental data and measurements.
- Given the sensitivity of the models for interfacial closures it is recommended to compare all the variables that will define the two-phase flow characteristics at different locations:
  - Pressure
  - Void fraction.
  - Bubble and liquid velocities.
  - Turbulence quantities of both phases.
  - Bubble frequency.
  - Interfacial area concentration.
  - Bubble size distribution.
  - Chord lengths (mean and distribution).
  - Missing ratio.
- Axial evolution of vertical bubbly flow in pipes was validated with an excellent agreement. VNPS was used to explain some of the aspects in the validation.
- Preliminary results of bubbly flow through a perforated plate shown reasonable results.

A 3D TFM coupled with the QMOM to solve the population balance equation was implemented in OpenFOAM®. It was used to investigate its performance and the several assumptions applied in classical formulations:

- A two-fluid model with QMOM was developed with interfacial forces for bubbly flow. The simulations reproduced reasonably well experimental data for different pipes.
- Tuning coefficients were required to obtain optimal results when common interfacial closures used for TFM were applied.
- Wall lubrication force played a key role in the simulation, acting as the main force opposite to the lift.
- A critical approach was performed, comparing the performance of CFD-DEM and TFM with equivalent modelling.
- The attempt shown in this thesis failed to reproduce properly good results as for CFD-DEM.
- Preliminary results of bubbly flow through a perforated plate failed to predict the blockage of bubbles.

The 1D TFM is an effective tool when spatial resolution is not important or required. The system code RELAP5/MOD3 is commonly used in the nuclear industry. It is used in this work to analyse and improve the modelling of the interfacial drag term:

- The Chexal-Lellouche drift correlation fails predicting bubbly flow in vertical pipes at low liquid velocities.
- The drag coefficient approach predicts relatively well the interfacial area at expenses of underestimating the mean bubble size around a 50%.
- The proposed drag coefficient approach is able to reproduce all the variables as the size distribution is considered and interfacial area is calculated directly from the size distribution.
- PBE applied to 1D TFM should be investigated to predict complex scenarios and its evolution.

9.2 Future work

The open-source multiscale framework presented is useful for future contributions aimed to investigate the modelling for presence of surfactants, chemical reactions, heat transfer or boiling and condensation. Furthermore, this is intended to serve as a basis for future hybrid codes or coupling between the solvers for solutions at different scales in the same simulations. The following tasks would continue this work in the short-term and long-term:

- Investigating with VOF the capability of a dynamic mesh solver to capture the wake and the effect that it has in the bubble.
- Extending the investigation of VOF to multiple bubbles or swarms applied to a multiscale investigation.
- Implementing the effect of surfactants in the VOF simulations to analyse the wake structure.
- Developing an hybrid approach to simulate scenarios where resolved and unresolved particles take place as slug flow with the consideration of small and "big bubbles" using approaches as VOF, CFD-DEM or IBM.
- Investigating the use of a VOF-Level Set approach to simulate phase change or chemical reactions.
- Applying the virtual needle probe concept to simulations with microscale approaches needing massive parallel computing to obtain results without needing to save data at different time steps (reducing data writing, time and storage).
- Investigating the effect of path instabilities and pseudo-turbulence induced, and the possibilities to model this interfacial effects and interactions with the wake in CFD-DEM or TFM.
- Investigating in TFM the effect that velocity fluctuations have in non-drag forces in pipes.
- Investigating the modelling of bubble collision with CFD-DEM and TFM compared with new separate experiments.
- Extending the study performed in this work with CFD-DEM and TFM to other flow regimes including more complex phenomenology as non-sphericity of bubbles, near-wall modelling, and bubble breakup or coalescence.
- Extending the virtual measurements (VNPS) to front tracking or volume of fluid methods to investigate the validation methodology and experimental measurements with needle probes.

- Investigating the CFD-DEM and TFM models in a perforated plate case, comparing the results with detailed experiments.
- Implementing a 1D TFM in OpenFOAM®.
- Implementing a PBE in a 1D TFM to investigate flow regime transitions.

Bibliography

Abdulkadir, M., Hernandez-Perez, V., Lowndes, I., Azzopardi, B., and Dzomeku, S. (2014). "Experimental study of the hydrodynamic behaviour of slug flow in a vertical riser". In: *Chemical Engineering Science* 106, pp. 60–75. ISSN: 00092509 (cit. on p. 23).

Adrian, R. J. (2005). "Twenty years of particle image velocimetry". In: *Experiments in Fluids* 39.2, pp. 159–169. ISSN: 0723-4864 (cit. on p. 22).

Adrian, R. J.R. J. and Westerweel, J. J. (2011). *Particle Image Velocimetry*. Cambridge University Press, p. 558. ISBN: 9780521440080 (cit. on p. 21).

Ahmed, H. (2006). "Capacitance Sensors for Void-Fraction Measurements and Flow-Pattern Identification in AirOil Two-Phase Flow". In: *IEEE Sensors Journal* 6.5, pp. 1153–1163. ISSN: 1530-437X (cit. on p. 22).

Alajbegović, A, Assad, A, Bonetto, F, and Lahey, R. T. (1994). "Phase distribution and turbulence structure for solid/fluid upflow in a pipe". In: *International Journal of Multiphase Flow* 20.3, pp. 453–479. ISSN: 0301-9322 (cit. on p. 71).

Alajbegovic, A., Drew, D. A., and Lahey, R. T. (1999). "An analysis of phase distribution and turbulence in dispersed particle/liquid flows". In: *Chemical Engineering Communications* 174.1, pp. 85–133. ISSN: 0098-6445 (cit. on pp. 70, 71, 139).

Alam, M. and Luding, S. (2003). "Rheology of bidisperse granular mixtures via eventdriven simulations". In: *Journal of Fluid Mechanics* 476, pp. 69–103 (cit. on p. 26).

Ali, M. I., Sadatomi, M., and Kawaji, M. (1993). "Adiabatic two-phase flow in narrow channels between two flat plates". In: *The Canadian Journal of Chemical Engineering* 71.5, pp. 657–666. ISSN: 00084034 (cit. on p. 20).

Allen, H. S. (1900). "XXXI. The motion of a sphere in a viscous fluid". In: *Philosophical Magazine Series 5* 50.304, pp. 323–338 (cit. on pp. 20, 27).

Alopaeus, V, Koskinen, J, Keskinen, K. I., and Majander, J (2002). "Simulation of the population balances for liquid-liquid systems in a non-ideal stirred tank. II. Parameter fitting and the use of the multi-block model for dense dispersions". In: *Chem. Eng. Sci.* 57, pp. 1815–1825 (cit. on p. 170).

Andersson, R and Andersson, B (2006). "On the breakup of fluid particles in turbulent flows". In: *AlChE J.* 52, pp. 2020–2030 (cit. on p. 170).

ANSYS CFX (2014). *ANSYS Academic Research, Release 14.0, Help System, ANSYS CFX-Solver Theory Guide, ANSYS, Inc.* (Cit. on p. 178).

Antal, S. P., Lahey Jr, R. T., and Flaherty, J. E. (1991). "Analysis of phase distribution in fully developed laminar bubbly two-phase flow". In: *International Journal of Multiphase Flow* 17.5, pp. 635–652. ISSN: 0301-9322 (cit. on pp. 69, 111, 166, 178, 185).

Auton, T. R., Cambridge, U. of, Physics, U. o.C.D.o.A. M., and Theoretical (1983). *The Dynamics of Bubbles, Drops and Particles in Motion in Liquids*. The Author (cit. on p. 62).

Auton, T. R., Hunt, J. C. R., and Prud'Homme, M (1988). "The force exerted on a body in inviscid unsteady non-uniform rotational flow". In: *J. Fluid Mech.* 197, pp. 241–257. ISSN: 1469-7645 (cit. on pp. 66–68, 111, 165).

Auton, T. R. (1984). "Dynamics of bubbles, drops, and particles in motion in liquids." In: (cit. on p. 62).

Aybers, N. M. and Tapucu, A (1969). "The motion of gas bubbles rising through stagnant liquid". In: *Wärme - und Stoffübertragung* 2.2, pp. 118–128. ISSN: 0042-9929 (cit. on p. 20).

Barnhart, D. H., Adrian, R. J., and Papen, G. C. (1994). "Phase-conjugate holographic system for high-resolution particle-image velocimetry." In: *Applied optics* 33.30, pp. 7159–70. ISSN: 0003-6935 (cit. on p. 21).

Barrau, E., Rivière, N., Poupot, C., and Cartellier, A. (1999). "Single and double optical probes in air-water two-phase flows: real time signal processing and sensor performance". In: *International Journal of Multiphase Flow* 25.2, pp. 229–256. ISSN: 03019322 (cit. on p. 44).

Bauer, A. B. (1965a). "Direct measurement of velocity by hot-wire anemometry". In: *AIAA Journal* 3.6, pp. 1189–1191. ISSN: 0001-1452 (cit. on p. 22).

Bauer, A. B. (1965b). "Direct measurement of velocity by hot-wire anemometry". In: *AIAA Journal* 3.6, pp. 1189–1191 (cit. on p. 43).

Becker, S., Sokolichin, A., and Eigenberger, G. (1994). "Gasliquid flow in bubble columns and loop reactors: Part II. Comparison of detailed experiments and flow simulations". In: *Chemical Engineering Science* 49.24, pp. 5747–5762. ISSN: 00092509 (cit. on pp. 28, 29).

Behzadi, A, Issa, R. I., and Rusche, H (2001). "Effects of turbulence on interphase forces in dispersed flow". In: *ICMF'2001, 4th Int. Conf. Multiphase Flow*, pp. 1–12 (cit. on pp. 76, 78, 79, 192).

Besagni, G., Brazzale, P., Fiocca, A., and Inzoli, F. (2016). "Estimation of bubble size distributions and shapes in two-phase bubble column using image analysis and optical probes". In: *Flow Measurement and Instrumentation* 52, pp. 190–207. ISSN: 0955-5986 (cit. on pp. 40, 49, 50).

Bocksell, T. L. and Loth, E (2006). "Stochastic modeling of particle diffusion in a turbulent boundary layer". In: *International Journal of Multiphase Flow* 32, pp. 1234–1253 (cit. on p. 135).

Brooks, C. S., Hibiki, T., and Ishii, M. (2012). "Interfacial drag force in one-dimensional two-fluid model". In: *Progress in Nuclear Energy* 61.0, pp. 57–68. ISSN: 0149-1970 (cit. on pp. 194–197).

Bruun, H. H. (1996). "Hot-Wire Anemometry: Principles and Signal Analysis". In: *Measurement Science and Technology* 7.10. ISSN: 0957-0233 (cit. on p. 22).

Buffo, A., Marchisio, D. L., Vanni, M., and Renze, P. (2013). "Simulation of polydisperse multiphase systems using population balances and example application to bubbly flows". In: *Chemical Engineering Research and Design* 91.10, pp. 1859–1875. ISSN: 0263-8762 (cit. on pp. 25, 28, 29, 53, 81, 161, 162).

Burns, A. D., Frank, T., Hamill, I., and Shi, J.-M. (2004). "The Favre averaged drag model for turbulent dispersion in Eulerian multi-phase flows". In: *5th international conference on multiphase flow, ICMF*. Vol. 4, pp. 1–17 (cit. on pp. 76–78, 167, 186, 192).

Buwa, V. V., Deo, D. S., and Ranade, V. V. (2006). "Eulerian-Lagrangian simulations of unsteady gasliquid flows in bubble columns". In: *International Journal of Multiphase Flow* 32.7, pp. 864–885. ISSN: 0301-9322 (cit. on p. 134).

Cachaza Gianzo, E. M. (2011). "Hydrodynamics and mass transfer effects in bubble columns". PhD thesis. Universidad de Salamanca, Salamanca, Spain (cit. on pp. 28, 29).

Cano-Lozano, J. C., Bolaños-Jiménez, R, Gutiérrez-Montes, C, and Martínez-Bazán, C. (2017). "On the bubble formation under mixed injection conditions from a vertical needle". In: *International Journal of Multiphase Flow* 97, pp. 23–32. ISSN: 0301-9322 (cit. on p. 86).

Cano-Lozano, J.-C. and José-Carlos (2015). "Bubble formation and rising dynamics analises". PhD thesis. ISBN: 9788484399926 (cit. on p. 86).

Cano-Lozano, J. C., Martínez-Bazán, C., Magnaudet, J., and Tchoufag, J. (2016). "Paths and wakes of deformable nearly spheroidal rising bubbles close to the transition to path instability". In: *Physical Review Fluids* 1.5, p. 053604. ISSN: 2469-990X (cit. on p. 86).

Cartellier, A. (1998). "Measurement of gas phase characteristics using new monofiber optical probes and real-time signal processing". In: *Nuclear Engineering and Design* 184.2-3, pp. 393–408. ISSN: 00295493 (cit. on p. 44).

Chahed, J., Masbernat, L., and Véronique, R. (1998). "Turbulence and void fraction prediction in a turbulent bubbly wake". In: *3rd International Conference on Multiphase Flow (ICMF1998)*. Lyon, France (cit. on p. 79).

Chen, J., Li, F., Degaleesan, S., Gupta, P., Al-Dahhan, M. H., Dudukovic, M. P., and Toseland, B. A. (1999a). "Fluid dynamic parameters in bubble columns with internals". In: *Chemical Engineering Science* 54.1314, pp. 2187–2197. ISSN: 0009-2509 (cit. on p. 20).

Chen, L., Garimella, S. V., Reizes, J. A., and Leonardi, E. (1999b). "The development of a bubble rising in a viscous liquid". In: *Journal of Fluid Mechanics* 387, pp. 61–96 (cit. on p. 86).

Chen, P, Sanyal, J, and Dudukovic, M. P. (2004). "CFD modeling of bubble columns flows: implementation of population balance". In: *Chem. Eng. Sci.* 59.22-23, pp. 5201–5207. ISSN: 0009-2509 (cit. on p. 164).

Cheung, S. C. P., Deju, L, Yeoh, G. H., and Tu, J. Y. (2013). "Modeling of bubble size distribution in isothermal gas-liquid flows: Numerical assessment of population balance approaches". In: *Nucl. Eng. Des.* 265.0, pp. 120–136. ISSN: 0029-5493 (cit. on pp. 25, 81, 161, 162).

Cheung, S. C. P., Yeoh, G. H., and Tu, J. Y. (2007). "On the numerical study of isothermal vertical bubbly flow using two population balance approaches". In: *Chemical Engineering Science* 62.17, pp. 4659–4674. ISSN: 0009-2509 (cit. on pp. 28, 29).

Chexal, B and Lellouche, G (1985). *Full-range drift-flux correlation for vertical flows*. Tech. rep. (cit. on p. 196).

Chexal, B., Lellouche, G., Horowitz, J., and Healzer, J. (1992). "A void fraction correlation for generalized applications". In: *Progress in Nuclear Energy* 27.4, pp. 255–295. ISSN: 01491970 (cit. on p. 196).

Clark, N. N. and Turton, R (1988). "Chord length distributions related to bubble size distributions in multiphase flows". In: *International Journal of Multiphase Flow* 14.4, pp. 413–424. ISSN: 0301-9322 (cit. on pp. 50, 56, 116, 153).

Clift, R. R., Grace, J. R., and Weber, M. E. (1978). *Bubbles, drops, and particles*. Academic Press, p. 380. ISBN: 012176950X (cit. on pp. 24, 68).

Corre, J.-M. L. and Ishii, M. (2002). "Numerical evaluation and correction method for multi-sensor probe measurement techniques in two-phase bubbly flow". In: *Nuclear Engineering and Design* 216.13, pp. 221–238. ISSN: 0029-5493 (cit. on pp. 38, 48, 56, 152).

Coulaloglou, C. A. and Tavlarides, L. L. (1977). "Description of interaction processes in agitated liquid-liquid dispersions". In: *Chem. Eng. Sci.* 32, pp. 1289–1297 (cit. on p. 170).

Crowe, C. T., Sharma, M. P., and Stock, D. E. (1977). "The Particle-Source-In Cell (PSI-CELL) Model for Gas-Droplet Flows". In: *Journal of Fluids Engineering* 99.2, pp. 325–332. ISSN: 0098-2202 (cit. on p. 117).

Cundall, P. A. and Strack, O. D. L. (1979). "A discrete numerical model for granular assemblies". In: *Géotechnique* 29.1, pp. 47–65 (cit. on pp. 70, 108).

Damián, S. M. and Nigro, N. M. (2014). "An extended mixture model for the simultaneous treatment of small-scale and large-scale interfaces". In: *Inter-*

national Journal for Numerical Methods in Fluids 75.8, pp. 547–574. ISSN: 1097-0363 (cit. on p. 173).

Davidson, L. (2001). *An introduction to turbulence models* (cit. on p. 72).

Davies, R. M. and Taylor, G. (1950). "The mechanics of large bubbles rising through extended liquids and through liquids in tubes". In: *Proceedings of the Royal Society of London. Series A. Mathematical and Physical Sciences* 200.1062, pp. 375–390 (cit. on p. 20).

Deen, N. G., van Sint Annaland, M, and Kuipers, J. A. M. (2004). "Multi-scale modeling of dispersed gasliquid two-phase flow". In: *Chemical Engineering Science* 59.89, pp. 1853–1861. ISSN: 0009-2509 (cit. on pp. 30, 117).

Degaleesan, S. (1997). "Fluid dynamic measurements and modeling of liquid mixing in bubble columns". PhD thesis. Washington University, 1997. Department of Chemical Engineering. (cit. on p. 20).

Dehbi, A (2008). "Turbulent particle dispersion in arbitrary wall-bounded geometries: A coupled CFD-Langevin-equation based approach". In: *International Journal of Multiphase Flow* 34, pp. 819–828 (cit. on p. 135).

Delnoij, E, Lammers, F. A., Kuipers, J. A. M., and Swaaij, W. P. M. van (1997). "Dynamic simulation of dispersed gas-liquid two-phase flow using a discrete bubble model." In: *Chemical Engineering Science* 52.9, pp. 1429–1458 (cit. on pp. 26, 28, 29).

Dhotre, M. T., Deen, N. G., Niceno, B, Khan, Z, and Joshi, J. B. (2013). "Large Eddy Simulation for Dispersed Bubbly Flows: A Review". In: *International Journal of Chemical Engineering* 2013, p. 22 (cit. on p. 27).

Dias, S. G., Franc, F. A., and Rosa, E. S. (2000). "Statistical method to calculate local interfacial variables in two-phase bubbly ows using intrusive crossing probes". In: *International Journal of Multiphase Flow* 26, pp. 1797–1830 (cit. on p. 44).

Dietrich, N., Mayoufi, N., Poncin, S., Midoux, N., and Li, H. Z. (2013a). "Bubble formation at an orifice: A multiscale investigation". In: *Chemical Engineering Science* 92, pp. 118–125. ISSN: 00092509 (cit. on pp. 89, 93, 94).

Dietrich, N., Mayoufi, N., Poncin, S., and Li, H.-Z. (2013b). "Experimental investigation of bubble and drop formation at submerged orifices". In: *Chemical Papers* 67.3, pp. 313–325. ISSN: 1336-9075 (cit. on pp. 20, 89, 94, 95).

Dijkhuizen, W, Hengel, E. I. V. van den, Deen, N. G., van Sint Annaland, M, and Kuipers, J. A. M. (2005). "Numerical investigation of closures for interface forces acting on single air-bubbles in water using Volume of Fluid and Front Tracking models". In: *Chemical Engineering Science* 60.22, pp. 6169–6175. ISSN: 0009-2509 (cit. on pp. 68, 86).

Dijkhuizen, W, Roghair, I, Annaland, M. V. S., and Kuipers, J. A. M. (2010a). "DNS of gas bubbles behaviour using an improved 3D front tracking model - Drag force on isolated bubbles and comparison with experiments". In: *Chemical Engineering Science* 65.4, pp. 1415–1426. ISSN: 0009-2509 (cit. on p. 64).

— (2010b). "DNS of gas bubbles behaviour using an improved 3D front tracking model - Model development". In: *Chem. Eng. Sci.* 65.4, pp. 1427–1437. ISSN: 0009-2509 (cit. on pp. 27, 85).

Drew, D. A. and Lahey, R. T. (1987). "The virtual mass and lift force on a sphere in rotating inviscid flow". In: *Int. J. Multiphase Flow* 13.1, pp. 113–121 (cit. on pp. 66, 68, 111, 165, 185, 186).

Drew, D. (1982). *Continuum modeling of two-phase flows*. Tech. rep. Wisconsin Univ., Madison. Mathematics Research Center (cit. on pp. 61, 62, 68, 163).

Drew, D. and Segel, L. (1971a). "Averaged equations for two- phase flows". In: *Stud. Appl. Math.* 50.3, pp. 205–231 (cit. on pp. 24, 25, 161).

— (1971b). "Averaged equations for two- phase flows". In: *Stud. Appl. Math.* 50.3, pp. 205–231 (cit. on pp. 61, 62, 163).

Duineveld, P. C. (1995). "The rise velocity and shape of bubbles in pure water at high Reynolds number". In: *Journal of Fluid Mechanics* 292, pp. 325–332. ISSN: 1469-7645 (cit. on p. 20).

Dukowicz, J. K. (1980). "A particle-fluid numerical model for liquid sprays". In: *Journal of Computational Physics* 35.2, pp. 229–253. ISSN: 0021-9991 (cit. on p. 25).

Durst, F., Melling, A., and Whitelaw, J. H. (1976a). *Principles and practice of laser-Doppler anemometry*. Academic Press, p. 405. ISBN: 0122252500 (cit. on p. 21).

Durst, F, Melling, A, and Whitelaw, J. H. (1976b). *Principles and practice of laser-Doppler anemometry*. Academic Press. ISBN: 9780122252501 (cit. on p. 42).

Durst, F, Jovanović, J, and Sender, J (1995). "LDA measurements in the near-wall region of a turbulent pipe flow". In: *Journal of Fluid Mechanics* 295, pp. 305–335 (cit. on pp. 21, 42).

E. Shams, Finn, J, and Apte, S. V. (2010). "A Numerical Scheme for Euler-Lagrange Simulation of Bubbly Flows in Complex Systems". In: *International Journal for Numerical Methods in Fluids* 67.12, pp. 1865–1898 (cit. on p. 26).

Ekambara, K, Sanders, R. S., Nandakumar, K, and Masliyah, J. H. (2008). "CFD simulation of bubbly two-phase flow in horizontal pipes". In: *Chemical Engineering Journal* 144.2, pp. 277–288. ISSN: 1385-8947 (cit. on pp. 25, 161).

Elghobashi, S. E. and Abou-Arab, T. W. (1983). "A two-equation turbulence model for two-phase flows". In: *Physics of Fluids* 26.4, pp. 931–938 (cit. on pp. 75, 134).

Ellingsen, K. and Risso, F. (2001). "On the rise of an ellipsoidal bubble in water: oscillatory paths and liquid-induced velocity". In: *Journal of Fluid Mechanics* 440, pp. 235–268 (cit. on p. 49).

Essa, M. A.A.E. A. (2012). "Coupled Lagrange-Euler model for simulation of bubbly flow in vertical pipes considering turbulent 3D random walks models and bubbles interaction effects". PhD thesis. Universitat Politècnica de València (cit. on p. 26).

Fu, X. (2001). "Interfacial area measurement and transport modeling in air -water two -phase flow". PhD thesis. Purdue University (cit. on pp. 21, 44).

Geraets, J. and Borst, J. (1988). "A capacitance sensor for two-phase void fraction measurement and flow pattern identification". In: *International Journal of Multiphase Flow* 14.3, pp. 305–320. ISSN: 03019322 (cit. on p. 22).

Gordon, R. G. (1968). "Error bounds in equilibrium statistical mechanics". In: *J. Math. Phys.* 9, pp. 655–662 (cit. on pp. 162, 172).

Gosman, A. D. and Loannides, E (1983). "Aspects of computer simulation of liquid-fueled combustors". In: *Journal of Energy* 7.6, pp. 482–490 (cit. on p. 134).

Grace, J. (1973). "Shapes and velocities of bubbles rising in infinite liquids". In: *Trans. Inst. Chem. Eng.* (Cit. on p. 63).

Griffiths, M., Schlegel, J., Clark, C., Chen, S., Hibiki, T., Ishii, M., Kinoshita, I., and Yoshida, Y. (2014). "Uncertainty evaluation of the ChexalLellouche correlation for void fraction in rod bundles". In: *Progress in Nuclear Energy* 74, pp. 143–153. ISSN: 01491970 (cit. on p. 196).

Grossetête, C. (1995). "Caractérisation expérimentale et simulations de l'évolution d'un écoulement diphasique à bulles ascendant dans une conduite verticale". PhD thesis. Ecole centrale Paris 1995, 2 vol. (425 p.) (Cit. on pp. 20, 28, 29, 38, 75, 168).

Gui, N., Fan, J. R., and Luo, K. (2008). "DEMLES study of 3-D bubbling fluidized bed with immersed tubes". In: *Chemical Engineering Science* 63.14, pp. 3654–3663. ISSN: 0009-2509 (cit. on p. 117).

Gunsing, M. (2004). "Modelling Bubbly flows using volume of fluid, front tracking and discrete bubble models." PhD thesis. University of Twente (cit. on p. 30).

Gupta, A. and Roy, S. (2013). "Euler-Euler simulation of bubbly flow in a rectangular bubble column: Experimental validation with Radioactive Particle Tracking". In: *Chemical Engineering Journal* 225, pp. 818–836. ISSN: 1385-8947 (cit. on pp. 25, 161).

Haberman, W. L. and Morton, R. K. (1953). *An experimental investigation of the drag and shape of air bubbles rising in various liquids*. Tech. rep. DTIC Document (cit. on p. 20).

Hadamard, J. (1911). "Mouvement permanent lent d'une sphere liquide et visqueuse dans un liquide visqueux". In: *CR Acad. Sci* 152.25, pp. 1735–1738 (cit. on pp. 24, 63).

Hibiki, T, Hogsett, S, and Ishii, M (1998). "Local measurement of interfacial area, interfacial velocity and liquid turbulence in two-phase flow". In: *Nuclear Engineering and Design* 184.23, pp. 287–304. ISSN: 0029-5493 (cit. on pp. 21, 22, 48).

Hibiki, T., Ishii, M., and Xiao, Z. (2001a). "Axial interfacial area transport of vertical bubbly flows". In: *International Journal of Heat and Mass Transfer* 44.10, pp. 1869–1888. ISSN: 0017-9310 (cit. on pp. 21, 174).

— (2001b). "Axial interfacial area transport of vertical bubbly flows". In: *International Journal of Heat and Mass Transfer* 44.10, pp. 1869–1888. ISSN: 0017-9310 (cit. on pp. 28, 29, 38–40, 105).

Hibiki, T. and Ishii, M. (2007). "Lift force in bubbly flow systems". In: *Chemical Engineering Science* 62.22, pp. 6457–6474. ISSN: 0009-2509 (cit. on pp. 66, 67, 166).

Hilton, J. E., Mason, L. R., and Cleary, P. W. (2010). "Dynamics of gassolid fluidised beds with non-spherical particle geometry". In: *Chemical Engineering Science* 65.5, pp. 1584–1596. ISSN: 0009-2509 (cit. on p. 117).

Hirt, C. and Nichols, B. (1981). "Volume of fluid (VOF) method for the dynamics of free boundaries". In: *Journal of Computational Physics* 39.1, pp. 201–225. ISSN: 00219991 (cit. on pp. 24, 27, 61, 88).

Hosokawa, S. and Tomiyama, A. (2009). "Multi-fluid simulation of turbulent bubbly pipe flows". In: *Chem. Eng. Sci.* 64.24, pp. 5308–5318. ISSN: 0009-2509 (cit. on pp. 25, 28, 29, 38–40, 66, 105, 161, 164, 174, 180, 182).

Hu, G. and Celik, I. (2008). "Eulerian-Lagrangian based large-eddy simulation of a partially aerated flat bubble column". In: *Chemical Engineering Science* 63.1, pp. 253–271. ISSN: 0009-2509 (cit. on pp. 28, 29).

Hua, J. and Lou, J. (2007). "Numerical simulation of bubble rising in viscous liquid". In: *Journal of Computational Physics* 222.2, pp. 769–795 (cit. on p. 86).

Iliopoulos, I. and Hanratty, T. J. (1999). "Turbulent dispersion in a non-homogeneous field". In: *Journal of Fluid Mechanics* 392, pp. 45–71 (cit. on p. 135).

Ishii, M (1975). *Thermo-fluid dynamic theory of two-phase flow*. Paris: Eyrolles (cit. on pp. 62, 193).

Ishii, M. and Chawla, T. (1979). *Local drag laws in dispersed two-phase flow* (cit. on pp. 197, 198).

Ishii, M and Mishima, K (1984). "Two-fluid model and hydrodynamic constitutive relations". In: *Nucl. Eng. Des.* 82.2-3, pp. 107–126. ISSN: 0029-5493 (cit. on p. 164).

Ishii, M and Hibiki, T (2006a). *Thermo-fluid Dynamics of Two-Phase Flow*. Smart Energy Systems. Springer. ISBN: 9780387283210 (cit. on p. 18).

Ishii, M. and Hibiki, T. (2006b). "Drift-Flux Model". In: *Thermo-Fluid Dynamics of Two-Phase Flow*. Boston, MA: Springer US, pp. 345–379 (cit. on p. 195).

Islam, M. T., Ganesan, P. B., Sahu, J. N., and Sandaran, S. C. (2015). "Effect of orifice size and bond number on bubble formation characteristics: A CFD study". In: *Canadian Journal of Chemical Engineering* 93.10, pp. 1869–1879. ISSN: 1939019X (cit. on p. 86).

Issa, R. I. (1986). "Solution of the implicitly discretised fluid flow equations by operator-splitting". In: *J. Comput. Phys.* 62.1, pp. 40–65. ISSN: 0021-9991 (cit. on pp. 113, 173).

Jamialahmadi, M., Zehtaban, M., Müller-Steinhagen, H., Sarrafi, A., and Smith, J. (2001). "Study of Bubble Formation Under Constant Flow Conditions". In: *Chemical Engineering Research and Design* 79.5, pp. 523–532. ISSN: 02638762 (cit. on pp. 86, 91, 93).

Jaworek, A., Krupa, A., and Trela, M. (2004). "Capacitance sensor for void fraction measurement in water/steam flows". In: *Flow Measurement and Instrumentation* 15.5-6, pp. 317–324. ISSN: 09555986 (cit. on p. 22).

Jensen, K. D. (2004). "Flow measurements". In: *Journal of the Brazilian Society of Mechanical Sciences and Engineering* 26.4, pp. 400–419. ISSN: 1678-5878 (cit. on p. 21).

Johnson, I. D. (1987). *Method and apparatus for measuring water in crude oil* (cit. on p. 23).

Jørgensen, F. E. (2001). *How to measure turbulence with hot-wire anemometers: a practical guide*. Dantec dynamics (cit. on pp. 22, 43).

Kalkach-Navarro, S., Lahey, R., Drew, D., and Meyder, R. (1993). "Interfacial area density, mean radius and number density measurements in bubbly two-phase flow". In: *Nuclear Engineering and Design* 142.2-3, pp. 341–351. ISSN: 00295493 (cit. on p. 152).

Kataoka, I and Serizawa, A (1989). "Basic equations of turbulence in gas-liquid two-phase flow". In: *International Journal of Multiphase Flow* 15.5, pp. 843–855 (cit. on pp. 74, 133).

Kataoka, I., Ishii, M., and Serizawa, A. (1986). "Local formulation and measurements of interfacial area concentration in two-phase flow". In: *International Journal of Multiphase Flow* 12.4, pp. 505–529. ISSN: 0301-9322 (cit. on p. 48).

Kazakis, N. A., Mouza, A. A., and Paras, S. V. (2008). "Experimental study of bubble formation at metal porous spargers: Effect of liquid properties and

sparger characteristics on the initial bubble size distribution". In: *Chemical Engineering Journal* 137.2, pp. 265–281. ISSN: 1385-8947 (cit. on pp. 40, 204).

Kim, S., Fu, X., Wang, X., and Ishii, M. (2000). "Development of the miniaturized four-sensor conductivity probe and the signal processing scheme". In: *International Journal of Heat and Mass Transfer* 43.22, pp. 4101–4118. ISSN: 0017-9310 (cit. on p. 44).

Kim, S, Fu, X. Y., Wang, X, and Ishii, M (2001). "Study on interfacial structures in slug flows using a miniaturized four-sensor conductivity probe". In: *Nuclear Engineering and Design* 204.13, pp. 45–55. ISSN: 0029-5493 (cit. on p. 48).

Kocamustafaogullari, G and Ishii, M (1983). "Interfacial area and nucleation site density in boiling systems". In: *International Journal of Heat and Mass Transfer* 26.9, pp. 1377–1387. ISSN: 0017-9310 (cit. on pp. 81, 162).

Končar, B. and Krepper, E. (2008). "CFD simulation of convective flow boiling of refrigerant in a vertical annulus". In: *Nucl. Eng. Des.* 238.3, pp. 693–706. ISSN: 0029-5493 (cit. on p. 164).

Krepper, E., Lucas, D., and Prasser, H.-M. (2005). "On the modelling of bubbly flow in vertical pipes". In: *Nucl. Eng. Des.* 235.5, pp. 597–611. ISSN: 0029-5493 (cit. on pp. 25, 28, 29, 70, 161, 179).

Kuang, S. B., Chu, K. W., Yu, A. B., Zou, Z. S., and Feng, Y. Q. (2008). "Computational Investigation of Horizontal Slug Flow in Pneumatic Conveying". In: *Industrial & Engineering Chemistry Research* 47.2, pp. 470–480 (cit. on p. 117).

Kumar, R. and Kuloor, N. (1970). "The Formation of Bubbles and Drops". In: *Advances in Chemical Engineering* 8.1970, pp. 255–368 (cit. on p. 86).

Kumar, S, Munshi, P, and Khanna, A (2012). "High Pressure Experiments and Simulations in Cocurrent Bubble Columns". In: *Procedia Eng.* 42.0, pp. 842–853. ISSN: 1877-7058 (cit. on p. 164).

Kumar, S. B., Duduković, M. P., and Toseland, B. A. (1997a). "Chapter 1 - Measurement techniques for local and global fluid dynamic quantities in two and three phase systems". In: *Non-Invasive Monitoring of Multiphase Flows*. Ed. by J. C.L. P. Duduković. Amsterdam: Elsevier Science B.V., pp. 1–45. ISBN: 978-0-444-82521-6 (cit. on p. 20).

Kumar, S. B. (1994). "Computed tomographic measurements of void fraction and modeling of the flow in bubble columns". PhD thesis. Florida Atlantic University Boca Raton, FL (cit. on p. 20).

Kumar, S. B., Moslemian, D., and Duduković, M. P. (1997b). "Gas-holdup measurements in bubble columns using computed tomography". In: *AIChE Journal* 43.6, pp. 1414–1425 (cit. on p. 20).

Kumar, S. and Ramkrishna, D (1996a). "On the solution of population balance equations by discretization-I. A fixed pivot technique". In: *Chem. Eng. Sci.* 51.8, pp. 1311–1332. ISSN: 0009-2509 (cit. on pp. 80, 162).

— (1996b). "On the solution of population balance equations by discretization-II. A moving pivot technique". In: *Chem. Eng. Sci.* 51.8, pp. 1333–1342. ISSN: 0009-2509 (cit. on pp. 80, 162).

Laakkonen, M., Alopaeus, V., and Aittamaa, J. (2006). "Validation of bubble breakage, coalescence and mass transfer models for gas-liquid dispersion in agitated vessel". In: *Chemical Engineering Science* 61.1, pp. 218–228. ISSN: 0009-2509 (cit. on pp. 53, 170).

Laakkonen, M., Moilanen, P., Alopaeus, V., and Aittamaa, J. (2007). "Modelling local bubble size distributions in agitated vessels". In: *Chemical Engineering Science* 62.3, pp. 721–740. ISSN: 0009-2509 (cit. on p. 40).

Lage, P. L. C. and Espósito, R. O. (1999). "Experimental determination of bubble size distributions in bubble columns: prediction of mean bubble diameter and gas hold up". In: *Powder Technology* 101.2, pp. 142–150. ISSN: 0032-5910 (cit. on pp. 40, 49).

Lahey Jr, R. T. and Drew, D. A. (2000). "An analysis of two-phase flow and heat transfer using a multidimensional, multi-field, two-fluid computational fluid dynamics (CFD) model". In: *Japan/US Seminar on Two-Phase Flow Dynamics*. Santa Barbara, CA, pp. 5–8 (cit. on p. 71).

Laín, S, Bröder, D, and Sommerfeld, M (1999). "Experimental and numerical studies of the hydrodynamics in a bubble column". In: *Chemical Engineering Science* 54.21, pp. 4913–4920. ISSN: 0009-2509 (cit. on pp. 28, 29).

Laín, S, Bröder, D, Sommerfeld, M, and Göz, M. F. (2002). "Modelling hydrodynamics and turbulence in a bubble column using the EulerLagrange procedure". In: *International Journal of Multiphase Flow* 28.8, pp. 1381–1407. ISSN: 0301-9322 (cit. on pp. 28, 29).

Lamb, H (1895). *Hydrodynamics*. University Press (cit. on pp. 68, 111, 165).

Lance, M and Bataille, J (1991). "Turbulence in the liquid phase of a uniform bubbly airwater flow". In: *Journal of Fluid Mechanics* 222, pp. 95–118 (cit. on pp. 21, 42).

Lau, Y. M., Deen, N. G., and Kuipers, J. A. M. (2013). "Development of an image measurement technique for size distribution in dense bubbly flows". In: *Chemical Engineering Science* 94, pp. 20–29. ISSN: 0009-2509 (cit. on p. 49).

Launder, B. E. and Spalding, D. B. (1974). "The numerical computation of turbulent flows". In: *Comput. Method. Appl. M.* 3.2, pp. 269–289. ISSN: 0045-7825 (cit. on pp. 27, 72–75, 133, 134, 168).

Lee, S. L., Lahey, R. T., and Jones, O. C. (1989). "The Prediction of Two-Phase Turbulence and Phase Distribution Phenomena Using a k-ϵ Model". In: *Japanese Journal of Multiphase Flow* 3.4, pp. 335–368 (cit. on pp. 75, 76, 168, 177).

Legendre, D. and Magnaudet, J. (1998). "The lift force on a spherical bubble in a viscous linear shear flow". In: *Journal of Fluid Mechanics* 368, S0022112098001621. ISSN: 00221120 (cit. on p. 110).

Leung, W., Revankar, S., Ishii, Y., and Ishii, M. (1995). "Axial development of interfacial area and void concentration profiles measured by double-sensor probe method". In: *International Journal of Heat and Mass Transfer* 38.3, pp. 445–453. ISSN: 00179310 (cit. on p. 21).

Levich, V (1962). *Physicochemical hydrodynamics*. Englewood Cliffs N.J.: Prentice-Hall (cit. on p. 63).

Lim, K. S., Agarwal, P. K., and O'neill, B. K. (1990). "Measurement and modelling of bubble parameters in a two-dimensional gas-fluidized bed using image analysis". In: *Powder Technology* 60.2, pp. 159–171. ISSN: 0032-5910 (cit. on p. 40).

Link, J. M., Cuypers, L. A., Deen, N. G., and Kuipers, J. A. M. (2005). "Flow regimes in a spoutfluid bed: A combined experimental and simulation study". In: *Chemical Engineering Science* 60.13, pp. 3425–3442. ISSN: 0009-2509 (cit. on p. 117).

Liu, T. J. (1998). "The role of bubble size on liquid phase turbulent structure in two-phase bubbly flow". In: *Proc. Third International Congress on Multiphase Flow ICMF*. Vol. 98, pp. 8–12 (cit. on pp. 28, 29).

Liu, T. J. and Bankoff, S. G. (1993a). "Structure of air-water bubbly flow in a vertical pipeI. liquid mean velocity and turbulence measurements". In: *International Journal of Heat and Mass Transfer* 36.4, pp. 1049–1060. ISSN: 0017-9310 (cit. on p. 38).

— (1993b). "Structure of air-water bubbly flow in a vertical pipeII. Void fraction, bubble velocity and bubble size distribution". In: *International Journal of Heat and Mass Transfer* 36.4, pp. 1061–1072. ISSN: 0017-9310 (cit. on pp. 28, 29, 38).

Liu, W. and Clark, N. (1995). "Relationships between distributions of chord lengths and distributions of bubble sizes including their statistical parameters". In: *International Journal of Multiphase Flow* 21.6, pp. 1073–1089. ISSN: 03019322 (cit. on pp. 56, 57).

Liu, W., Clark, N. N., and Karamavruç, A. I. (1998). "Relationship between bubble size distributions and chord-length distribution in heterogeneously bubbling systems". In: *Chemical Engineering Science* 53.6, pp. 1267–1276. ISSN: 0009-2509 (cit. on pp. 50, 116, 147, 153).

Lo, S (1996). "Application of the MUSIG model to bubbly flows". In: *AEAT-1096, AEA Technology* (cit. on pp. 80, 162).

López de Bertodano, M. (1992). "Turbulent bubbly two-phase flow in a triangular duct". PhD thesis. Rensselaer Polytechnic Institute (cit. on pp. 77, 78, 167, 192).

— (1998). "Two fluid model for two-phase turbulent jets". In: *Nucl. Eng. Des.* 179.1, pp. 65–74. ISSN: 0029-5493 (cit. on pp. 74, 77, 78, 133, 167).

Lord˜Kelvin (1873). "On the motion of rigid solids in a liquid circulating irrotationally through perforations in them or a fixed solid". In: *Philos. Mag* 45, p. 1873 (cit. on p. 68).

Lord˜Rayleigh (1876). "LIII. On the resistance of fluids". In: *Philosophical Magazine Series 5* 2.13, pp. 430–441. ISSN: 1941-5982 (cit. on p. 63).

Lucas, D, Krepper, E, and Prasser, H.-M. (2005). "Development of co-current air-water flow in a vertical pipe". In: *International Journal of Multiphase Flow* 31.12, pp. 1304–1328. ISSN: 0301-9322 (cit. on p. 20).

Luo, H. P. (2005). *Analyzing and Modeling of Airlift Photobioreactors for Microalgal and Cyanobacteria Cultures*. Washington University, 2005. Department of Chemical Engineering. (cit. on pp. 28, 29).

M. Ishii, G. D. J. (1982). "Inverted Annular Flow Modeling". In: Advanced Code Review Group Meeting (cit. on p. 194).

M.A. Vince, R. T. L. (1982). "On the Development of An Objective Flow Regime Indicator". In: *International Journal of Multiphase Flow* 8, p. 93124 (cit. on p. 194).

MacInnes, J. M. and Bracco, F. V. (1992). "Stochastic particle dispersion modeling and the tracerparticle limit". In: *Physics of Fluids A: Fluid Dynamics* 4.12, pp. 2809–2824 (cit. on p. 135).

Macpherson, G. and Reese, J. (2008). "Molecular Dynamics in Arbitrary Geometries: Parallel Evaluation of Pair Forces". In: *Molecular Simulation* 34.01, pp. 97–115 (cit. on p. 113).

Macpherson, G. B., Nordin, N., and Weller, H. G. (2009). "Particle tracking in unstructured, arbitrary polyhedral meshes for use in CFD and molecular dynamics". In: *Communications in Numerical Methods in Engineering* 25.3, pp. 263–273. ISSN: 1099-0887 (cit. on pp. 113, 118).

Magnaudet, J. and Eames, I. (2000). "The Motion of High-Reynolds-Number Bubbles in Inhomogeneous Flows". In: *Annual Review of Fluid Mechanics* 32.1, pp. 659–708. ISSN: 0066-4189 (cit. on pp. 26, 62, 110).

Magnaudet, J. and Legendre, D. (1997). "Some Aspects of the Lift Force on a Spherical Bubble". In: *Appl. Sci. Res.* 58.1-4, pp. 441–461 (cit. on pp. 66, 164).

Manon, E. and Delhaye, J.-M. (2000). "Contribution à l'analyse et à la modélisation locale des écoulements bouillants sous-saturés dans les conditions des Réacteurs à Eau sous Pression". PhD thesis. Ecole centrale Paris 1997 (cit. on pp. 75, 168).

Marchisio, D. L., Vigil, R. D., and Fox, R. O. (2003a). "Implementation of the quadrature method of moments in CFD codes for aggregation-breakage prob-

lems". In: *Chem. Eng. Sci.* 58.15, pp. 3337–3351 (cit. on pp. 80, 162, 171, 172).

— (2003b). "Quadrature method of moments for aggregation-breakage processes". In: *J. Colloid Interface Sci.* 258.2, pp. 322–334 (cit. on pp. 80, 162, 171, 172).

Marchisio, D. L. and Fox, R. O. (2013). *Computational models for polydisperse particulate and multiphase systems*. Cambridge: Cambridge University Press (cit. on pp. 162, 171, 172).

Margaris, D. P. (2007). "T-junction separation modelling in gasliquid two-phase flow". In: *Chemical Engineering and Processing: Process Intensification* 46.2, pp. 150–158. ISSN: 0255-2701 (cit. on p. 20).

Marrucci, G. and Nicodemo, L. (1967). "Coalescence of gas bubbles in aqueous solutions of inorganic electrolytes". In: *Chemical Engineering Science* 22.9, pp. 1257–1265. ISSN: 00092509 (cit. on p. 20).

Martínez-Bazán, C., Montanes, J. L., and Lasheras, J. C. (1999). "On the breakup of an air bubble injected into a fully developed turbulent flow. Part 2. Size PDF of the resulting daughter bubbles". In: *Journal of Fluid Mechanics* 401, pp. 183–207. ISSN: 1469-7645 (cit. on p. 20).

Matuttis, H. G., Luding, S, and Herrmann, H. J. (2000). "Discrete element simulations of dense packings and heaps made of spherical and non-spherical particles". In: *Powder Technology* 109.13, pp. 278–292. ISSN: 0032-5910 (cit. on p. 26).

Maucci, E., Briens, C., Martinuzzi, R., and Wild, G. (1999). "Detection and characterization of piston flow regime in three-phase fluidized beds". In: *Powder Technology* 103.3, pp. 243–259. ISSN: 00325910 (cit. on p. 22).

Maxey, M. R. (1983). "Equation of motion for a small rigid sphere in a nonuniform flow". In: *Physics of Fluids* 26.4, p. 883. ISSN: 00319171 (cit. on p. 62).

McGraw, R (1997). "Description of aerosol dynamics by the quadrature method of moments". In: *Aerosol Sci. Technol.* 27, pp. 255–265 (cit. on pp. 80, 162, 171).

McLaughlin, D. K. and Tiederman, W. G. (1973). "Biasing correction for individual realization of laser anemometer measurements in turbulent flows". In: *The Physics of Fluids* 16.12, pp. 2082–2088 (cit. on p. 136).

Mei, R., Klausner, J. F., and Lawrence, C. J. (1994). "A note on the history force on a spherical bubble at finite Reynolds number". In: *Phys. Fluids* 6.1, pp. 418–420 (cit. on p. 65).

Mendez Díaz, S (2008). "Medida experimental de la concentración de área interfacial en flujos bifásicos finamente dispersos y en transición." PhD thesis. Universitat Politècnica de València (cit. on pp. 28, 29, 38, 43).

Mendez-Díaz, S., Serrano-García, J. C., Zenit, R., and Hernández-Cordero, J. A. (2013). "Power spectral distributions of pseudo-turbulent bubbly flows". In: *Physics of Fluids* 25.4, p. 043303. ISSN: 1070-6631 (cit. on p. 22).

Miller, N and Mitchie, R. E. (1970). *Measurement of local voidage in liquid/gas two-phase flow systems using a universal probe*. Tech. rep. Atomic Power Constructions Ltd., Heston, Eng. (cit. on p. 44).

Mohd-Akbar, M bin, Hayashi, K., Hosokawa, S., and Tomiyama, A. (2012). "Bubble tracking simulation of bubble-induced pseudoturbulence". In: *Multiphase Science and Technology* 24.3, pp. 197–222. ISSN: 0276-1459 (cit. on pp. 28, 29).

Monrós-Andreu, G., Martinez-Cuenca, R., Torró, S., and Chiva, S. (2016). "LDA and Impedance Needle-probes for local measurements in multiphase flows." In: *Specialist Workshop on Advanced Instrumentation and Measurement Techniques for Nuclear Reactor Thermal Hydraulics (SWINTH)*. Livorno, Italy (cit. on p. 21).

Monrós-Andreu, G., Martínez-Cuenca, R., Torró, S., and Chiva, S. (2017). "Local parameters of airwater two-phase flow at a vertical T-junction". In: *Nuclear Engineering and Design* 312, pp. 303–316. ISSN: 00295493 (cit. on pp. 40, 105).

Monrós-Andreu, G. (2018). "Needle probe sensors for multiphase flow measurements. Design and processing methodology improvements (in progress)". PhD Thesis. Universitat Jaume I (cit. on p. 32).

Monrós-Andreu, G., S. Chiva, R. Martínez-Cuenca, S. Torró, J. E. Juliá, L. Hernández, and R. Mondragón (2013). "Water temperature effect on upward air-water flow in a vertical pipe: Local measurements database using four-sensor conductivity probes and LDA". In: *EPJ Web Conf.* 45, p. 1105 (cit. on pp. 40, 105, 174, 175, 182).

Moore, D. W. (1963). "The boundary layer on a spherical gas bubble". In: *Journal of Fluid Mechanics* 16.02, pp. 161–176 (cit. on p. 24).

— (1965). "The velocity of rise of distorted gas bubbles in a liquid of small viscosity". In: *Journal of Fluid Mechanics* 23.04, pp. 749–766 (cit. on p. 24).

Morel, C. (2016). *Mathematical modeling of disperse two-phase flows.* Springer International Publishing. ISBN: 9783319369129 (cit. on pp. 74, 133).

Morel, C. and Delhaye, J.-M. (1997). "Modélisation multidimensionnelle des écoulements diphasiques gaz - liquide: application à la simulation des écoulements à bulles ascendants en conduite verticale". PhD thesis. Ecole centrale Paris, 1 vol. (390 p.) (Cit. on pp. 75, 134, 168, 177).

Mougin, G. and Magnaudet, J. (2001). "Path Instability of a Rising Bubble". In: *Physical Review Letters* 88.1, p. 014502. ISSN: 0031-9007 (cit. on p. 86).

Mudde, R. F. and Groen, J. S. (1997a). "Liquid Velocity Field in Bubble Columns: LDA Experiments". In: *Chem. Eng. Sci*, pp. 4217–4224 (cit. on p. 43).

Mudde, R., Groen, J., and Van Den Akker, H. (1997b). "Liquid velocity field in a bubble column: LDA experiments". In: *Chemical Engineering Science* 52.21-22, pp. 4217–4224. ISSN: 00092509 (cit. on p. 21).

Mugele, R. A. and Evans, H. D. (1951). "Droplet size distribution in sprays". In: *Industrial & Engineering Chemistry* 43.6, pp. 1317–1324 (cit. on p. 49).

Müller-Fischer, N., Tobler, P., Dressler, M., Fischer, P., and Windhab, E. J. (2008). "Single bubble deformation and breakup in simple shear flow". In: *Experiments in Fluids* 45.5, pp. 917–926. ISSN: 0723-4864 (cit. on p. 20).

Muñoz-Cobo, J. L., Chiva, S., Essa, M. A.A.E. A., and Mendes, S. (2012). "Simulation of bubbly flow in vertical pipes by coupling Lagrangian and Eulerian models with 3D random walks models: Validation with experimental data using multi-sensor conductivity probes and Laser Doppler Anemometry". In: *Nuclear Engineering and Design* 242.0, pp. 285–299. ISSN: 0029-5493 (cit. on pp. 28, 29).

Muradoglu, M. and Tryggvason, G. (2008). "A Front-tracking Method for Computation of Interfacial Flows with Soluble Surfactants". In: *J. Comput. Phys.* 227.4, pp. 2238–2262. ISSN: 0021-9991 (cit. on p. 27).

Narsimhan, G, Gupta, J. P., and Ramkrishna, D (1979). "A model for transitional brekage probability of droplets in agitated lean liquid-liquid dispersions". In: *Chem. Eng. Sci.* 34, pp. 257–265 (cit. on p. 170).

Neal, L. G. and Bankoff, S. G. (1963). "A high resolution resistivity probe for determination of local void properties in gas-liquid flow". In: *AIChE Journal* 9.4, pp. 490–494. ISSN: 1547-5905 (cit. on p. 44).

Newton, I. (1687). *Philosophiae naturalis principia mathematica.* Latin. Londini: Jussu Societatis Regiæ ac Typis Josephi Streater. Prostat apud plures Bibliopolas. (cit. on p. 62).

Norouzi, H. R., Zarghami, R., Sotudeh-Gharebagh, R., and Mostoufi, N. (2016a). "CFD-DEM Formulation and Coupling". In: *Coupled CFD-DEM Modeling.* Chichester, UK: John Wiley & Sons, Ltd, pp. 257–340. ISBN: 9781119005315 (cit. on p. 61).

— (2016b). "DEM Formulation". In: *Coupled CFD-DEM Modeling.* John Wiley & Sons, Ltd. Chap. DEM Formul, pp. 15–67. ISBN: 9781119005315 (cit. on p. 117).

— (2016c). "Introduction". In: *Coupled CFD-DEM Modeling.* Chichester, UK: John Wiley & Sons, Ltd, pp. 1–13. ISBN: 9781119005315 (cit. on p. 117).

Nuclear Regulatory Commission, ed. (1995). *RELAP5/MOD3 code manual. Volume 4, Models and correlations* (cit. on pp. 197, 198).

O'brien, M. P. and Gosline, J. E. (1935). "Velocity of Large Bubbles in Vertical Tubes". In: *Industrial & Engineering Chemistry* 27.12, pp. 1436–1440 (cit. on p. 20).

Oguz, H. N. and Prosperetti, A. (1993). "Dynamics of bubble growth and detachment from a needle". In: *Journal of Fluid Mechanics* 257.-1, p. 111. ISSN: 0022-1120 (cit. on p. 86).

Oliveira, P. J. and Issa, R. I. (2003). "Numerical aspects of an algorithm for the Eulerian simulation of two-phase flows". In: *Int. J. Numer. Methods Fluids* 43.10-11, pp. 1177–1198 (cit. on pp. 163, 173).

Oliveira, P. J.D.S. P. (1992). "Computer modelling of multidimensional multiphase flow and application to T-junctions". PhD thesis. Imperial College London (cit. on p. 79).

OpenCFD (2013). *OpenFOAM Programmer Guide* (cit. on p. 173).

O'Rourke, P. (1981). "Collective drop effects on vaporizing liquid sprays". PhD thesis. Princeton University (cit. on p. 25).

— (1985). "The KIVA computer program for multidimensional chemically reactive fluid flows with fuel sprays". In: *Numerical Simulation of Combustion Phenomena*. Ed. by R. Glowinski, B. Larrouturou, and R. Temam. Vol. 241. Lecture Notes in Physics. Springer Berlin Heidelberg, pp. 74–89. ISBN: 978-3-540-16073-1 (cit. on p. 25).

Osher, S. and Sethian, J. A. (1988). "Fronts Propagating with Curvature-dependent Speed: Algorithms Based on Hamilton-Jacobi Formulations". In: *J. Comput. Phys.* 79.1, pp. 12–49. ISSN: 0021-9991 (cit. on p. 24).

Pan, Y, Dudukovic, M. P., and Chang, M (1999). "Dynamic simulation of bubbly flow in bubble columns". In: *Chemical Engineering Science* 54.13-14, pp. 2481–2489. ISSN: 0009-2509 (cit. on pp. 25, 161).

Parthasarathy, R. and Ahmed, N. (1996). "Size Distribution of Bubbles Generated by Fine-Pore Spargers." In: *Journal of chemical engineering of Japan* 29.6, pp. 1030–1034 (cit. on p. 40).

Passalacqua, A. (2013). *http://openfoamwiki.net/index.php/BubbleFoam* (cit. on p. 163).

Patankar, S. V. (1980). *Numerical Heat Transfer and Fluid Flow*. Electro Skills Series. Hemisphere Publishing Corporation. ISBN: 9780070487406 (cit. on p. 173).

Peebles, F. N. and Garber, H. J. (1953). "Studies on the motion of gas bubbles in liquids". In: *Chemical Engineering Progress* 49.2, pp. 88–97 (cit. on pp. 20, 63).

Pellegrini, F. and Roman, J. (1996). "Scotch: A software package for static mapping by dual recursive bipartitioning of process and architecture graphs". In: *High-Performance Computing and Networking*. Springer, pp. 493–498 (cit. on p. 91).

Peng, Z., Doroodchi, E., Luo, C., and Moghtaderi, B. (2014). "Influence of void fraction calculation on fidelity of CFD-DEM simulation of gas-solid bubbling fluidized beds". In: *AIChE Journal* 60.6, pp. 2000–2018. ISSN: 1547-5905 (cit. on pp. 117, 118).

Petitti, M., Nasuti, A., Marchisio, D. L., Vanni, M., Baldi, G., Mancini, N., and Podenzani, F. (2010). "Bubble size distribution modeling in stirred gas-liquid reactors with QMOM augmented by a new correction algorithm". In: *AIChE Journal* 56.1, pp. 36–53. ISSN: 1547-5905 (cit. on pp. 53, 169, 170, 172).

Pfleger, D, Gomes, S, Gilbert, N, and Wagner, H.-G. (1999). "Hydrodynamic simulations of laboratory scale bubble columns fundamental studies of the Eulerian-Eulerian modelling approach". In: *Chemical Engineering Science* 54.21, pp. 5091–5099. ISSN: 0009-2509 (cit. on pp. 25, 28, 29, 161).

Poorte, R. E. G. and Biesheuvel, A (2002). "Experiments on the motion of gas bubbles in turbulence generated by an active grid". In: *Journal of Fluid Mechanics* 461, pp. 127–154. ISSN: 0022-1120 (cit. on p. 21).

Pope, S. B. (2000). *Turbulent Flows*. Cambridge University Press. ISBN: 9780521598866 (cit. on pp. 74, 133, 135, 182).

Popinet, S. and Stéphane (2003). "Gerris: a tree-based adaptive solver for the incompressible Euler equations in complex geometries". In: *Journal of Computational Physics* 190.2, pp. 572–600. ISSN: 00219991 (cit. on p. 86).

Prasser, H.-M, Böttger, A, and Zschau, J (1998). "A new electrode-mesh tomograph for gasliquid flows". In: *Flow Measurement and Instrumentation* 9.2, pp. 111–119. ISSN: 09555986 (cit. on pp. 22, 23).

Prasser, H.-M., Krepper, E., and Lucas, D. (2002). "Evolution of the two-phase flow in a vertical tube-decomposition of gas fraction profiles according to bubble size classes using wire-mesh sensors". In: *International Journal of Thermal Sciences* 41.1, pp. 17–28. ISSN: 1290-0729 (cit. on p. 20).

Prince, M. J. and Blanch, H. W. (1990). "Bubble coalescence and break-up in air-sparged bubble columns". In: *AIChE Journal* 36.10, pp. 1485–1499. ISSN: 0001-1541 (cit. on p. 20).

Prosperetti, A and Tryggvason, G (2007). *Computational Methods for Multiphase Flow*. Cambridge University Press. ISBN: 9781139459907 (cit. on pp. 18, 88).

Prosperetti, A. (2004). "Bubbles". In: *Physics of Fluids* 16.6, pp. 1852–1865. ISSN: 1070-6631 (cit. on pp. 20, 86).

Raffel, M, Willert, C., and Velocimetry, J. K.P. I. (1998). *Particle Image Velocimetry*. Springer-Verlag Berlin Heidelberg (cit. on p. 21).

Ramkrishna, D. (2000). *Population balances: theory and applications to particulate systems in engineering*. San Diego, {CA}: Academic Press. ISBN: 0125769709 9780125769709 (cit. on pp. 79, 169).

Reeks, M. W. (1991). "On a kinetic equation for the transport of particles in turbulent flows". In: *Physics of Fluids A: Fluid Dynamics* 3.3, pp. 446–456. ISSN: 0899-8213 (cit. on p. 77).

— (1992). "On the continuum equations for dispersed particles in nonuniform flows". In: *Physics of Fluids A: Fluid Dynamics* 4.6, pp. 1290–1303. ISSN: 0899-8213 (cit. on p. 77).

Revankar, S. T. and Ishii, M (1993). "Theory and measurement of local interfacial area using a four sensor probe in two-phase flow". In: *International Journal of Heat and Mass Transfer* 36.12, pp. 2997–3007. ISSN: 0017-9310 (cit. on p. 48).

Ribeiro Jr., C. P. and Lage, P. L. C. (2004). "Experimental study on bubble size distributions in a direct-contact evaporator". In: *Brazilian Journal of Chemical Engineering* 21, pp. 69–81. ISSN: 0104-6632 (cit. on pp. 40, 49).

Richardson, B. L., Laboratory, A. N., and Commission, U. S.A. E. (1958). *Some problems in horizontal two-phase two component flow*. AEC research and development report. Argonne National Laboratory (cit. on p. 20).

Roghair, I., Van Sint Annaland, M., and Kuipers, H. J.A. M. (2013). "Drag force and clustering in bubble swarms". In: *AlChE J.* 59.5, pp. 1791–1800. ISSN: 1547-5905 (cit. on pp. 27, 65, 85).

Rosenberg, B. (1950). *The drag and shape of air bubbles moving in liquids*. Tech. rep. DTIC Document (cit. on p. 24).

Rusche, H (2002). "Computational Fluid Dynamics of Dispersed {Two-Phase} Flows at High Phase Fractions". {PhD} Thesis. Imperial College (cit. on pp. 61, 163).

Rzehak, R. and Krepper, E. (2013). "Bubble-induced turbulence: Comparison of CFD models". In: *Nucl. Eng. Des.* 258.0, pp. 57–65. ISSN: 0029-5493 (cit. on pp. 73, 168).

Rzehak, R., Ziegenhein, T., Kriebitzsch, S., Krepper, E., and Lucas, D. (2016). "Unified modeling of bubbly flows in pipes, bubble columns, and airlift columns". In: *Chemical Engineering Science* 157, pp. 147–158. ISSN: 0009-2509 (cit. on pp. 28, 29).

Saffman, P. G. (1965). "The lift on a small sphere in a slow shear flow". In: *Journal of Fluid Mechanics* 22.02, pp. 385–400. ISSN: 1469-7645 (cit. on p. 66).

Sanyal, J., Marchisio, D. L., Fox, R. O., and Dhanasekharan, K. (2005). "On the Comparison between Population Balance Models for CFD Simulation of Bubble Columns". In: *Ind. Eng. Chem. Res.* 44.14, pp. 5063–5072 (cit. on pp. 80, 162).

Sanyal, J., Vásquez, S., Roy, S., and Dudukovic, M. P. (1999). "Numerical simulation of gas-liquid dynamics in cylindrical bubble column reactors". In: *Chem. Eng. Sci.* 54.21, pp. 5071–5083 (cit. on p. 169).

Sato, Y and Sekoguchi, K (1975). "Liquid velocity distribution in two-phase bubble flow". In: *International Journal of Multiphase Flow* 2.1, pp. 79–95. ISSN: 0301-9322 (cit. on pp. 73, 74, 168).

Scarano, F (2013). "Tomographic PIV: principles and practice". In: *Measurement Science and Technology* 24.1, p. 012001. ISSN: 0957-0233 (cit. on p. 21).

Schiller, L and Naumann, Z (1935). "A drag coefficient correlation". In: *Ver. Deutsch. Ing.* Pp. 77–318 (cit. on pp. 64, 164).

Schmitz, D (2000). "Tomographic imaging of transient multiphase flow in bubble columns". In: *Chemical Engineering Journal* 77.1-2, pp. 99–104. ISSN: 13858947 (cit. on p. 22).

Serizawa, A., Kataoka, I., and Michiyoshi, I. (1975). "Turbulence structure of air-water bubbly flow. Parts I-III". In: *International Journal of Multiphase Flow* 2.3, pp. 235–246. ISSN: 0301-9322 (cit. on p. 133).

Shen, X. and Nakamura, H. (2013). "Local interfacial velocity measurement method using a four-sensor probe". In: *International Journal of Heat and Mass Transfer* 67, pp. 843–852. ISSN: 0017-9310 (cit. on p. 48).

Shew, W., Poncet, S., and Pinton, J.-F. (2005). "Path instability and wake of a rising bubble". In: *<hal-00013378v1>* (cit. on p. 86).

Siebert, H., Lehmann, K., Shaw, R. A., Siebert, H., Lehmann, K., and Shaw, R. A. (2007). "On the Use of Hot-Wire Anemometers for Turbulence Measurements in Clouds". In: *Journal of Atmospheric and Oceanic Technology* 24.6, pp. 980–993. ISSN: 0739-0572 (cit. on p. 22).

Silva, L. and Lage, P. L. C. (2011). "Development and implementation of a polydispersed multiphase flow model in OpenFOAM". In: *Comput. Chem. Eng.* 35.12, pp. 2653–2666. ISSN: 0098-1354 (cit. on pp. 81, 162).

Silva, M. J. D., Schleicher, E, and Hampel, U (2007). "Capacitance wire-mesh sensor for fast measurement of phase fraction distributions". In: *Measurement Science and Technology* 18.7, pp. 2245–2251. ISSN: 0957-0233 (cit. on p. 23).

Silva, M. J. da. (2008). *Impedance sensors for fast multiphase flow measurement and imaging*. TUDpress. ISBN: 9783940046994 (cit. on p. 23).

Simonnet, M, Gentric, C, Olmos, E, and Midoux, N (2007). "Experimental determination of the drag coefficient in a swarm of bubbles". In: *Chem. Eng. Sci.* 62.3, pp. 858–866. ISSN: 0009-2509 (cit. on pp. 65, 182).

Sokolichin, A and Eigenberger, G (1999). "Applicability of the standard kϵ turbulence model to the dynamic simulation of bubble columns: Part I. Detailed numerical simulations". In: *Chemical Engineering Science* 54.13, pp. 2273–2284. ISSN: 0009-2509 (cit. on pp. 28, 29).

Solsvik, J. and Jakobsen, H. A. (2015). "Single Air Bubble Breakup Experiments in Stirred Water Tank". In: *International Journal of Chemical Reactor Engineering* 13.4, pp. 477–491. ISSN: 2194-5748 (cit. on p. 20).

Stokes, G. G. (1851). "On the Effect of the Internal Friction of Fluids on the Motion of Pendulums". In: *Transactions of the Cambridge Philosophical Society, Vol. 9, p.8* 9, p. 8 (cit. on p. 62).

Subramaniam, S. (2013). "Lagrangian–Eulerian methods for multiphase flows". In: *Progress in Energy and Combustion Science* 39.2-3, pp. 215–245. ISSN: 0360-1285 (cit. on p. 26).

Sugioka, K.-I. and Komori, S. (2009). "Drag and lift forces acting on a spherical gas bubble in homogeneous shear liquid flow". In: *Journal of Fluid Mechanics* 629, p. 173. ISSN: 0022-1120 (cit. on p. 110).

Sweby, P. K. (1984). "High resolution schemes using flux limiters for hyperbolic conservation laws". In: *SIAM J. Numer. Anal.* 21.5, pp. 995–1011 (cit. on p. 175).

Tennekes, H. H. and Lumley, J. L.J. L. (1972). *A first course in turbulence*. MIT Press, p. 300. ISBN: 9780262200196 (cit. on p. 72).

Theremin, L (1830). "Recherches sur la figure et le mouvement d'une bulle d'air, dans un liquide de densité constante.(Suite)." In: *Journal für die reine und angewandte Mathematik* 5, pp. 374–379 (cit. on p. 24).

Thomson, D. J. (1987). "Criteria for the selection of stochastic models of particle trajectories in turbulent flows". In: *Journal of Fluid Mechanics* 180, pp. 529–556 (cit. on p. 134).

Tian, D., Yan, C., Sun, L., and Liu, G. (2014). "Local interfacial parameter distribution for two-phase flow under rolling conditions using a four-sensor optical probe". In: *Annals of Nuclear Energy* 66, pp. 124–132. ISSN: 0306-4549 (cit. on p. 47).

Tomiyama and A. (2004). "Drag, Lift and Virtual Mass Forces Acting on a Single Bubble". In: *3rd Int. Symp. on Two-Phase Flow Modeling and Experimentation, 2004* (cit. on p. 68).

Tomiyama, A., Celata, G., Hosokawa, S., and Yoshida, S. (2002a). "Terminal velocity of single bubbles in surface tension force dominant regime". In: *International Journal of Multiphase Flow* 28.9, pp. 1497–1519. ISSN: 03019322 (cit. on p. 65).

Tomiyama, A., Kataoka, I., Fukuda, T., and Sakaguchi, T. (1995). "Drag Coefficients of Bubbles : 2nd Report, Drag Coefficient for a Swarm of Bubbles and its Applicability to Transient Flow". In: *Trans. Jpn. Soc. Mech. Eng. Ser. B* 61.588, pp. 2810–2817 (cit. on p. 65).

Tomiyama, A., Kataoka, I., Zun, I., and Sakaguchi, T. (1998). "Drag Coefficients of Single Bubbles under Normal and Micro Gravity Conditions". In: *JSME Int. J. Ser. B* 41.2, pp. 472–479 (cit. on pp. 63, 64, 99, 109, 110, 165, 185, 186, 198).

Tomiyama, A., Tamai, H., Zun, I., and Hosokawa, S. (2002b). "Transverse migration of single bubbles in simple shear flows". In: *Chemical Engineering Science* 57.11, pp. 1849–1858. ISSN: 0009-2509 (cit. on pp. 67, 110, 166, 185, 186).

Trip, R., Kuik, D. J., Westerweel, J., and Poelma, C. (2012). "An experimental study of transitional pulsatile pipe flow". In: *Physics of Fluids* 24.1, p. 014103. ISSN: 1070-6631 (cit. on p. 44).

Tripathi, M. K., Sahu, K. C., and Govindarajan, R. (2015). "Dynamics of an initially spherical bubble rising in quiescent liquid". In: *Nature communications* 6, p. 6268. ISSN: 2041-1723 (cit. on p. 86).

Troniewski, L. and Ulbrich, R. (1984). "Two-phase gas-liquid flow in rectangular channels". In: *Chemical Engineering Science* 39.4, pp. 751–765. ISSN: 00092509 (cit. on p. 20).

Troshko, A. A. and Hassan, Y. A. (2001a). "A two-equation turbulence model of turbulent bubbly flows". In: *International Journal of Multiphase Flow* 27.11, pp. 1965–2000. ISSN: 0301-9322 (cit. on pp. 74, 75, 133, 134).

— (2001b). "Law of the wall for two-phase turbulent boundary layers". In: *International Journal of Heat and Mass Transfer* 44.4, pp. 871–875. ISSN: 0017-9310 (cit. on p. 134).

Tryggvason, G., Lu, J., Biswas, S., and Esmaeeli, A. (2009). "Studies of Bubbly Channel Flows by Direct Numerical Simulations". In: *Turbulence and Interactions: Keynote Lectures of the TI 2006 Conference*. Ed. by M. Deville, T.-H. Lê, and P. Sagaut. Berlin, Heidelberg: Springer Berlin Heidelberg, pp. 93–111. ISBN: 978-3-642-00262-5 (cit. on pp. 27, 86).

Uga, T. (1972). "Determination of bubble-size distribution in a BWR". In: *Nuclear Engineering and Design* 22.2, pp. 252–261. ISSN: 0029-5493 (cit. on p. 40).

Unverdi, S. O. and Tryggvason, G. (1992). "A front-tracking method for viscous, incompressible, multi-fluid flows". In: *Journal of Computational Physics* 100.1, pp. 25–37. ISSN: 00219991 (cit. on p. 24).

Vaidya, A. M., Subbarao, P. M. V., and Gaur, R. R. (2006). "A Novel and Efficient Method for Particle Locating and Advancing over Deforming, NonOrthogonal Mesh". In: *Numerical Heat Transfer, Part B: Fundamentals* 49.1, pp. 67–88 (cit. on p. 118).

Vakhrushev, I. A. and Efremov, G. I. (1970). "Interpolation formula for computing the velocities of single gas bubbles in liquids". In: *Chem. Technol. Fuels Oils* 6.5, pp. 376–379 (cit. on pp. 66, 165).

Veysey, J. and Goldenfeld, N. (2007). "Simple viscous flows: From boundary layers to the renormalization group". In: *Reviews of Modern Physics* 79.3, pp. 883–927. ISSN: 0034-6861 (cit. on p. 63).

Vries, A. W. G. de (2001). "Path and wake of a Rising Bubble". PhD thesis. Enschede (cit. on pp. 20, 70, 73, 86, 97, 98, 140).

Wallis, G. B. (1969). *One-dimensional two-phase flow*. McGraw-Hill (cit. on p. 197).

Wambsganss, M. W., Jendrzejczyk, J. A., and France, D. M. (1991). "Two-phase flow patterns and transitions in a small, horizontal, rectangular channel". In: *International Journal of Multiphase Flow* 17.3, pp. 327–342. ISSN: 0301-9322 (cit. on p. 20).

Wang, S. K., Lee, S. J., Jr., O. C. J., and Jr, R. T. L. (1987). "3-D turbulence structure and phase distribution measurements in bubbly two-phase flows". In: *Int. J. Multiphase Flow* 13.3, pp. 327–343. ISSN: 0301-9322 (cit. on pp. 20, 67, 166).

Wang, T., Wang, J., and Jin, Y. (2005). "Population Balance Model for Gas-Liquid Flows: Influence of Bubble Coalescence and Breakup Models". In: *Industrial & engineering chemistry research* 44.19, pp. 7540–7549 (cit. on pp. 25, 161).

Weller, H. G. (2005). *Derivation, modelling and solution of the conditionally averaged two-phase flow equations*. Tech. rep. United Kingdom: OpenCFD Ltd. (cit. on pp. 61, 163, 173).

Wheeler, J. C. (1974). "Modified moments and Gaussian quadratures". In: *Rocky Mountain J. Math.* 4, pp. 287–296 (cit. on pp. 162, 172, 182).

Wijngaarden, L van (1998). "On Pseudo Turbulence". In: *Theoretical and Computational Fluid Dynamics* 10.1, pp. 449–458 (cit. on p. 133).

Williams, F. A. (1958). "Spray Combustion and Atomization". In: *Physics of Fluids (1958-1988)* 1.6, pp. 541–545 (cit. on p. 25).

Wilson, J. D., Thurtell, G. W., and Kidd, G. E. (1981). "Numerical simulation of particle trajectories in inhomogeneous turbulence, II: Systems with variable turbulent velocity scale". In: *Boundary-Layer Meteorology* 21.4, pp. 423–441. ISSN: 1573-1472 (cit. on p. 135).

Witold (1911). *Über die fortschreitende Bewegung einer flüssigen Kugel in einen zähen Medium*. Akademia Umiejetnosci (cit. on p. 24).

Wu, C. L., Zhan, J. M., Li, Y. S., Lam, K. S., and Berrouk, A. S. (2009a). "Accurate void fraction calculation for three-dimensional discrete particle model on unstructured mesh". In: *Chemical Engineering Science* 64.6, pp. 1260–1266. ISSN: 0009-2509 (cit. on p. 117).

Wu, C. L., Berrouk, A. S., and Nandakumar, K (2009b). "Three-dimensional discrete particle model for gassolid fluidized beds on unstructured mesh". In: *Chemical Engineering Journal* 152.23, pp. 514–529. ISSN: 1385-8947 (cit. on p. 117).

Xiao, H. and Sun, J. (2011). "Algorithms in a Robust Hybrid CFD-DEM Solver for Particle-Laden Flows". In: *Communications in Computational Physics* 9.2, pp. 297–323 (cit. on p. 117).

Xu, B. and Yu, A. (1997). "Numerical simulation of the gas-solid flow in a fluidized bed by combining discrete particle method with computational fluid dynamics". In: *Chemical Engineering Science* 52.16, pp. 2785–2809. ISSN: 00092509 (cit. on p. 117).

Yang, G. and Chen, I.-M. (2006). "Equivolumetric partition of solid spheres with applications to orientation workspace analysis of robot manipulators." In: *IEEE Transactions on Robotics* 22.5, pp. 869–879 (cit. on pp. 118, 119).

Yao, W. and Morel, C. (2004a). "Volumetric interfacial area prediction in upward bubbly two-phase flow". In: *International Journal of Heat and Mass Transfer* 47.2, pp. 307–328. ISSN: 0017-9310 (cit. on pp. 28, 29, 168).

— (2004b). "Volumetric interfacial area prediction in upward bubbly two-phase flow". In: *International Journal of Heat and Mass Transfer* 47.2, pp. 307–328. ISSN: 0017-9310 (cit. on pp. 75, 134).

Yuan, C, Kong, B, Passalacqua, A, and Fox, R. O. (2014). "An extended quadrature-based mass-velocity moment model for polydisperse bubbly flows". In: *Can. J. Chem. Eng.* 92.12, pp. 2053–2066 (cit. on p. 171).

Zaepffel, D. (2011). "Modelling of polydisperse bublly flows". Theses. Université Grenoble Alpes (cit. on p. 49).

Zaruba, A., Lucas, D., Prasser, H.-M., and Höhne, T. (2007). "Bubble-wall interactions in a vertical gas–liquid flow: Bouncing, sliding and bubble deformations". In: *Chemical Engineering Science* 62.6, pp. 1591–1605. ISSN: 0009-2509 (cit. on pp. 20, 187).

Zenit, R., Koch, D. L., and Sangani, A. S. (2001). "Measurements of the average properties of a suspension of bubbles rising in a vertical channel". In: *Journal of Fluid Mechanics* 429, pp. 307–342. ISSN: 1469-7645 (cit. on p. 20).

Zenit, R. and Legendre, D. (2009). "The coefficient of restitution for air bubbles colliding against solid walls in viscous liquids". In: *Physics of Fluids* 21.8, p. 83306 (cit. on pp. 20, 68).

Zhang, D, Deen, N. G., and Kuipers, J. A. M. (2006). "Numerical simulation of the dynamic flow behavior in a bubble column: A study of closures for turbulence and interface forces". In: *Chemical Engineering Science* 61.23, pp. 7593–7608 (cit. on pp. 25, 161).

Zhang, Z. (2010). *LDA Application Methods*. Berlin, Heidelberg: Springer Berlin Heidelberg. ISBN: 978-3-642-13513-2 (cit. on pp. 21, 136).

Zuber, N. and Findlay, J. A. (1965). "Average Volumetric Concentration in Two-Phase Flow Systems". In: *Journal of Heat Transfer* 87.4, p. 453. ISSN: 00221481 (cit. on p. 195).

Žun, I. (1980). "The transverse migration of bubbles influenced by walls in vertical bubbly flow". In: *International Journal of Multiphase Flow* 6.6, pp. 583–588. ISSN: 03019322 (cit. on p. 66).

Žun, I. and Grošelj, J. (1996). "The structure of bubble non-equilibrium movement in free-rise and agitated-rise conditions". In: *Nuclear Engineering and Design* 163.1-2, pp. 99–115. ISSN: 00295493 (cit. on p. 63).